Constraining alternative cosmological models with current and future observations

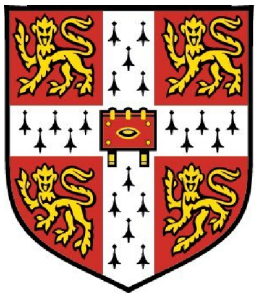

José-Alberto Vázquez-González

Kavli Institute for Cosmology/ Cavendish Laboratory

$\sim$ St Edmund's College $\sim$

This dissertation is submitted for the degree of

Doctor of Philosophy

April 08, 2013

Declaration

This dissertation is the result of my own work and includes nothing which is the outcome of work done in collaboration except where specifically indicated in the text.

This dissertation contains 57,629 words, 59 figures and 8 tables, which is within limits set by the Physics Department.

JA Vázquez
Cambridge, April 08, 2013

Publications

Those parts of this dissertation which have been published or accepted for publication are as follow:

1. *A Bayesian study of the primordial power spectrum from a novel closed universe model.*
   J. Alberto Vázquez, A.N. Lasenby, M.P. Hobson, M. Bridges, MNRAS, 422, 1948-1956, 2011, [arXiv:1103.4619].
2. *Bayesian reconstruction of the Primordial Power Spectrum.*
   J. Alberto Vázquez, M.P. Hobson, M. Bridges, A.N. Lasenby, JCAP, 006(106), 2012, [arXiv:203.1252].
3. *Reconstruction of the Dark Energy equation of state.*
   J. Alberto Vázquez, M.P. Hobson, M. Bridges, A.N. Lasenby, JCAP, 09(020), 2012, [arXiv:1205.0847].
4. *Reciprocity invariance of the Friedmann equation, missing matter and double dark energy.*
   J. Alberto Vázquez, M.P. Hobson, A.N. Lasenby, M. Ibison, M. Bridges, Submitted to PRD, [arXiv:1208.2542].
5. *Constraints on the Tensor-to-Scalar ratio for non-power-law models.*
   J. Alberto Vázquez, M. Bridges, Yin-Zhe Ma, M. Hobson, Sumitted to JCAP, [arXiv:1303.4014].
6. *Cosmological constraints on Modified Gravity.*
   J. Alberto Vázquez, M.P. Hobson, A.N. Lasenby, M. Bridges, In preparation.

A mis padres y hermana:

Yolanda González Soto,

José-Alberto Vázquez Zagal,

Alba-Yolanda Vázquez González.

Mil Gracias.

Acknowledgements

I would like to thank Professor Anthony Lasenby and Professor Mike Hobson for the opportunity to pursue a doctoral degree at the Astrophysics Group, University of Cambridge; for their guidance and example as people and researchers. I would also like to thank Doctor Michael Bridges for his patience and very helpful advices.

Many thanks to the people in the Cavendish Laboratory and Kavli Institute for Cosmology for their valuable comments that have contributed to the realisation of this project.

Special gratitude to my college friends and colleagues in Cambridge, to my family and friends in Cuernavaca. Thanks to all of them for their encouragement and support during my doctoral studies. Also, to those whose patience and caring helped me throughout my studies.

Finally, I would like to acknowledge the Mexican National Council for Science and Technology (CONACYT, 184531/200401) for funding my studies; to the Secretariat of Public Education (SEP) for a complementary grant; and to the Astrophysics group and St Edmund's college for their financial support.

Abstract

Rapid advance in the development of powerful observational instruments has led to the establishment of precision cosmology. The principal aim of this dissertation is to analyse both existing and forthcoming astronomical observations, through advanced statistical techniques, to search for possible deviations from the concordance ΛCDM model. Particular emphasis is placed on epochs where the universe undergoes an acceleration period: the inflationary epoch generated by a scalar-field at the earliest stages of the universe, and the late-time accelerated expansion attributed to a yet-unknown component termed dark energy. The general properties of each epoch are commonly summarised, respectively, via the primordial power spectrum $\mathcal{P}(k)$ and the dark energy equation-of-state $w(z)$. Departures from standard values are sought by, first, the implementation of an optimal node-based reconstruction to determine the global structure of $\mathcal{P}(k)$ and $w(z)$. Then, alternative models and more general theories are also explored, for instance the Lasenby & Doran model used to construct inflationary models in closed universes. Models to provide a possible explanation of the late-time acceleration of the universe are also considered, either by the inclusion of a second dark energy component in standard ΛCDM, or by modifying the laws of gravity on cosmological scales. The search for new cosmological features is carried out through current observational data coming from studies of the Cosmic Microwave Background radiation (CMB), Large-Scale Structure (LSS) and supernovae Type Ia. In addition to present observations, simulations of future CMB surveys are also incorporated into the analysis. In this work we have found models that exhibit mild deviations from the minimal form of the standard cosmological model. These models are in good agreement with current data and, in spite of their complexity and extra parameters, they share a similar Bayesian evidence compared to the ΛCDM model.

Contents

List of Figures

LIST OF FIGURES

LIST OF FIGURES

List of Tables

LIST OF TABLES

Notation

Some of the notation adopted throughout this dissertation is as follows:

- We use the natural unit system, wherein the speed of light c, Planck's constant $\hbar$ and Boltzmann's constant $k_{\rm B}$, are set to unity

$$c = \hbar = k_{\rm B} = 1. \tag{1}$$

- Greek indices run over time coordinate (labelled by '0') and three spatial-Latin coordinates:

$$\alpha, \beta, \cdots \in \{0, 1, 2, 3\}, \qquad \text{and} \qquad i, j, \cdots \in \{1, 2, 3\}. \tag{2}$$

- A dot over any quantity denotes time derivative of that quantity, prime represents conformal-time derivatives and subscript comma derivatives with respect to space coordinates or fields:

$$\dot{f} \equiv \frac{\partial f}{\partial t}, \quad , f' \equiv \frac{\partial f}{\partial \eta}, \quad \text{and} \quad f_{,\phi} \equiv \frac{\partial f}{\partial \phi}. \tag{3}$$

- We adopt the sign convention commonly used in relativity and cosmology:

$$\eta_{\mu\nu} = \text{diag}(-1, 1, 1, 1). \tag{4}$$

- Quantities evaluated at present time ($t = t_0$) are also expressed by a subscript '0'.

- Spatial vectors are represented by any of these forms: $\mathbf{x}, x^i, \vec{x}$.

Chapter 1

Outline

The outline of the thesis is as follows. In **Chapter 2** we start by introducing the theoretical framework that underlies the standard model of modern cosmology: the concordance ΛCDM. Here we present the basic concepts that will be used in later chapters. We then provide a brief description of the homogeneous and perturbed universe, and for completeness, a short overview of the inflationary model is also given. The main goal of this chapter is the computation of the distance modulus, cosmic microwave background spectrum and matter power spectrum which allows us to establish a connection between theoretical models and cosmological observations, through statistical tools described in the next chapter. **Chapter 3** is focussed on the analysis of cosmological observations for a given theoretical model. We provide a short introduction to the principal quantities that describe the properties of the universe. Then, we highlight present and future experimental results used throughout this work, e.g. cosmic microwave background, supernovae Type Ia and large-scale-structure observations. Finally, with the use of Bayesian analysis, we illustrate the parameter estimation and model selection in the context of the standard ΛCDM model, for a spatially flat and non-flat universe. The current constraints on the standard parameters, as well as the Bayesian evidence, are compared for each model. As part of the analysis, dataset consistency is also investigated.

Chapter 4 is devoted to determining the preferred shape of the primordial spectrum of curvature perturbations. We first reconstruct the spectrum modelled as piecewise linear in $\log k$ between nodes in k-space whose amplitudes and positions are allowed to vary. The number of nodes together with their positions are chosen by the Bayesian evidence, so that we can both determine the complexity supported by the data and locate any features present in the spectrum. In addition to the node-based reconstruction, we consider a set of models for the primordial spectrum: the standard power-law parameterisation, the spectrum produced from the Lasenby & Doran (LD) model and a simple variant parameterisation. In particular we explore in a more detail the LD model, which is based on the restriction of the total conformal time available in a closed Universe. An important feature of the LD spectrum is that it naturally incorporates an exponential fall-off at large scales without the need to parameterise it, while, at small scales it automatically incorporates a degree of negative running compared with the standard power-law parameterisation. In addition to parameter estimation, we select the preferred model by comparing the different classes of models through its Bayesian evidence. We find the power-law parameterisation is *significantly disfavoured* by current cosmological observations, which show a preference for the LD model.

In **Chapter** 4 we show that recent cosmological observations hint at a deviation from the simple power-law form of the primordial spectrum of curvature perturbations. In **Chapter** 5 we find that in the presence of a tensor component, the turn-over in the initial spectrum is enhanced and hence non-power-law models ought to be considered. For instance, for a power-law parameterisation with both a tensor component and running parameter, current data show a preference for a negative running at more than 2.5σ C.L. As a consequence of this deviation from a power-law, constraints on the tensor-to-scalar ratio r are slightly broader. Here, we also present constraints on the inflationary parameters for a model-independent reconstruction and the Lasenby & Doran model. In particular, the constraints on the tensor-to-scalar ratio from the LD model are: $r_{\rm LD} = 0.11 \pm 0.024$. In addition to current data, we show expected constraints from Planck-like and CMB-Pol sensitivity experiments by using Markov-Chain-Monte-Carlo sampling chains. The Bayes factor, using current observations, shows

a *strong preference* for the LD model over the standard power-law parameterisation, and provides an insight into the accuracy of differentiating models through future surveys.

One of the main challenges of modern cosmology is to investigate the nature of the dark energy, introduced to explain the present accelerated-expansion of the universe. The properties of such a component are normally summarised as a perfect fluid with a (potentially) time-dependent equation-of-state parameter $w(z)$. In **Chapter** 6 we investigate the evolution of this parameter with redshift by performing an optimal model-independent reconstruction. The process is essentially identical to the approach used to recover the preferred shape of the primordial spectrum. We compare this reconstruction with some previously well-studied parameterisations: the Chevallier-Polarski-Linder (CPL), the Jassal-Bagla-Padmanabhan (JBP) and the Felice-Nesseris-Tsujikawa (FNT). We find an indication towards *possible time-dependence* in the dark energy equation-of-state. It is also worth noting that the CPL and JBP models are strongly disfavoured, whilst the FNT is just significantly disfavoured, when compared to a simple cosmological constant.

In **Chapter** 7, we explore the possibility that, in fact, there exist two dark-energy components: the cosmological constant Λ, with equation-of-state parameter $w_\Lambda = -1$, and a 'missing matter' component X with $w_X = -2/3$, which we introduce here to allow the Friedmann equation written in terms of conformal time η to be form-invariant under the reciprocity transformation $a(\eta) \to 1/a(\eta)$ of the scale factor. Using recent cosmological observations, we constrain the present-day energy density of missing matter to be $\Omega_{X,0} = -0.11 \pm 0.14$. This is consistent with the standard ΛCDM model, but constraints on the energy densities of all the components are considerably broadened by the introduction of missing matter; significant relative probability exists even for $\Omega_{X,0} \sim 0.2$, and so the presence of a missing matter component cannot be ruled out. We extend our analysis by allowing w_X to be a free parameter. For this more generic 'double dark energy' model, we find $w_X = -1.02 \pm 0.20$ and $\Omega_{X,0} = 0.08 \pm 0.57$, which is again consistent with the standard ΛCDM model, although once more the posterior distributions are

sufficiently broad that the existence of a second dark-energy component cannot be ruled out. Moreover, the two-dimensional posterior in the $(w_X, \Omega_{X,0})$-plane is strongly bimodal with both peaks offset from the standard ΛCDM model corresponding to $(-1, 0)$, although the latter is still admissible; this bimodality is in contrast to the correctly-centred unimodal posterior typically obtained when analysing realisations of simulated observations from a ΛCDM model. The model including the second dark energy component also has a similar Bayesian evidence to ΛCDM to within the numerical uncertainty.

Modifications to general relativity have been suggested as viable alternatives to dark energy. In **Chapter** 8 we investigate the evolution both of the background universe and density perturbations for a modified gravity theory. While the cosmic expansion can be recast using an effective equation-of-state $w_{\rm eff}(a)$, the evolution of linear perturbations is studied by the introduction of two parametric functions: the ratio of the two metric potentials and the ratio of an effective gravitational constant to the Newtonian constant in the Poisson equation. With the use of current observational data we impose constraints on the parameters λ, α and n used to parameterise a variant of the Starobinsky model $f(R) = R - \lambda\, R_c \left[1 - \left(1 + \alpha \frac{R}{R_c}\right)^{-n}\right]$. In particular, we find that for $n = 2$, current cosmological observations limit the present value of the field-amplitude to be $|F_0 - 1| < 0.002$, and its effective equation-of-state $|w_{\rm eff,0} + 1| < 0.002$, both at 95% C.L. We also find that our $f(R)$ model with $n = 2$ is significantly preferred over the standard ΛCDM model.

Chapter 2

Theoretical Framework

In this Chapter, we start by introducing the theoretical framework that underlies the standard model of modern cosmology: the concordance ΛCDM model. We briefly review the equations determining the evolution of a homogeneous and isotropic universe and present, to first-order, the formalism of cosmological perturbation theory. For the sake of completeness, we have included the inflationary model as a solution to some of the shortcomings of the Hot Big Bang model. Finally, the computation of the distance modulus, cosmic microwave background spectrum and matter power spectrum allows us to establish a connection between cosmological models and current (future) observations, through statistical tools described in the next chapter. Some reference books have been used throughout this short review: Dodelson [60], Hobson et al. [92], Liddle and Lyth [139], Mukhanov [167]; as well as some course notes: Peiris [177], Pettini [182], Challinor [39].

2.1 The Homogeneous Universe

The standard description of the dynamical properties of the universe is provided by the Einstein's theory of General Relativity (GR), which builds a connection between the curvature of the space-time and its matter-content, through fundamental quantities: the *metric* $g_{\mu\nu}$ and the *energy-momentum tensor* $T_{\mu\nu}$. In order to specify the geometry of the universe, an essential assumption is the *Cosmo-*

logical Principle: when averaged over sufficiently large-scales, the universe looks essentially *Homogeneous* and *Isotropic*. For instance, at scales larger than 100 Mpc, the distribution of galaxies over the celestial sphere does seem to justify the assumption of isotropy [46]. Moreover, the current uniformity in the temperature distribution of the *Cosmic Microwave Background* (CMB) radiation, to a few parts in 10^5 [120], is the best observational evidence we have in support of an isotropic universe. If isotropy is thus taken for granted and considering the *Copernican Principle* (our position in the universe is by no means preferred to any other), then homogeneity follows from isotropy at every point.

Under these conditions, the most general expression for the metric $g_{\mu\nu}$ that incorporates the property of a *spatially* homogeneous and isotropic universe, can be written in the Friedmann-Robertson-Walker (FRW) form:

$$ds^2 \equiv g_{\mu\nu}dx^\mu dx^\nu = -dt^2 + R^2(t)\gamma_{ij}dx^i dx^j. \tag{2.1}$$

The evolution of the universe, represented by the scale factor $R(t)$, depends only on the cosmic time t because of the homogeneity assumption. Isotropy is implied by requiring that time-time g_{00} and space-space g_{ii} are the only non-zero components, otherwise a particular direction in space could be preferred. Over the years, cosmological observations have provided decisive evidence that the universe is currently expanding, hence the scale factor satisfies $\dot{R}(t) > 0$, see Hubble [102], Perlmutter et al. [180], Riess et al. [193]. The spatial part of the metric is written as

$$\gamma_{ij}dx^i dx^j = \frac{d\tilde{r}^2}{1 - k\tilde{r}^2} + \tilde{r}^2 d\Omega^2, \tag{2.2}$$

where $\tilde{r}$ is the radial coordinate and $d\Omega^2 = d\theta^2 + \sin^2\theta d\phi^2$ is the metric on the 2-sphere. The constant k classifies the curvature of the spatial sections, with closed, flat and open universes corresponding to $k = +1, 0, -1$, respectively.
A convenient form in which to express the FRW metric is by using coordinates normalised to present time, labelled with subscript '0', i.e.

$$a(t) \equiv \frac{R(t)}{R_0}, \qquad r \equiv R_0\tilde{r}, \tag{2.3}$$

and the curvature parameter $\kappa = k/R_0^2$, of dimensions [length]$^{-2}$. Note that κ can take any value and not just be restricted to $\{+1, 0, -1\}$. The *general FRW metric* written in terms of the normalised scale factor $a(t)$ is thus given by

$$ds^2 = -dt^2 + a^2(t)\left[\frac{dr^2}{1-\kappa r^2} + r^2 d\Omega^2\right]. \tag{2.4}$$

The physical meaning of the curvature term becomes more apparent by redefining the radial coordinate in the metric (2.4), to give

$$ds^2 = -dt^2 + a^2(t)\left[d\chi^2 + S_k^2(\chi)d\Omega^2\right], \tag{2.5}$$

where the function $S_k(\chi)$ is specified by the curvature term:

$$S_k(\chi) = \begin{cases} \sin\chi, & \text{for} \quad \kappa > 0 \quad \text{(closed universe)} \\ \chi, & \text{for} \quad \kappa = 0 \quad \text{(flat universe)} \\ \sinh\chi, & \text{for} \quad \kappa < 0 \quad \text{(open universe)} \end{cases} \tag{2.6}$$

and the comoving radial χ-coordinate, on a null geodesic, is computed from

$$\chi = \frac{1}{R_0}\int \frac{dt}{a(t)}. \tag{2.7}$$

Therefore the dynamics of the space-time, in a homogeneous and isotropic universe, reduces to determining the normalised scale factor $a(t)$, which is computed from Einstein's equations once the matter content is specified, as we shall see below.

2.1.1 The Einstein equations

Once we have specified the metric to describe the homogeneous and isotropic expanding universe, the evolution of both the scale factor and matter density follow from Einstein's equations:

$$G_{\mu\nu} \equiv R_{\mu\nu} - \frac{1}{2}g_{\mu\nu}R = 8\pi G\, T_{\mu\nu}. \tag{2.8}$$

Here $G_{\mu\nu}$ is the *Einstein metric tensor*, the *Ricci tensor* $R_{\mu\nu}$ is a combination of first and second derivatives of $g_{\mu\nu}$, and its trace is defined as the *Ricci scalar* $R \equiv g^{\mu\nu}R_{\mu\nu}$; G is Newton's constant. On the right hand side, the energy-momentum

tensor $T_{\mu\nu}$ contains the constituents of the universe. An acceptable modification to Einstein's equations is the introduction of a Lorentz-invariant constant-term $\Lambda g_{\mu\nu}$ into the field equations:

$$R_{\mu\nu} - \frac{1}{2} g_{\mu\nu} R + \Lambda g_{\mu\nu} = 8\pi G\, T_{\mu\nu}, \tag{2.9}$$

where Λ is called the *cosmological constant* and its value, according to astrophysical observations, is $\Lambda \sim 10^{-52}\mathrm{m}^{-2}$ [36, 174]; we will see more about this component in subsequent sections. Equation (2.9) is in general a complicated set of coupled non-linear second-order partial differential equations for the ten elements of the metric $g_{\mu\nu}$. Nevertheless, they may exhibit simple analytical solutions in the presence of generic symmetries, for instance, under the assumption of the FRW metric. Considering $g_{\mu\nu}$ in the form of (2.4), the only non-vanishing curvature terms are given by

$$R_0^0 = -\frac{3\ddot{a}}{a}, \tag{2.10}$$

$$R_j^i = \left(\frac{\ddot{a}}{a} + \frac{2\dot{a}^2}{a^2} + \frac{2\kappa}{a^2}\right)\delta_j^i, \tag{2.11}$$

$$R = 6\left(\frac{\ddot{a}}{a} + \frac{\dot{a}^2}{a^2} + \frac{\kappa}{a^2}\right), \tag{2.12}$$

where an overdote indicates derivative with respect to cosmic time t ($\dot{\cdot} \equiv d/dt$).

The geometry of the space-time is determined by equations (2.10)-(2.12), then to solve Einstein's equations we just need to specify the matter content under consideration. Let us start by assuming an ideal *perfect-fluid* as the main source of the energy-momentum tensor

$$T^{\mu\nu} = (p + \rho)u^\mu u^\nu - p g^{\mu\nu}, \tag{2.13}$$

where ρ is the energy density and p the isotropic pressure of the fluid, both of them measured by an observer in a local inertial frame in which the fluid is at rest. In the rest frame, where the 4-velocity of the fluid is $u^\mu = (1, 0, 0, 0)$, the energy-momentum tensor reduces to $T^\mu_\nu = \mathrm{diag}(-\rho, g^{ii}p)$. Thus, Einstein's equations for a perfect fluid in a FRW background provide two independent expressions

(time-time and space-space components), which together yield the *Friedmann* and *acceleration* equations:

$$\left(\frac{\dot{a}}{a}\right)^2 = \frac{8\pi G}{3}\rho - \frac{\kappa}{a^2} + \frac{1}{3}\Lambda, \tag{2.14}$$

$$\frac{\ddot{a}}{a} = -\frac{4\pi G}{3}(\rho + 3p) + \frac{1}{3}\Lambda. \tag{2.15}$$

The cosmological equations, in which $a(t)$ is computed under the aforementioned conditions, are known as Friedmann-Lemaître-Robertson-Walker equations; we simply refer to them as Friedmann equations.

Another equation of interest is the conservation of the energy-momentum tensor, $T^{\mu}_{\nu;\,\mu} = 0$, which leads to the *continuity equation*:

$$\dot{\rho} + 3\frac{\dot{a}}{a}(\rho + p) = 0. \tag{2.16}$$

In order to solve the full set of cosmological equations, we still need to specify an extra condition, for instance the pressure for every kind of material the universe is filled with. The usual, and well-founded, assumption is that there is a pressure contribution associated to each energy density, so that $p \equiv p(\rho)$. Such a relationship is known as the *equation-of-state*. The Friedmann equations (2.14), the energy-momentum conservation (2.16), and the equation-of-state $p = p(\rho)$ are therefore the fundamental expressions that describe the dynamics of a homogeneous and isotropic universe.

2.1.2 Cosmic Inventory

In order to understand the dynamical properties of the universe, we first need to bear in mind the whole content of it. Let us focus on single-barotropic perfect-fluids that satisfy, in general, a time-dependent equation-of-state $w(a)$, of the form

$$p = w(a)\rho. \tag{2.17}$$

For any component, with constant w, the continuity equation (2.16) can be easily integrated to give [1]

$$\rho \propto a^{-3(1+w)}. \tag{2.19}$$

Moreover, in a universe dominated by the energy density ρ, the Friedmann equation leads to the time evolution of the scale factor:

$$a \propto t^{2/3(1+w)}, \qquad \forall \quad w \neq -1. \tag{2.20}$$

That is, the evolution of a universe filled with a given perfect fluid is known once its equation-of-state is specified. The standard Λ-Cold Dark Matter model (ΛCDM) relies upon four main ingredients, described by radiation (photons, massless neutrinos), matter (baryons), the inclusion of a dark matter component (DM) and vacuum energy (Λ). The behaviour of each of these components is summarised as follows:

Radiation

This relativistic component dominates during the earliest stages of the universe. Radiation is characterised by an associated pressure $p_{\rm r} = \rho_{\rm r}/3$, with equation-of-state $w_{\rm r} = 1/3$. The evolution of its energy-density and scale factor are thus given by

$$\rho_{\rm r}(t) \propto a^{-4}, \qquad \text{and} \qquad a(t) \propto t^{1/2}. \tag{2.21}$$

The total radiation energy-density ρ_r in the universe may be written as the sum of two main contributions: photons (γ) and massless neutrinos (ν):

$$\rho_{\rm r}(t) = \rho_\gamma(t) + \rho_\nu(t). \tag{2.22}$$

Photons - Primordial photons play a key role in observational cosmology as they constitute the cosmic microwave background radiation we nowadays observed, as we shall see in more detail in Sections 2.4.2 and 3.2.1.

[1] For a more general description of $w(a)$, the evolution of the energy density is given by

$$\rho \propto \exp[-3X(a)], \qquad \text{with} \qquad X(a) = \int_1^a [1 + w(a')] d\ln a'. \tag{2.18}$$

Neutrinos - Neutrinos are very weakly interacting leptons, which come in three types or 'flavours': electron, muon, and tau; all of them with an associated antiparticle. Under the assumption that neutrinos are massless, their contribution to the energy density would be

$$\rho_\nu = N_{\rm eff} \times \frac{7}{8} \times \left(\frac{4}{11}\right)^{4/3} \rho_\gamma, \qquad m_\nu = 0, \tag{2.23}$$

where $N_{\rm eff}$ is the effective number of neutrino species; note that $N_{\rm eff} = 3.046$ for the standard neutrino species [153]. Nevertheless, various experiments suggest they do have a very small mass (experiments detecting atmospheric neutrinos, solar neutrinos) and therefore a density parameter (2.34) corresponding to

$$\Omega_\nu = \frac{m_\nu}{94h^2{\rm eV}}, \qquad m_\nu \neq 0. \tag{2.24}$$

Cosmological observations have also provided limits on the neutrino mass, some reviews in the subject can be found in: Dolgov [61], Elgarøy and Lahav [69], Hannestad [87], Lesgourgues and Pastor [132].

Matter

Any type of material with negligible pressure is often referred as 'dust'. It is represented by an equation-of-state $w_{\rm m} = 0$, with energy-density given by

$$\rho_{\rm m}(t) \propto a^{-3}, \qquad \text{and} \qquad a(t) \propto t^{2/3}. \tag{2.25}$$

The total matter content of the universe comes in several different forms. In addition to the familiar baryonic matter, observations of the Large-Scale Structure (LSS) suggest that most of the galactic content is in the form of non-baryonic matter, called *dark matter*. The total matter density may be expressed as the sum of baryonic (b) and dark matter (dm) contributions:

$$\rho_{\rm m}(t) = \rho_{\rm b}(t) + \rho_{\rm dm}(t). \tag{2.26}$$

Baryons - make up the familiar matter of our universe (protons and neutrons). Since the universe is charge neutral, there must be equal number of protons and electrons (charged leptons). An elaborate review of Big Bang Nucleosynthesis (BBN) is given by Steigman [221].

Dark matter - The existence of non-baryonic dark matter has been inferred from its gravitational manifestations through the flat rotation curves of galaxies, the mass-to-light ratios in clusters of galaxies, and gravitational lensing of background sources. An extended discussion of the current status of particle dark matter, including experimental evidence and theoretical motivations, is presented by Bertone et al. [22], Sellwood and Kosowsky [207].

Vacuum

If the cosmological constant term is moved to the right-hand-side on Einstein's equations, it can be associated to the *vacuum energy-density*, given by

$$\rho_\Lambda \equiv \frac{\Lambda}{8\pi G}. \tag{2.27}$$

At future cosmic times, while the matter and radiation density dilute away, the vacuum energy-density remains with the same constant value ρ_Λ. The vacuum energy can be modelled as a perfect fluid with negative pressure equal to $p_\Lambda = -\rho_\Lambda$, which corresponds to an equation-of-state $w_\Lambda = -1$. For a review about the cosmological constant term see e.g. Carroll [36], Padmanabhan [174], Peebles and Ratra [176]. The cosmological constant is also seen as the simplest form of a more generic *'dark energy'* component, commonly considered as the main candidate to explain the current acceleration of the universe. We shall see in Chapter 6 that $w_{\rm DE}(a)$ evolving in time provides a slightly better description for the dark-energy equation-of-state.

Curvature

The contribution of the spatial curvature can be considered as any other energy component by defining a fictitious energy density:

$$\rho_k \equiv -\frac{3\kappa}{8\pi G} a^{-2}. \tag{2.28}$$

This energy-density is described by an equation-of-state $w_k = -1/3$, for which the scale factor evolves proportionally to the cosmic time $a \propto t$. The general

behaviour of the curvature term is easily understood if we rewrite the Friedmann equation, with a vanish cosmological constant, in the following way

$$\left(\frac{\dot{a}}{a}\right)^2 = \frac{8\pi G}{3}(\rho + \rho_\kappa). \tag{2.29}$$

For a positive density contribution ρ, the universal expansion can only be stopped if the universe is closed $\kappa > 0$ ($\rho_\kappa < 0$), otherwise it will expand forever.

Missing matter

If the Friedmann equation is written in terms of the present energy-density components, we have

$$\left(\frac{\dot{a}}{a}\right)^2 = \frac{8\pi G}{3}\left[\rho_{\mathrm{r},0}\, a^{-4} + \rho_{\mathrm{m},0}\, a^{-3} + \rho_{k,0} a^{-2} + \rho_{\Lambda,0} a^0\right]. \tag{2.30}$$

Notice that the right-hand-side can be seen as a power series expansion, however with a missing component with contribution a^{-1}. To complete the series, we include this term and named it as the *missing-energy* component [235], for which its energy-density satisfies

$$\rho_X(t) = \rho_{X,0}\, a^{-1}, \qquad \text{and} \qquad a \propto t^2. \tag{2.31}$$

The missing-energy component has therefore an equation-of-state $w_X = -2/3$, and behaves similarly to domain walls [20, 240]. We explain in more detail about this new term in Chapter 7.

A summary of the main components of the universe, along with their behaviour, is shown in Table 2.1. Before solving the cosmological equations for the whole mixture of perfect-fluid components, we include some essential notation:

Hubble parameter: The expansion rate of the universe is characterised by the *Hubble parameter*:

$$H(t) \equiv \frac{\dot{a}(t)}{a(t)}, \tag{2.32}$$

component	Ω_i	w_i	$\rho(a)$	$a(t)$	$H(t)$
radiation	$\Omega_{\rm r}$	1/3	$\propto a^{-4}$	$\propto t^{1/2}$	1/2t
matter	$\Omega_{\rm m}$	0	$\propto a^{-3}$	$\propto t^{2/3}$	2/3t
curvature	Ω_k	-1/3	$\propto a^{-2}$	$\propto t$	1/t
missing matter	Ω_X	-2/3	$\propto a^{-1}$	$\propto t^2$	2/t
cosmological constant	Ω_Λ	-1	$\propto a^0$	$\propto \exp(\sqrt{\frac{\Lambda}{3}}t)$	const

Table 2.1: Constituents of the universe and their cosmological parameters: density parameter Ω_i, equation-of-state parameter w_i; and their behaviour: density evolution $\rho(a)$, scale factor $a(t)$, Hubble parameter $H(t)$.

where the present expansion rate, being $H(t = t_0)$, is called the Hubble constant H_0. As the Hubble constant is still not known with great accuracy, it is conventional to denote it through the dimensionless parameter h, such that $H_0 = 100\,h$ $\mathrm{km\,s^{-1}Mpc^{-1}} = h/3000$ $\mathrm{Mpc^{-1}}$.

Deceleration parameter: The deceleration parameter $q(t)$, is defined by

$$q(t) \equiv -\frac{\ddot{a}(t)a(t)}{\dot{a}^2(t)}. \tag{2.33}$$

As the name suggests, it describes whether the expansion of the universe is slowing down ($q > 0$) or accelerating ($q < 0$).

Density parameter: We also introduce the ratio of the energy-density relative to the critical density $\rho_{\rm c} \equiv 3H^2/8\pi G$, as the dimensionless density parameter:

$$\Omega_i(t) \equiv \frac{\rho_i(t)}{\rho_{\rm c}(t)}, \tag{2.34}$$

where the index 'i' labels a single type of component, such as matter, radiation, etcetera. The present critical density is $\rho_{\rm c,0} = 1.88h^2 \times 10^{-22}$ $\mathrm{gcm^{-3}}$.

Redshift: For convenience, we express the scale factor in terms of the redshift z of light emitted at time t_1 from a cosmological source, as:

$$1 + z = \frac{a(t_0)}{a(t_1)}. \tag{2.35}$$

Redshift is used to refer to the time at which the scale factor was a fraction $1/(1+z)$ of its present value. It is also used to refer to the distance that light has travelled since that time [139].

2.1.3 The cosmological field equations

We have computed the evolution of the scale factor for a universe composed by single-independent fluids: radiation, matter, vacuum, spatial curvature, vacuum energy and missing energy. To make the basic Friedmann models more realistic, we need to take into account the whole mixture of these components. Suppose that within the mixture, the distinct fluids do not interact with each other but only through their mutual gravitation. The total energy-momentum tensor of a multiple-component fluid is thus given by

$$T^{\mu\nu} = \sum_i (T^{\mu\nu})_i, \tag{2.36}$$

where i labels the sum over various constituents, each of them individually modelled as a single perfect-fluid with $p_i = w_i \rho_i$. Using the definitions introduced above, the Friedmann equations (2.14) and (2.15) for a multi-fluid universe are now written in the following way

$$\left(\frac{H}{H_0}\right)^2 = \sum_i \Omega_{i,0} a^{-3(1+w_i)} + \Omega_{k,0} a^{-2}, \tag{2.37}$$

$$\dot{H} + H^2 = -\frac{4\pi G}{3} \sum_i \rho_i (1 + 3w_i). \tag{2.38}$$

These equations, at any cosmic time, can be written in the elegant forms:

$$\Omega_T \equiv \sum_i \Omega_i = 1 - \Omega_k, \tag{2.39}$$

$$q = \frac{1}{2} \sum_i \Omega_i (1 + 3w_i). \tag{2.40}$$

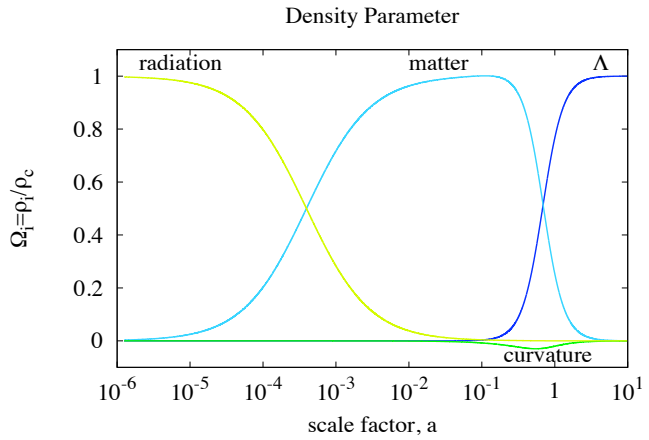

Figure 2.1: The evolution of density parameters $\Omega_i(a)$ are seen as a succession of several epochs, each of them dominated by different components: radiation, matter, curvature and cosmological constant.

The curvature density-parameter $\Omega_k = -k/H^2R^2$, determines the normalisation of the scale factor (2.3), or *curvature radius*:

$$R_0 = H_0^{-1}\sqrt{-k/\Omega_{k,0}} = \frac{H_0^{-1}}{\sqrt{|\Omega_{k,0}|}}. \tag{2.41}$$

In a universe with positive curvature, R_0 is just the radius of the 3-sphere. On the other hand, we notice that the matter distribution (2.39) clearly determines the spatial geometry of the universe: $\Omega_T < 1$ (open), $\Omega_T = 1$ (flat) and $\Omega_T > 1$ (closed).

The Friedmann equations have exact solutions in just a few simple cases, for instance in a universe modelled by perfect-fluids. For this particular case, the density parameters and their dependence on the scale factor are plotted in Figure 2.1. In this Figure, the cosmic evolution of the different constituents are seen as a succession of several epochs, each of them corresponding to a different perfect-fluid. At the earliest stages, radiation dominates because of its behaviour $\rho_{\rm r} \propto a^{-4}$. Then, at $a_{\rm eq} \approx 4.2 \times 10^{-5} h^{-2}$, the radiation contribution equals that of matter, which starts dominating afterwards. It is noticeable that the curvature

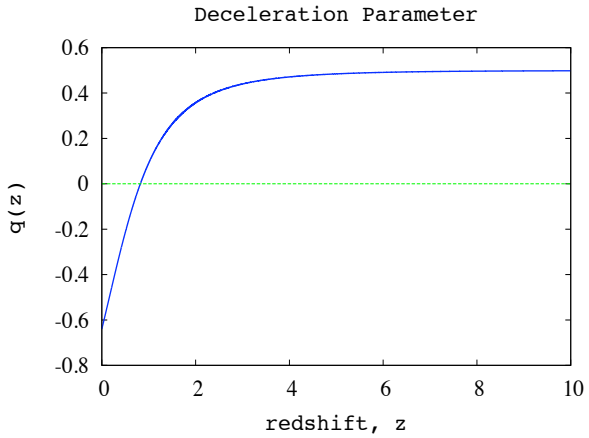

Figure 2.2: Deceleration parameter $q(z)$ as a function of redshift z for a multi-fluid universe. Notice that the universe is currently accelerating ($q(z = 0) < 0$).

term is almost negligible due to the initial conditions taken (see Section 3.4). Finally, the cosmological constant term dominates over the late-time evolution of the universe, and remains so for all time due to its constant energy-density behaviour.

From expression (2.40), we observe that the sign of $(1 + 3w_i)$ determines whether the universe is accelerating ($q < 0$) or decelerating ($q > 0$). If the major contribution comes from a fluid(s) with $w_i > -1/3$ the expansion of the universe will gradually slow-down due to the action of gravity. On the other hand, if $w_i < -1/3$ the pressure component acts as a 'repulsive' term leading to an accelerated expansion. For instance the cosmological constant term, which dominates over the dynamics of the universe at low-redshift, is the main reason for the present accelerated expansion of the universe, seen in Figure 2.2.

2.1.4 Distances and Horizons

The particle horizon is the distance light could have travelled since the origin of the universe. Regions further apart could never have been causally connected. In a time dt light travels a comoving distance $dx = dt/R$, thus the total comoving

distance travelled since the big-bang corresponds to

$$\eta \equiv \int_0^t \frac{dt}{R(t)} = \frac{1}{R_0}\int_0^a \frac{da}{a^2 H(a)} = \frac{1}{R_0}\int_z^\infty \frac{dz}{H(z)}. \tag{2.42}$$

No information could have propagated further than η on the comoving grid since the beginning of time [60], hence η is called the *comoving horizon*. We can also think of η as a time variable, named the *conformal time*. The FRW metric, in terms of the conformal time, then becomes

$$ds^2 = a^2(\eta)\left[d\eta^2 - \frac{dr^2}{1-\kappa r^2} - r^2 d\Omega^2\right]. \tag{2.43}$$

In conformal coordinates null geodesics are always at 45° angles and light cones are Minkowskian, since the metric is conformally flat: $g_{\mu\nu} = a^2\eta_{\mu\nu}$. Moreover, by changing the order of integration of (2.42), we can also define the *comoving distance* d_c, or *event horizon*, light could have travelled between a source at scale factor R and an observer today [60], as

$$d_\mathrm{c} = \int_t^{t_0} \frac{dt}{R(t)} = \frac{1}{R_0}\int_0^z \frac{dz}{H(z)} = \chi. \tag{2.44}$$

A related concept is the *proper distance* d_p corresponding to the particle horizon:

$$d_\mathrm{p}(t) \equiv R(t)\int_0^t \frac{dt}{R(t)} = R(t)\eta(t). \tag{2.45}$$

Regions separated by distances greater that the proper distance d_p are not causally connected. Furthermore, the *Hubble radius* or *Hubble distance* is defined by

$$d_\mathrm{H}(t) = H^{-1}(t). \tag{2.46}$$

The Hubble distance $d_\mathrm{H}(t)$, often described simply as the *'horizon'*, corresponds to the typical length-scale over which physical processes in the universe operate coherently. It is also the length-scale at which general-relativistic effects become important; on scales much less than $d_\mathrm{H}(t)$ (within the horizon), Newtonian theory is often sufficient to describe the effects of gravitation [92].

We also introduce the *comoving Hubble distance* as:

$$\chi_\mathrm{H} = \frac{d_\mathrm{H}(t)}{R(t)} = \frac{1}{H(t)R(t)} = \frac{1}{\dot{R}(t)}, \tag{2.47}$$

which gives the χ-coordinate corresponding to the Hubble distance.

A classical way of measuring distances in astronomy is to measure the flux from an object of known luminosity, for example from Supernovae Type Ia (SNe Ia). Let us consider the observed flux F at a distance d_L from a source of known luminosity L:

$$F = \frac{L}{4\pi d_L^2}. \tag{2.48}$$

Then, the *luminosity distance* d_L in terms of measurable quantities is

$$d_L \equiv (1+z) R_0 S_k(\chi). \tag{2.49}$$

The distance-redshift relation is, in fact, one of the most important cosmological tests. This is because given the observables H_0, $\Omega_{i,0}$ and the expression (2.49) we can compute the luminosity distance to an object at any redshift z. Conversely, for a population of standard candles with absolute magnitude M, and apparent magnitude m, we can measure the distance modulus μ at a given redshift z, defined by

$$\mu \equiv m - M = 5\log(d_L) + 25. \tag{2.50}$$

Then, the relationship of μ with redshift allows us to estimate the luminosity distance and thereby constrain the cosmological parameters, as we will see in Chapter 3. Another classical distance measurement in astronomy is to measure the angle $\delta\theta$ subtended by an object of known physical size l. The *angular distance* is then defined as $d_A = l/\delta\theta$. From the angular part of the FRW metric, we have

$$d_{\mathrm{A}} \equiv \frac{R_0 S_k(\chi)}{(1+z)}. \tag{2.51}$$

Figure 2.3 sketches the distances d_{c}, d_L and d_{A} in terms of redshift. It is worthwhile noticing that for small scales, all these distance measures coincide

$$d \simeq \frac{z}{H_0}, \tag{2.52}$$

where the linear evolution of distance with redshift is referred as the *Hubble law* [102].

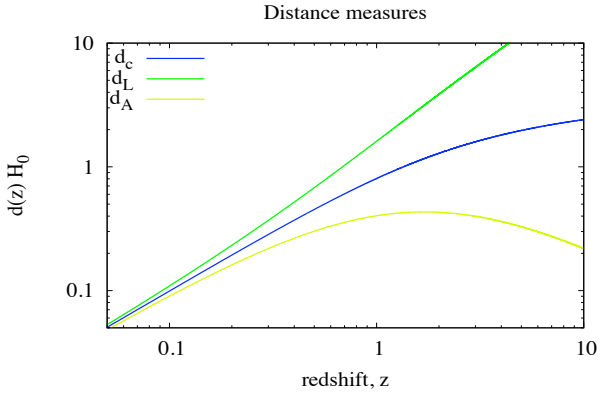

Figure 2.3: Comoving distance $d_{\rm c}$, luminosity distance d_L, and angular distance $d_{\rm A}$ for a universe filled with the same constituents as in Figure 2.1.

2.2 Inflation

Even though the Hot Big Bang model possesses a strong observational support, there are still certain inconsistencies or unexplained features to deal with: the flatness, horizon and monopole problems, amongst many others. The *inflationary model* offers the most elegant way so far proposed to solve these problems and therefore to understand why the universe is so remarkably in agreement with the standard cosmology. This model was initially introduced by Guth [85], followed by Linde [142]. For an extended review we refer to the textbooks Liddle and Lyth [139], Linde [143], Mukhanov [167]; and papers: Baumann [21], Liddle [135], Lyth and Riotto [148], Olive [172], Riotto [194].
Let us examine some of the problems of the Hot Big Bang model.

2.2.1 Shortcomings of the Hot Big Bang

Flatness problem

The Friedmann equation (2.39) can be seen in the following form

$$\Omega_T - 1 = \frac{\kappa}{(aH)^2}. \tag{2.53}$$

Written in this way, we notice that $\Omega_T = 1$ is a very special case. If at the beginning the universe was perfectly flat, then it remains so for all time. Nevertheless, a flat geometry is an unstable critical situation, that is, for even a tiny deviation from it, Ω_T would have evolved quite differently and very quickly the universe would become more curved. This can be seen as a consequence of aH being a decreasing function of time during radiation or matter domination epoch. We observe that from (2.53) and Table 2.1:

$$\begin{aligned} |\,\Omega_T - 1\,| &\propto t \qquad \text{radiation domination,} \\ |\,\Omega_T - 1\,| &\propto t^{2/3} \qquad \text{dust domination.} \end{aligned}$$

Since the present age of the universe is estimated to be $t_0 \simeq 10^{17}\,\text{sec}$ [125], from the above equations we can deduce the required value of $|\,\Omega_T - 1\,|$ at different early-times in order to obtain the correct value of spatial-geometry at present time. For instance, let us consider some particular epochs:

- Decoupling ($t \simeq 10^{13}\,\text{sec}$), we need $|\,\Omega_T - 1\,| \leq 10^{-3}$.
- Nucleosynthesis ($t \simeq 1\,\text{sec}$), we need $|\,\Omega_T - 1\,| \leq 10^{-16}$.
- Planck epoch ($t \simeq 10^{-43}\,\text{sec}$), we need $|\,\Omega_T - 1\,| \leq 10^{-64}$.

Consequently, at early times $|\,\Omega_T - 1\,|$ had to be fine-tuned extremely close to zero in order to reach its actual observed value [120].

Horizon problem

The *horizon problem* is one of the most important problems within the Big Bang model, as it refers to the communication between different regions of the universe. The age of the universe is finite and hence even light should have only travelled a finite distance by any given time. According to the standard cosmology, photons decoupled from the rest of the components at temperatures about $T_{\text{dec}} \approx 0.3\,eV$ ($z_{\text{dec}} \approx 1100$), from this time on photons free-streamed and travelled basically uninterrupted until reach us, giving rise to the region known as the *observable universe*. This spherical surface at which decoupling process occurred is called the *surface of last scattering*. The primordial photons are responsible for the CMB

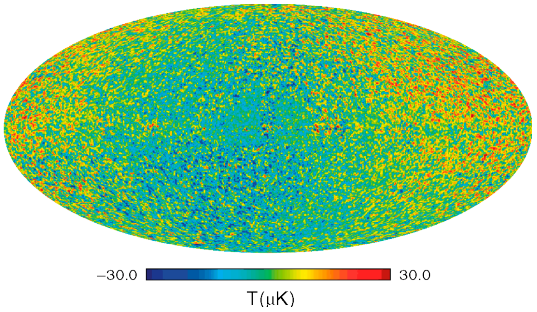

Figure 2.4: Temperature fluctuations observed in the CMB measured by the WMAP-7 experiment. The colour scale represents temperature fluctuations: from -30μK to 30μK. Figure reprinted from [125].

radiation we observe today. Looking at their fluctuations is thus analogous to taking a snapshot of the universe at that time (about $t_{\rm dec} \approx 380,000$ years after the Big Bang), as seen in Figure 2.4.

Figure 2.4 shows light seen in all directions of sky. These primordial photons have nearly the same temperature $T_{\rm cmb} = 2.725$ K plus small fluctuations (about one part in one hundred thousand). Being at the same temperature is a property of thermal equilibrium, hence observations are easily explained if different regions of the sky have been able to interact and moved towards thermal equilibrium before decoupling. Oddly, the comoving horizon over which causal interactions occurred before photons decoupled was significantly smaller than the comoving distance that radiation travelled after decoupling. This means that photons coming from sky regions separated by more than the horizon scale at last scattering, typically about 1°, would not have been able to interact and establish thermal equilibrium before decoupling. Therefore, the Big Bang model by itself does not offer an explanation of why temperatures seen in opposite directions of the sky are so nearly the same; the homogeneity must have been part of the initial conditions.

Monopole problem

The *monopole problem* was initially the motivation to develop the Inflationary cosmology [84]. The monopole, and other relics, are components of the universe that are expected to emerge as consequence of topological defects in the Higgs

field which appear in Grand Unified Theories (GUTs). From particle physics models, the number density of monopoles, at $T_{\rm GUT} \simeq 10^{15}$ GeV, is estimated to be $n_{\rm M} > 10^{-10} n_\gamma$. Any subsequent physical processes are expected to be inefficient at reducing the ratio $n_{\rm M}/n_\gamma$. Hence, the present density of monopoles per volume is

$$n_{0,\rm M} > 10^{-10} n_{0,\gamma} \simeq n_{0,b}. \tag{2.54}$$

For typical GUTs, $m_{\rm GUT} \simeq 10^{14} - 10^{15}$ GeV, we have $m_{\rm M} \simeq 10^{16}$ GeV ($\simeq 10^{-8}\, g$), which corresponds to a density parameter of order [47]:

$$\Omega_{\rm M,0} > \frac{m_{\rm M}}{m_{\rm p}} \Omega_b \simeq 10^{16}. \tag{2.55}$$

According to this prediction, the universe would be dominated by magnetic monopoles, in contrast with current observations: no one has found any monopole yet [9].

2.2.2 Cosmological Inflation

Inflation is defined as the epoch in the evolution of the universe in which the scale factor is quickly accelerated in just a fraction of a second:

$$\text{INFLATION} \iff \ddot{a} > 0, \tag{2.56}$$

$$\iff \frac{d}{dt}\left(\frac{1}{aH}\right) < 0. \tag{2.57}$$

The factor $1/(aH)$ corresponds to the comoving Hubble radius (2.47), which is interpreted as the observable universe becoming smaller during the inflationary period (sketched by the red circle in Figure 2.5). This process allowed our present observable universe to lie within a region located well inside the Hubble radius early on during inflation [139]. If this brief period of accelerated expansion occurred, then it is possible that the aforementioned problems of the Big Bang can be solved. From the acceleration equation, we can write the condition for inflation in terms of the required material to drive the expansion:

$$\ddot{a} > 0 \iff (\rho + 3p) < 0. \tag{2.58}$$

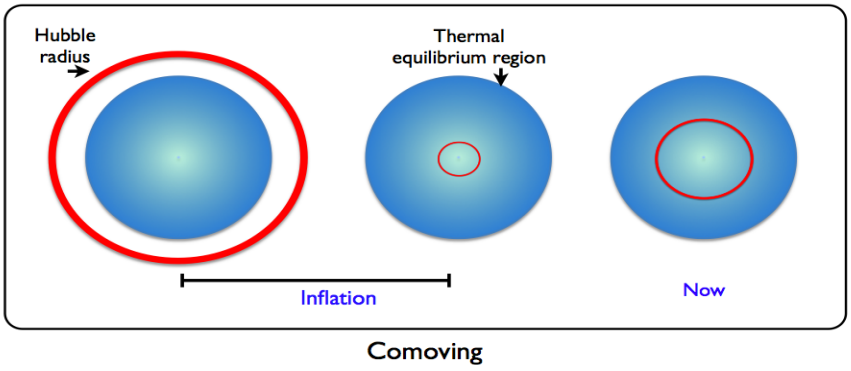

Figure 2.5: Schematic behaviour of the comoving Hubble radius during the Inflationary period (sketched by the red circle).

Because in standard physics it is commonly assumed ρ as positive, then to satisfy the acceleration condition it is necessary for the overall pressure to have $p < -\rho/3$. Nonetheless, neither a radiation nor a matter dominated epoch satisfies such condition. A typical solution would be a universe dominated by a cosmological constant Λ at the earliest stages. As we have shown in Table 2.1, a cosmological constant leads to an exponential expansion, and hence the condition (2.57) would be naturally fulfilled; this epoch is called *de Sitter stage*. Let us postpone for a bit the problem of finding a component which may satisfy this inflationary condition, and look what happens when a general solution is considered.

Flatness solution

If somehow there was an accelerated expansion, $1/(aH)$ tends to decrease with time, and hence from the expression (2.53), Ω_T is driven towards the unity rather than away from it. In this sense, inflation magnifies the curvature radius of the universe, so locally the universe seems to be flat with great precision, as shown in Figure 2.6. Then, we may ask ourselves by how much should $1/(aH)$ decrease. If the inflationary period started at time $t = t_i$ and ended approximately at the beginning of the radiation dominated era ($t = t_f$), then

$$\mid \Omega_T(10^{-34}\text{sec}) - 1 \mid_{t=t_f} \sim 10^{-54},$$

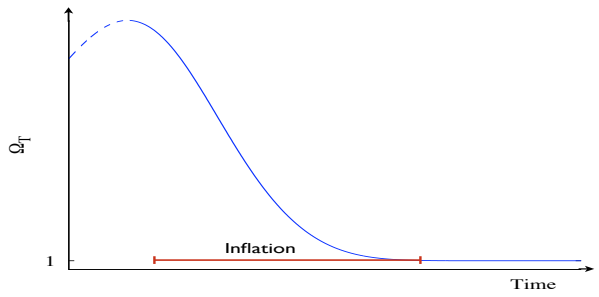

Figure 2.6: Evolution of the density parameter Ω_T, during the inflationary period. Ω_T is driven towards unity.

and

$$\frac{\mid \Omega_T - 1 \mid_{t=t_f}}{\mid \Omega_T - 1 \mid_{t=t_i}} = \left(\frac{a_i}{a_f}\right)^2 \equiv e^{-2N}. \tag{2.59}$$

So, the required condition to reproduce the value of $\Omega_{T,0}$ today is that inflation lasted for at least $N \equiv \ln a \gtrsim 50$, then Ω_T will be extraordinarily close to one that we still observe it today.

Horizon problem

During inflation the universe expanded drastically and there was a reduction in the comoving Hubble length. That is, a tiny region located inside the Hubble radius evolved and constituted our present observable universe, as seen in Figure 2.7, which represents the physical process of Figure 2.5. Scales that were outside the horizon at CMB decoupling were in fact inside the horizon before inflation. The region of space corresponding to the observable universe therefore was in thermal equilibrium before inflation and the uniformity of the CMB is essentially explained.

Monopole problem

The monopole problem is solved by noticing that during the inflationary epoch the universe led to a dramatic expansion over which the density of the unwanted particles were diluted away. Generating enough expansion, the dilution made sure

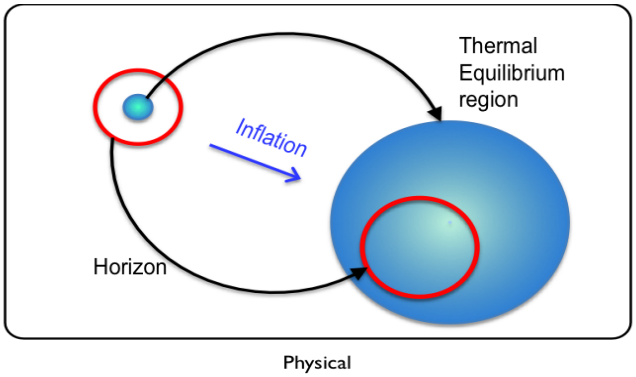

Figure 2.7: Physical evolution of the observable universe during the inflationary period.

that particles stayed completely out of our observable universe, making pretty difficult to localise any single monopole.

2.2.3 Single-field Inflation

As we have pointed out, a period of accelerated expansion can be created by a cosmological constant Λ, and hence solve the aforementioned problems. After a brief period of time, however, inflation must end and its energy be converted into conventional matter/radiation; this process is called *reheating*. In a universe dominated by a cosmological constant, the reheating process is seen as Λ decaying into conventional particles. Nevertheless, claiming that Λ is able to decay is still a naive way to face the problem. On the other hand, scalar fields (spin-0 particles) can behave like a *dynamical cosmological constant*. There currently exists a broad diversity of models suggested to give rise the Inflationary period, see for instance [144, 148, 172]. Here, we limit ourselves to single scalar-field models based on general gravity, i.e. derived from the Einstein-Hilbert action.

Let us consider a scalar field minimally coupled to gravity, with an arbitrary potential $V(\phi)$, specified by the action

$$S = \int d^4x \sqrt{-g} \left[\frac{1}{2} \partial_\mu \phi \partial^\mu \phi + V(\phi) \right]. \tag{2.60}$$

The energy-momentum tensor corresponding to this scalar field is given by

$$T_{\mu\nu} = \partial_\mu\phi\partial_\nu\phi - g_{\mu\nu}\,[\frac{1}{2}\partial_\sigma\phi\partial^\sigma\phi + V(\phi)]. \tag{2.61}$$

By comparing (2.61) to the energy-momentum tensor of perfect fluids (2.13), one can identify an associated energy-density ρ_ϕ and pressure p_ϕ for the scalar-field. In a FRW background, they are found to be

$$T_{00} = \rho_\phi = \frac{1}{2}\dot{\phi}^2 + V(\phi) + \frac{1}{2a^2}(\nabla\phi)^2, \tag{2.62}$$

$$T_{ii} = p_\phi = \frac{1}{2}\dot{\phi}^2 - V(\phi) + \frac{1}{6a^2}(\nabla\phi)^2, \tag{2.63}$$

with its corresponding equation-of-state $p_\phi = w_\phi\rho_\phi$.
To provide a better understanding of the inflaton field, ϕ can be split up as

$$\phi(t, \mathbf{x}) = \phi(t) + \delta\phi(t, \mathbf{x}), \tag{2.64}$$

where $\phi(t)$ is considered a classical field, that is, the mean value of the inflaton field on the homogeneous and isotropic state; whereas $\delta\phi(t, \mathbf{x})$ describes the quantum fluctuations around $\phi(t)$ (we will see more about $\delta\phi$ in Section 2.4.1). The evolution equation for the background field ϕ is thus given by

$$\ddot{\phi} + 3H\dot{\phi} + \frac{dV}{d\phi} = 0. \tag{2.65}$$

From the structure of the effective energy-density and pressure, the Friedmann and the acceleration equations for a homogeneous single-scalar field become

$$H^2 = \frac{8\pi G}{3}\left[\frac{1}{2}\dot{\phi}^2 + V(\phi)\right], \tag{2.66}$$

$$\frac{\ddot{a}}{a} = -\frac{8\pi G}{3}\left[\dot{\phi}^2 - V(\phi)\right]. \tag{2.67}$$

Therefore, the inflationary condition to be satisfied is $\dot{\phi}^2 < V(\phi)$, which is easily fulfilled with a suitable flat potential.

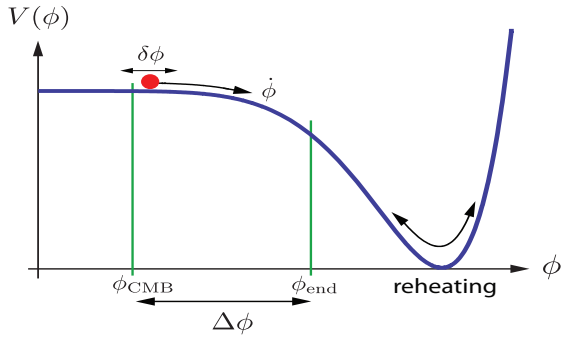

Figure 2.8: Schematic Inflationary process followed by a reheating epoch. Figure reprinted from [21].

2.2.4 Slow-Roll approximation

Based on the single scalar-field approach, it is useful to suggest a model starting with a nearly flat potential, i.e. initially satisfies the condition $\dot{\phi}^2 \ll V(\phi)$. In this case the field is slowly rolling down on its potential; such an approximation is called *slow-roll* [138, 140]. In this case $\ddot{\phi}$ is negligible because the universe is dominated by the cosmological expansion. The equations of motion (2.65) and (2.66), under the slow-roll approximation, then become

$$3H\dot{\phi} \simeq -\frac{dV}{d\phi}, \tag{2.68}$$

$$H^2 \simeq \frac{8\pi G}{3}V(\phi). \tag{2.69}$$

The slow-roll approximation is consistent if the slope and curvature of the potential are small: $V_{,\phi}, V_{,\phi\phi} \ll V$. The inflationary process can be summarised as an accelerated universe which takes place when the kinetic part of the inflaton field is subdominant over the potential $V(\phi)$ term. Then, when both quantities become comparable inflation ends giving rise to the *reheating process*. Figure 2.8 displays the schematic behaviour of the inflationary process. It is now useful to introduce the potential slow-roll parameters $\epsilon_{\rm v}$ and $\eta_{\rm v}$ in the following way [138]:

$$\epsilon_{\rm v}(\phi) \equiv \frac{1}{16\pi G}\left(\frac{V_{,\phi}}{V}\right)^2, \qquad \eta_{\rm v}(\phi) \equiv \frac{1}{8\pi G}\frac{V_{,\phi\phi}}{V}, \tag{2.70}$$

where $\epsilon_{\rm v}$ measures the slope of the potential and $\eta_{\rm v}$ the curvature. Equations (2.68) and (2.69) are in agreement with the slow-roll approximation when the following conditions hold

$$\epsilon_{\rm v}(\phi) \ll 1, \quad \mid \eta_{\rm v}(\phi) \mid \ll 1. \tag{2.71}$$

These conditions are necessary but not sufficient since even if the potential is flat, as it may be that the scalar field has a large velocity. The physical meaning of $\epsilon_{\rm v}(\phi)$ can be explicitly seen by expressing equation (2.58) in terms of ϕ:

$$\ddot{a} \;>\; 0 \;\Longrightarrow\; \epsilon_{\rm v}(\phi) < \;1. \tag{2.72}$$

Hence, inflation ends when the value $\epsilon_{\rm v}(\phi_{\rm end}) = 1$ is approached. Within these approximations, it is straightforward to find out the scale factor a between the beginning and end of inflation. Because the size of the expansion is an enormous quantity, it is useful to compute it in terms of the e-fold number N defined by

$$N \equiv \ln \frac{a(t_{\rm end})}{a(t)} = \int_t^{t_e} H\, dt \simeq 8\pi G \int_{\phi_e}^{\phi} \frac{V}{V_{,\phi}} d\phi. \tag{2.73}$$

An estimate of the e-folds number $N(k)$ is given by [139]:

$$N(k) = 62 - \ln \frac{k}{a_0 H_0} + \text{corrections},$$

where the comoving wavenumber k is evaluated at the crossing Hubble radius during inflation. The last 'correction' is a small term related with energy scales during the inflationary process. The precise value for the second quantity depends on the model as well as normalisation factors, however it does not present any significant change to the total amount of e-folds. Therefore, the value of the e-folds number is ranged to 50-70 [148].

2.3 The Perturbed Universe

The homogeneous and isotropic model provides an accurate description of the physical properties of the universe on large scales: the expansion history and the evolution of its energy content. Nevertheless, at small scales homogeneity and

isotropy are no longer valid approximations, and therefore we have to make use of a more complex theory to describe, for instance, the temperature anisotropies observed in the CMB and the matter distribution. We have seen that the temperature of the photons in the CMB presents small anisotropies compared to the background temperature $\Delta T/\bar{T} \sim 10^{-5}$. This tiny value supports the use of linear perturbation theory to predict accurately its statistical distribution. The idea of perturbation theory is straightforward: perturb the metric and the stress-energy tensor in the Einstein's equations about the background and, to first order, drop products of small quantities. Then solve the coupled system of equations

$$\delta G_{\mu\nu} = 8\pi G \delta T_{\mu\nu}. \tag{2.74}$$

This section is aimed to present an outline of linear perturbation theory, but for an extended review, we refer to Bardeen [17], Dodelson [60], Hu and Dodelson [98], Kodama and Sasaki [119], Liddle and Lyth [139], Ma and Bertschinger [149], Mukhanov [167], Mukhanov et al. [168]; special attention is paid to the papers written by Challinor [39], Doran [63], Durrer [65], Knobel [118], Kurki-Suonio [123].

2.3.1 Linear perturbations

Metric perturbations

We begin the study of relativistic linear-perturbation theory by introducing a small perturbation $h_{\mu\nu}$ to the metric, in the form of

$$g_{\mu\nu} \longrightarrow \bar{g}_{\mu\nu} + a^2 h_{\mu\nu}, \tag{2.75}$$

where the unperturbed spacetime $\bar{g}_{\mu\nu}$ is referred as the background, described by the FRW metric, and $h_{\mu\nu}$ satisfies $h_{\mu\nu} \ll \bar{g}_{\mu\nu}$. In this section, to avoid unnecessary complications, we shall only consider flat ($k = 0$) universes and work in terms of the conformal time (2.42); e.g. the conformal Hubble parameter $\mathcal{H} \equiv \partial_\eta a/a = aH$.

The most general perturbation to the background metric is given by

$$h_{\mu\nu} dx^\mu dx^\nu = -2A d\eta^2 - 2B_i d\eta dx^i + 2H_{ij} dx^i dx^j. \tag{2.76}$$

The three new functions represent a scalar field $A(\eta, \mathbf{x})$, a vector field $B_i(\eta, \mathbf{x})$ and a symmetric trace-free tensor field $H_{ij}(\eta, \mathbf{x})$, all of them defined over the background 3-space. One has to bear in mind, however, that this scalar, vector and tensor quantities are not yet the true scalar, vector, tensor perturbations, as they can also be decomposed, such as

$$B_i = \underbrace{\partial_i B}_{\text{scalar part}} + \underbrace{B_i^{(V)}}_{\text{vector part}} , \tag{2.77}$$

where the vector part is transverse (divergence free) $\partial^i B_i = 0$. A similar decomposition applies to tensors:

$$H_{ij} = \underbrace{H_L \gamma_{ij} + \partial_{\langle i}\partial_{j\rangle} H_T}_{\text{scalar part}} + \underbrace{\partial_{(i} H_{j)}^{(V)}}_{\text{vector part}} + \underbrace{H_{ij}^{(T)}}_{\text{tensor part}} , \tag{2.78}$$

where

$$\partial_{\langle i}\partial_{j\rangle} H \equiv \partial_i\partial_j H - \frac{1}{3}\delta_{ij}\nabla^2 H, \tag{2.79}$$

$$\partial_{(i}\partial_{j)} H \equiv \partial_i\partial_j H + \frac{1}{3}\delta_{ij}\nabla^2 H. \tag{2.80}$$

H_T is trace-free; $H_i^{(V)}$ is transverse; and $H_{ij}^{(T)}$ is symmetric, trace-free and transverse $\delta^{ik}\partial_k H_{ij}^{(T)} = 0$. This decomposition is unique in Euclidean space for a smooth, bounded H_{ij} that decays at infinity [222]. The most general scalar-perturbation of the metric has therefore ten separate degrees-of-freedom: $A\,(1)$, $B_i\,(3)$ and $H_{ij}\,(6)$. But as discussed earlier, there are only six independent Einstein field equations, and hence we must fix the remaining four degrees-of-freedom by a choice of coordinates or the *gauge choice*.

Energy-momentum perturbations

In a similar way we have perturbed the metric, we now introduce a perturbation to the energy-momentum tensor:

$$T^\mu_\nu \longrightarrow \bar{T}^\mu_\nu + \delta T^\mu_\nu, \tag{2.81}$$

where $\bar{T}^{\mu}_{\nu}$ represents a fluid (2.13) with the addition of an anisotropic stress Π^{μ}_{ν}, defined on the FRW background. Considering perturbations up to linear order, the energy-momentum tensor is thus given by

$$T^0_0 = -\bar{\rho}(1+\delta), \tag{2.82}$$
$$T^i_0 = (\bar{\rho}+\bar{p})v^i \equiv q^i, \tag{2.83}$$
$$T^0_i = -(\bar{\rho}+\bar{p})(v_i + B_i) \tag{2.84}$$
$$T^i_j = \bar{p}[(1+\pi_L)\delta^i_j + \Pi^i_j]. \tag{2.85}$$

where q^i is defined as the 3-momentum density, Π is the anisotropic-stress tensor with traceless part $\pi^i_j = \bar{p}\Pi^i_j$, $\Pi^0_0 = \Pi^0_i = \Pi^i_0 = 0$, and $\bar{p}\pi_L \equiv \delta p$. The density perturbation and the velocity are, respectively, defined by

$$\delta(\eta, \mathbf{x}) \equiv \frac{\rho - \bar{\rho}}{\bar{\rho}}, \qquad u^i = a v^i. \tag{2.86}$$

Gauge transformations

The perturbation of a generic field $Q = \bar{Q} + \epsilon Q^{(1)}$ obeys the gauge transformation law:

$$Q^{(1)} \to Q^{(1)} + \mathcal{L}_X \bar{Q}, \tag{2.87}$$

where $\mathcal{L}_X$ denotes the Lie derivative in direction of the vector field X. Let us consider the behaviour of $h_{\mu\nu}$ (2.76) under gauge transformations:

$$h_{\mu\nu} \to h_{\mu\nu} + \mathcal{L}_\xi \bar{g}_{\mu\nu}, \qquad \text{with} \qquad \xi^\alpha = (T, L^i), \tag{2.88}$$

where $T(\eta)$ is a scalar function, and the vector $L_i(\eta)$ is decomposed into its scalar and vector part. At linear order, the scalar, vector and tensor perturbations evolve independently (they decouple), and it is therefore possible to analyse them separately. Here we concentrate on scalar perturbations, as they account by far for the largest contributions of anisotropies measured by today's experiments, and just quote tensor results at the end of this section. Then, after some identities from differential geometry, and following Doran [63] and Durrer [65], we have the

gauge transformations for the scalar metric variables:

$$A \rightarrow A - \frac{a'}{a}T - T', \tag{2.89}$$
$$B \rightarrow B + L' + kT, \tag{2.90}$$
$$H_L \rightarrow H_L - \frac{a'}{a}T - \frac{k}{3}L, \tag{2.91}$$
$$H_T \rightarrow H_T + kL, \tag{2.92}$$

and similarly for the energy-momentum perturbations:

$$\delta \rightarrow \delta + 3(1+w)\frac{a'}{a}T, \tag{2.93}$$
$$v \rightarrow v + L', \tag{2.94}$$
$$\pi_L \rightarrow \pi_L - \frac{\bar{p}'}{\bar{p}}T = \pi_L + 3(1+w)\frac{c_s^2}{w}\frac{a'}{a}T, \tag{2.95}$$

where the sound speed is given by $c_s^2 \equiv \bar{p}'/\bar{\rho}'$.

There is an infinite number of choices for the functions $T(\eta)$ and $L(\eta)$, however it is common to choose them such that two of the perturbation variables vanish. A popular choice is the *longitudinal* or *Newtonian gauge*[1]. This gauge chooses $kL = -H_T$ and $kT = -L' - B$, so that $H_T = B = 0$, and the scalar metric perturbation is of the form [168]

$$h_{\mu\nu}^{(S)} = -2\Psi d\eta^2 + 2\Phi\gamma_{ij}dx^i dx^j, \tag{2.96}$$

where Ψ and Φ are gauge-invariant quantities, called *Bardeen potentials* [17]; we shall see that Ψ plays the role of the gravitation potential. In general they are defined by

$$\Psi \equiv A - \frac{a'}{a}k^{-1}\sigma - k^{-1}\sigma', \tag{2.97}$$
$$\Phi \equiv H_L + \frac{1}{3}H_T - \frac{a'}{a}k^{-1}\sigma. \tag{2.98}$$

[1] Two mores gauges will be useful throughout this chapter:

$$\text{Comoving} - \text{orthogonal gauge}: \quad q_i = B = 0.$$
$$\text{Spatially} - \text{flat gauge}: \quad H_L = H_T = 0.$$

where $\sigma \equiv k^{-1}H_T' - B$ vanishes in the longitudinal gauge.

Choosing a particular gauge may however introduce 'gauge artifacts', i.e. degrees of freedom which are not physical, nevertheless the calculations turn out to be simpler. The gauge invariant energy-momentum perturbations are defined in Appendix B.

Perturbed Einstein's and conservation equation

Having defined the linear perturbations of the metric and the energy-momentum tensor, we are now in position to solve the perturbed Einstein's equations. We derive the equations for perturbed variables in the longitudinal gauge and just quote the gauge-invariant equations in Appendix B.

The first-order perturbed Einstein's equations give [63, 167]:

$$k^2\Phi + 3\frac{a'}{a}\left(\Phi' - \frac{a'}{a}\Psi\right) = 4\pi G a^2 \bar{\rho}\delta, \tag{2.99}$$

$$k\left(\frac{a'}{a}\Psi - \Phi'\right) = 4\pi G a^2 v(\bar{\rho} + \bar{p}), \tag{2.100}$$

$$-k^2(\Phi + \Psi) = 8\pi G a^2 \bar{p}\Pi, \tag{2.101}$$

and the energy-momentum conservation equations:

$$-\delta' = (1+w)[kv + 3\Phi'] + 3\frac{a'}{a}w\Gamma + 3\frac{a'}{a}\delta(c_s^2 - w), \tag{2.102}$$

$$v' = \frac{a'}{a}(3c_s^2 - 1)v + k\Psi + \frac{kc_s^2}{1+w}\delta + \frac{kw}{1+w}\left[\Gamma - \frac{2}{3}\Pi\right], \tag{2.103}$$

where $\Gamma \equiv \pi_L - c_s^2\delta/w$ can be viewed as an entropy production rate. Notice that for perfect fluids, where $\Pi^\mu_\nu = 0$, we have $\Phi = -\Psi$. We also observe that perturbations vanish for a cosmological constant component, e.g. $\delta_\Lambda' = 0$. The previous equations can be better understood by assuming *the quasi-static approximation*. This approximation considers wavenumbers k deep inside the Hubble radius ($k \gg aH$), where any function F satisfies

$$\frac{k^2}{a^2}|F| \gg H^2|F|, \qquad \text{and} \qquad |\dot{F}| \lesssim |FH|. \tag{2.104}$$

Under this conditions, we recover the classical Poisson equation and, combining (2.102), (2.103), the evolution of scalar perturbations for dust particles:

$$k^2\Phi = 4\pi G a^2 \bar{\rho}\delta, \tag{2.105}$$

$$\delta'' + \frac{a'}{a}\delta' = -k^2\Psi. \tag{2.106}$$

Adiabatic and Isocurvature initial conditions

Adiabaticity requires that matter and radiation perturbations are initially in perfect thermal equilibrium. This implies that their velocity fields agree

$$v^{(\gamma)} = v^{(\nu)} = v^{(b)} = v^{(\mathrm{dm})}, \tag{2.107}$$

and the density contrast satisfies the relation

$$\frac{1}{4}\delta_\gamma = \frac{1}{4}\delta_\nu = \frac{1}{3}\delta_b = \frac{1}{3}\delta_{\mathrm{dm}}. \tag{2.108}$$

For adiabatic perturbations we have $\Gamma = 0$.
Isocurvature refers to those metric perturbations that initially vanish, i.e. $\Psi = 0$. The most general perturbation on the energy-density is described by a linear combination between adiabatic perturbations as well as isocurvature perturbations, which the latter ones play an important role when more than one scalar field is considered [139, 194].

2.3.2 The Boltzmann equation

The evolution of perturbations in the universe is quantified by the Boltzmann equation:

$$\frac{df}{d\eta} = \frac{\partial f}{\partial x^i}\frac{\partial x^i}{\partial \eta} + \frac{\partial f}{\partial P}\frac{\partial P}{\partial \eta} + \frac{\partial f}{\partial n^i}\frac{\partial n^i}{\partial \eta} = C[f], \tag{2.109}$$

which relates the effects of gravity on the photon distribution function f to the rate of interactions with other species, given by the *collision term* C. The complete distribution function for each species can be split into background plus a perturbation part:

$$f(\eta, \mathbf{x}, P, \mathbf{n}) = \bar{f}(P) + F(\eta, \mathbf{x}, P, \mathbf{n}), \tag{2.110}$$

where the distribution function of the cosmic microwave background with temperature $\bar{T}$ is

$$\bar{f} = \left[\exp\left(\frac{E}{\bar{T}} - 1\right)\right]^{-1}. \tag{2.111}$$

We see that $\bar{f}$ depends just upon the energy E of a photon; for observers at rest $E = -a\,p$. The comoving momentum $P = a^2 p$ has spatial momentum of magnitude p and unit vector $\mathbf{n}$, such that $p^i \equiv p\,n^i$. Writing the temperature function T in terms of the photon *brightness temperature perturbation* $\Delta \equiv \Delta T/\bar{T}$, we have

$$T(\eta, \mathbf{x}, \mathbf{n}) = \bar{T}(\eta)[1 + \Delta(\eta, \mathbf{x}, \mathbf{n})], \tag{2.112}$$

and the perturbation part F can be written as

$$F(\eta, \mathbf{x}, P, \mathbf{n}) = -P\frac{\partial \bar{f}}{\partial P}\Delta(\eta, \mathbf{x}, \mathbf{n}). \tag{2.113}$$

The expansion of the temperature perturbation (Δ) and polarisations (Q and U), in terms of the spherical harmonics $Y_l^m(\mathbf{n})$, are

$$\Delta(\eta, \mathbf{x}, \mathbf{n}) = \sum_l (-i)^l \Delta_l(k, \eta) P_l(\hat{\mathbf{k}} \cdot \mathbf{n}), \tag{2.114}$$

$$(Q \pm iU)(\eta, \mathbf{x}, \mathbf{n}) = \sum_{l=2} (-i)^l (E_l^0 \pm iB_l^0)\sqrt{\frac{4\pi}{2l+1}}\,{}_{\mp 2}Y_l^0(\mathbf{n}), \tag{2.115}$$

where E and B are the electric and magnetic modes and the P_l's represent the Legendre polynomials. The Boltzmann equation thus leads (after a long calculation) to the evolution equation of temperature perturbations [63]:

$$\Delta' + ik\mu\Delta + \kappa'\Delta = -i\mu k[\Phi + \Psi] - 2\Phi' + \kappa'\left\{\frac{1}{4}\delta_\gamma - \Phi - i\mu v_b + \frac{1}{10}P_2(\mu)[\sqrt{6}E_2 - \Delta_2]\right\}. \tag{2.116}$$

Note that the temperature perturbation $\Delta(\mathbf{n})$ is a function of either $\Delta(\eta, \mathbf{x}, \mathbf{n})$ or, in Fourier space, $\Delta(\eta, \mathbf{k}, \mathbf{n})$; κ' is the differential optical depth and $\mu = k^{-1}\mathbf{k} \cdot \mathbf{n}$ the direction cosine.

The same discussion applies to polarisation, by simply replacing $F \to G$ and $\bar{f}' \to 0$ (G denotes the linear polarisation distribution function). The evolution of the polarisation perturbation is therefore

$$Q' + ik\mu Q + \kappa' Q = \frac{\kappa'}{10}\{P_2(\mu) - 1\}\left[\sqrt{6}E_2 - \Delta_2\right]. \tag{2.117}$$

We notice that (2.116) is not manifestly gauge-invariant, however by defining the gauge invariant temperature perturbation $\mathcal{M} = \Delta + 2\Phi$, and its multipole decomposition

$$\mathcal{M}(\eta, \mathbf{x}, \mathbf{n}) = \sum_l (-i)^l \mathcal{M}_l(\eta, \mathbf{k}) P_l(\mathbf{n}), \tag{2.118}$$

the evolution equation (2.116) in gauge-invariant components (see Appendix B), becomes:

$$\mathcal{M}' + ik\mu\mathcal{M} + \kappa'\mathcal{M} = i\mu k[\Phi - \Psi] + \kappa'\left\{\frac{1}{4}D_g^\gamma - i\mu v_b + \frac{1}{10}P_2(\mu)\left[\sqrt{6}E_2 - \mathcal{M}_2\right]\right\}. \tag{2.119}$$

After integrating (2.119) for each l and applying orthogonality relations of the Legendre polynomials, the hierarchy for $\mathcal{M}$ is hence given by [100]:

$$\mathcal{M}_0' = -\frac{k}{3}V_\gamma, \tag{2.120}$$

$$\mathcal{M}_1' = \kappa'(V_b - V_\gamma) + k(\Psi - \Phi) + k\left(\mathcal{M}_0 - \frac{2}{5}\mathcal{M}_2\right), \tag{2.121}$$

$$\mathcal{M}_2' = -\kappa'(\mathcal{M}_2 - \mathcal{C}) + k\left(\frac{2}{3}V_\gamma - \frac{3}{7}\mathcal{M}_3\right), \tag{2.122}$$

$$\mathcal{M}_l' = -\kappa'\mathcal{M}_l + k\left(\frac{l}{2l-1}\mathcal{M}_{l-1} - \frac{l+1}{2l+3}\mathcal{M}_{l+1}\right), \quad l > 2, \tag{2.123}$$

and similarly for the polarisation

$$E_2' = -\frac{k\sqrt{5}}{7}E_3 - \kappa'(E_2 + \sqrt{6}\mathcal{C}), \tag{2.124}$$

$$E_l' = k\left(\frac{{}_2\kappa_l}{2l-1}E_{l-1} - \frac{{}_2\kappa_{l+1}}{2l+3}E_{l+1}\right) - \kappa' E_l, \quad l > 2. \tag{2.125}$$

Here $\mathcal{C} = \mathcal{M}_2 - \sqrt{6}E_2/10$ and ${}_2\kappa_l = \sqrt{l^2 - 4}$ are combinatorial factors.

Massless neutrinos follow the same multipole hierarchy as $\mathcal{M}$, however without polarisation and Thompson scattering. Hence, the perturbed neutrino distribution $\mathcal{N}$ satisfies [63]:

$$\mathcal{N}_0' = -\frac{k}{3}V_\nu, \tag{2.126}$$

$$\mathcal{N}_0' = k(\Psi-\Phi)+k\left(\mathcal{N}_0-\frac{2}{5}\mathcal{N}_2\right), \tag{2.127}$$

$$\mathcal{N}_l' = k\left(\frac{l}{2l-1}\mathcal{N}_{l-1}-\frac{l+1}{2l+3}\mathcal{N}_{l+1}\right), \quad l>1. \tag{2.128}$$

For completeness, we quote the hierarchy for the tensor multipoles, temperature $\tilde{\Delta}_l^T$, polarisation $\tilde{\Delta}_l^P$ and cross-correlation $\tilde{\Delta}_l^{T,P}$ [63, 248]:

$$\tilde{\Delta}_0^T = -k\tilde{\Delta}_1^T-\kappa'[\tilde{\Delta}_0^T-\psi]-h', \tag{2.129}$$

$$\tilde{\Delta}_0^P = -k\tilde{\Delta}_2^T-\kappa'[\tilde{\Delta}_1^T+\psi], \tag{2.130}$$

$$\tilde{\Delta}_l^{T,P} = \frac{k}{2l+1}\left[l\tilde{\Delta}_{l-1}^{T,P}-(l+1)\tilde{\Delta}_{l+1}^{T,P}\right]-\kappa'\tilde{\Delta}_l^{T,P}; \quad l\geq 1, \tag{2.131}$$

where h is the longitudinal-scalar part of tensor decomposition in (2.78), and ψ is given by

$$\psi = \frac{1}{10}\tilde{\Delta}_0^T+\frac{1}{7}\tilde{\Delta}_2^T+\frac{3}{70}\tilde{\Delta}_4^T-\frac{3}{5}\tilde{\Delta}_0^P+\frac{6}{7}\tilde{\Delta}_2^P-\frac{3}{70}\tilde{\Delta}_4^P. \tag{2.132}$$

The Boltzmann hierarchy is nowadays solved numerically with software packages such as CMBFAST [206] to produce the CMB spectrum. Also, a widely used implementation is the CAMB code [134], often embedded in the analysis package CosmoMC. Different codes have also been implemented to compute the CMB spectrum, i.e. CMBEASY is fully object oriented C++ [62], CLASS is written in C [131], and CMBQuick is written in Mathematica, but is unavoidably slow [184].

2.4 The Power Spectrum

The density contrast δ, introduced in the previous section, can be considered statistically as a random field with zero mean, $\langle\delta(\mathbf{x})\rangle = 0$. The measure of the

clustering degree in the spatial direction $\mathbf{r}$ is determined by the *correlation function* ξ, which is defined as the product of the density contrast at two separate points, $\mathbf{x}$ and $\mathbf{x}+\mathbf{r}$:

$$\xi(r) \equiv \langle \delta(\mathbf{x})\delta(\mathbf{x}+\mathbf{r})\rangle. \tag{2.133}$$

Because of statistical homogeneity and isotropy of a random field, the two-point correlator depends only on the distance $r = |\mathbf{r}|$ between the two points. On the other hand, the amplitude of fluctuations on different lengths are described by the *power spectrum* $\mathcal{P}(k)$, which is simply the inverse Fourier transform of the correlation function ξ:

$$\langle \hat{\delta}(\mathbf{k})\hat{\delta}(\mathbf{k}')\rangle = \frac{2\pi^2}{k^3}\mathcal{P}(k)\delta_D(\mathbf{k}-\mathbf{k}'), \tag{2.134}$$

where $\hat{\delta}$ is the Fourier transform of the density contrast δ. The Dirac's delta distribution δ_D guarantees that modes relative to different wave-numbers are uncorrelated in order to preserve homogeneity; $\mathcal{P}(k)$ has dependency only on the magnitude of the momenta no on $\mathbf{k}$ direction because of isotropy. The normalisation factor $2\pi^2/k^3$ in the definition of the power spectrum is conventional and has the virtue of making $\mathcal{P}(k)$ dimensionless if $\delta(\mathbf{x})$ is.

2.4.1 Primordial power spectrum

Inflationary models have the merit that they do not only explain the homogeneity of the universe on large-scales, but also provide a theory for explaining the observed level of anisotropy. During the inflationary period, quantum fluctuations of the field were driven to scales much larger than the Hubble horizon and then became classical perturbations. *Scalar, or curvature,* perturbations are coupled with matter in the universe and form the initial 'seeds' of structure formation. *Vector* contributions are expected to be negligible since these modes decayed very rapidly once they entered the Hubble horizon. *Tensor perturbations* do not couple to matter, though they are associated to the generation of gravitational waves [167].

The fluctuations produced during the inflationary epoch are studied by considering quantum fluctuations $\delta\phi$ of the inflaton field introduced in (2.64):

$$\phi(\eta, \mathbf{x}) = \bar{\phi}(\eta) + \delta\phi(\eta, \mathbf{x}). \tag{2.135}$$

The quantity $\delta\phi$ is interpreted as the field fluctuations on hypersurfaces with zero intrinsic curvature. We assume linear perturbations generated by vacuum fluctuations have uncorrelated Fourier modes, the signature of *Gaussian perturbations*. It is convenient to write $\phi = \bar{\phi} + u/a$, where $u \equiv a\delta\phi$. Then, the expansion of the action (2.60) to second order in u, during slow-roll inflation, leads to

$$S^{(2)} \approx \int d^4x \, \frac{1}{2}\left[u'^2 + (a''/a)u^2 - (\partial_i u)^2\right]. \tag{2.136}$$

Varying the action $S^{(2)}$, bearing in mind the field equation for the background (2.65), follows to the equation of motion for u:

$$u'' - \frac{a''}{a}u - \partial^i\partial_i u = 0. \tag{2.137}$$

After following quantum-field theory methods of canonical quantisation, the normalised solution of Equation (2.137), in Fourier-space, is

$$u_k(\eta) = \frac{e^{-ik\eta}}{\sqrt{2k}}\left(1 - \frac{i}{k\eta}\right), \tag{2.138}$$

and a few e-folds after the Hubble exit, we have

$$\frac{u_k(\eta)}{a(\eta)} \approx \frac{iHe^{-ik\eta}}{\sqrt{2k^3}}. \tag{2.139}$$

Finally, combining (2.139), (2.134) and $u = a\delta\phi$, the power spectrum generated by the inflaton fluctuations is equal to

$$\mathcal{P}_{\delta\phi}(k) = \left[\frac{H}{2\pi}\right]^2_{k=aH}, \tag{2.140}$$

where the expression is evaluated at the horizon exit $k = aH$. This simple result is very important, as it states that a light scalar-field in quasi-de Sitter spacetime acquires an almost scale-invariant spectrum of fluctuations with amplitude $(H/2\pi)^2$.

There is an important quantity that is conserved on large scales for adiabatic scalar fluctuations: the *comoving curvature perturbation* $\mathcal{R}$, also called the *primordial value* [39]. This quantity measures the spatial curvature on a comoving slicing of space-time, and is related to the scalar field perturbation $\delta\phi$ by

$$\mathcal{R} = -\frac{H}{\dot{\phi}}\,\delta\phi. \tag{2.141}$$

The primordial spectrum of curvature perturbations $\mathcal{P}_{\mathcal{R}}(k)$ is therefore

$$\mathcal{P}_{\mathcal{R}}(k) = \left[\left(\frac{H}{\dot{\phi}}\right)\left(\frac{H}{2\pi}\right)\right]^2_{k=aH}. \tag{2.142}$$

The creation of primordial gravitational waves corresponds to the tensor part of the metric perturbation in (2.76): $h_{ij} = H_{ij}^{(T)} = h_{\mu\nu}^{(T)}$. In Fourier space, tensor perturbations h_{ij} can be expressed as the superposition of two polarisation modes

$$h_{ij} = h_+ e_{ij}^+ + h_\times e_{ij}^\times, \tag{2.143}$$

where $+$, $\times$ represent the longitudinal and transverse modes. From Einstein's equations, it is found that each amplitude, h_+ and $h_\times$, behaves as a free scalar field in the sense that $h_{+,\times} \equiv 8\sqrt{\pi}\,\psi_{+,\times}$. Therefore, each $h_{+,\times}$ has a spectrum $\mathcal{P}_{\mathcal{T}}$ given by

$$\mathcal{P}_{\mathcal{T}}(k) = \left[\frac{16}{\pi}H^2\right]_{k=aH}. \tag{2.144}$$

The canonical normalisation of the field $\psi_{+,\times}$ was chosen such that the *ratio of tensor-to-scalar* spectra is

$$r \equiv \frac{\mathcal{P}_{\mathcal{T}}(k)}{\mathcal{P}_{\mathcal{R}}(k)} = 16\epsilon_{\rm v}, \tag{2.145}$$

where we have used the slow-roll parameters to write the last term.

2.4.2 CMB power spectrum

The primary anisotropies carried out by physical effects before the recombination epoch, encoded in the fractional temperature perturbation, are expanded in terms of the spherical harmonics on the surface of last scattering by

$$\frac{\Delta T}{\bar{T}}(\eta_0, \mathbf{x_0}, \mathbf{n}) = \sum_{l,m} a_{lm} Y_{lm}(\mathbf{n}), \tag{2.146}$$

where the a_{lm}'s define the multipoles of the CMB anisotropy; $\mathbf{x_0}$ is our position and η_0 the present conformal time. Assuming the $a_{l,m}$'s are Gaussian random fields, the two-point correlator gives

$$\langle a_{lm} a^*_{l'm'} \rangle = C_l \delta_{ll'} \delta_{mm'}. \tag{2.147}$$

The angular *CMB power spectrum* C_l^{TT} is computed through the two-point correlation function (2.133) by

$$C(\theta) \equiv \left\langle \frac{\Delta T(\mathbf{n})}{\bar{T}} \frac{\Delta T(\mathbf{n}')}{\bar{T}} \right\rangle = \sum_l \frac{2l+1}{4\pi} C_l P_l(\mathbf{n} \cdot \mathbf{n}'). \tag{2.148}$$

where $\mathbf{n} \cdot \mathbf{n}' = \cos\theta$, and we have used the addition theorem for spherical harmonics to express the sum of products of Y_{lm}'s in terms of the Legendre polynomials. We consider initial conditions in terms of the conformal Newtonian gauge potential $\Phi_{\rm ini} = \mathcal{R}$. Because the evolution equations for Δ are independent of the direction $\mathbf{k}$, we may write

$$\Delta_l(\eta_0, \mathbf{k}, \mathbf{n}) = \Phi_{\rm ini}(\mathbf{k}) \Delta_l(\eta_0, k, \mathbf{n}). \tag{2.149}$$

Therefore the C_l's are found to be

$$C_l^{XY} = \frac{4\pi}{(2l+1)^2} \int \frac{d^3k}{(2\pi)^3} \, \mathcal{P}_{\mathcal{R}}(k) \, \Delta_l^X(k) \Delta_l^Y(k), \tag{2.150}$$

where X and Y represent the *temperature* (T) and *polarisations* (E or B); $\mathcal{P}_{\mathcal{R}}(k)$ is the initial scalar power spectrum (2.142). The moments obtained from the line of sight integration method [206], in terms of the spherical Bessel functions j_l, are given by

$$\Delta_l^T = (2l+1) \int d\eta j_l(k[\eta - \eta_0]) S_T(k, \eta), \tag{2.151}$$

$$\Delta_l^E = (2l+1) \sqrt{\frac{(l-2)!}{(l+2)!}} \int_0^{\eta_0} d\eta S_E(k, \eta) j_l(x), \tag{2.152}$$

with the sources

$$\begin{aligned} S_T &= -e^{\kappa(\eta) - \kappa(\eta_0)} [\Phi' - \Psi'] + g' \left[\frac{V_b}{k} + \frac{3}{k^2} \mathcal{C}' \right] + g'' \frac{3}{2k^2} \mathcal{C} \\ &+ g \left[\frac{1}{4} D_g^\gamma + \frac{V_b'}{k} - (\Phi - \Psi) + \frac{\mathcal{C}}{2} + \frac{3}{2k^2} \mathcal{C}'' \right], \end{aligned} \tag{2.153}$$

$$S_E = \frac{3g\mathcal{C}}{4x^2}, \tag{2.154}$$

where we have used $x \equiv k(\eta_0 - \eta)$ and the visibility function $g \equiv \kappa' \exp(\kappa(\eta) - \kappa(\eta_0))$. Similar results are quoted for the *tensor contributions*:

$$C_{XY;l}^{\rm tens} = \frac{4\pi}{(2l+1)^2} \int \frac{d^3k}{(2\pi)^3}\, \mathcal{P}_{\mathcal{T}}(k)\, \Delta_{X;l}^{\rm tens}(k) \Delta_{Y;l}^{\rm tens}(k), \tag{2.155}$$

where $\mathcal{P}_{\mathcal{T}}(k)$ is the initial tensor power spectrum (2.144), and the moments:

$$\Delta_{T;l}^{\rm tens} = \sqrt{\frac{(l+2)!}{(l-2)!}} \int_0^{\eta_0} d\eta S_T^{\rm tens}(k,\eta) \frac{j_l(x)}{x^2}, \tag{2.156}$$

$$\Delta_{E,B;l}^{\rm tens} = \int_0^{\eta_0} d\eta S_{E,B}^{\rm tens}(k,\eta) j_l(x), \tag{2.157}$$

with the sources (using (2.132)):

$$S_T^{\rm tens}(k,\eta) = h' \exp(-\kappa) + g\psi, \tag{2.158}$$

$$S_E^{\rm tens}(k,\eta) = g\left\{\psi - \frac{\psi''}{k^2} + \frac{2\psi}{x^2} - \frac{\psi'}{kx}\right\} - g'\left\{\frac{2\psi'}{k^2} + \frac{4\psi}{kx}\right\} - 2g''\frac{\psi}{k^2}, \tag{2.159}$$

$$S_B^{\rm tens}(k,\eta) = g\left\{\frac{4\psi}{x} + \frac{2\psi'}{k}\right\} + 2g'\frac{\psi}{k}. \tag{2.160}$$

Figure 2.9 shows the adiabatic CMB spectra for all the contributions: Temperature, E-mode, B-mode and T-E cross-correlation. The left-hand-side of the panel displays the CMB spectra for scalar perturbations, whereas the right-hand-side tensor perturbations (gravitational waves). All of them in units of $l(l+1)/2\pi[\mu K]^2$.

Let us examine in more detail the temperature power spectrum C_l^T, which is mainly determined by the expression (2.153). The density contrast D_g^γ is the main contribution, driving the spectrum towards the oscillatory behaviour. It can be seen as an intrinsic temperature variation over the background last-scattering surface: $\delta T/T \propto D_g^\gamma/4$. The Doppler shift, V_b-term, describes the blueshift caused by last scattering electrons moving towards the observer. The term involving time derivatives of the potentials, $(\Phi' - \Psi')$, is known as the *integrated Sachs-Wolfe* effect (ISW) [198]. It describes the change of the CMB photon energy due to

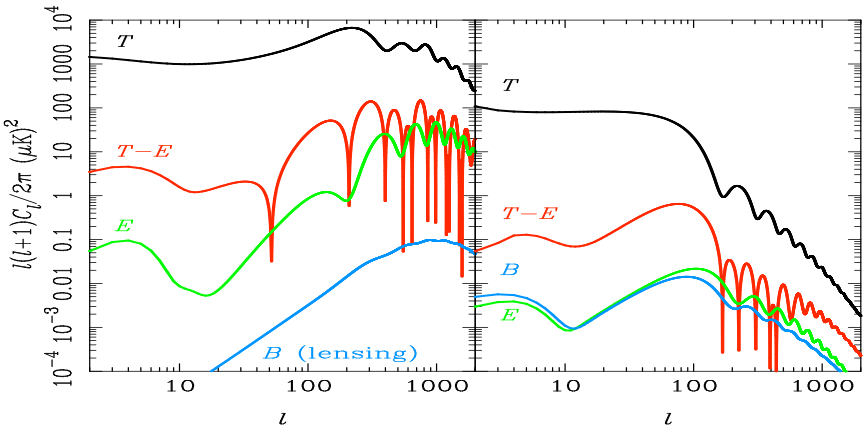

Figure 2.9: CMB spectra for all the contributions: Temperature, E-mode, B-mode and T-E cross-correlation. The left-hand-side displays the scalar perturbations whereas the right-hand-side tensor perturbations (gravitational waves). Figure reprinted from Challinor [40]

the evolution of the potentials along the line of sight. The terms involving $\mathcal{C}$ and its derivatives describe polarisation effects and are far less important than the D_g^γ term. Finally, the $(\Phi - \Psi)$ term arises from the gravitational redshift when climbing out of the potential well at last scattering. The combination $D_g^\gamma/4 - (\Phi - \Psi)$ is known as the *ordinary Sachs-Wolfe effect* (SW). This gives the main contribution on scales that at decoupling were well outside the horizon [39, 63]. Figure 2.10 displays all these different contributions. These effects exhibit a series of features at different scales of the universe, or in terms of the multipoles:

- The Sachs-Wolfe effect ($l < 100$) - The gravitational effects are the dominant contributions at large angular scales. If we assume a nearly scale-invariant scalar spectrum $n_s \approx 1$, then $l(l+1)C_l$ is approximately constant, shown as a flat plateau at low multipoles.

- Intermediate scales ($100 < l < 1000$) - Perturbations inside the horizon have evolved causally and produced the anisotropy at the last scattering

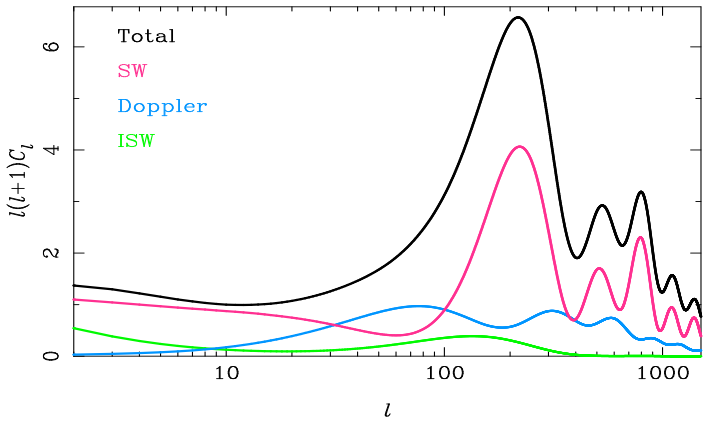

Figure 2.10: Total CMB temperature-spectrum and its different contributions: Sachs-Wolfe (SW) $D_g^\gamma/4 - (\Phi - \Psi)$; Doppler effect V_b^γ; and the integrated Sachs-Wolfe effect (ISW) coming from evolution of the potential along the line of sight. Figure from Challinor [40]

epoch ($l_{\rm hor} \approx 200$). The balance between the gravitational force and radiation pressure is presented as series of characteristic peaks called *acoustic oscillations*.

- Small scales ($l > 1000$) - The thickness of the last scattering surface leads to a damping of $C_l^T \sim l^{-4}$ at the highest multipoles, commonly called the *Silk effect*. At these scales, important contributions are also provided by secondary anisotropies: gravitational lensing, Rees-Sciama effect (RS), Sunyaev-Zel'dovich effect (SZ), kinetic Sunyaev-Zel'dovich effect, Ostriker-Vishniac effect (OV), foregrounds from discrete sources [1].

2.4.3 Matter power spectrum

The information regarding to the distribution of galaxies over the observed universe is encoded in the *matter power spectrum* $\mathcal{P}_m$:

$$\langle \delta_m(\mathbf{k}) \delta_m(\mathbf{k}') \rangle = \frac{2\pi^2}{k^3} \mathcal{P}_m(k) \delta_D(\mathbf{k} - \mathbf{k}'), \tag{2.161}$$

where the matter overdensity $\delta_{\rm m}$ is related to the potential $\Phi(a, \mathbf{k})$ via the Poisson equation (2.105):

$$\delta_{\rm m}(a, \mathbf{k}) = \frac{2}{3}\left(\frac{k}{aH}\right)\Phi(a, \mathbf{k}). \tag{2.162}$$

The gravitational potential $\Phi(a, \mathbf{k})$ at late times can be written in terms of the primordial value $\Phi_{\rm ini}$ set up during inflation, as

$$\Phi(a, \mathbf{k}) = T(k)g(a)\Phi_{\rm ini}, \tag{2.163}$$

where the transfer function $T(k)$ describes the evolution of perturbations through the epochs of horizon crossing and radiation/matter transition, while the growth factor $g(a)$ describes the wavelength-independent growth at late times.
On the other hand, the comoving curvature perturbation (B.11), in the comoving gauge, can be written in terms of the potentials:

$$\mathcal{R}^{(\rm m)} = \frac{5+3w}{3+3w}\Phi, \tag{2.164}$$

where we have made use of Equation (2.100) to eliminate v. Hence, during matter domination, the density perturbation is given by

$$\delta_{\rm m}(a, k) = \frac{2}{5}\left(\frac{k}{aH}\right)\mathcal{R}^{(\rm m)}. \tag{2.165}$$

Combining these results, the power spectrum of matter density perturbations when they re-enter the horizon during matter domination is

$$\mathcal{P}_{\rm m}(a, k) = \frac{4}{25}\left(\frac{k}{aH}\right)^4 T^2(k)\mathcal{P}_{\mathcal{R}}(k). \tag{2.166}$$

An alternative definition for the matter power spectrum is $P_{\rm m} = 2\pi^2\mathcal{P}_{\rm m}/k^3$. It has been shown that the transfer function of a matter component has the asymptotic behaviour

$$T(k) \simeq \begin{cases} 1, & \text{if} \quad k_{\rm eq}/k \gg 1, \\ (k_{\rm eq}/k)^2, & \text{if} \quad k_{\rm eq}/k \ll 1. \end{cases} \tag{2.167}$$

where $k_{\rm eq}$ is the mode that enters the horizon at matter-radiation equality $t_{\rm eq}$. The precise form of the transfer function at all scales is found by solving the full

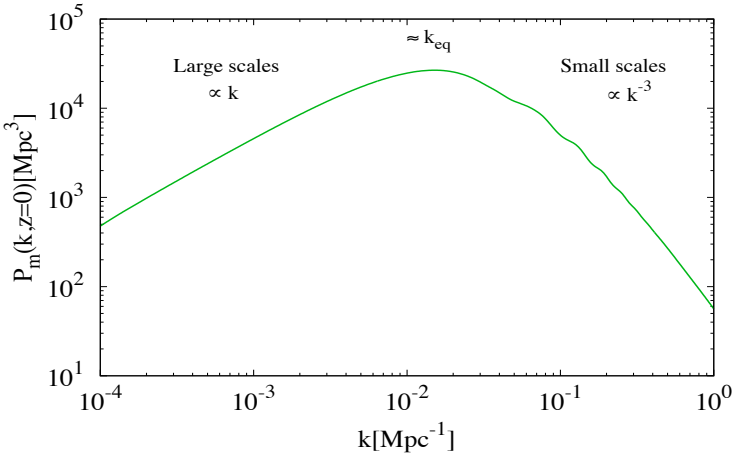

Figure 2.11: The matter power spectrum $P_{\rm m}(k)$. At large scales the spectrum behaves as $\propto k$, whereas at small scales $\propto k^{-3}$.

general relativistic Boltzmann equation [60]. The matter power spectrum, in its asymptotic form, behaves as:

$$P_{\rm m}(k) \simeq \begin{cases} \propto k & \text{large scales,} \\ \propto k^{-3} & \text{small scales.} \end{cases} \tag{2.168}$$

Figure 2.11 shows the linear matter power spectrum at present time, in which we can observe the behaviour described by (2.168).

An outline of the theoretical concepts revised in this chapter is displayed in Figure 2.12 . The quantities shown in the bottom panel will allow us to establish the connection with current and future cosmological observations, as we shall see in the next chapter.

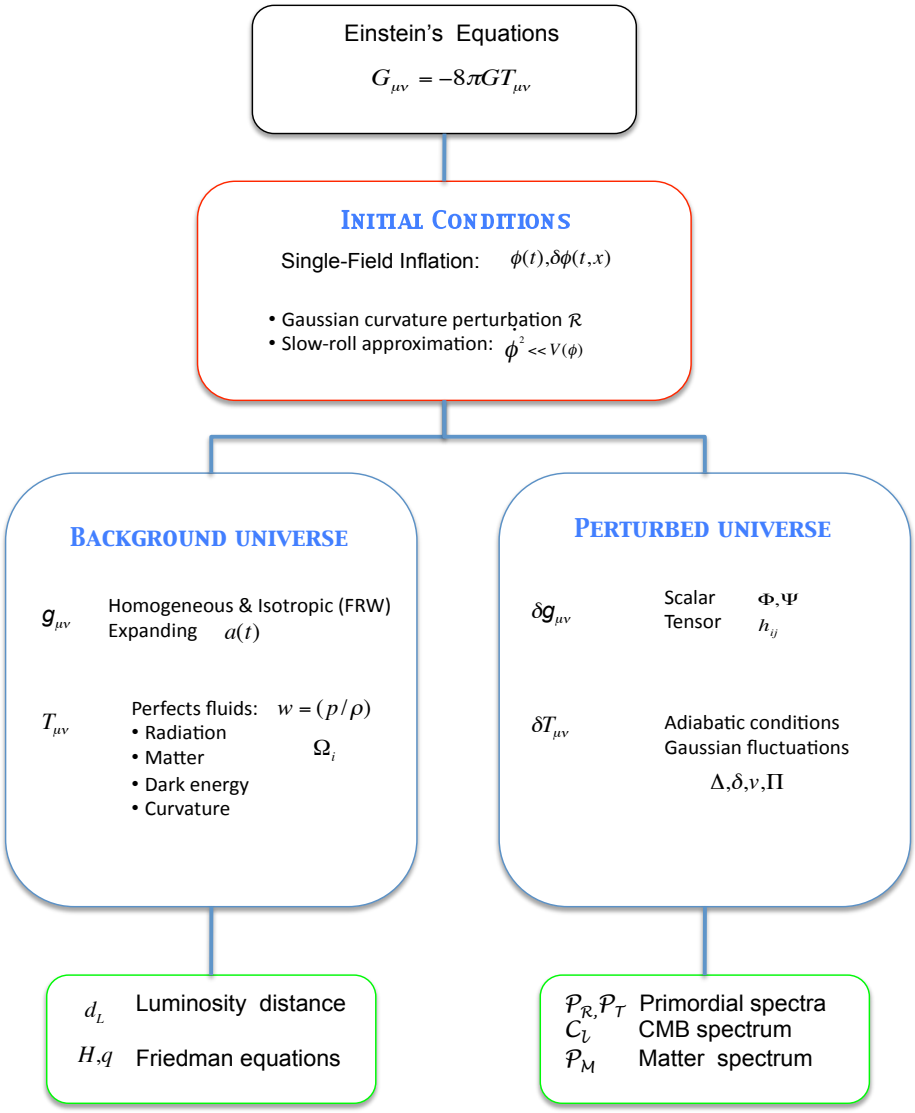

Figure 2.12: Outline of the theoretical concepts reviewed throughout this chapter.

Chapter 3

Statistics in Cosmology

In the previous chapter we have developed the main equations to describe the evolution of the background and perturbed universe. We noticed, however, that the whole structure of the CMB, matter power spectrum and luminosity distance depend strongly on the initial conditions emerging from the inflationary era ($\mathcal{P}_{\mathcal{R},\mathcal{T}}$), on the matter-energy content ($\Omega_{i,0}$), and on the expansion rate history (H_0). This chapter seeks to give a brief introduction of such quantities used to describe the properties of the universe. We show current and future experimental results used throughout the analysis: CMB, SNe and LSS amongst many others. It also includes a short description of the Bayesian analysis to perform the parameter estimation and model selection. Finally, at the end of the chapter, by making use of the theoretical, observational and statistical tools included in this work, we examine the standard ΛCDM model (spatially flat and non-flat), and present the current constraints on the cosmological parameters.

3.1 The Cosmological Parameters

3.1.1 Base parameters

These parameters, commonly called *standard parameters*, are considered as the principal quantities used describe the universe. They are not, however, predicted by any fundamental theory, rather we have to fit them by hand in order to determine which combination best describes the current astrophysical observations

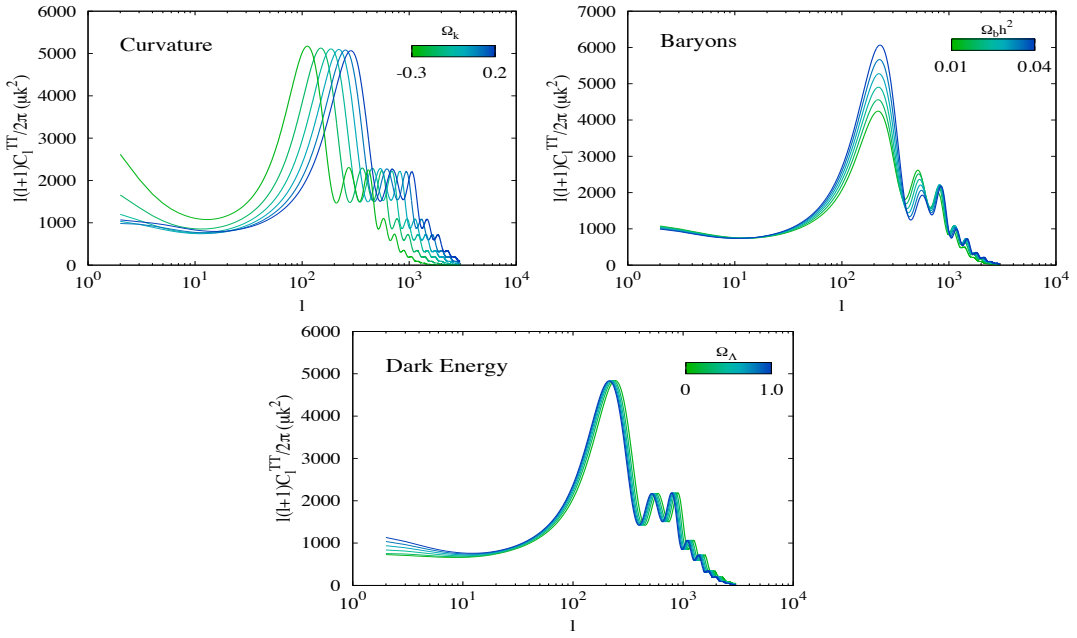

Figure 3.1: Dependence of the temperature power spectrum for three fundamental quantities: Curvature (Ω_k), Baryons (Ω_b) and Dark energy in the form of a cosmological constant (Ω_Λ).

[124, 136]. Variations of these parameters affect the amplitude and shape of the spectra as well as the background evolution in many different ways, yielding to very different universes. They are classified depending on whether they characterise the background or the perturbed universe:

Background parameters

The present description of the homogeneous universe can be given in terms of the density parameters $\Omega_{i,0}$ and the Hubble parameter H_0, through the Friedmann equation (2.37):

$$H^2 = H_0^2 \left[(\Omega_{\gamma,0} + \Omega_{\nu,0})\, a^{-4} + (\Omega_{\mathrm{b},0} + \Omega_{\mathrm{dm},0})\, a^{-3} + \Omega_{k,0} a^{-2} + \Omega_{X,0} a^{-1} + \Omega_{\Lambda,0} \right], \tag{3.1}$$

From these parameters the radiation contribution is accurately measured, for instance by the WMAP satellite, corresponding to $\Omega_{\gamma,0} = 2.469 \times 10^{-5} h^{-2}$ for

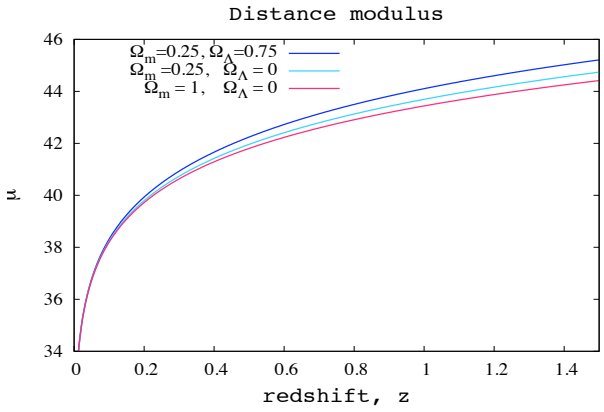

Figure 3.2: Theoretical values of the distance modulus μ for three different models; with various combinations of matter $\Omega_{\mathrm{m},0}$ and dark energy in the form of a cosmological constant $\Omega_{\Lambda,0}$.

$T_{\mathrm{cmb}} = 2.725K$. Similarly for neutrinos, while taken as relativistic, they can be related to the photon density through (2.23). However, variations of the rest of the parameters imprint different signatures on the background history and evolution of perturbations, observed through the CMB spectrum as it is illustrated in Figure 3.1. We observe that the first peak (and the most prominent, at $l \approx 200$) is particularly related to the spatial geometry $\Omega_{k,0}$; the relative heights of the intermediate peaks probe the baryon density; the largest scales are mainly affected by the dark energy component.

These base parameters also play a key role on measurements of the distance modulus μ, through the luminosity distance (2.50). Figure 3.2 shows the theoretical values of the distance modulus for three different models with various combinations of $\Omega_{\mathrm{m},0}$ and $\Omega_{\Lambda,0}$. Note that objects appear to be further away (dimmer) in a universe with cosmological constant than one dominated by only matter today.

The existence of strong degeneracies amongst different combinations of parameters is also noticeable. In particular the well-known *geometrical degeneracy* involving Ω_{m}, Ω_{Λ} and the curvature parameter $\Omega_k = 1 - \Omega_{\mathrm{m}} - \Omega_{\Lambda}$. To reduce

degeneracies it is common to introduce a combination of the cosmological parameters such that they have orthogonal effects on the power spectrum [121]. For instance, a standard parameterisation is based on the *physical energy-densities* of cold dark matter $\Omega_{\rm dm}h^2$, and baryons $\Omega_{\rm b}h^2$, and the ratio of the sound horizon to the angular diameter distance at decoupling time:

$$\theta = \frac{r_{\rm s}(a_{\rm dec})}{D_A(a_{\rm dec})}. \tag{3.2}$$

There is an extra parameter that accounts for the reionisation history of the universe, the *optical depth to scattering* τ (i.e. the probability that a given photon scatters once), given by

$$\tau = \sigma_{\rm T} \int_{t_r}^{t_0} n_e(t) dt, \tag{3.3}$$

where $\sigma_{\rm T}$ is the Thompson cross-section and $n_e(t)$ is the electron number density as a function of time.

Inflationary parameters

After the horizon exit, H and $\dot{\phi}$ have small variations during few e-folds. Thus, the scalar (2.142) and tensor (2.144) spectra are nearly scale independent. The standard assumption is therefore to parameterise each of the spectra in terms of a power-law

$$\mathcal{P}_{\mathcal{R}}(k) = A_{\rm s} \left(\frac{k}{k_0}\right)^{n_{\rm s}-1}, \tag{3.4}$$

$$\mathcal{P}_{\mathcal{T}}(k) = A_{\rm t} \left(\frac{k}{k_0}\right)^{n_{\rm t}}. \tag{3.5}$$

where $A_{\rm s}$, $A_{\rm t}$ are the *spectral amplitudes*, and $n_{\rm s}$, $n_{\rm t}$ the *spectral indices* or *tilt parameters*, for both scalar and tensor perturbations respectively; k_0 denotes an arbitrary scale at which the tilted spectrum pivots, usually fixed to $k_0 = 0.002$ Mpc^{-1}. A scale-invariant spectrum, called Harrison-Zel'dovich (HZ), has constant variance on all length scales and it is characterised by $n_{\rm s} = 1$, $n_{\rm t} = 0$. Small deviations from scale-invariance are also considered as typical signatures of inflationary models [138]. The spectrum of perturbations is said to be blue if $n_{\rm s} > 1$ (more power in ultraviolet), and red if $n_{\rm s} < 1$ (more power in infrared).

The spectral indices, $n_{\rm s}$ and $n_{\rm t}$, and the tensor-to-scalar ratio r can be expressed in terms of the slow-roll parameters $\epsilon_{\rm v}$ and $\eta_{\rm v}$ (2.70), as:

$$n_{\rm s} - 1 \simeq -6\,\epsilon_{\rm v}(\phi) + 2\,\eta_{\rm v}(\phi), \tag{3.6}$$

$$n_{\rm t} \simeq -2\,\epsilon_{\rm v}(\phi), \tag{3.7}$$

$$r \simeq 16\,\epsilon_{\rm v}(\phi). \tag{3.8}$$

These parameters are not completely independent each other, but the tensor spectral index is proportional to the tensor-to-scalar ratio $r = -8n_{\rm t}$ [53]. This expression is considered as the *consistency relation* for slow-roll inflation. Any single-field inflationary model can hence be described, to the lowest order in slow-roll, in terms of three independent parameters: the amplitude of density perturbations $A_{\rm s}$, the scalar spectral index $n_{\rm s}$, and the tensor-to-scalar ratio r. Variations of the CMB T-spectrum over different values of $n_{\rm s}$ are shown in the left panel of Figure 3.3.

In addition to the temperature T and polarisation E spectra, produced by scalar perturbations, there is also the B-mode polarisation only produced by tensor perturbations. Therefore, measurements of B-modes are important tests for the existence of primordial gravitational waves. Unfortunately, there is no observational evidence of tensor perturbations yet, and r is commonly set to zero. The next generation of CMB polarisation experiments will substantially improve these limits (see Section 3.2.2). Variations of the C^{BB} tensor spectrum with respect to the tensor-to-scalar ratio r are displayed in the right panel of Figure 3.3.

3.1.2 Nuisance parameters

We do not have particular interest on these type of parameters, however they may influence the rest of the parameter-space constraints. These type of parameters may be related to insufficiently constrained aspects of physics, or uncertainties in the measuring process [228]. Therefore, considering their uncertainty is important in order to obtain accurate error-estimates on the physical parameters we are seeking to determine. Examples of nuisance parameters are, for instance, the bias

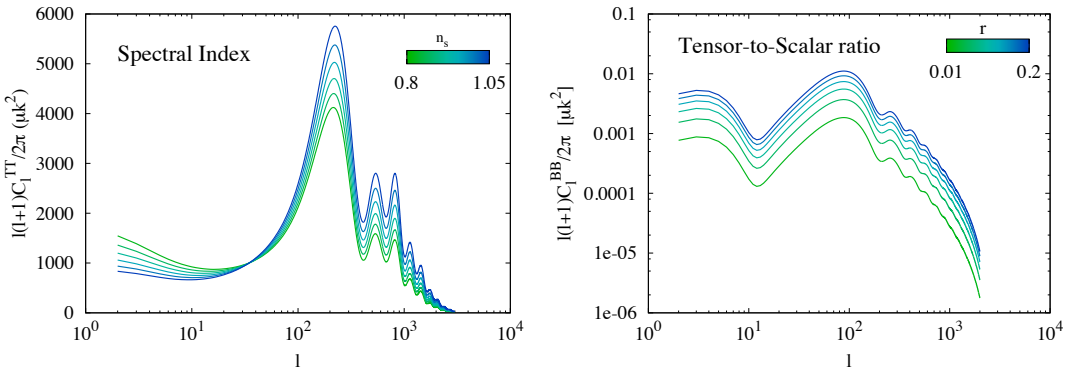

Figure 3.3: Variations of the C^{TT} scalar spectrum for different values of the spectral index n_s (left), and variations of the C^{BB} tensor spectrum with respect to the tensor-to-scalar ratio r (right).

factor in galaxy surveys b, calibrations and beams uncertainties, galactic foregrounds. The new ACT measurements (three seasons of data [214]) incorporate nine parameters describing secondary emissions. Nuisance parameters also control the stretch α and colour β corrections on measurements of distance modulus of SNe Type Ia [154].

3.1.3 Derived parameters

The standard set of parameters, introduced previously, provide an adequate description of the cosmological models in agreement with observational data. However, it is not unique and other parameterisations may be as good as this one. Some parameterisations make use of knowledge about physics or sensitivity of observations and are hence more naturally interpreted. In general we could have used different parameters to describe the universe, those include: the age of the universe, the present neutrino background temperature, the epoch of matter-radiation equality, the reionisation epoch, the baryon to dark matter density ratio, or some other combinations of parameters, i.e. the overall amplitude of the CMB anisotropy $\exp(-2\tau)A_{\rm s}$ [228]. In the ΛCDM model, to ameliorate degeneracies, we use as base parameters the physical energy densities $\Omega_{\rm dm,0}h^2$ and $\Omega_{\rm b,0}h^2$,

Table 3.1: Candidate parameters used to describe models beyond the concordance ΛCDM. The highlighted models are studied in detail throughout this work.

αR^n	Modifications to gravity
	[or more complex theories]
$d\tilde{s}^2$	Anisotropic universe
$d\alpha/dz$, dG/dz	Variations of fundamental constants
$f_{\rm NL}$	Non-gaussianity
$n_{\rm run}$	Running of the scalar spectral index
$k_{\rm cut}$	Large-scale cut-off in the spectrum
	[or a more complex parameterisation of $\mathcal{P}_{\mathcal{R}}(k)$]
$r + 8n_{\rm t}$	Violation of the inflationary consistency relation
$n_{\rm t,run}$	Running of the tensor spectral index
	[or a more complex parameterisation of $\mathcal{P}_{\mathcal{T}}(k)$]
$P_{\rm iso}$	CDM isocurvature perturbations
$\Omega_{k,0}$	Spatial curvature
$\Omega_{X,0}$	Additional components
$m_{\rm dm}$	Warm dark matter mass
	[or scalar field dark matter]
m_{ν_i}	Neutrino mass for species 'i'
$w_{\rm DE}$	Dark energy equation-of-state
	[or a more complex parameterisation of $w(z)$]
ρ^α	Polytropic equation of state
Γ	Interacting fluids

and the ratio of the sound horizon to the angular diameter distance θ; we consider as derived quantities the density parameters $\Omega_{i,0}$ and Hubble parameter H_0.

3.1.4 Beyond the concordance ΛCDM

The best model in agreement with data, at present time, is given by the concordance ΛCDM model. However, this model might not be the final one and several extensions have already been implemented. A non-exhaustive list of candidates

beyond the standard cosmological model is shown in Table 3.1. The definite answer on how many parameters we must include or which set of parameters represents the most plausible will be given by high-quality cosmological observations in the coming years. In the same table, we have highlighted the models studied in detail throughout this work.

3.2 Observations

Rapid advance in the development of powerful observational-instruments has led to the establishment of *precision cosmology*. In particular, experiments employed to measure CMB anisotropies, luminosity distances and large-scale structure. In this section, we highlight these type of experiments used to impose constraints on the cosmological parameters.

3.2.1 Current observations

CMB experiments

A number of experiments over the past decade or so have been very successful in measuring the anisotropies of the CMB. They include the Cosmic Background Explorer satellite [COBE; 160] as the pioneer of detecting the anisotropy. Nowadays with highly-improved experiments it is possible to find accurate measurements of the temperature and polarisation CMB spectrum from:

Satellite experiments:

- The Wilkinson Microwave Anisotropy Probe [WMAP; 120, 125], with CMB T-spectrum measurements over the multipoles ($2 < l < 1200$). Recently the WMAP collaboration has released the 9-year of observations [90].

Ground-based telescopes:

- The Background Imaging of Cosmic Extragalactic Polarization [BICEP; 42], probes intermediate scales ($21 \leq l \leq 335$).

- The Quest (Q and U Extra-Galactic Sub-mm Telescope) at DASI (Degree Angular Scale Interferometer) [QUAD; 31], improve polarisation constraints, whose primary aim is high resolution measurements ($154 \leq l \leq 2026$) of the polarisation signals.

- The Cosmic Background Imager [CBI; 215], constrains the CMB spectrum in the range ($300 \leq l \leq 1700$).

- The Atacama Cosmology Telescope [ACT; 64], observes the small angle CMB T-spectrum from l= 300 to l=10000, and recently released the three seasons of data [214].

- The South Pole Telescope [SPT; 115], with CMB T-measurements between ($650 < l < 9500$), and recent improved data from the 2500-square-degree SPT-SZ survey [223].

Ballon-borne experiments:

- Balloon Observations Of Millimetric Extragalactic Radiation AND Geophysics [BOOMERanG; 114], measures CMB temperature fluctuations over the multipole range $50 \leq l \leq 1500$.

Figure 3.4 summarises the current status of some experiments constraining the temperature (TT), polarisation (EE) and cross-correlation (T-E) CMB power spectra. In particular the CMB T-power spectrum is now well-constrained over a wide range of scales. For example, WMAP and BICEP observations provide good constraints on the late-time ISW effect arising at the largest scales on the first three acoustic peaks, whilst ACT and SPT data accurately measure the power of higher acoustic peaks and damping tail. Intermediate scales are well constrained by QUAD and CBI experiments, and the overlapping of all of them. In addition to T, E and T-E CMB spectra, Figure 3.5 shows the theoretical B-mode spectrum predicted from a power-law parameterisation, with $r = 0.1$, along with 1σ constraints obtained from current observations: WMAP, BICEP and QUAD.

At this point it is worthwhile mentioning the existence of an intrinsic uncertainty in the cosmological measurements. This limitation comes from the fact

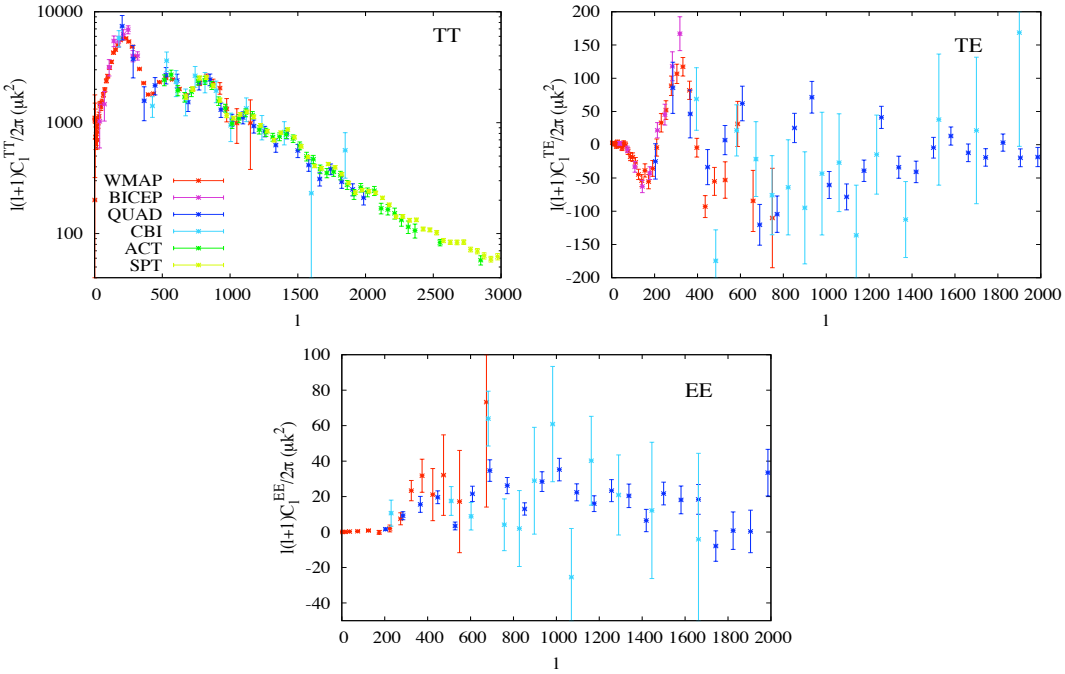

Figure 3.4: Current status of temperature (TT), polarisation (EE) and cross-correlation (T-E) measurements of the CMB power spectra, by various observational probes.

that we have to do statistics with only one universe. For a given multipole l, we expect to have a variance, called the *cosmic variance*, of the C_l's given by

$$(\Delta C_l)^2 = \frac{2}{2l+1} C_l^2. \tag{3.9}$$

In real experiments, the error is increased due to the limited sky coverage by f_{sky}^{-1}.

CMB measurements by themselves cannot, however, place strong constraints on all the parameters because the existence of parameter degeneracies, such as the $\tau - A_\mathrm{s}$ and the geometrical degeneracy. Nevertheless, when CMB observations are combined with other cosmological probes, they together increase the constraining power and considerably weaken degeneracies.

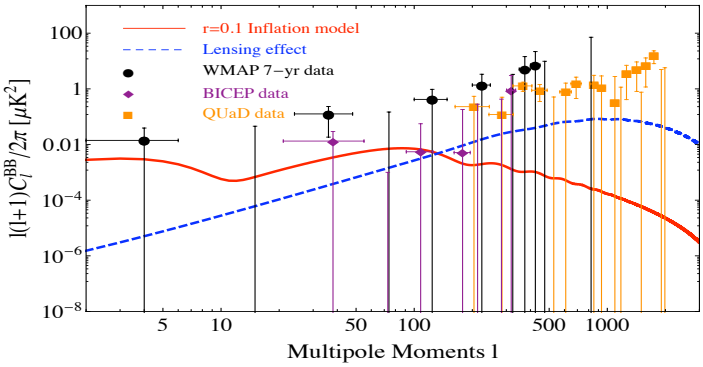

Figure 3.5: WMAP, BICEP and QUaD constraints for the B-mode power spectrum. The solid line represents the theoretical prediction of a $r = 0.1$.

Supernovae observations

Throughout the past two decades supernovae observations have provided decisive evidence that the present expansion of the universe is accelerating. In particular studies of Type Ia supernovae as standard candles: they have the same intrinsic magnitude with high accuracy, up to a rescaling factor, e.g. Perlmutter et al. [180], Riess et al. [193]. Hence, the current acceleration suggests the existence of an exotic component or alternative theories which would produce such an effect, as we will see in Chapters 7 and 8. Branch and Tammann [25] provides a brief introduction to Type Ia supernovae (SNe Ia) as standard candles, and Leibundgut [130] shows their use in cosmology. Some samples of supernovae Type Ia worth mentioning include:

- The Sloan Digital Sky Survey-II [SDSS-II; 76], discovered and measured multi-band lightcurves for 327 spectroscopically confirmed Type Ia supernovae in the redshift range $0.05 < z < 0.35$.
- The Equation of State: SupErNovae trace Cosmic Expansion program [ESSENCE; 163], discovered and analysed 60 Type Ia supernovae over the redshift interval $0.15 < z < 0.70$,
- The Supernova Legacy Survey 3-year sample [SNLS; 224], presented 252 high redshift Type Ia supernovae ($0.15 < z < 1.1$).

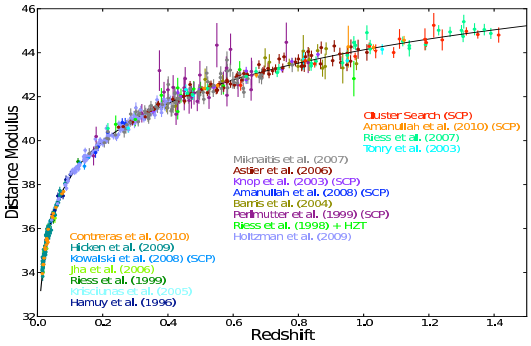

Figure 3.6: Current status of measurements of the Hubble diagram of Type Ia supernovae. Reprinted from the Union 2.1 compilation [225].

- The Hubble Space Telescope [HST; 191], discovered 21 Type Ia supernovae at $z \geq 1$.
- Recently the compilation of data from all the above, namely the 'Union' [122], 'Union 2' [8] and 'Union 2.1' [225].

Supernovae measurements can be plotted on a Hubble diagram with distance modulus vs. redshift (as seen in Figure 3.6), and then be used to fit the best cosmological parameters, for instance those shown in Figure 3.2.

LSS measurements

The matter power spectrum is nowadays one of the most important measures of large-scale structure. Many observations have been made to infer the spectrum:

- The sample of Luminous Red Galaxies (LRGs) from the Sloan Digital Sky Survey Seventh Data Release (DR7) [190], provides measurements on the matter spectrum between $0.02 < k < 0.19\text{Mpc}^{-1}$. Nowadays with improved measurements, one has the ninth data released (DR9) of the SDSS-III [2].
- Measurements of the transmitted flux in the Lyα forest probe the smallest scales in the matter power spectrum [161].

An illustration of the matter power spectrum of density fluctuations is shown in Figure 3.7 (see [91] and references therein).

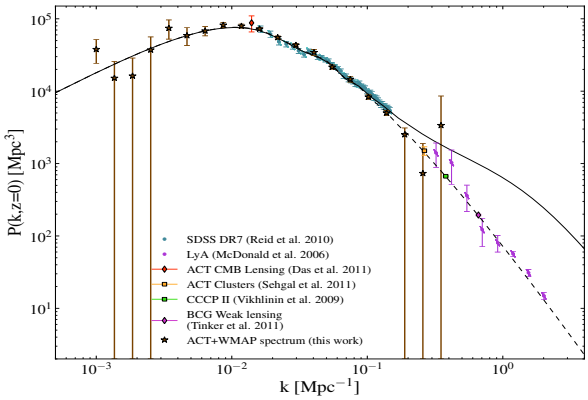

Figure 3.7: Current status of the perturbation power spectrum as measured by different experiments. Figure reproduced from [91].

3.2.2 Future surveys

An impressive array of ambitious projects have been implemented, or are underway, to provide high resolution measurements of the physical properties of the universe, and hence the search for possible signatures of new cosmology. The Planck satellite [185] will improve measurements on the E and B polarisation modes. Along with Planck satellite there will be several experiments aiming to provide measurements of small-scale fluctuations and polarisations, such as the E and B EXperiment [EBEX; 173], Q-U-I JOint TEnerife CMB experiment [QUIJOTE; 196] and Spider [54]. Besides CMB experiments, the Euclid satellite [70] will explore the expansion history of the universe and the evolution of cosmic structures over a very large fraction of the sky. The Dark Energy Survey [DES; 226] is designed to probe the origin of the accelerating universe and help uncover the nature of dark energy.

Previously we have shown current constraints of the temperature and polarisation CMB spectra. Here, we aim to explore future constraints coming from Planck satellite and CMB-Pol experiments. Performance assumptions for Planck and CMB-Pol are taken from [185] and [16]. In order to do this we need to simulate these experiments by generating mock data of the $\hat{C}_l^{XY}$'s from a χ^2_{2l+1}

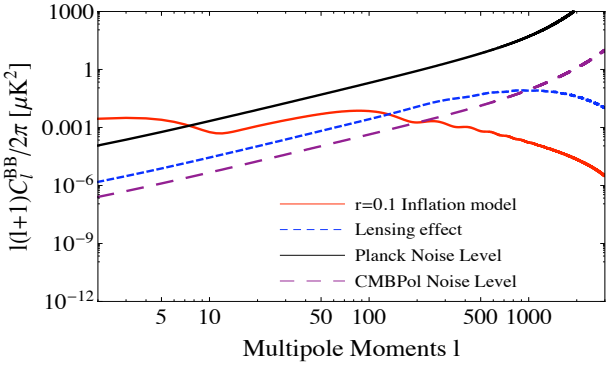

Figure 3.8: Polarisation noise power spectra of forthcoming experiments. Note that these curves include uncertainties associated with the instrumental beam. The red line shows the B-mode power spectrum for the standard inflationary model with $r = 0.1$.

distribution with variances [187]:

$$(\Delta\hat{C}_l^{XX})^2 = \frac{2}{(2l+1)f_{sky}}\left(C_l^{XX} + N_l^{XX}\right)^2, \tag{3.10}$$

$$(\Delta\hat{C}_l^{TE})^2 = \frac{2}{(2l+1)f_{sky}}\left[\left(C_l^{TE}\right)^2 + \left(C_l^{TT} + N_l^{TT}\right)\left(C_l^{EE} + N_l^{EE}\right)\right], \tag{3.11}$$

where $X = T, E$ and B label the temperature and polarisations; f_{sky} is the fraction of the observed sky. The C_l^{XY}'s represent the theoretical spectra and N_l^{XY} the instrumental noise spectra for each experiment. In experiments with multiple frequency channels c, the noise spectrum is approximated [24] by

$$N_l^X = \left(\sum_c \frac{1}{N_{l,c}^X}\right)^{-1}, \tag{3.12}$$

where the noise spectrum of an individual frequency channel, assuming a Gaussian beam, is

$$N_{l,c}^X = (\sigma_{\rm pix}\,\theta_{\rm fwhm})^2 \exp\left[l(l+1)\frac{\theta_{\rm fwhm}^2}{8\ln 2}\right]\delta_{XY}. \tag{3.13}$$

The pixel noise from temperature and polarisation maps are considered as uncorrelated. The noise per pixel $\sigma_{\rm pix}^X$ (and $\sigma_{\rm pix}^P = \sqrt{2}\sigma_{\rm pix}^T$) depends on the instrumental

parameters; $\theta_{\rm fwhm}$ is the *full width at half maximum* (FHWM) of the Gaussian beam.

For the Planck experiment, we include three channels with frequencies (100 GHz, 143 GHz, 217 GHz) and noise levels per beam $(\sigma^T_{\rm pix})^2$= (46.25 μK^2, 36 μK^2, 171 μK^2). The FHWM of the three channels are $\theta_{\rm fwhm}$ =(9.5, 7.1, 5.0) arc-minute. These figures are taken from the values given in [185]. We combine three channels for the CMBPol experiment [16] with frequencies (100 GHz, 150 GHz, 220 GHz), noise levels $(\sigma^T_{\rm pix})^2$ = (729 nK^2, 676 nK^2, 1600 nK^2) and $\theta_{\rm fwhm}$ = (8, 5, 3.5) arc-minute. Sky coverages of $f_{\rm sky} = 0.65, 0.8$ are respectively assumed and integration time of 14 months. In Figure 3.8, we show the noise levels for these experiments as a function of multipole number l. The blue line corresponds to the B-mode power spectrum using the standard power-law parameterisation with $r = 0.1$. The lensed C_l^B is also shown in the same figure, which can be treated as a part of the total noise power spectrum N_l^B as well as the instrumental noise power spectra [181]. For more information of the noise and beam profile of each frequency channel, refer to [151].

3.3 Bayesian Analysis

Over the last decade or so, the vast amount of information coming from a wide range of sources, including CMB, SNe and LSS, has increased amazingly. We would like to translate this experimental/observational information into constraints of our model(s), summarised by the estimation of the cosmological parameters involved. The concordance ΛCDM model, previously described, depends on a set of cosmological parameters shown in Section 3.1. A primary goal concerning observational cosmology is to determine best-fit parameter values for a given model, as well as to decide which model is in best-agreement with observational data. To do this we focus on *Bayesian inference*. Some excellent reviews of Bayesian statistics applied to cosmology are given by Heavens [89], Liddle [137], Liddle et al. [141], Trotta [228], Verde [237, 238], von Toussaint [242], and the textbook for data analysis Sivia and Skilling [216].

3.3.1 Parameter estimation

A Bayesian analysis provides a consistent approach to estimating the values of the parameters $\mathbf{\Theta}$ within a model M, which best describe the data $\mathbf{D}$. The method is based on the assignment of probabilities to the quantities of interest, and then the manipulation of these probabilities given a series of rules, in which Bayes' theorem plays the main role [137]. Bayes' theorem states that

$$P(\mathbf{\Theta}|\mathbf{D}, M) = \frac{P(\mathbf{D}|\mathbf{\Theta}, M)\ P(\mathbf{\Theta}|M)}{P(\mathbf{D}|M)}. \tag{3.14}$$

In this expression, the *prior* probability $\mathrm{P}(\mathbf{\Theta}|\mathrm{M}) \equiv \pi$ represents what we thought the probability of $\mathbf{\Theta}$ was before considering the data. This probability is modified through the *likelihood* $\mathrm{P}(\mathbf{D}|\mathbf{\Theta},\mathrm{M}) \equiv \mathcal{L}$. The posterior probability $\mathrm{P}(\mathbf{\Theta}|\mathbf{D},\mathrm{M})$ represents the state of knowledge once we have taken the experimental data $\mathbf{D}$ into account. The normalisation constant in the denominator is the marginal likelihood or *Bayesian evidence* $\mathrm{P}(\mathbf{D}|\mathrm{M}) \equiv \mathcal{Z}$, as is normally called in cosmology. Since this quantity is independent of the parameters $\mathbf{\Theta}$, it is commonly ignored in parameter estimation but it takes the central role for model comparison.

The central step for parameter estimation is to construct the likelihood function $\mathcal{L}$ for the measurements, and then the exploration of the region around its maximum value $\mathcal{L}_{\max}$. A simple chi-squared function is often used $\chi^2 = -2\ln\mathcal{L}$. when the distributions are Gaussian. However, some current problems in cosmology present obstacles for carrying out this procedure straightforwardly (some of them discussed by Liddle [137]). Fortunately, models of our interest can be easily tackled by numerical techniques developed on statistical fields, in particular the methods known as *Markov Chain Monte Carlo (MCMC)*. There have been developed different codes employing MCMC techniques to carry out the exploration of the cosmological parameter-space, for instance CosmoMC [133], CosmoHammer [4], CMBEASY [62]. Although some of them use a simple Metropolis-Hasting algorithm by default, nowadays improved algorithms have been adapted to explore complex posterior probability distributions.

Discriminating among models and determining which of them is the most plausible given some data is a task for model comparison techniques, whose application is discussed in the next section.

3.3.2 Model selection

There is nowadays a rich diversity of models trying to describe the vast amount of cosmological information. Some of them might involve complex interactions or introduce a high number of parameters, but provide just as good fit as the standard ΛCDM model (see Table 3.1). So, how can we perform an objective comparison between them and choose the appropriate model? The solution was proposed by William of Occam: the simplest model which covers all the facts ought to be preferred. That is, a complex model that explains the data slightly better than a simple one should be penalised by the inclusion of extra parameters, because this additional information reflects a lack of predictability in the model. Moreover, if a model is too simple, it might not fit certain data equally well, then it can be discarded [141, 228].

Many attempts have been performed to translate Occam's razor into a mathematical language for model selection. Two major types have been used so far: Bayesian evidence and *Information criteria*; where the latter one can be used as an useful approximation when the Bayesian evidence cannot be computed.

Information criteria is based on some simplifying approximations to the full Bayesian evidence. The method considers the best-fit values and attaches a penalty term for more complex models:

- The Akaike Information criterion (AIC), introduced by Hirotugu Akaike has the form

$$AIC \equiv -2 \ln \mathcal{L}_{max} + 2k, \tag{3.15}$$

  where the penalty term is induced by the number of free parameters k to be estimated.

- The Bayesian Information Criterion (BIC), was derived by Gideon E. Schwarz and it is given by

$$BIC \equiv -2 \ln \mathcal{L}_{max} + k \ln N, \tag{3.16}$$

  where N is the number of datapoints. It follows from a Gaussian approximation of the Bayesian evidence for a large number of samples.

- The Deviance Information Criterion (DIC), was proposed by David J Spiegelhalter. It is a generalization of the AIC and BIC written as

$$DIC \equiv -2\widehat{D_{KL}} + 2\mathcal{C}_b, \tag{3.17}$$

  where the former term is the estimated KL divergence and the latter one is the effective number of parameters.

An extended discussion of the different information criteria can be found in [136, 141, 228].

Bayesian evidence. This is the primordial tool for the model selection we focus on. It applies the same type of analysis as in parameter estimation, but now at the level of models rather than parameters. The Bayesian evidence is the key quantity to bear in mid as it balances the complexity of cosmological models and then, naturally, incorporates Occam's razor. It has been applied to a wide diversity of cosmological contexts, see for example [93, 109, 113].

Let us consider several models M, each of them with prior probability $P(M)$. Bayes' theorem for model selection is

$$P(M|\mathbf{D}) = \frac{P(\mathbf{D}|M)P(M)}{P(\mathbf{D})}. \tag{3.18}$$

The left-hand side denotes the probability of the model given the data, which is exactly what we are looking for in model selection. We need, therefore, to obtain an expression that allows us to compute the Bayesian evidence in terms of the information we already have. As we previously mentioned, the Bayesian evidence is simply the normalisation constant of the posterior distribution expressed by

$$\mathcal{Z} = \int \mathcal{L}(D|\Theta)\pi(\Theta)d^N\Theta. \tag{3.19}$$

where N is the dimensionality of the parameter space. More explicitly, it is the average likelihood weighted by the prior for a specific model choice:

$$Evidence = \int (Likelihood \times Prior) d^N \Theta. \tag{3.20}$$

A model containing wider regions of prior parameter-space along with higher likelihoods will have a high evidence and vice versa. Therefore, the Bayesian evidence does provide a natural mechanism to balance the complexity of cosmological models and then, elegantly incorporates Occam's razor.

When comparing two models, M_i and M_j, the important quantity to bear in mind is the ratio of the posterior probabilities, or *posterior odds*, given by

$$\frac{P(M_i|\mathbf{D})}{P(M_j|\mathbf{D})} = \frac{\mathcal{Z}_i}{\mathcal{Z}_j} \frac{P(M_i)}{P(M_j)}, \tag{3.21}$$

where $P(M_i)/P(M_j)$ is the prior probability ratio for the two models, usually set to unity. The ratio of two evidences $\mathcal{Z}_i/\mathcal{Z}_j$ (or equivalently the difference in log evidences $\ln \mathcal{Z}_i - \ln \mathcal{Z}_j$) is often termed the *Bayes factor* $\mathcal{B}_{i,j}$:

$$\mathcal{B}_{i,j} = \ln \frac{\mathcal{Z}_i}{\mathcal{Z}_j}. \tag{3.22}$$

Then, the quantity $\mathcal{B}_{i,j}$ measures the relative probability of how well model i may fit the data when is compared to model j. Jeffreys [112] provided a suitable guideline scale on which we are able to make qualitative conclusions (see Table 3.2). In this work, we refer to positive (negative) values of $\mathcal{B}_{i,j}$ when the i model being favoured (disfavoured) over model j.

The calculation of the integral in Equation (3.19) is a very computationally demanding process, since it requires a multidimensional integration over the likelihood and prior. For many years much progress has been made in the construction of efficient algorithms to allow faster and more accurate computation of the Bayesian evidence. Until recently, algorithms such as simulating annealing or thermodynamic integration [27], required around 10^7 likelihood evaluations making the procedure hardly treatable. A powerful algorithm was recently invented

Table 3.2: Jeffreys guideline scale for evaluating the strength of evidence when two models are compared.

$\lvert\mathcal{B}_{i,j}\rvert$	Odds	Probability	Strength
< 1.0	$< 3:1$	< 0.750	Inconclusive
1.0-2.5	$\sim 12:1$	0.923	Significant
2.5-5.0	$\sim 150:1$	0.993	Strong
> 5.0	$> 150:1$	> 0.993	Decisive

by Skilling [217], known as *nested sampling algorithm*, which has been proven to be ten times more efficient than previous methods. The first computationally-efficient code to compute the Bayesian evidence in cosmology, named CosmoNest, was implemented by Mukherjee et al. [170]. In this work we incorporate into the CosmoMC software [133] a substantially improved and fully-parallelized version of the *nested sampling* algorithm, called the MultiNest algorithm, initially proposed by Feroz & Hobson [73, 74]. The MultiNest algorithm increases the sampling efficiency for calculating the evidence and allows one to obtain posterior samples even from distributions with multiple modes and/or pronounced degeneracies between parameters. There is also CosmoPMC which is based on an adaptative importance sampling method called Population Monte Carlo [117]. For more complex models with high number of parameters, there also exist improved codes to increase the speed of the whole process by employing, for instance, neuronal networks: CosmoNet [15]. BAMBI is an algorithm that combines the benefits of both the nested sampling and artificial neural networks [80].

3.3.3 Dataset consistency

Combining multiple datasets to obtain tight constraints on the cosmological parameters has been a very common practice. Marshall et al. [156] established a test to quantify the consistency of different cosmological datasets analysed under the same model (see also Hobson et al. [94]). The Bayesian consistency analysis relies on partitioning the full combined dataset D into its constituent parts D_i

$(i = 1, \ldots, n)$, namely CMB, SNe, LSS data, so on, and analyses the model with each dataset independently. The evidence ratio is defined as

$$R = \frac{\Pr(D|H)}{\prod_{i=1}^{n} \Pr(D_i|H)}, \tag{3.23}$$

where the hypothesis H denotes the model under study. This ratio compares the probability that all the datasets were generated from a cosmological model characterised by the same parameter values, with the probability that each dataset was generated from an independent set of cosmological parameters. Thus, one expects $R > 1$ if the datasets are all consistent, and $R < 1$ otherwise. The Bayes factor for data sets is given by $\mathcal{B}_R = \ln R$.

3.4 The concordance ΛCDM model

In this section, we make use of the theoretical (Section 3.1), Observational (Section 3.2.1) and Statistical (Section 3.3) tools to examine the standard cosmological model. The minimal form of the standard cosmological model, in agreement with several independent observations, considers a FRW background, purely Gaussian adiabatic scalar perturbations and neglect tensor contributions. It also assumes a flat universe fill up with baryons, cold dark matter and a dark energy component in the form of a cosmological constant Λ. The key aspects that describe the standard model here, and throughout the work, are specified by:

- Theory/Parameters

Base parameters: the physical baryon and dark matter densities $\Omega_{\mathrm{b},0}h^2$ and $\Omega_{\mathrm{dm},0}h^2$, $100\times$ the ratio of the sound horizon to angular diameter distance at last scattering surface θ, the optical depth at reionisation τ, the amplitude of the primordial spectrum A_{s} and the spectral index n_{s} defined at a pivot scale $k_0 = 0.002$ Mpc^{-1}. Aside from the base parameters, recent observations include additional secondary parameters: the Sunyaev-Zel'dovich (SZ) amplitude A_{SZ}, the total Poisson power A_p at $l = 3000$ and the amplitude of the clustered power A_c. The parameters, along with the flat priors, are shown in Table 3.3.

Parameters	Description	Prior range
Background		
$\Omega_{\rm b,0}h^2$	Physical baryon density	$[0.01, 0.03]$
$\Omega_{\rm dm,0}h^2$	Physical cold dark matter density	$[0.01, 0.3]$
θ	Ratio of the sound horizon to the angular diameter distance	$[1, 1.1]$
τ	Reionization optical depth	$[0.01, 0.3]$
Inflationary		
$\log[10^{10}A_{\rm s}]$	Curvature perturbation amplitude	$[2.5, 4]$
$n_{\rm s}$	Spectral scalar index	$[0.5, 1.2]$
Secondary		
$A_{\rm SZ}$	Sunyaev-Zel'dovich amplitude	$[0, 3]$
$A_{\rm c}$	Total Poisson power	$[0, 20]$
$A_{\rm p}$	Amplitude of the clustered power	$[0, 30]$

Table 3.3: Parameter description along with the flat-uniform priors assumed on the standard ΛCDM.

-Observations/Experiments:

To compute posterior probabilities for each model in the light of temperature and polarisation measurements, we use WMAP 7-year data release [120] and the ACT observations [64]. In addition to CMB data, we include distance measurements of 557 Supernovae Type Ia from the Union 2 compilation [122]. We also incorporate large-scale structure data from the SDSS-DR7 [190] power spectrum. We consider baryon density information from BBN [33] and impose a Gaussian prior on H_0 using measurements from the HST [192]. This comprises our dataset I. In addition to dataset I, we include recent results from QUaD [31] and BICEP [42] experiments. Together these observations make up our dataset II.

-Analysis/Codes:

The computation of the CMB spectrum is perform by a modified version of the CAMB code [134] to include any additional components and calculate the predicted power spectra of CMB anisotropies and matter perturbations. The exploration of the parameter-space is carried out by using the CosmoMC software

[133] with the addition of the MULTINEST algorithm [73]. The latter is included to perform the calculation of the Bayesian evidence.

We have analysed a standard flat ΛCDM model and, for pedagogical purposes, also the same model but with the addition of curvature, with priors $\Omega_{k,0} = [-0.1, 0.1]$. The top panel of Figure 3.9 shows 1D marginalised posterior distributions of the base and some relevant derived parameters, for both models: flat (red) and non-flat (black) ΛCDM. At the top of the same figure, we have included the Bayes factor comparing both of them. For the non-flat model, we notice that the marginalised posteriors of $\Omega_{\rm dm,0}h^2$, H_0 and the Age of the universe have broadened due to correlations created by the inclusion of $\Omega_{k,0}$. These correlations can be observed in the 2D marginalised posterior distribution shown in the bottom panel of Figure 3.9. The constraints on the cosmological parameters are displayed in Table 3.4 along with 1σ confidence levels. In this Table, both models assume the presence of ΛCDM with a scalar power spectrum described by a power-law and no tensor contributions. The first set of rows show the base parameters whereas the second set some derived parameters. Current cosmological observations provide, in general terms, a strong support for a nearly-flat accelerating universe dominated by 72% of dark energy in the form of a cosmological constant, 24% of non-baryonic dark matter and 4% of baryon contributions; the primordial spectrum is red ($n_{\rm s} < 1$) with the Harrison-Zel'dovich excluded with high confidence level. On the other hand, the Bayes factor between these two models, $\mathcal{B}_{\Lambda,\Lambda+\Omega_k} = +1.90 \pm 0.35$, indicates a significant preference for a flat universe, according to the Jeffreys guideline shown in Table 3.2. The last row of Table 3.4 shows that both models are consistent with the full combined dataset I.

Throughout the rest of the chapters we incorporate features beyond the standard ΛCDM model in the search of a better description of cosmological observations. In Chapter 4, with the use of present data, we determine the structure of the primordial scalar spectrum by implementing an optimal model-free reconstruction. Our aim is to consider models that slightly deviate from the simple power-law form. Then, in Chapter 5, we incorporate tensor contributions to the

Table 3.4: The constraints on the cosmological parameters using our dataset II. We report the mean of the marginalised posterior distribution and 1σ confidence levels. The Bayes factor for models $\mathcal{B}_{\Lambda,\Lambda+\Omega_k}$, and for datasets $\mathcal{B}_R$ are also included.

Description		Flat ΛCDM	Non-flat ΛCDM
Base parameters	$\Omega_{\mathrm{b},0}h^2$	0.02206 ± 0.00042	0.0221 ± 0.00043
	$\Omega_{\mathrm{dm},0}h^2$	0.1130 ± 0.0028	0.112 ± 0.0041
	θ	1.039 ± 0.0019	1.039 ± 0.0020
	τ	0.082 ± 0.013	0.083 ± 0.014
	n_{s}	0.956 ± 0.010	0.957 ± 0.011
	$\log[10^{10}A_{\mathrm{s}}]$	3.21 ± 0.035	3.21 ± 0.039
	$\Omega_{k,0}$	-	-0.0022 ± 0.0058
Derived parameters	$\Omega_{\mathrm{m},0}$	0.282 ± 0.015	0.285 ± 0.018
	$\Omega_{\Lambda,0}$	0.717 ± 0.015	0.717 ± 0.016
	H_0	69.2 ± 1.27	68.7 ± 2.13
	Age(Gyrs)	13.84 ± 0.086	13.93 ± 0.27
Bayes factor	$-2\ln\mathcal{L}_{\max}$	8240.46	8240.80
	$\mathcal{B}_{\Lambda,\Lambda+\Omega_k}$	$+1.6 \pm 0.4$	-
Dataset consistency	$\mathcal{B}_R$	$+5.06 \pm 0.4$	$+5.07 \pm 0.4$

analysis and present current and future constraints on the scalar spectrum. Chapter 6 explores the possibility of a dynamical behaviour of dark energy. Here, the dark energy equation-of-state $w_{\mathrm{de}}(z)$ is modelled as a linear interpolation between a set of 'nodes' with varying amplitudes and redshifts, similarly to the approach used in Chapter 4. In the search of mechanisms or candidates to explain the mild time-dependence of $w_{\mathrm{de}}(z)$, in Chapter 7 we remain focussed on the ΛCDM model but now include a second dark energy component Ω_X with equation-of-state w_X. Finally, in Chapter 8 the Einstein-Hilbert Lagrangian is considered as a limit case of a more general form of it, namely Modified Gravity. We explore these models as an alternative to the dark energy component. The summary of the work done throughout this dissertation is sketched in Figure 3.10.

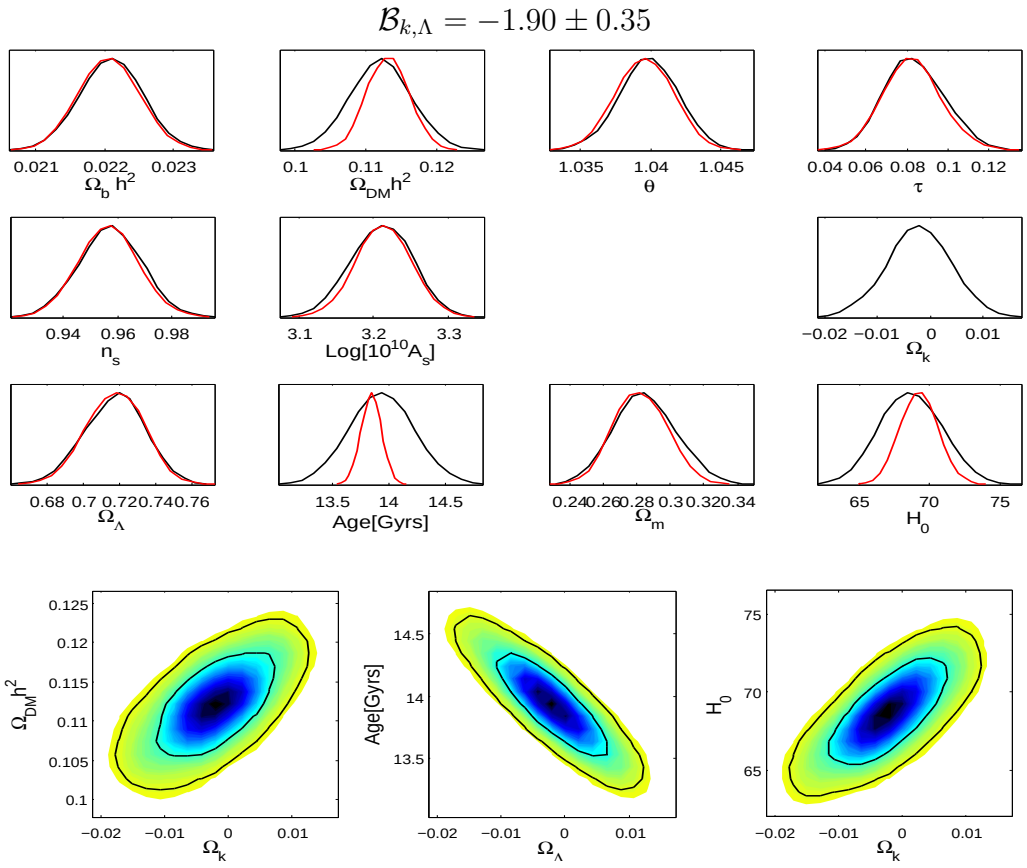

Figure 3.9: Top: 1D marginalised posterior distributions on the standard ΛCDM parameters using current cosmological observations; for flat (red) and non-flat (black) ΛCDM models. Bottom: 2D marginalised posterior distributions of non-flat ΛCDM parameters; constraints are plotted with 1σ and 2σ confidence contours.

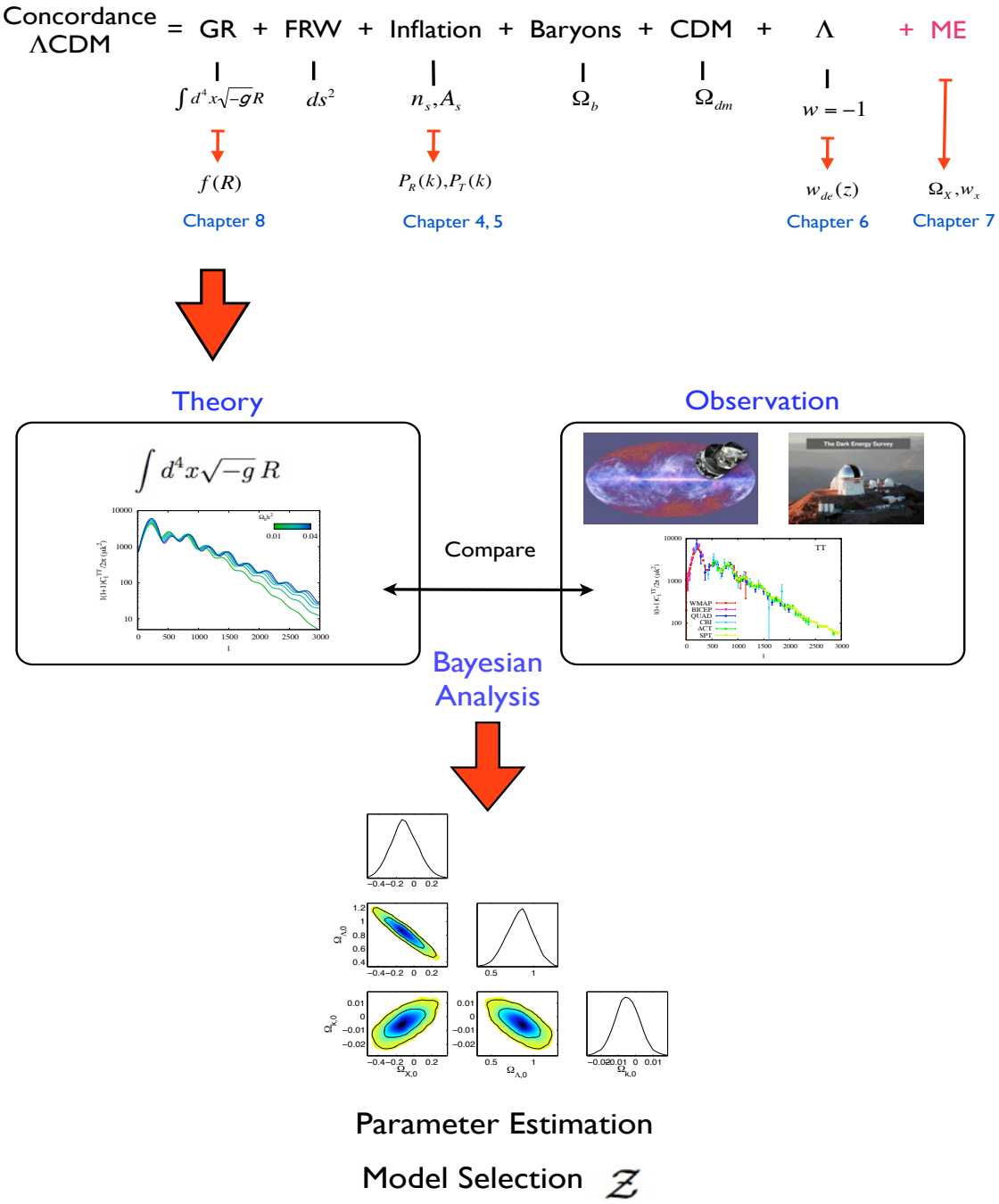

Figure 3.10: Summary of the work performed throughout this dissertation. The top panel of the Figure displays the features beyond the concordance ΛCDM model considered through the following chapters.

Chapter 4

Scalar Power spectrum

Inflationary models generically predict the initial power spectrum of scalar density fluctuations to be close to scale-invariant with just a slight scale dependence. The simplest proposal for the shape of the spectrum is to assume a power-law parameterisation (3.4) in terms of a spectral amplitude A_s and a spectral index or tilt parameter n_s. Although this form has been in good agreement with cosmological observations, recent analyses from the WMAP [120], and the ACT [64] have confirmed that the scale invariant ($n_s = 1$) spectrum is now excluded at 3σ C.L. Similar results are obtained when measurements from the SPT [115] in combination with the WMAP data are considered. It has also been shown that if a running of the spectral index is taken into account, allowing deviations from the power-law spectrum, WMAP+ ACT and WMAP+ SPT data show a preference for a negative running value at 1.8σ C.L. Thus, consideration of models that slightly deviate from the simple power-law might be required. There have been several alternatives proposed. Some physically motivated models include an exponential large scale cut-off [68], discontinuities in the early universe from phase transitions [18], closed universe inflation [126], models in which the power spectrum drops to zero below some cut-off scale [30]. Some use observational data to constrain an *a priori* parameterisation or attempt a direct reconstruction using, for instance, wavelets [169], deconvolution methods [86, 107, 227], by binning the spectrum into an arbitrary number of band powers [27, 28, 82, 91], Bayesian reconstruction techniques [29], principle component analysis [81] or minimising

the level of complexity needed via a cross-validation [178], amongst many others.

In this chapter, we are interested in selecting the preferred shape for the primordial spectrum using the Bayesian evidence as an implementation of Occam's razor. First, we determine the structure of the primordial power spectrum using an optimal model-free reconstruction. Our approach considers possible deviations from the power-law parameterisation by modelling the spectrum as a linear interpolation between a set of 'nodes' which can vary in both amplitude and k-position. Within this analysis we have included phenomenological features which might be relevant to the description of CMB observations, such as a large scale cut-off, a broken spectrum and a spectrum with a possible turn-over at any position in k-space. The reconstruction process is essentially the same *binning* format used previously by a number of authors, however here we allow the data to decide the level of complexity of the model – the number of nodes and their optimum position – via the Bayesian evidence. Then, for comparison, we compute the Bayesian evidence for a set of existing model proposals: a power-law parameterisation including both tilt and running parameter, a modified power-law spectrum to account for a drop off at large scales and the Lasenby & Doran (LD) model based on a closed universe. Finally, for each model we compare its Bayesian evidence and according to the Jeffreys guideline we select the best model preferred by current data.

The base and secondary parameters used throughout this chapter, along with their flat priors, are displayed in Section 3.4. Parameters describing the primordial spectrum are mentioned in each section below. To constrain the parameter-space, we use the dataset I shown in Section 3.4.

The chapter is organised as follows: in the next Section we carry out the reconstruction for the primordial power spectrum, we then consider different existing parameterisations suggested to describe the form of the spectrum (Section 4.2). In a more elaborate way, we present the Lasenby and Doran model (Section 4.3). We show the resulting parameter constraints and the evidence for each worked model. Finally, in Section 4.4 we decide which model of the primordial

scalar spectrum provides the best description for current observational data and present some conclusions.

4.1 Power Spectrum Reconstruction

4.1.1 Node-based spectrum

First, to perform a reconstruction for the shape of the primordial spectrum, we parameterise $\mathcal{P}_\mathcal{R}(k)$ with a specific number of bins, logarithmically spaced in k, and varying only each amplitude, denoted A_{s,k_i}. Throughout, we assume that most of the current relevant information is encompassed within the scales $k_{\mathrm{min}} = 0.0001$ Mpc^{-1} and $k_{\mathrm{max}} = 0.3$ Mpc^{-1}, where the combined WMAP+ACT data significantly improves the parameter constraints. Outside of these boundaries we take the spectrum to be constant with values equal to those at k_{min} and k_{max} respectively. We allow variations in the spectral amplitudes with a conservative prior $A_{\mathrm{s},k_i} \in [1, 50] \times 10^{-10}$.

To model the spectrum between k-nodes, a linear interpolation is performed such that the form of the power spectrum is described by

$$\mathcal{P}_\mathcal{R}(k) = \begin{cases} A_{\mathrm{s},k_{\mathrm{min}}} & k \leq k_{\mathrm{min}} \\ A_{\mathrm{s},k_i} & k \in \{k_i\} \\ A_{\mathrm{s},k_{\mathrm{max}}} & k \geq k_{\mathrm{max}} \end{cases} \tag{4.1}$$

$$\text{and with linear interpolation for} \qquad k_{\mathrm{min}} \leq k_i < \quad k \quad < k_{i+1} \leq k_{\mathrm{max}}.$$

We start our reconstruction by considering the base model which is equivalent to the Harrison-Zel'dovich (HZ) spectrum ($n_\mathrm{s} = 1$) where the spectral amplitude $\mathcal{P}_\mathcal{R}(k) = A_\mathrm{s}$ is the only parameter, see Figure 4.1. The next model, (b), allows for two amplitudes located at k_{min} and k_{max} to vary independently, thus emulating a tilted spectrum. We then add a third point (c) placed midway between the two existing nodes in (b). This model mimics a degree of spectral running by allowing slight variations in the interpolated slopes between the three nodes. Since these amplitudes are independent of each other, however, there is no need to pick any

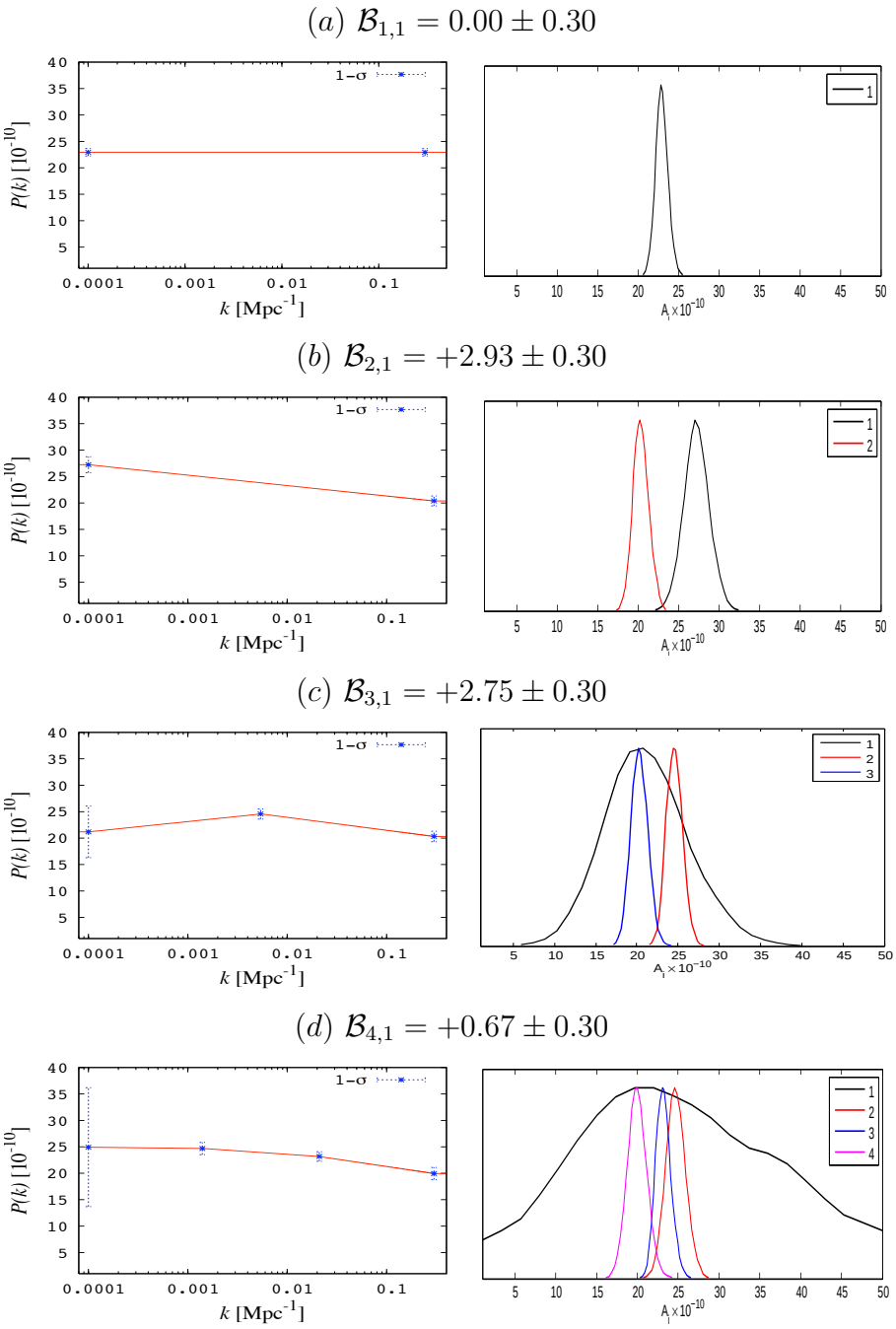

Figure 4.1: Left: Reconstruction of the primordial scalar spectrum modelled as piecewise linear between nodes with fixed wavenumber k_i, along with mean amplitude values and their corresponding 1σ error bars. On large scales the power spectrum is constrained by WMAP data, whereas at small scales ACT/LRG data yield tight constraints up to $k = 0.3$ Mpc^{-1}. Right: 1D marginalised posterior distribution of the amplitudes A_i at each bin in each reconstruction. The top label in each panel denotes the associated Bayes factor respect to the base model (HZ) (a).

particular pivot point as in the case of power-law parameterisation, hence providing more freedom in the shape of the spectrum. The presence of a turn-over in the global structure of the resultant spectrum, shown in Figure 4.1 (c), points to some deviation from a simple tilt. We might continue adding nodes in this fashion until some arbitrary accuracy of model fit is achieved, but always bearing in mind that the inclusion of new unnecessary nodes is penalised through the Bayesian evidence. We, then consider a fourth stage where the k-space is logarithmically split into three equally spaced regions, (d). At small scales the shape of the power spectrum is well constrained with tight error bars on each node, whereas on large scales the error bars tell us there is still room for new features (within the limited amount of information due to cosmic variance (3.9)). Notice the increased error bars due to the addition of an arbitrary number of band-powers and correlations created between them. We also observe the evidence has dropped for four k-nodes, therefore this stage seems to be a reasonable point to stop adding parameters in the reconstruction process. Figure 4.1 illustrates the corresponding form of the reconstructed spectra from the mean posterior estimates (with 1σ error bars on its corresponding amplitudes), together with 1D marginalised posterior distribution for the amplitude at each node and for each reconstruction. In each model we include the Bayes factor compared to the base model (HZ).

The reconstructed spectra are assessed according to the Jeffreys guideline shown in Table 3.2. The Bayesian evidence between the base model and the two-node model $\mathcal{B}_{2,1} = +2.93 \pm 0.30$ points out that the HZ is strongly disfavoured when compared to a tilted spectrum, in agreement with WMAP/ACT [64] results. The addition of complexity in the third stage provides more flexibility in the shape of the reconstructed spectrum. The evidence between the two-node and three-node model, $\mathcal{B}_{2,3} = +0.18 \pm 0.30$, is too small to draw any decisive conclusion, though the evidence marginally prefers the simple tilted spectrum. Although the reconstructed shape of the spectrum in the fourth stage is similar to the one obtained in the second stage, the four k-node model is penalised because of the inclusion of unnecessary information. Thus, the peak of the evidence at model (b) shows that the optimal reconstruction contains, surprisingly, just two nodes, as is shown in Figure 4.1. Therefore, according to this reconstruction

process, parameterisations such as the HZ and those containing more than three k-nodes are hence disfavoured by current observations. At this point of the analysis, with fixed k-node positions, our results are consistent with those obtained by [82], where according to the Akaike information criterion, the preferred model is given by a two-node spectrum.

To extract the global structure of the spectrum we have carried out a reconstruction process by placing nodes at particular positions in k-space. However, to localise features in k-space, we may consider moving either back or forth the internal k-nodes until we find their optimal position; we reconsider this option in an improved method in the next Section.

4.1.2 Node-based spectrum II

In Section 4.1.1 we reconstructed the primordial spectrum using a standard binning process: fix k-node positions and vary only the amplitudes. We now consider a reconstruction of the spectrum where the internal k-node positions vary, as well as their amplitudes. [1]

In order to look for deviations from the simple power-law model, we consider a model with two fixed k-nodes at sufficiently separated positions $[k_{\rm min}, k_{\rm max}]$, with varying amplitudes $[A_{{\rm s},k_{\rm min}}, A_{{\rm s},k_{\rm max}}]$, and place inside additional 'nodes' with the freedom to move around in both position k_i and amplitude $A_{{\rm s},k_i}$. Despite the simplicity of this approach, it covers a large variety of shapes for the primordial spectrum. The freedom of the position of the internal k-nodes allows us to localise the best position for a turn-over (if any) and the amplitudes are able to describe the global structure of the spectrum.

Analogously to Section 4.1.1, we have maintained the same priors for the spectral amplitude $A_{{\rm s},k_i} = [1, 50] \times 10^{-10}$, whereas on the k-position we restrict

[1] A modied CAMB code version which allows a Node-based Parameterisation for the primordial power spectrum is a available at `http://www.mrao.cam.ac.uk/software/`.

to the physical prior $\log k_i = [\log k_{\rm min}, \log k_{\rm max}]$. Hence, for this type of nodal-reconstruction the spectrum is described by

$$\mathcal{P}_{\mathcal{R}}(k) = \begin{cases} A_{{\rm s},k_{\rm min}} & k \leq k_{\rm min} \\ A_{{\rm s},k_i} & k_{\rm min} < k_i < k_{i+1} < k_{\rm max} \\ A_{{\rm s},k_{\rm max}} & k \geq k_{\rm max} \end{cases} \tag{4.2}$$

$$\text{and with linear interpolation for} \quad k_{\rm min} \leq \quad k_i \quad \leq k_{\rm max}.$$

The internal nodes generalise the spectral running by allowing slight variations in the interpolated slopes between external nodes. Figure 4.2 illustrates the reconstruction of the shape of the primordial spectrum from the mean posterior estimates - with 1σ error bars on the amplitudes - (left), along with the 1D marginalised posterior distributions on the parameters used to describe the spectrum (right). On large scales, the reconstructed shape of the one-internal-node model (k_1) resembles a similar spectrum to that obtained in Figure 4.1 (c), but now the probability distribution suggests a preferred turn-over position localised at the largest scales. A similar turn-over has also been identified using principle component analysis [81]. In the two and three-internal-nodes cases, it is interesting to note that at small scales the marginalised posterior peaks at scales where the combined WMAP/ACT constraints are improved; at these scales ($0.1 < k\,[{\rm Mpc}^{-1}] < 0.14$) CMB data now considerably overlap with measurements from SDSS DR7 LRG. This reduced power at small scales might be identified as a feature produced from a phase transition in the early universe [18]. Both, the two and three-internal models (middle and bottom panel of Figure 4.2), present a similar behaviour on the reconstructed spectra, also seen on the marginalised posterior distributions.

4.1.3 Cut-off and Broken spectra

For completeness, we consider the possible existence of a large-scale cut-off on the primordial spectrum. A possible motivation to consider this model has been discussed for instance by [48]. In order to perform the reconstruction for this particular case we fix an extremal node at $k_{\rm max}$ with varying amplitude $A_{{\rm s},k_{\rm max}}$

$(k_1)\ \mathcal{B}_{k_1,1} = +4.26 \pm 0.30$

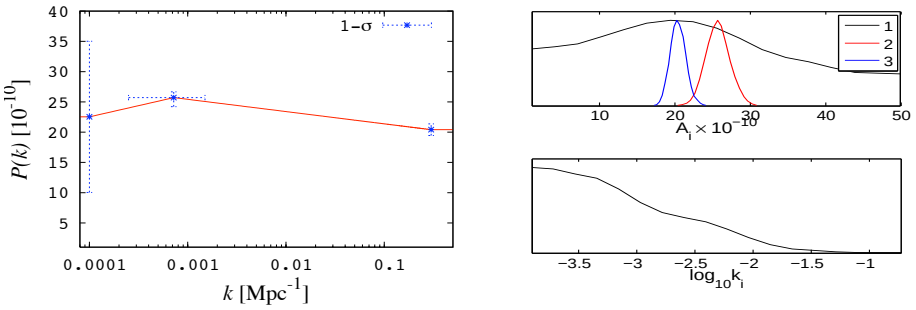

$(k_2)\ \mathcal{B}_{k_2,1} = +3.73 \pm 0.30$

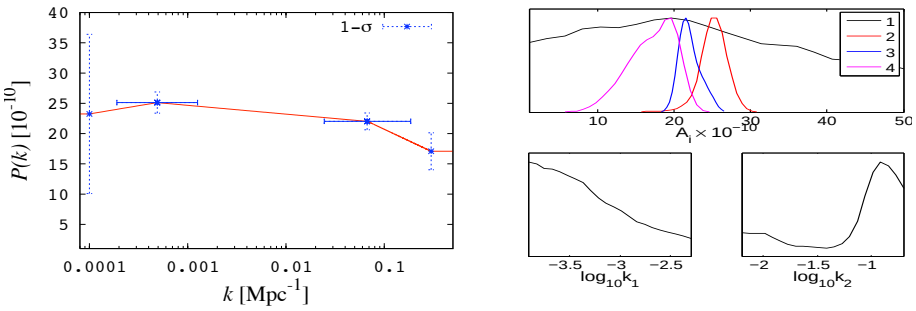

$(k_3)\ \mathcal{B}_{k_3,1} = +3.49 \pm 0.30$

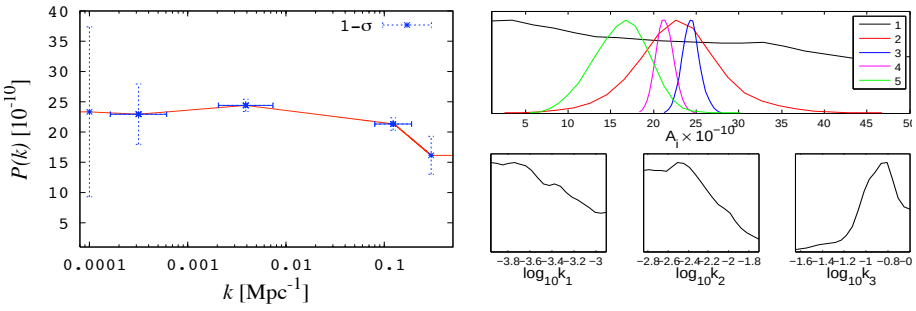

Figure 4.2: Reconstruction of the primordial scalar spectrum letting one internal k-node (top), two internal k-nodes (middle) and three internal k-nodes (bottom) move freely in both amplitude A_i and position k_i. The right panel corresponds to the 1D marginalised posterior distribution of the amplitudes and k-node position in each reconstruction. The top label in each panel denotes the associated Bayes factor with respect to the base model (HZ) shown in Figure 4.1 (a).

and let the cut-off scale k_c vary across the prior $[k_{\rm min}, k_{\rm max}]$ as well as its amplitude $A_{{\rm s},c}$. The form of the spectrum is described as follows:

$$\mathcal{P}_{\mathcal{R}}(k) = \begin{cases} 0 & k \leq k_c \\ A_{{\rm s},c} & k_c < k < k_{\rm max} \\ A_{\rm s,max} & k \geq k_{\rm max} \end{cases} \tag{4.3}$$

$$\text{and with linear interpolation for} \quad k_c < \quad k \quad < k_{\rm max}.$$

Also, we consider a broken spectrum which might have been produced from phase transitions in the early universe. A similar broken spectrum, motivated by double or multiple field inflation, has been considered by [18, 30]. This spectrum is obtained by placing two nodes k_1 and k_2 within $[k_{\rm min}, k_{\rm max}]$, and letting them move freely in amplitude $A_{{\rm s},k_i}$ and k-position, such that

$$\mathcal{P}_{\mathcal{R}}(k) = \begin{cases} A_{{\rm s},k_1} & k < k_1 \\ A_{{\rm s},k_2} & k \geq k_2 \end{cases} \tag{4.4}$$

$$\text{and with linear interpolation for} \qquad k_1 \quad < k_2.$$

The reconstruction of the cut-off and broken primordial spectra along with 1σ limits of the marginalised distributions are shown in the left panels of Figure 4.3. Their corresponding posterior distribution in each parameter used to describe the spectra are illustrated in the right panels. The obtained best-fit parameters for the cut-off spectrum (top), show a preferred scale at which the power drops to zero with an upper limit $\log_{10} k_c < -3.45$ at 95% C.L. Our constraints on k_c also show a significant likelihood at large scales, thereby disfavouring the presence of an abrupt cut-off. With respect to the broken model (bottom), on the other hand, the best fit parameters indeed predict a break in the primordial spectrum, located approximately at $\log_{10} k \simeq -2.2$. That could be an indicative of the existence of a phase transition, and it is similarly obtained in the two and three-internal-nodes models shown in Figure 4.2.

In this section we have considered three types of spectra with different features: turn-over, large scale cut-off and broken spectrum (Figures 4.2-4.3). In each figure we have included the Bayes factor compared to the base model (HZ).

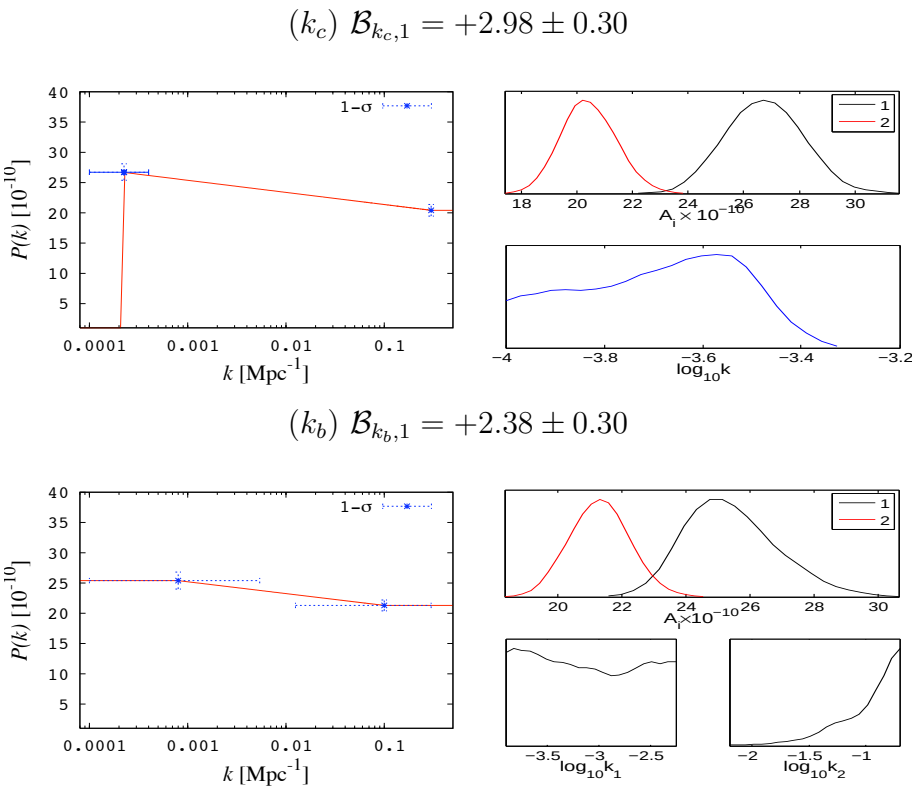

Figure 4.3: Reconstruction of the large-scale cut-off spectrum (top) and broken spectrum (bottom); their corresponding 1D marginalised posterior distribution of the amplitudes $A_{\rm i}$ and node positions k_i in each reconstruction (right). The top label in each panel denotes the associated Bayes factor with respect to the base model (HZ) shown in Figure 4.1 (a).

According to the Jeffreys guideline the one-internal-node spectrum, shown in the top panel of Figure 4.2, is significantly preferred over the cut-off and broken spectrum models, $\mathcal{B}_{k_1,k_c} = +1.28 \pm 0.30$ and $\mathcal{B}_{k_1,k_b} = +1.88 \pm 0.30$ respectively. Even though the model with one-internal node is described by four parameters, when it is compared to the Harrison-Zel'dovich spectrum (with only one parameter), the Bayes factor $\mathcal{B}_{k_1,1} = +4.26 \pm 0.30$ shows that the presence of a turn-over is strongly favoured by current cosmological information and significantly so when compared to the tilted spectrum (with two parameters) $\mathcal{B}_{k_1,2} = +1.33 \pm 0.30$, see Figure 4.1. Therefore, the presence of a turn-over in $\mathcal{P}_{\mathcal{R}}(k)$ plays an important

role in explaining current observations. Notice that, in the bottom panel of Figure 4.2 the Bayesian evidence has dropped off, hence the reason we have stopped the addition of nodes in the reconstruction process.

4.2 Power Spectrum Parameterisation

4.2.1 Power-law and running spectra

We have considered, so far, a $\mathcal{P}_{\mathcal{R}}(k)$ shape reconstructed directly from data. For comparison we include the standard approach by assuming the power-law parameterisation (3.4) in terms of a spectral amplitude $A_{\rm s}$ and a spectral index or tilt parameter $n_{\rm s}$:

$$\mathcal{P}_{\mathcal{R}}(k) = A_{\rm s}\left(\frac{k}{k_0}\right)^{n_{\rm s}-1}, \tag{4.5}$$

k_0 denotes the pivot point, fixed to $k_0 = 0.002$ Mpc^{-1}. We assume the prior $A_{\rm s} = [1, 50]\times 10^{-10}$ on the amplitude, together with the conservative prior $n_{\rm s} = [0.7, 1.2]$ on the spectral index. We find a mean value of $n_{\rm s} = 0.963 \pm 0.011$ which confirms that our constraints are in good agreement with results from [64, 115, 120] and Section 3.4. As a further extension we consider possible deviations from power-law by allowing the spectral index to vary as a function of scale $n_{\rm s}(k)$. Then the primordial spectrum becomes

$$\mathcal{P}_{\mathcal{R}}(k) = A_{\rm s}\left(\frac{k}{k_0}\right)^{n_{\rm s}-1+\frac{1}{2}\ln\left(\frac{k}{k_0}\right)n_{\rm run}}, \tag{4.6}$$

where $n_{\rm run}$ is termed the running parameter and is expected to be $n_{\rm run} \approx 0$ for standard inflationary models. In order to minimise the correlation between $n_{\rm s}$ and $n_{\rm run}$ we have considered a pivot scale of $k_0 = 0.015$ Mpc^{-1}, as pointed out by [51]. We use the same priors as above on $A_{\rm s}$ and $n_{\rm s}$, and the conservative prior $n_{\rm run} = [-0.3, 0.3]$ on the running parameter. From the combined dataset we find the marginalised posteriors show a preference for a negative running parameter $n_{\rm run} = -0.026 \pm 0.015$ and $n_{\rm s} = 0.968 \pm 0.011$ for the spectral index, as expected by [64, 115, 120]. Figure 4.4 shows the marginalised posterior distributions for the parameters used to describe $\mathcal{P}_{\mathcal{R}}(k)$ and the obtained spectrum from mean posterior estimates of a simple tilted parameterisation with $n_{\rm s}$ (left) and including the

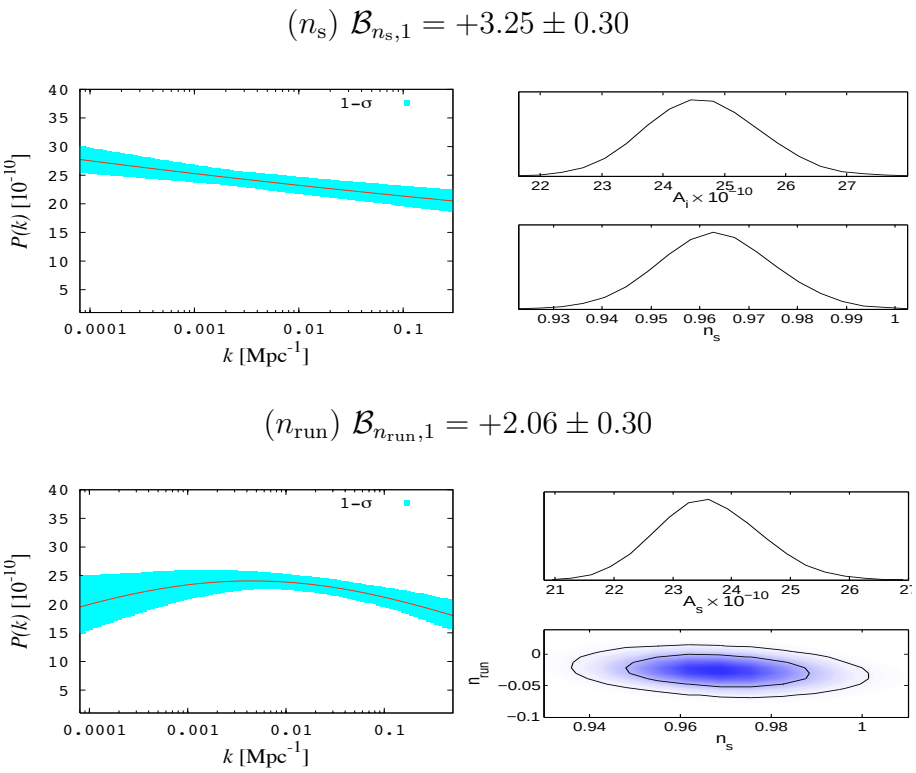

Figure 4.4: Reconstruction of the primordial scalar spectrum assuming a simple tilted parameterisation with n_s (top) and including the running parameter n_{run} (bottom); the coloured region denotes 1σ error bands on the reconstruction. Right: marginalised 1D and 2D probability posterior distributions for the power spectrum parameters; 2D constraints are plotted with 1σ and 2σ confidence contours. The top label in each panel denotes the associated Bayes factor with respect to the base model (HZ) shown in Figure 4.1 (a).

running parameter n_{run} (right) respectively. In each panel we have included the Bayes factor compared to the base model (HZ).

According to the Jeffreys guideline, present observations significantly prefer a simple tilted model when compared to a model which includes a running parameter by a factor $\mathcal{B}_{n_s,n_{run}} = +1.19 \pm 0.30$. Similarly, a tilted spectrum is strongly preferred when compared to the HZ model: $\mathcal{B}_{n_s,1} = +3.25 \pm 0.30$. We also confirm

the agreement between the simple tilted model and the two-fixed-noded spectrum through its Bayes factor, shown in Figure 4.1 (b). An important point to emphasise is that the simple tilt and running model present a significantly and strongly disfavoured Bayes factor, $\mathcal{B}_{n_{\rm s},k_1} = -1.01 \pm 0.30$, $\mathcal{B}_{n_{\rm run},k_1} = -2.20 \pm 0.30$, compared to the reconstructed one-internal-node spectrum shown in Figure 4.2. Thus a simple power-law parameterisation seems to be not enough to describe current cosmological observations, hence slight deviations of it should be taken into account.

4.2.2 Modified Power-law spectrum

We have observed that models which present a turn-over at large scales are slightly preferred by the evidence. Based on this observation, we suggest the following phenomenological shape for the primordial power spectrum:

$$\mathcal{P}_{\mathcal{R}}(k) = A_{\rm s}\frac{\left(\frac{k}{k_{\rm v}}\right)^{n_{\rm v}}}{\frac{k}{k_{\rm v}}+1}. \tag{4.7}$$

In this particular parameterisation, assuming $n_{\rm v} < 1$, the parameter $k_{\rm v}$ determines the transition between a standard power-law model with red tilt ($k \gg k_{\rm v}$) to a blue tilt model ($k \ll k_{\rm v}$):

$$\mathcal{P}_{\mathcal{R}}(k) = A_{\rm s}\begin{cases} \left(\frac{k}{k_{\rm v}}\right)^{n_{\rm v}-1} & k \gg k_{\rm v}, \\ \left(\frac{k}{k_{\rm v}}\right)^{n_{\rm v}} & k \ll k_{\rm v}, \end{cases} \tag{4.8}$$

where the prior on $n_{\rm v}$ is similarly chosen to the spectral index $n_{\rm s}$ in the power-law parameterisation: $n_{\rm v} = [0.7, 1.2]$. We expect the constraints on the parameter $k_{\rm v}$ are mainly located on large scales, hence, for this extra-parameter we consider the following flat prior $\ln k_{\rm v} = [-15, -5]$. The reconstruction of the shape of this spectrum along with the posterior distribution in each parameter are shown in Figure 4.5. We observe the constraints for the new tilt-parameter $n_{\rm v} = 0.955 \pm 0.014$ are similar to those obtained from the power-law models, where the scale-invariant spectrum is ruled out at a high confidence level and the spectrum exhibits a red tilt at small scales. The marginalised posterior probability on $k_{\rm v}$ shows the existence of a blue-tilted spectrum on large scales $\ln k_{\rm v} < -8.1$ at 95% C.L.

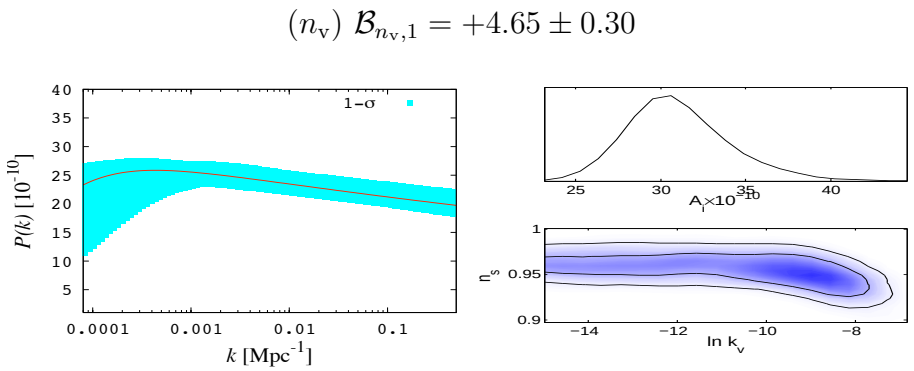

Figure 4.5: Reconstruction of the primordial scalar spectrum from mean posterior estimates of the modified power-law parameterisation, along with 1σ error bands (left). Right: marginalised 1D and 2D probability posterior distributions for the power spectrum parameters; 2D constraints are plotted with 1σ and 2σ confidence contours. The top label in each panel denotes the associated Bayes factor with respect to the base model (HZ) shown in Figure 4.1 (a).

Hence, the global shape for this spectrum presents a slight running behaviour with reduced power at both large and small scales, compared to the simple tilt parameterisation.

The modified power-law parameterisation decisively rules out the HZ, since the Bayes factor between the models is $\mathcal{B}_{n_{\rm v},1} = +4.65 \pm 0.30$. Moreover, even though the modified power-law model has an extra parameter compared to the simple power-law model, the data significantly prefer it with $\mathcal{B}_{n_{\rm v},n_{\rm s}} = +1.40 \pm 0.30$.

4.3 Lasenby & Doran spectrum

Assuming the cosmological constant is the origin of dark energy, Lasenby and Doran [126] provided a construction for embedding closed-universe models in a de Sitter background. As a consequence of this novel approach, a boundary condition on the total available conformal time emerges. Remembering the total

conformal time η (2.42), the LD model requires:

$$\eta \equiv \int_0^\infty \frac{dt}{R(t)} = \frac{\pi}{2}. \tag{4.9}$$

For more details about the choice of the boundary condition, including how it can be reinterpreted as an eigenvalue condition on the solution of a differential equation, see Lasenby and Doran [126], Lasenby [127], Lasenby and Doran [128]. In order to understand some consequences of the new boundary condition we split the history of the universe in two main contributions to the total conformal time: matter (radiation and dust) and inflationary era. Hence, we want to compute the conformal time η_{M} elapsed during the matter era and add it to that elapsed in the inflationary era η_{I}, such that the boundary condition is satisfied:

$$\eta_{\mathrm{I}} + \eta_{\mathrm{M}} = \frac{\pi}{2}. \tag{4.10}$$

It is found that this constraint leads to a 'see-saw' mechanism linking the parameters describing the current state of the universe with the initial conditions [128].

Matter era

We have shown that the general description of the large-scale universe, based on the FRW space-time, is governed by the Friedmann equations. If we assume the matter density is made up of decoupled dust and radiation, the Friedmann equations can be solved exactly and its solution is controlled by two arbitrary constants α and β given by

$$\begin{aligned} \alpha &= \frac{\Omega_{\mathrm{m},0}^2 \Omega_{\Lambda,0}}{(\Omega_{\mathrm{m},0} + \Omega_{r,0} + \Omega_{\Lambda,0} - 1)^3}, \\ \alpha\beta &= \frac{\Omega_{r,0} \Omega_{\Lambda,0}}{(\Omega_{\mathrm{m},0} + \Omega_{r,0} + \Omega_{\Lambda,0} - 1)^2}. \end{aligned} \tag{4.11}$$

The total conformal time for this type of universe can be written in terms of the dimensionless parameters α and β [126], as

$$\eta_M = \int_0^\infty \frac{dx}{(\beta x^4 + x^3 - x^2 + \alpha)^{1/2}}. \tag{4.12}$$

Inflationary era

The computation of the conformal time in the inflationary epoch is a more elaborate process. Let us consider a basic inflationary model where the particle responsible for this process is simply a real, time-dependent, homogeneous, free, massive scalar field ϕ, described by the equations (2.65)-(2.67) with cosmological constant:

$$\dot{H} + H^2 - \frac{\Lambda}{3} + \frac{4\pi G}{3}(2\dot{\phi}^2 - m^2\phi^2) = 0, \tag{4.13}$$

$$\ddot{\phi} + 3H\dot{\phi} + m^2\phi = 0. \tag{4.14}$$

For closed universe models, the scale factor is given explicitly by

$$\frac{1}{R^2} = \frac{4\pi G}{3}(\dot{\phi}^2 + m^2\phi^2) - H^2 + \frac{\Lambda}{3}. \tag{4.15}$$

In order to compute the conformal time η_I, it is necessary to seek out suitable conditions before the onset of inflation and then solve the dynamics for the scalar field encoded in equations (4.13) and (4.14). To do this, Lasenby and Doran [126] developed formal series expansions out of the initial singularity, $t = 0$, in terms of dimensionless variables $u = t/t_{\rm p}$ and $\mu = m/m_{\rm p}$, where the subscript 'p' denotes a variable in Planck units. The series are given by

$$\phi(u) = \frac{1}{l_{\rm p}}\sum_{n=0}^{\infty}\phi_n(u)\ln^n(u), \qquad H(u) = \frac{1}{t_{\rm p}}\sum_{n=0}^{\infty}H_n(u)\ln^n(u), \tag{4.16}$$

with

$$\begin{aligned}
\phi_0 &= b_0 + b_4u^{4/3} - \frac{118\sqrt{3\pi}b_4^2}{99}u^{8/3} - \frac{u^2}{1296\pi}(11\sqrt{3\pi}\mu^2 - 54\sqrt{3\pi}\Lambda \\
&\quad -216\sqrt{3}\pi^{3/2}\mu^2b_0^2 + 36\pi\mu^2b_0), \\
\phi_1 &= -\sqrt{\frac{1}{12\pi} - \frac{\mu^2}{216\pi}\left(-\sqrt{3\pi} + 36\pi b_0\right)}\,u^2, \\
H_0 &= \frac{1}{3u} + \frac{32\sqrt{3\pi}}{27}b_4u^{1/3} + (\frac{2\mu^2}{81} + \frac{\Lambda}{3} + \frac{4\pi}{3}\mu^2b_0^2 + \frac{4\sqrt{3\pi}}{27}\mu^2b_0)u \\
&\quad -\frac{6656\pi b_4^2}{891}u^{5/3}, \\
H_1 &= -u\frac{dH_0}{du} - uH_0^2 + \frac{u\Lambda}{3} - \frac{8\pi\ u}{3}\left(\frac{d\phi_0}{du}\right)^2 - \frac{16\pi\phi_1}{3}\frac{d\phi_0}{du} \\
&\quad -\frac{8\pi\phi_1^2}{3u} + \frac{4\pi\mu^2u\phi_0^2}{3}.
\end{aligned} \tag{4.17}$$

We observe that two new free parameters b_0 and b_4, appear in the series expansions. Together with the mass of the scalar field μ, they control the magnitude of the field and how long the inflationary period lasts. In order to decide on the priors we shall employ in our subsequent Bayesian analysis, it is worth pointing out some features related with these new parameters.

- The amplitude of the perturbations is determined by the scalar field mass μ. To match the observed level of CMB anisotropies, we shall need to set it to be about
$$\mu \sim 10^{-6}. \tag{4.18}$$

- The number of e-foldings N is primarily determined by b_0 and may be approximated as
$$N \approx 2\pi b_0^2. \tag{4.19}$$
Hence, to obtain realistic models we need b_0 to be of order $\sim$ a few.

- The conformal time is estimated by
$$\eta_I \approx 0.92 \left(\frac{|b_4|}{\mu^{4/3}}\right)^{1/2} \left(\frac{1}{b_0^2}\right). \tag{4.20}$$
Employing the constraint (4.10), $|b_4|\mu^{-4/3}$ should thus be around unity.

- The parameter b_4 controls the initial curvature, as can be seen from (4.15):
$$\frac{R}{l_{\rm p}} \approx \left(\frac{2187}{12544\pi}\right)^{1/4} \frac{u^{1/3}}{\sqrt{-b_4}}. \tag{4.21}$$
Therefore b_4 must be negative. Making use of the rest of the parameters and (4.20), $|b_4|$ should be around 10^{-9}.

The restriction on the values for the model parameters together with the boundary condition, severely limits the class of models allowed to reproduce current cosmological observations.

Once we have found the initial conditions (4.17), it is straightforward to solve numerically the dynamics of the scalar field ϕ and the expansion history H to

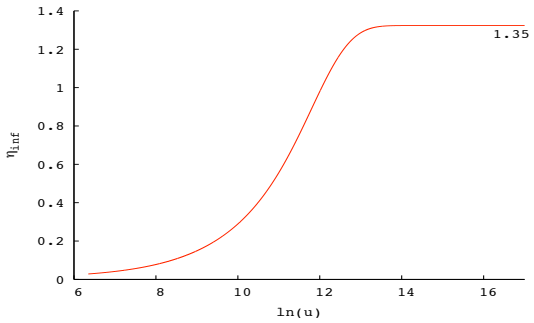

Figure 4.6: Evolution of the conformal time η_I as a function of $\ln(u)$. We observe that η_I saturates at a value of around 1.35 by the end of inflation. The parameters used in this model are $b_0 = 2.47$, $b_4 = -17.7 \times 10^{-9}$ and $\mu = 1.68 \times 10^{-6}$.

determine the evolution of the universe. As an example, let us consider the best-fit values for the cosmological parameters given by WMAP+BAO+H_0 [120], in which case the conformal time elapsed during the matter epoch is $\eta_M = 0.22$. In order to satisfy the boundary condition we should choose appropriate values $\{b_0, b_4, \mu\}$ such that by the end of the inflationary period the achieve conformal time is $\eta_I \approx 1.35$, as shown on Figure 4.6. Then, the expected shape of the primordial power spectrum $\mathcal{P}(k)$ for this model is directly computed from (2.142):

$$\mathcal{P}_{\mathcal{R}}(k) = \left[\left(\frac{H}{\dot{\phi}} \right)^2 \left(\frac{H}{2\pi} \right)^2 \right]_{k=RH} . \tag{4.22}$$

As a consequence of the restriction of the total conformal time available in the entire history of a closed Universe and the proper construction of the initial conditions, the LD primordial spectrum has some worth noted features. The spectrum derived from this model naturally incorporates an exponential cut-off on large scales which might provide a possible explanation for the lower-than-expected CMB power spectrum at low multipoles. On small scales, the relationship between $\mathcal{P}_{\mathcal{R}}^{1/2}(k)$ and $\ln k$ is linear, thus predicting a reduced power at large k as compared to a simple tilted spectrum (for which $\ln \mathcal{P}_{\mathcal{R}}^{1/2}(k)$ versus $\ln k$ is linear). For further details about the LD model see, for instance [127, 128]. To compute the LD spectrum we refer our analysis to [236]. We have also chosen the priors

$(n_{\rm LD})\ \mathcal{B}_{\rm LD,1} = +4.94 \pm 0.30$

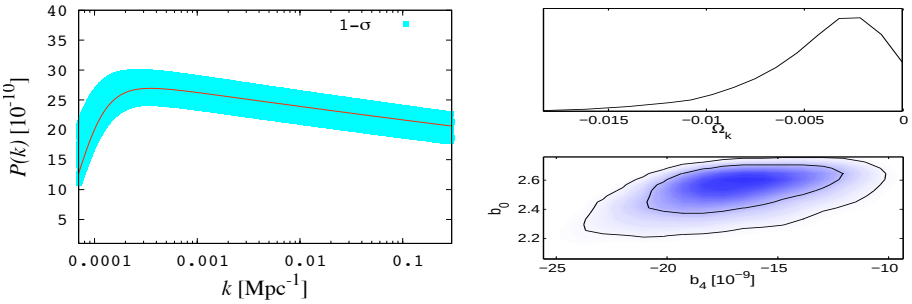

Figure 4.7: Reconstruction of the primordial scalar spectrum assuming a Lasenby & Doran model along with 1σ error bands (left). Right: marginalised 1D and 2D probability posterior distributions for the power spectrum parameters; 2D constraints are plotted with 1σ and 2σ confidence contours. The top label on the panel denotes the associated Bayes factor with respect to the base model (HZ) shown in Figure 4.1 (a).

based on the same paper: $\Omega_{k,0} = [-0.05, 10^{-4}]$, $b_0 = [1, 4]$, $b_4 = [-30, -1] \times 10^{-9}$. Figure 4.7 shows the reconstructed shape of the primordial spectrum along with the posterior distribution in each additional parameter for this model; the constraints on the present Hubble parameter are $H_0 = 69.4 \pm 1.4$, whereas the number of e-folds is $N = 50.6 \pm 4.3$ (see Figure 4.8) [236]. From the top label of Figure 4.7, we observe the LD model is significantly preferred over the simple power-law parameterisation with a Bayes factor of $\mathcal{B}_{\rm LD,}{}_{n_{\rm s}} = +1.69 \pm 0.30$ and decisive when compared to the HZ spectrum: $\mathcal{B}_{\rm LD,1} = +4.94 \pm 0.30$.

Indeed, the LD model has the largest evidence of all the models investigated, followed closely by the modified power-law spectrum. It should be noted, however, that the latter was constructed specifically to exhibit a turn-over on large scales, having already found that the data prefer such a feature. A fairer comparison would be between the LD model and the third most favoured model, namely the one-internal-node linear-interpolation model described in Section 4.1.2, since both of these models were proposed *a priori*. To this end, and as a check on our analy-

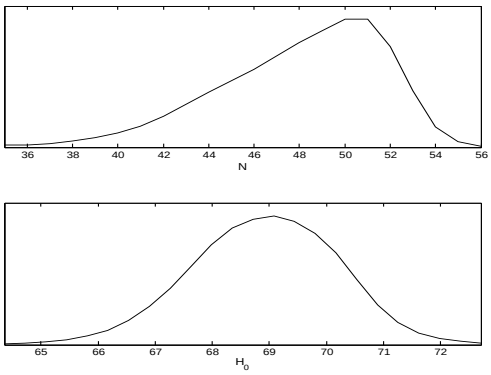

Figure 4.8: Marginalised 1D probability distributions for the number of e-foldings produced during inflation (top) and Hubble constant (bottom), obtained from the LD model.

sis, we use the best-fit LD model (shown in Figure 4.7) as the input spectrum to simulate an idealised CMB observation containing only cosmic-variance-limited noise (3.9). Figure 4.9 (left panel) shows the resulting CMB temperature spectrum. We then analysed these simulated data using the one-internal-node linear interpolation model to reconstruct the primordial power spectrum. Figure 4.9 (right panel) shows the resulting reconstruction (dotted line), which recovers well the shape of the input LD spectrum (solid line), except on the very largest scales, where there is little information in the simulated CMB data. Moreover, the reconstructed spectrum has a similar shape to the one obtained from real data using the one-internal-node model (see Figure 4.2). We may therefore understand the higher evidence for the LD model spectrum as resulting from its similar quality fit to the data, but requiring fewer free parameters than the one-internal-node linear-interpolation model.

Finally, we note that, in the node-based reconstruction, the use of linear interpolation between the nodes may seem crude. It is straightforward to generalise the node-based approach to more sophisticated interpolation schemes, but this may not always yield better results. In Appendix A, we illustrate this point by reanalysing the simulated CMB data using a cubic spline interpolation through

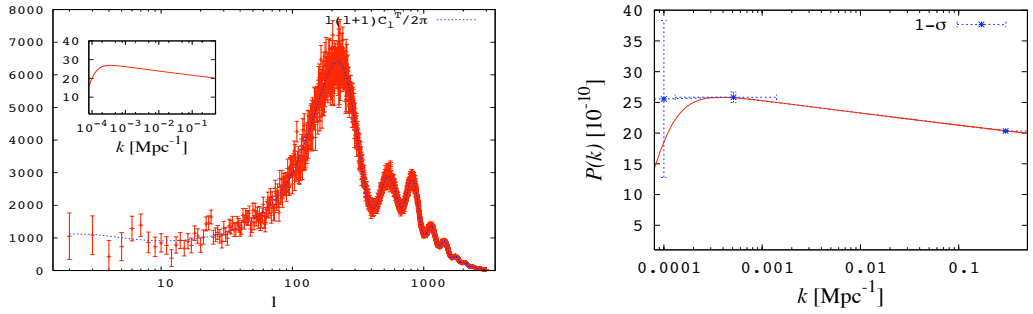

Figure 4.9: Reconstruction of the Lasenby & Doran primordial scalar spectrum based on the binning format with linear interpolation described in Section 4.1.2. We have assumed an idealised CMB spectrum with limitation only due to cosmic variance (left). Right panel shows the reconstructed spectrum in the binning format together with the LD input spectrum (solid line).

the nodes, thus allowing one to reconstruct a smooth shape for the primordial spectrum, but one that is less satisfactory than that obtained using linear interpolation.

4.4 Discussion and Conclusions

In this chapter we have attempted to fit an optimal degree of structure for the primordial power spectrum of curvature perturbations using Bayesian model selection as our discriminating criterion. We have modelled the spectrum as a linear interpolation between a set of 'nodes' with varying amplitude and k-position. We have also explored different parameterisations of the primordial spectrum which include: a power-law parameterisation with both tilt and running parameter, a modified power-law spectrum and the Lasenby & Doran model.

All the considered models have in common the standard ΛCDM parameters: $\Omega_{\rm b}h^2$, $\Omega_{\rm DM}h^2$, θ, τ, as well as the secondary parameters: A_{SZ}, A_p, A_c. Thus, priors on these parameters remained the same in each model. The best-fit values for these standard parameters are consistent with those obtained using the con-

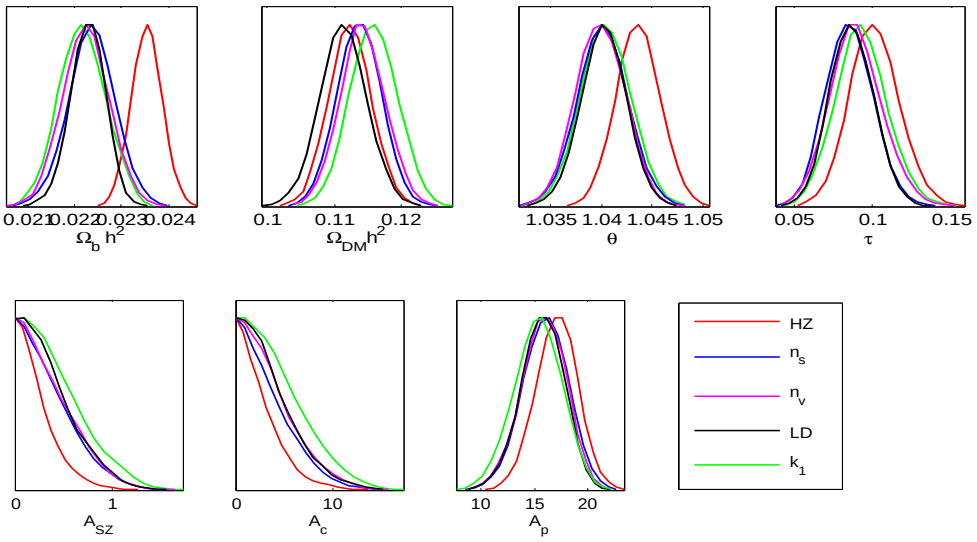

Figure 4.10: 1D marginalised posterior distributions for the primary (top) and secondary (bottom) cosmological parameters, for each corresponding model listed on the bottom-right box.

cordance 6-parameter model with power-law primordial spectrum (see Section 3.4). We show, in Figure 4.10, 1D marginalised posterior distributions for the cosmological parameters of each of the preferred models. We observe the values of the standard parameters remain well constrained despite the addition of extra freedom on the shape of the primordial spectrum, although the constraints resulting from the HZ spectrum clearly differ from the others. Note also that the constraints on the parameters corresponding to the LD model are slightly tighter than the rest of the models.

We have considered wide-enough priors in our analysis, such that they do not interfere with the inferred parameter values. We used priors on the amplitudes of $A_i = [1, 50] \times 10^{-10}$ and on spectral indices of $n_{\rm s} = n_{\rm v} = [0.7, 1.2]$, while the parameters describing the k-space have physical priors restricted by $[k_{\rm min}, k_{\rm max}]$. We now compute the Bayesian evidence for a wider prior range of $n_{\rm s} = n_{\rm v} = [0.5, 1.5]$, $b_4 = [-50, -1] \times 10^{-9}$, and also for $n_{\rm s} = [0.7, 1.2]$ with narrow priors for

Model	N_{par}	$-2\Delta \ln \mathcal{L}_{max}$	Bayes factor
HZ	8	0.0	$\mathcal{B}_{1,1} = +0.0 \pm 0.3$
n_s	9	-8.6	$\mathcal{B}_{n_s,1} = +3.3 \pm 0.3$
n_v	10	-9.4	$\mathcal{B}_{n_v,1} = +4.7 \pm 0.3$
LD	10	-9.4	$\mathcal{B}_{LD,1} = +4.9 \pm 0.3$
k_1	11	-9.1	$\mathcal{B}_{k_1,1} = +4.3 \pm 0.3$

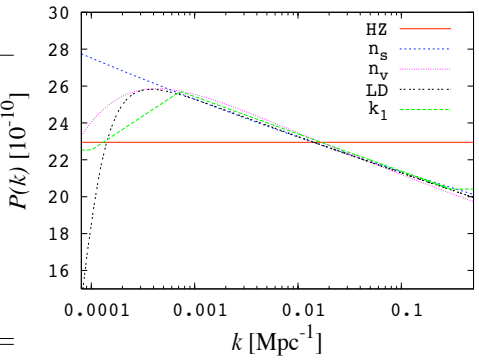

Figure 4.11: Comparison of the primordial scalar power spectra for the preferred models along with their Bayesian evidence. We also include the maximum likelihood $\mathcal{L}_{max}$ for a model with number of parameters N_{par}. Each Bayes factor is compared respect to the one-node model (HZ).

$n_{run} = [-0.1, 01]$, to illustrate the robustness of a model over small variations of the prior range:

$$\mathcal{B}_{n_s,1} = +2.25 \pm 0.30 \qquad \text{(wide priors)}$$

$$\mathcal{B}_{n_v,1} = +4.24 \pm 0.30 \qquad \text{(wide priors)}$$

$$\mathcal{B}_{LD,1} = +4.47 \pm 0.30 \qquad \text{(wide priors)}$$

$$\mathcal{B}_{run,1} = +2.85 \pm 0.30 \qquad \text{(narrow priors)}$$

We observe that even when wider priors are considered, the HZ model is strongly disfavoured when compared to n_v and LD models. Similarly, the simple tilted and running model are still significantly disfavoured.

To summarise the analysis, in Figure 4.11 we plot the reconstructed spectra for the preferred selected models together with their corresponding Bayesian evidence. It shows that the HZ spectrum is decisively excluded as a viable model to describe $\mathcal{P}_{\mathcal{R}}(k)$. The preferred model given current observations is provided by the LD model followed by a modified power-law version. We have found that the power-law parameterisation, including either cases n_s and $n_s + n_{run}$, are both

significantly disfavoured. The presence of a turn-over at large scales [1] and the reduced power at small scales seem to provide an important contribution on choosing the best-fit model through its Bayesian evidence.

[1] At the largest scales, the addition of tensor perturbations might considerably affect the shape of the primordial spectrum. Hence, we consider this possibility in Chapter 5.

Chapter 5

Tensor-to-Scalar ratio

Although the power-law assumption on the scalar spectrum provides reasonable agreement with cosmological observations, some recent analyses show that if a running of the scalar spectral-index, within the standard ΛCDM model, is taken into account, there exists a preference for a negative running-value at 2.2σ C.L. with WMAP7+QUaD. In the previous chapter we found, by using model-independent techniques, that the existence of a turn-over in $\mathcal{P}_{\mathcal{R}}(k)$ is preferred. This turn-over plays an important role in explaining current cosmological observations and cannot therefore be ignored when constraining the inflationary parameters. In the slow-roll approximation, the shape of the spectrum of tensor perturbations is

$$\mathcal{P}_{\mathcal{T}}(k) = \left[\frac{16}{\pi}H^2\right]_{k=aH}, \tag{5.1}$$

which depends on the form of the scalar spectrum and vice-versa, via the potential of the single scalar-field. To place constraints on the amplitude of tensor contributions, it is customary to define the tensor-to-scalar ratio as

$$r(k) \equiv \frac{\mathcal{P}_{\mathcal{T}}(k)}{\mathcal{P}_{\mathcal{R}}(k)} = 64\pi \left[\frac{\dot{\phi}^2}{H^2}\right]_{k=aH}. \tag{5.2}$$

The dependence of the scalar spectrum on the tensor spectrum is more evident in the Lasenby & Doran model, where both spectra depend upon the same best-fit parameters. In this chapter, by assuming a power-law parameterisation on the

tensor spectrum, we show that the bending of the scalar spectrum is enhanced due to the presence of a tensor component. We show that current constraints on the tensor-to-scalar ratio (5.2) are broadened for non-power law $\mathcal{P}_{\mathcal{R}}(k)$ models. We also discuss the constraints on r for a massive scalar-field in the Lasenby & Doran model. Finally, we consider future experiments and present their expected constraints on the inflationary parameters. For all the models, we compute the Bayes factor in order to perform a model comparison.

The chapter is organised as follows: in Section 5.2 we present different models suggested to describe the form of the scalar spectrum. We then show the resulting parameter constraints on the tensor-to-scalar ratio and the preferred form of the power spectrum, using current cosmological observations. In the same section we provide future constraints on r expected by Planck-like and CMB-Pol experiments. We present some conclusions in Section 5.4.

5.1 Theoretical Framework

Even though the primary parameters in the standard ΛCDM model have already been tightly constrained and have little impact on the B-mode spectrum, it is worthwhile to perform a full parameter-space exploration to determine the tensor-to-scalar ratio constraints in each model. We consider the tensor-to-scalar ratio for each model i, as $r_i = \mathcal{P}_{\mathcal{T}(i)}(k)/\mathcal{P}_{\mathcal{R}(i)}(k)$. Hereafter we set $r_i = r_i(k_0)$ at a scale of $k_0 = 0.015\text{Mpc}^{-1}$. A study of the appropriate scale to use is given by [52]. The base and secondary parameters used throughout this chapter, along with their flat priors, are displayed in Section 3.4. To constrain the parameter-space, we consider dataset II introduced in Section 3.4, and additionally use Planck and CMBPol realisations to show future expected constraints (see Section 3.2.2).

5.2 Primordial power spectra constraints

5.2.1 Power-law parameterisation

Here, for simplicity, we assume the scalar and tensor spectra are described by power law functions given by (3.4) and (3.5):

$$\mathcal{P}_{\mathcal{R}}(k) = A_{\rm s}\left(\frac{k}{k_0}\right)^{n_{\rm s}-1}, \qquad \mathcal{P}_{\mathcal{T}}(k) = A_{\rm t}\left(\frac{k}{k_0}\right)^{n_{\rm t}}, \tag{5.3}$$

where the tensor amplitude $A_{\rm t}$ is related to tensor-to-scalar ratio $r_{\rm s} = A_{\rm t}/A_{\rm s}$. For this parameterisation, we assume that $r_{\rm s}(k_0)$ and the tensor spectral index $n_{\rm t}$ satisfy the consistency relation for a single field slow-roll inflation $r_{\rm s} = -8n_{\rm t}$ [53]. The power-law parameterisation thus contains only three free parameters: $A_{\rm s}$, $n_{\rm s}$, and $r_{\rm s}$. For these parameters, we assume similar priors as we did in the previous chapter: $A_{\rm s} = [1, 50] \times 10^{-10}$ for the amplitude, a conservative prior for the spectral index $n_{\rm s} = [0.7, 1.2]$ and a tensor-to-scalar ratio prior of $r_{\rm s} = [0, 1]$.

Figure 5.1 shows 1D and 2D marginalised posterior distributions of the scalar spectrum index $n_{\rm s}$ and the tensor-to-scalar ratio $r_{\rm s}$, using both current cosmological observations (black line) and future experiments (red for Planck and green for CMBPol). The bottom panel shows the limits imposed by current and future experiments. For present observations: $n_{\rm s} = 0.964 \pm 0.011$ and $r_{\rm s} < 0.171$ (mean values of 68% C.L. are quoted for two-tailed distributions, whilst one-tailed distribution only the upper 95% C.L.). These results are in agreement with previous studies, i.e. [64, 115, 120]. With regards to future constraints, we have used mean values obtained from current observations as the fiducial model (with fixed $r_{\rm s} = 0.1$). We notice that 1σ error bars of the spectral index $n_{\rm s}$, shown in the bottom panel of the same figure, reduce by about four times using a Planck-like experiment and five times for a CMBPol experiment. Whereas Planck will be able to distinguish tensor components with an accuracy of $\sigma_r = 0.013$, this is highly improved by CMBPol data $\sigma_r = 0.0009$. If we consider only one channel for comparison, e.g. 100 GHz, the constraints on the tensor-to-scalar ratio are given by $\sigma_r = 0.02$, in agreement with previous results [32]. The top-right panel illustrates

(n_s)

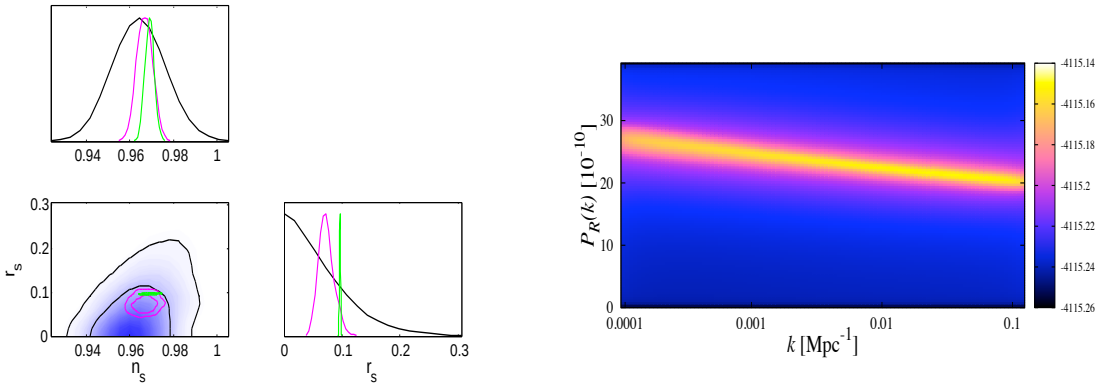

	Current	Planck (σ_i)	CMBPol (σ_i)
$A_{\rm s}[10^{-10}]$	22.74 ± 0.63	0.19	0.131
$n_{\rm s}$	0.964 ± 0.011	0.0034	0.002
$r_{\rm s}$	< 0.171	0.013	0.0009

Figure 5.1: Left panel: 1D and 2D probability posterior distributions for the power spectra parameters, assuming a simple tilt parameterisation ($n_{\rm s}$); using both current observations (black line) and future experiments (red for Planck and green for CMBPol). 2D constraints are plotted with 1σ and 2σ confidence contours. Right panel: Reconstruction of the scalar spectrum using present data; lighter regions represent an improved fit.

the resulting shape of $\mathcal{P}_{\mathcal{R}}(k)$ corresponding to the posterior distributions using present data.

5.2.2 Running scalar spectral-index

A further extension is possible by allowing the scalar spectral index to vary as a function of scale, such that $n_{\rm s}(k)$. This can be achieved by including a second

order term in the expansion of the power spectrum (4.6):

$$\mathcal{P}_{\mathcal{R}}(k) = A_{\rm s}\left(\frac{k}{k_0}\right)^{n_{\rm s}-1+\frac{1}{2}\ln\left(\frac{k}{k_0}\right)n_{\rm run}} . \tag{5.4}$$

We have kept the same tensor spectrum as in the simple power-law parameterisation, with a tensor-to-scalar ratio $r_{\rm run}$ at a scale of $k_0 = 0.015$ Mpc^{-1} to avoid correlations amongst parameters [52]. We maintained the same priors for the inflationary parameters $A_{\rm s}$, $n_{\rm s}$, and $r_{\rm run}$ and select a prior of the running parameter of $n_{\rm run} = [-0.1, 0.1]$ as used by [175].

Figure 5.2 shows the 1D and 2D marginalised posterior distributions for the inflationary parameters, using current experiments (black line): $n_{\rm s} = 0.985 \pm 0.017$, $n_{\rm run} = -0.043 \pm 0.018$ and $r_{\rm run} < 0.324$; and Planck (red line) and CMBPol (green line) realisations. The top label of the figure indicates the Bayes factor using present observations, which in this case and throughout the paper is compared with respect to the power-law parameterisation. We first note that in the presence of a tensor component, the bending of the scalar spectrum is enhanced through a larger running parameter [1]. We also observe that using current experiments a negative $n_{\rm run}$ parameter in preferred by more than 2.5σ C.L. Hence the necessity to include a turn-over in the power spectrum. This result is confirmed by noticing the Bayes factor is significantly favoured compared to the simple power-law model, $\mathcal{B}_{n_{\rm run},n_{\rm s}} = +2.0 \pm 0.3$. Considerations of the running of running of the spectral index are also being explored [188]. Notice that correlations created by the inclusion of the running parameter broaden the constraints on the tensor-to-scalar ratio by about 1.5 times. Future constraints are also broadened compared to the power-law parameterisation. The summary of the constraints on the inflationary parameters is shown in the bottom panel of Figure 5.2, and the reconstruction of $\mathcal{P}_{\mathcal{R}}(k)$, using present data, in the right panel.

[1] The constraints of the running parameter without tensor components are $n_{\rm run} = -0.028 \pm 0.014$.

$(n_{\rm run})\ \mathcal{B}_{n_{\rm run},n_{\rm s}} = +2.0 \pm 0.3$

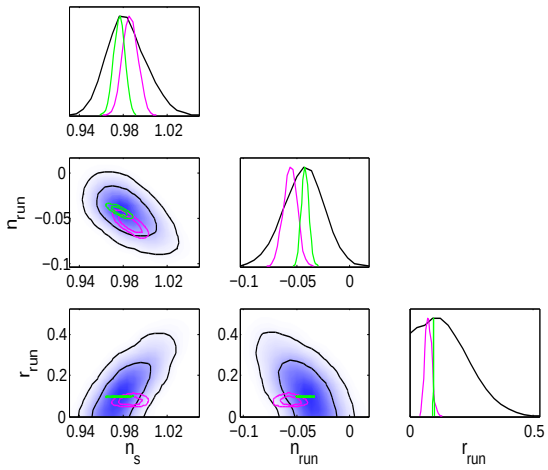

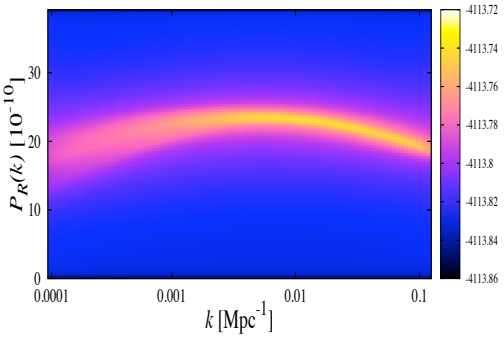

	Current	Planck (σ_i)	CMBPol (σ_i)
$A_{\rm s}[10^{-10}]$	23.66 ± 0.83	0.19	0.0142
$n_{\rm s}$	0.985 ± 0.017	0.0064	0.0048
$n_{\rm run}$	-0.043 ± 0.018	0.0062	0.0034
$r_{\rm run}$	< 0.324	0.013	0.00097

Figure 5.2: Left panel: 1D and 2D probability posterior distributions for the inflationary parameters, assuming a power-law with a running parameter ($n_{\rm run}$); using both current data (black line) and future experiments (red for Planck and green for CMBPol). 2D constraints are plotted with 1σ and 2σ confidence contours. Right panel: Reconstruction of the scalar spectrum using present data; lighter regions represent an improved fit. The top label denotes the Bayes factor of the $n_{\rm run}$-model compared to the power-law $n_{\rm s}$-model, using current observations.

5.2.3 Model-independent reconstruction

We have seen that deviations from the simple power-law, by the introduction of the running parameter, are relevant in explaining present data. In order to corroborate this result and look for deviations from the power-law parameterisation, we consider the model-independent reconstruction shown in Section 4.1.2. That is, we place two fixed k-nodes at sufficiently separated positions $[k_{\rm min}, k_{\rm max}]$, with

varying amplitudes $[A_{\mathrm{s},k_{\mathrm{min}}}, A_{\mathrm{s},k_{\mathrm{max}}}]$, and place inside additional 'nodes' with the freedom to move around in both position k_i and amplitude A_{s,k_i}. To maintain continuity between k-nodes, a linear interpolation is performed such that the form of the power spectrum is described by

$$\mathcal{P}_{\mathcal{R}}(k) = \begin{cases} A_{\mathrm{s},k_{\mathrm{min}}} & k \leq k_{\mathrm{min}} \\ A_{\mathrm{s},k_i} & k_{\mathrm{min}} < k_i < k_{i+1} < k_{\mathrm{max}} \\ A_{\mathrm{s},k_{\mathrm{max}}} & k \geq k_{\mathrm{max}} \end{cases} \tag{5.5}$$

$$\text{and with linear interpolation for} \quad k_{\mathrm{min}} \leq \quad k_i \quad \leq k_{\mathrm{max}}.$$

We have restricted the model-independent reconstruction to two internal-nodes which we consider are sufficient to provide an accurate description of the shape of the power spectrum. The tensor spectrum is parameterised by a power-law form, similarly to the one in Section 5.2.2. Here, the tensor-to-scalar ratio, given by $r_{2k_i} = A_{\mathrm{t}}/P_{\mathcal{R}}(k_0)$, is computed at the scale $k_0 = 0.015$ Mpc^{-1}, and also satisfies the consistency relation $n_{\mathrm{t}} = -8r_{2k_i}$; with prior $r_{2k_i} = [0, 1]$.

The left panel of Figure 5.3 presents the 1D and 2D marginalised posterior distributions for the parameters used in the model-independent reconstruction. At the largest scales, we observe the lack of tight constraints on the amplitude A_1, mainly due to the cosmic variance and correlations with other parameters. At smaller scales, the constraints on the amplitues (i.e. A_2, A_3 and A_4) get tighter. We notice the presence of a bi-modal distribution in the medium/small scales, represented by k_2, where the highest peak ($k \sim 0.01$Mpc^{-1}) matches the position of the turn-over in the primordial spectrum, as seen in the top-right panel of Figure 5.3. The other peak is located where the constraints seem to improve by updated data sets: at the overlapping of WMAP/ACT observations ($0.1 < k < 0.14$) with LRG7 measurements. The reconstructed spectrum clearly presents a turn-over, however with the bending at small scales less pronounced that in the running model. Notice that the Bayes factor, shown in the top label of the same figure, is significantly preferred over the simple tilt model, even though the two-internal-node reconstruction contains four additional parameters; it is also marginally preferred over the running model. Future experiments will be able to pin-down accurately the shape of the primordial spectrum at medium and small

$$(2\mathrm{k_i})\ \mathcal{B}_{2\mathrm{k_i},n_\mathrm{s}} = +2.3 \pm 0.3$$

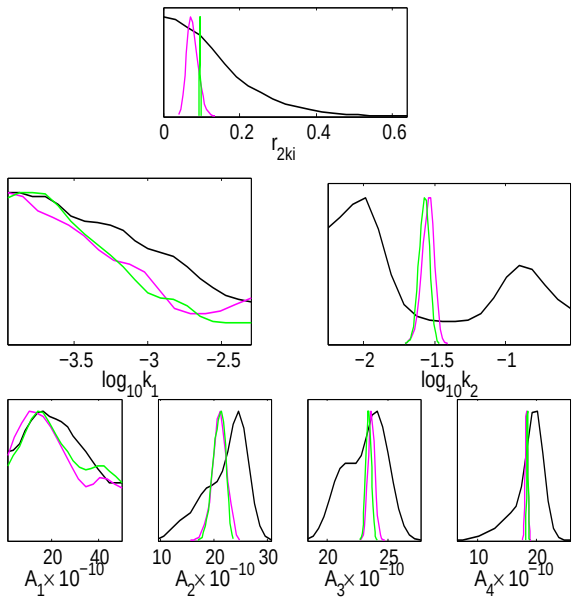

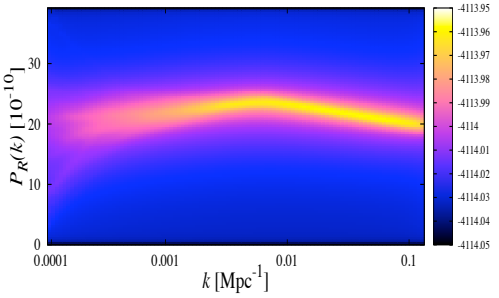

	Current	Planck (σ_i)	CMBPol (σ_i)
$A_1[10^{-10}]$	–	–	–
$A_2[10^{-10}]$	$22.02^{+3.74}_{-4.43}$	1.29	1.09
$A_3[10^{-10}]$	$23.68^{+1.72}_{-1.98}$	0.27	0.21
$A_4[10^{-10}]$	$18.67^{+2.06}_{-2.37}$	0.20	0.10
$\log_{10} k_1$	–	–	-
$\log_{10} k_2$	–	0.04	0.034
r_{2ki}	< 0.34	0.014	0.00096

Figure 5.3: Left panel: 1D and 2D probability posterior distributions for the power spectrum parameters, assuming a two internal-node reconstruction ($2k_i$); using both current cosmological observations (black line) and future experiments (red for Planck and green for CMBPol). 2D constraints are plotted with 1σ and 2σ confidence contours. Right panel: Reconstruction of the scalar spectrum using present data; lighter regions represents an improved fit. Top label denotes the Bayes factor of the $2k_i$-model compared to the power-law n_s-model, using current observations.

scales (k_2), however at the largest scales (k_1) the cosmic variance still dominates, as seen in the 1D posterior distribution of A_1. Current and future constraints of the inflationary parameters are summarised in the bottom panel of Figure 5.3.

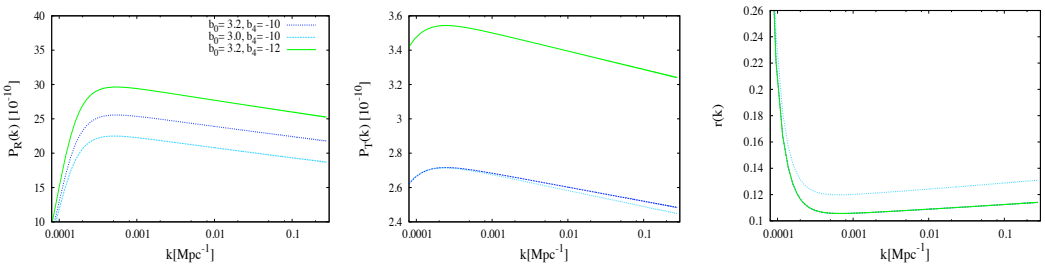

Figure 5.4: Derived primordial power spectra, $P_{\mathcal{R}}(k)$ and $P_{\mathcal{T}}(k)$, from the Lasenby & Doran model, using a different set of parameters of b_0 and b_4 (left and middle panels); units of b_4 are given in $[10^{-10}]$. The right panel shows the tensor-to-scalar ratio $r_{\rm LD} = P_{\mathcal{T}}/P_{\mathcal{R}}$.

5.2.4 Lasenby & Doran model

The Lasenby & Doran model is based on the restriction of the total conformal time available in a closed universe [126]. At the largest scales, the predicted scalar and tensor spectra naturally incorporate a drop-off without the need to parameterise them, whilst, at small scales they mimic a slight running behaviour. An important point to bear in mind is that in the LD model the functional forms of H and $\dot{\phi}$ during inflation are expressed using just two parameters b_0 and b_4. These parameters describe the initial conditions, along with the standard cosmological parameters, and therefore the primordial spectra generated by the LD model are given in terms of

$$P_{\mathcal{R}}(k) = P_{\mathcal{R}}(k; b_0, b_4, \Omega_{i,0}, H_0), \qquad P_{\mathcal{T}}(k) = P_{\mathcal{T}}(k; b_0, b_4, \Omega_{i,0}, H_0). \tag{5.6}$$

Notice that the tensor-to-scalar ratio $r_{\rm LD}$ is a derived quantity in terms of the cosmological parameters, H_0, Ω_i, and the initial-conditions parameters b_0 and b_4:

$$r_{LD}(k) = r_{LD}(k; b_0, b_4, \Omega_{i,0}, H_0). \tag{5.7}$$

That is, if we use values of b_0 and b_4 along with the cosmological parameters there is no need to introduce additional variables to describe the tensor-to-scalar ratio r_{LD}. Figure 5.4 shows the primordial spectra, both scalar and tensor, for a given combination of b_0 and b_4 parameters. In the right panel of this figure,

we illustrate the tensor-to-scalar ratio and its degeneracy with a selection of the parameters, for instance, the combination of $\{b_0 = 3.2, b_4 = -10 \times 10^{-10}\}$ or $\{b_0 = 3.0, b_4 = -12 \times 10^{-10}\}$ provides the same tensor-to-scalar ratio, even though their scalar and tensor spectra differ considerably. To compute the LD spectra we refer to [234, 236]. We have also chosen the priors based on the same paper: $\Omega_{k,0} = [-0.05, 10^{-4}]$, $b_0 = [1, 4]$, $b_4 = [-30, -1] \times 10^{-9}$. Figure 5.5 shows 1D and 2D marginalised posterior distributions of the parameters involved in the description of the LD model. A novel result from the LD model is that its constraints on the tensor-to-scalar ratio are different from zero: $r_{\rm LD} = 0.11 \pm 0.024$, contrary to the standard power-law parameterisation. This happens mainly due to the ϕ^2-type potential assumed in the model. The Bayes factor of this model compared to the simple-tilt model is shown in the top label of the same figure. The low number of parameters and the reduced power at both large and small scales make the LD model strongly favoured compared to the simple tilt and significantly so compared to the running and the two-internal-node reconstruction. Future experiments will provide an insight on discriminating amongst models, as we will see in the next section.

5.3 Model Selection

Throughout the analysis, we have included the Bayes factor for each model and found that the Lasenby & Doran model is the most preferred by current observations. Future experiments will be able to distinguish between models more effectively. Let us assume for a moment that the LD spectra represent the true model. We then use the LD spectra, with best-fit values obtained by using present data (shown in the bottom panel of Figure 5.5), as the fiducial model to simulate future CMB observations. We analyse this mock data to reconstruct the input spectrum using the set of models aforementioned. Table 5.1 shows the Bayes factor for the different models compared to the LD model. There is indeed a distinction between models, with the data clearly indicating a preference for the LD model, used to generate the input-simulated data. Planck data will be able to provide decisive conclusions on distinguishing the LD model from the simple-tilt $n_{\rm s}$-model, $\mathcal{B}_{n_s,LD} = -6.3 \pm 0.3$, and a running $n_{\rm run}$-model, $\mathcal{B}_{n_{run},LD} = -6.5 \pm 0.3$,

(LD) $\mathcal{B}_{\mathrm{LD},n_\mathrm{s}} = +3.4 \pm 0.3$

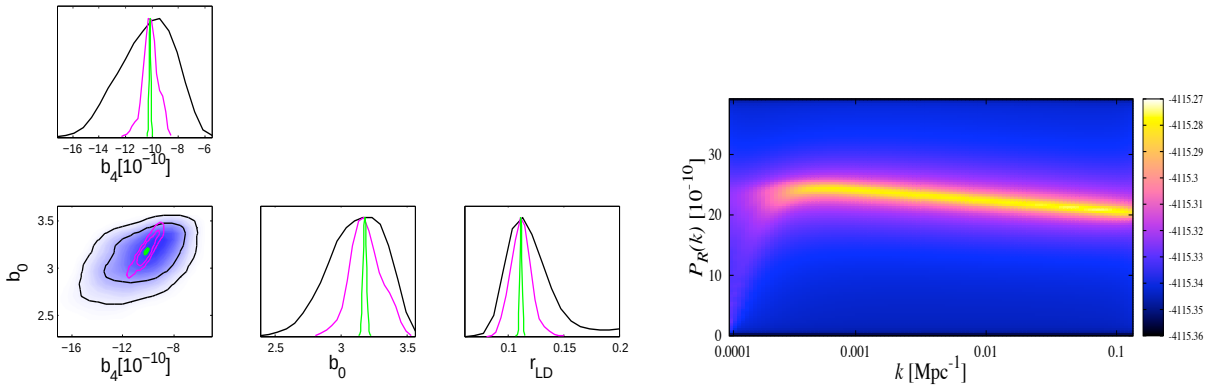

	Current	Planck (σ_i)	CMBPol (σ_i)
b_0	3.21 ± 0.41	0.24	0.013
$b_4[10^{-10}]$	-10.39 ± 2.95	1.09	0.065
* r_LD	0.11 ± 0.024	0.017	0.002

Figure 5.5: 1D and 2D probability posterior distributions for the power spectrum parameters, assuming a Lasenby & Doran model (LD); using both current cosmological observations (black line) and future experiments (red for Planck and green for CMBPol). 2D constraints are plotted with 1σ and 2σ confidence contours. The top label denotes the associated Bayes factor with respect to the power-law n_s model using present data. *In this model, r_LD is a derived parameter.

and strong preference when compared to the two-internal-node reconstruction $2k_i$-model, $\mathcal{B}_{2k_i,LD} = -3.1 \pm 0.3$. There also will be a strong preference for the model independent reconstruction over both the n_s and n_run models: $\mathcal{B}_{2k_i,n\mathrm{s}} = +3.2 \pm 0.3$ and $\mathcal{B}_{2k_i,n_\mathrm{run}} = +3.4 \pm 0.3$, respectively. With regards to the CMBPol experiment, this will definitely differentiate the LD spectrum from the rest of the spectra. In contrast to the Planck experiment, the model-independent reconstruction for CMBPol is now strongly favoured compared to the n_run model. CMBPol also provides a strong preference to differentiate the simple-tilt model n_s over the running model n_run: $\mathcal{B}_{n_\mathrm{s},n\mathrm{run}} = +2.5 \pm 0.3$. Therefore, future experiments will certainly be able to differentiate between these models and pin down the right form of the

Table 5.1: Model Selection. The input spectrum, given by the LD model, is reconstructed using different models. We show the Bayes factor for each model i, $\mathcal{B}_{i,LD}$, compared to the LD model.

	Planck	CMBPol
LD	0.0 ± 0.3	0.0 ± 0.3
$n_{\rm s}$	-6.3 ± 0.3	-13.0 ± 0.3
$n_{\rm run}$	-6.5 ± 0.3	-15.5 ± 0.3
$2k_i$	-3.1 ± 0.3	-10.2 ± 0.3

primordial spectrum.

5.4 Discussion and Conclusions

In this chapter we have performed a MCMC exploration of the full cosmological parameter-space and showed current and future constraints on the inflationary parameters, with particular attention to the tensor-to-scalar ratio. We have considered models that deviate from the standard power-law in the scalar power-spectrum: a power-law parameterisation with running behaviour and the spectra predicted from the Lasenby & Doran model. By implementing a model-independent reconstruction for $\mathcal{P}_{\mathcal{R}}(k)$, we have found that a turn-over in the scalar spectrum is preferred to explain cosmological observations. The inclusion of a tensor component enhances this turn-over, for instance, $n_{\rm run} = -0.043 \pm 0.018$ compared to $n_{\rm run} = -0.028 \pm 0.014$ without tensors. A similar form of the scalar spectrum has been previously obtained assuming different model-independent reconstructions, and some of them with different data sets [81, 82, 234]. We have assumed that a power-law parameterisation of $\mathcal{P}_{\mathcal{T}}(k)$ is sufficient to describe current data. Even though we have not given the results for the standard cosmological parameters $\Omega_{\rm b}h^2$, $\Omega_{\rm c}h^2$, θ, τ, the best-fit values remained essentially unaffected throughout the models, see Section 3.4. For all the models, we have computed the Bayes factor and compared each to the simple power-law parameterisation. We

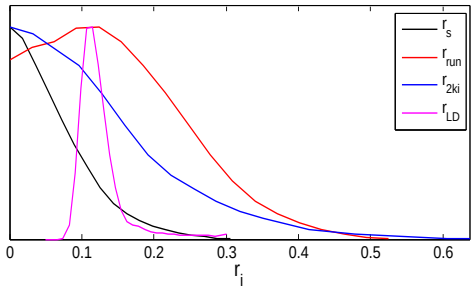

Current	N_{par}	$\mathcal{B}_{i,j}$
n_s	$+3$	$+0.0 \pm 0.3$
n_{run}	$+4$	$+2.0 \pm 0.3$
$2k_i$	$+7$	$+2.3 \pm 0.3$
LD	$+3$	$+3.4 \pm 0.3$

Figure 5.6: 1-D marginalised posterior distribution of the tensor-to-scalar ratio for the different models (left panel), along with their Bayesian evidence and number of parameters of each model (right panel). The Bayes factor is compared to the simple-tilt model (n_s.)

found, using current observations, that the preferred model is given by the LD model. The summary of the analysis, illustrated in Figure 5.6, displays how the constraints on the tensor-to-scalar ratio are broadened for non-power law models. We notice that the best-fit value of r_{run} is slighly offset from zero and coincides with the peak of r_{LD}. Throughout the models, the tensor-to-scalar ratio has been computed at a particular scale $k_0 = 0.015$ Mpc^{-1}. However, to illustrate the robustness of the model selection, over a different choice of scale k_0, we compute the Bayesian evidence for all models at $k_0 = 0.002$ Mpc^{-1}. The results are essentially unaffected and still show a preference for the LD model. The Bayesian evidece, for each model, compared to the power-law parameterisation (n_s) are as follow:

$\mathcal{B}_{run,n_s}$	$\mathcal{B}_{2ki,n_s}$	$\mathcal{B}_{LD,n_s}$
$+1.8 \pm 0.3$	$+2.29 \pm 0.3$	$+3.0 \pm 0.3$

With regards to future surveys, the Planck satellite will be able to differentiate the running and tilt model from the LD model, but not decisively from the two-internal-node reconstruction. The improvement using CMBPol selects the right form of the primordial spectrum, as shown in Table 5.1.

Chapter 6

Dark Energy equation-of-state

One of the most pressing goals of modern cosmology has been to explain the late-time accelerated expansion of the universe [180, 193]. Considerable observational and theoretical effort has been focused on understanding this remarkable phenomenon. It is often postulated that an exotic new source of stress-energy with negative pressure may be responsible for the cosmic acceleration: such a component is called *dark energy* (DE). The dynamical properties of dark energy are normally summarised as a perfect fluid with (in general) a time-dependent equation-of-state parameter $w(z)$. The simplest proposal, namely a cosmological constant Λ, is described by the redshift independent $w_\Lambda = -1$. Alternative cosmological models that deviate from standard ΛCDM, but still lead to an accelerating universe, include: K-essence, quintessence and non-minimally coupled scalar fields [14, 189, 231, 239], braneworld models [152], modified gravity [13, 35, 99, 171, 220], interacting dark energy [10, 45, 147], anisotropic universes [3, 155, 165, 232], amongst many others [34, 38, 57, 83, 159, 183, 199, 255]. In the absence of a fundamental and well-defined theory of dark energy, $w(z)$ has been parameterised in a number of different ways, including: the CPL, JBP and FNT models [41, 56, 111, 145], the Hannestad and Wetterich parameterisations [88, 246], polynomial, logarithmic and oscillatory expansions [150, 208, 250], Kink models [19], and quite a few others [212]. The *a priori* assumption of a specific model or the use of particular parameterisations can, however, lead to misleading results regarding the properties of the dark energy. Hence, some studies instead perform a direct,

model-independent ('free-form') reconstruction of $w(z)$ from observational data, using, for instance, a principal component analysis [79, 104, 108, 209, 252, 253], maximum entropy techniques [256], binning $w(z)$ in redshift space [58, 129], non-parametric approaches [96, 97, 205, 210, 211, 213] and several other techniques [5, 6, 7, 43, 55, 103, 105, 146, 195, 201, 202, 203, 243, 244, 245].

In this chapter we explore the possible dynamical behaviour of the dark energy based on the most minimal *a priori* assumptions. Given current cosmological observations and using the Bayesian evidence as an implementation of Occam's razor, we select the preferred shape of $w(z)$. Our method considers possible deviations from the cosmological constant by modelling $w(z)$ as a linear interpolation between a set of 'nodes' with varying w-values and redshifts (in the most general case). The reconstruction process is essentially identical to the approach used in Chapter 4 to recover the preferred shape of the primordial spectrum of curvature perturbations $P(k)$ [234]. For comparison, we also consider some existing models that propose a parameterised functional form for $w(z)$, namely the CPL, JBP and FNT models. For each model we compute its evidence and, according to the Jeffreys guidelines, we select the best model preferred by the data.

The base and secondary parameters used throughout this chapter, along with their flat priors, are displayed in Section 3.4. To describe the overall shape of the dark energy equation-of-state $w(z)$ in our nodal reconstruction, we introduce a set of amplitudes w_{z_i} at determined positions z_i. The CPL, JBP and FNT models depend upon additional parameters. The assumed flat priors on these models are discussed below. To carry out the exploration of the parameter space, we input $w(z)$ into a modied version of the CAMB code [134], which implements a parameterised post-Friedmann (PPF) presciption for the dark energy perturbations [71]. To constrain the parameter-space, we consider the set of experiments I mentioned in Section 3.4.

The chapter is organised as follows: in the next section we define the model-independent reconstruction and present existing parameterisations used by other authors. The resulting parameter constraints and evidences for each model are

then discussed. Finally, in Section 6.3, based on Jeffrey's guideline, we decide which model provides the best description for current observational data and present some conclusions.

6.1 Dark Energy Reconstruction

6.1.1 Nodal reconstruction I

We first perform the reconstruction of $w(z)$ by parameterising it as piecewise linear between a set of nodes with variable amplitudes (w_{z_i}-values), but with fixed, equally-spaced redshifts. Throughout, we bear in mind that current information, mainly coming from SN Ia, is encompassed between the present epoch $z_{\rm min} = 0$ and $z_{\rm max} = 2$. At higher redshifts there is no substantial information to place strong constraints on dark energy, thus beyond $z > 2$ we assume $w(z)$ to be constant, with a value equal to that at $z_{\rm max}$. At each node, we allow variations in amplitudes w_{z_i} with a conservative prior $w_{z_i} = [-2, 0]$. Our description of $w(z)$ can be summarised as:

$$w(z) = \begin{cases} w_{z_{\rm min}} & z = 0 \\ w_{z_i} & z \in \{z_i\} \\ w_{z_{\rm max}} & z \geq 2 \end{cases} \tag{6.1}$$

$$\text{and with linear interpolation for} \quad 0 \leq z_i < \quad z \quad < z_{i+1} \leq 2.$$

While the use of linear interpolation between nodes may seem crude, we have shown in the Appendix A that the use of smoothed interpolation functions, such as cubic splines, can lead to significant spurious features in the reconstruction, thus leading to poor fits to observational data and also unrepresentative errors.

We perform all of our model comparisons with respect to the simplest explanation of dark energy, namely the cosmological constant $w_\Lambda = -1$. First, we consider deviations of the ΛCDM model by letting the equation-of-state parameter vary only in amplitude: $w(z) = w_0 =$ constant (see Figure 6.1(a)). The incorporation of two or more parameters, as in models (b) and (c) respectively, allows us to test the dark energy time-evolution. Figure 6.1 also includes the 1D marginalised

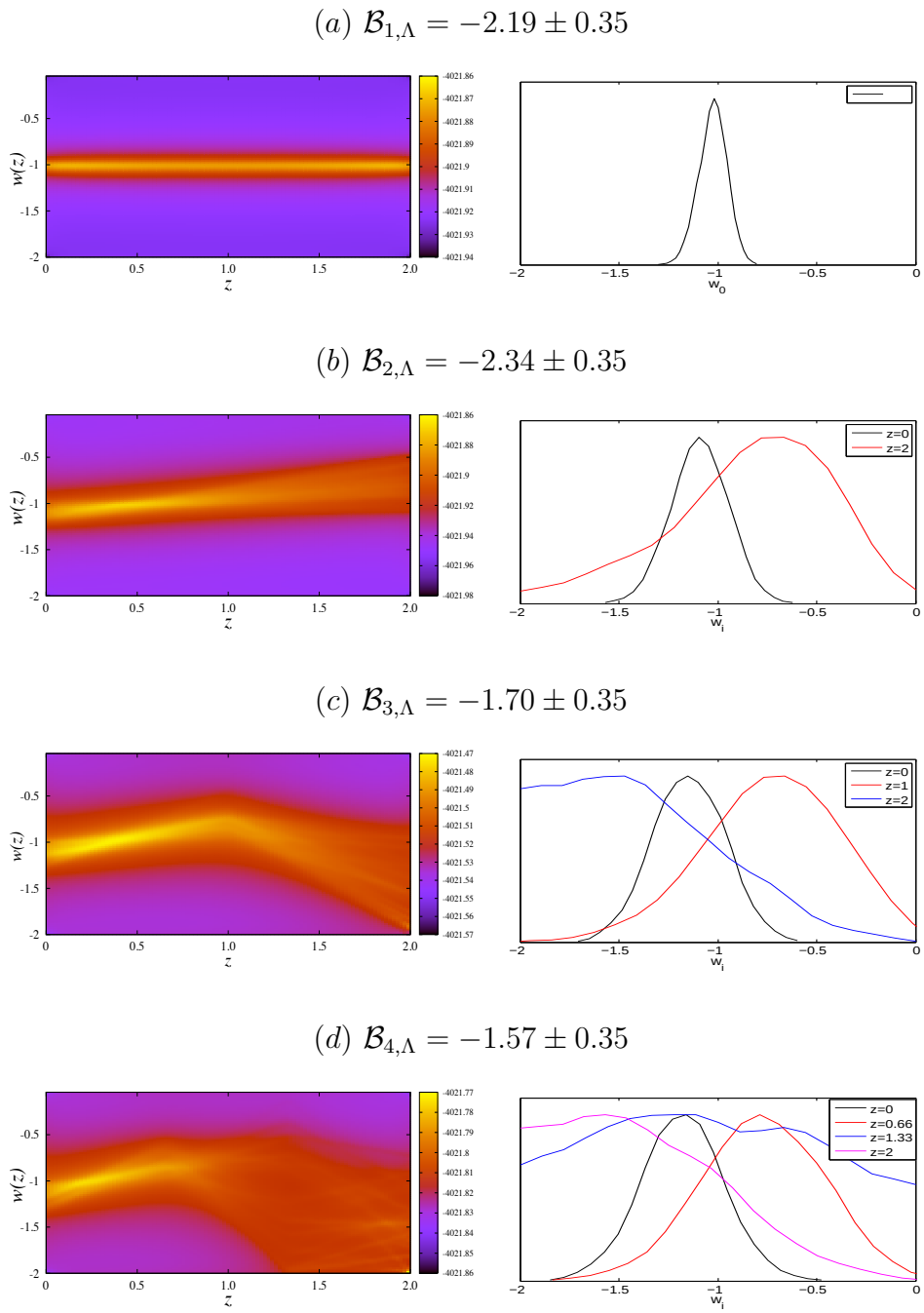

Figure 6.1: Left: Reconstruction of the dark energy equation-of-state parameter modelled as piecewise linear between nodes that may vary in amplitude w_i but are fixed in redshift z, showing the mean amplitude values and their corresponding 1σ error bands. The colour-code shows ln(likelihood), where lighter regions represents an improved fit. Right: 1D marginalised posterior distribution of the amplitudes w_i at each z-node (shown in the right-top corner), in each reconstruction. The top label in each panel denotes the associated Bayes factor respect to the ΛCDM model.

posterior distribution for the corresponding amplitude at each node and for each reconstruction. In the top label of each model we have included the Bayes factor compared to the ΛCDM model. In model (b), we notice the overall shape of $w(z)$ includes a slight positive tilt and a narrow waist located at $z \sim 0.3$. It is also observed that at the present epoch $w(z=0) \lesssim -1$ is slightly favoured, while at higher redshifts $w(z) \gtrsim -1$ is preferred, hence, the reconstructed $w(z)$ exhibit a crossing of the line $w = -1$. The crossing of the phantom divide line $w = -1$ (PDL), plays a key role in identifying the correct dark energy model [249]. If future surveys confirm its existence, single scalar field theories (with minimal assumptions) might be in serious problems as they cannot reproduce this essential feature, and therefore alternative models should be considered, e.g. scalar-tensor theories [23, 59], braneworld models [44, 200], $f(R)$ gravity [13, 99, 166, 220]. To continue with our reconstruction process, we then place a third point (c) midway between the two existing nodes in (b). This model mimics a running behaviour by allowing slight variations in the interpolated slopes between the three nodes. The freedom in its shape, together with the very weak constraints at high redshifts, lead to a $w(z)$ with slight negative slope at early times, in contrast to model (b). Furthermore the presence of a small bump in the resulting $w(z)$ at $z \sim 1$ (see Figure 6.1 (c)) might point to some weak departure from the cosmological constant $w_\Lambda = -1$.

We can continue this process of adding more nodes but always using the Bayesian evidence to penalise any unnecessary inclusion of model parameters. The inclusion of a fourth stage with z-space split into three equally spaced regions is given by model (d). At low redshifts the shape of the equation of state is well constrained with tight error bands on each node, whereas at high redshifts the error bands again indicate the lack of sufficient data to provide strong constraints. Notice also the increased error bands due to the addition of further nodes and (anti-)correlations created between them: for instance, the posterior distribution of the amplitude w_{z_i} at $z = 0$ is broadened as the number of nodes is increased. At this stage, the evidence has flattened off, and so it seems reasonable to stop adding parameters in the reconstruction process at this point. The constraints on the w_{z_i} amplitudes used on each reconstruction are given by (for two-tailed

distributions 68% C.L. are shown, whilst for one-tailed distributions the upper 95% C.L.):

(a) $w_0 = -1.02 \pm 0.07$,

(b) $w_{z=0} = -1.09 \pm 0.14$, $w_{z>2} = -0.83 \pm 0.39$,

(c) $w_{z=0} = -1.14 \pm 0.17$, $w_{z=1} = -0.73 \pm 0.33$, $w_{z>2} < -0.65$,

(d) $w_{z=0} = -1.18 \pm 0.20$, $w_{z=0.66} = -0.78 \pm 0.30$, $w_{z=1.33} = -1.03 \pm 0.53$, $w_{z>2} < -0.62$.

The models used in the reconstruction of $w(z)$ are assessed according to the Jeffreys guideline. The Bayes factor between the ΛCDM model and the one-node model $\mathcal{B}_{1,\Lambda} = -2.19 \pm 0.35$ points out that $w(z) = w_0$ (where w_0 is a free constant), is strongly disfavoured when compared to the cosmological constant, similarly, when two independent nodes are used $\mathcal{B}_{2,\Lambda} = -2.34 \pm 0.35$. Thus, parameterisations that contain one or two parameters are not able to provide an adequate description of the behaviour of $w(z)$, and hence are strongly disfavoured by current observations. The addition of nodes in the third and fourth stage provides more flexibility in the shape of the reconstructed $w(z)$. Thus, the evidence for these models shows an improvement, compared to the first and second models, indicating the possible presence of some features in the time evolution of the equation-of-state parameter. Nonetheless, when they are compared to ΛCDM, they are still marginally disfavoured: $\mathcal{B}_{3,\Lambda} = -1.70 \pm 0.35$ and $\mathcal{B}_{4,\Lambda} = -1.57 \pm 0.35$.

6.1.2 Nodal reconstruction II

We previously reconstructed $w(z)$ by placing nodes at particular fixed positions in z-space. However, to localise features, we now extend the analysis by also allowing the z-position of each node to move freely (see e.g. Section 4.1.2). In particular, we again fix two z-nodes at sufficiently separated positions $z_{\rm min} = 0$ and $z_{\rm max} = 2$, but now place inside additional 'nodes' with the freedom to move around in both position z_i and amplitude w_{z_i}. This method has the advantage that we do not have to specify the number and location of nodes describing $w(z)$; indeed, the form of any deviation from flat $w(z)$ can be mimicked through a change in the

amplitudes and/or positions of the internal nodes. Also, the reduced number of internal nodes avoids the creation of wiggles due to high (anti-)correlation between nodes, which might lead to a misleading shape for $w(z)$. We use the same priors for the amplitudes $w_{z_i} = [-2, 0]$ as we adopted in Section 6.1.1. Hence, for this type of nodal-reconstruction the equation of state is described by

$$w(z) = \begin{cases} w_{z_{\rm min}} & z = 0 \\ w_{z_1} & 0 < z_i < z_{i+1} < 2 \\ w_{z_{\rm max}} & z \geq 2 \end{cases} \tag{6.2}$$

$$\text{and with linear interpolation for } \; 0 \leq \; z_1 < z_{i+1} \; \leq 2.$$

Figure 6.2 illustrates the reconstruction of $w(z)$ from the mean posterior estimates for each node, with 1σ error bands on the amplitudes (left). Also plotted are the 1D and 2D marginalised posterior distributions on the parameters used to describe $w(z)$ (right). The reconstructed shape for the two-internal-node model (middle panel) resembles the form obtained in Figure 6.1(c), but now with a turn-over shifted to earlier times. A similar turn-over has been found using principal component analysis by [79, 209]. The narrow waist at $z \sim 0.3$ is also noticeable, where the SNe constraints seem to be tightest. For the one and three-internal-nodes case (top and bottom panel of Figure 6.2), we observe $w(z)$ has essentially the same behaviour as in the two-internal-node model, being the preferred model. Finally, a common feature throughout all the reconstructed equation of state $w(z)$ is observed: the presence of the crossing PDL within the range $0 < z < 0.5$. The constraints on the w_{z_i} amplitudes used on each reconstruction are given by (for two-tailed distributions 68% C.L. are shown, whilst for one-tailed distributions the upper 95% C.L.):

(z_1) $\quad w_{z=0} = -1.14 \pm 0.18, \quad w_{0<z<2} > -1.39 \pm 0.35, \quad w_{z>2} < -0.70,$

(z_2) $\quad w_{z=0} = -1.18 \pm 0.26, \quad w_{0<z<1} = -0.83 \pm 0.29, \quad w_{1<z<2} = -1.02 \pm 0.52,$
$w_{z>2} < -0.63,$

(z_3) $\quad w_{z=0} = -1.07 \pm 0.36, \quad w_{0<z<0.66} = -0.98 \pm 0.29,$
$w_{0.66<z<1.33} = -0.84 \pm 0.47, w_{1.33<z<2} = -1.02 \pm 0.55,$
$w_{z>2} < -0.63.$

$(z_1)\ \mathcal{B}_{z_1,\Lambda} = -1.27 \pm 0.35$

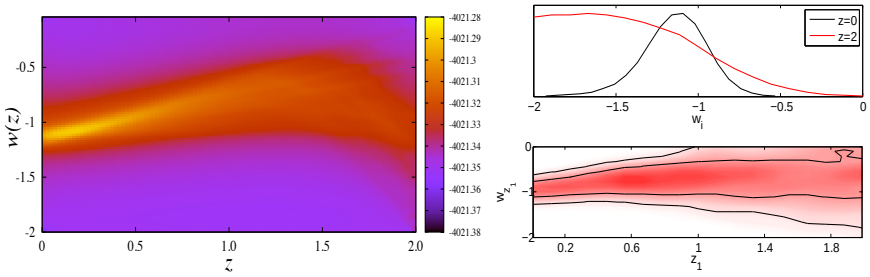

$(z_2)\ \mathcal{B}_{z_2,\Lambda} = -0.81 \pm 0.35$

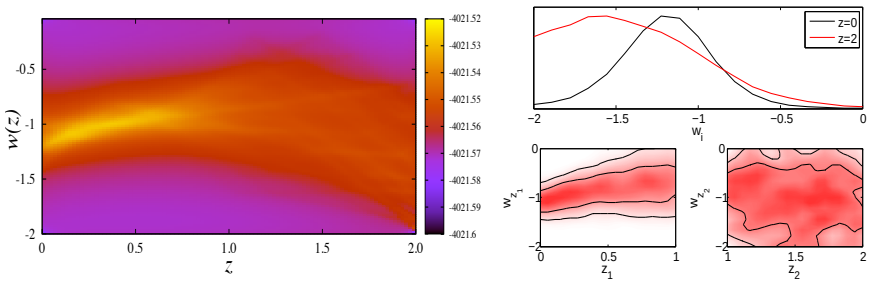

$(z_3)\ \mathcal{B}_{z_3,\Lambda} = -0.95 \pm 0.35$

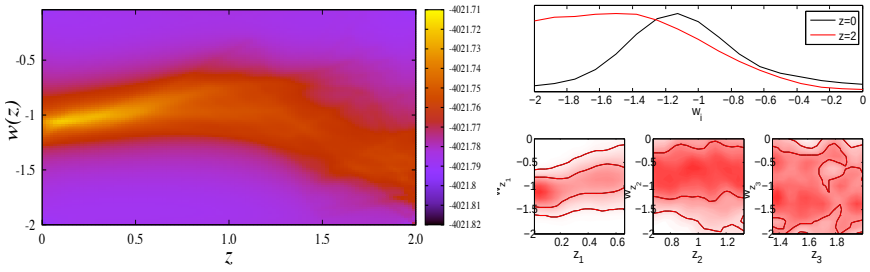

Figure 6.2: Left: Reconstruction of the dark energy equation-of-state parameter $w(z)$ using one-internal-node (top) and two-internal z-nodes (bottom) that move freely in both amplitude w_i and redshift z_i. Right: corresponds to the 1D and 2D marginalised posterior distribution of the amplitudes and z-node positions in each reconstruction. The colour-code indicates the ln(Likelihood), where lighter regions represents an improved fit, and the top label in each panel denotes the associated Bayes factor with respect to the ΛCDM model.

The similar shape of the three models are in good agreement with their Bayes factor: $\mathcal{B}_{z_2,z_1} = +0.46 \pm 0.35$, $\mathcal{B}_{z_3,z_2} = -0.14 \pm 0.35$. According to the Jeffreys guideline, even though the two internal-node model contains more parameters, it is significantly preferred over the models with one and two fixed-nodes, i.e. $\mathcal{B}_{z_2,2} = +1.53 \pm 0.35$. However, when compared to the cosmological constant model the Bayes factor is too small to draw any decisive conclusions: $\mathcal{B}_{z_2,\Lambda} = -0.81 \pm 0.35$. Thus we conclude that the internal-node models might be considered as viable models to characterise the dark energy dynamics. As seen in Figure 6.2, the Bayesian evidence has reached a plateau and thus we cease the addition of further nodes.

6.2 Dark Energy Parameterisations

6.2.1 CPL and JBP parameterisations

In this section we examine some existing parameterised models for $w(z)$ and compare these to our nodal reconstructions. In particular, we consider the simple parameterised description introduced by Chevallier-Polarski-Linder (CPL; [41, 145]), that has the functional form:

$$w(z) = w_0 + w_a \frac{z}{1+z}, \tag{6.3}$$

where the parameters w_0 and w_a are real numbers such that at the present epoch $w|_{z=0} = w_0$ and $dw/dz|_{z=0} = -w_a$, and as we go back in time $w(z \gg 1) \sim w_0 + w_a$. Thus, we limit the CPL parameters by the flat priors $w_0 = [-2, 0]$ and $w_a = [-3, 2]$.

We also consider the parameterisation suggested by Jassal-Bagla-Padmanabhan (JBP; [111]):

$$w(z) = w_0 + w_a \frac{z}{(1+z)^2}. \tag{6.4}$$

In this model, the parameter w_0 determines the properties of $w(z)$ at both low and high redshifts: $w(z = 0) = w_0$ and $w(z \gg 1) \sim w_0$. To explore the parameter space we consider the following flat priors on the JBP parameters: $w_0 = [-2, 0]$

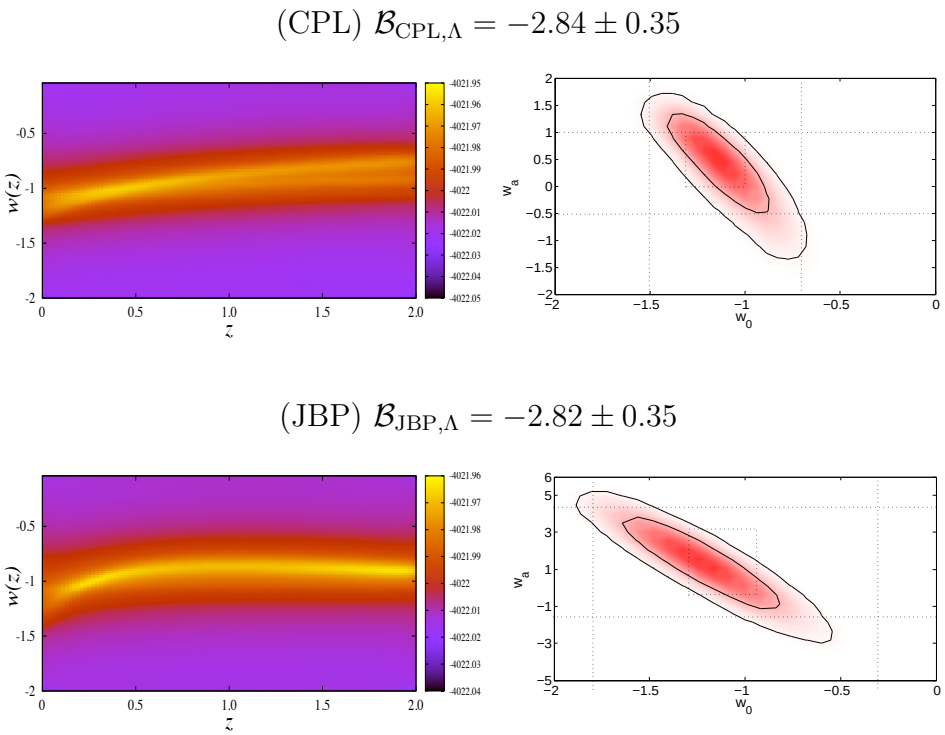

Figure 6.3: Reconstruction of the dark energy equation of state $w(z)$ assuming the Chevallier-Polarski-Linder (top) and the Jassal-Bagla-Padmanabhan parameterisation (bottom), along with their corresponding 2D constraints with 1σ and 2σ confidence contours (right panel). The colour-code indicates the ln(Likelihood), where lighter regions represents an improved fit; the top label in each panel denotes the associated Bayes factor with respect to the ΛCDM model. Dotted lines indicate the priors choice.

and $w_a = [-6, 6]$.

Figure 6.3 shows 2D joint constraints, with 1σ and 2σ confidence contours, for the parameters used to describe the CPL and JBP models, and the resulting shape of $w(z)$ corresponding to the mean posterior estimates of w_0 and w_a. In each panel we have included the Bayes factor compared to the ΛCDM model. Both of the models are in good agreement with a simple cosmological constant. The current constraints for the CPL and JBP parameters are essentially as we

expected:

$$\begin{aligned} &\text{(CPL)} \qquad w_0 = -1.11 \pm 0.17, \quad w_a = 0.34 \pm 0.60, \\ &\text{(JBP)} \qquad w_0 = -1.21 \pm 0.26, \quad w_a = 1.28 \pm 1.62. \end{aligned}$$

Given that the CPL and JBP parametererisations depend upon just two parameters, they seem to not posses enough freedom to capture local features of $w(z)$, i.e. the CPL model does not exhibit a turn-over, see Figure 6.3. This is reflected in the large difference in the Bayesian evidence for this model compared to that of the cosmological constant: $\mathcal{B}_{\mathrm{CPL},\Lambda} = -2.84 \pm 0.35$ and $\mathcal{B}_{\mathrm{JBP},\Lambda} = -2.82 \pm 0.35$. In fact, the CPL equation of state looks similar to that obtained in Figure 6.1 (b), confirming our results. An important point to emphasise is that, for the chosen priors, $\mathcal{B}_{\mathrm{CPL},z_2} = -2.03 \pm 0.35$ and $\mathcal{B}_{\mathrm{JBP},z_2} = -2.01 \pm 0.35$, indicating that both models are strongly disfavoured in comparison to the internal-node reconstruction, shown in Figure 6.2.

To illustrate the robustness of the model to small variations of the prior range, we compute the Bayesian evidence using different sets of priors, shown in Table 6.1; the prior ranges are illustrated with dotted lines in Figure 6.3. The reader will observe that even though the priors, in the first three choices, have been shrunk to within the region of the 2σ contours, the Bayes factor still disfavours significantly both the CPL and JBP parameterisations compared to the cosmological constant and the two-internal-node reconstruction. With respect to the extremely small prior (last row of Table 6.1), we notice that the JBP model does not contain the cosmological constant $w_0 = -1$. Its Bayes factor compared to the ΛCDM model $\mathcal{B}_{\mathrm{JBP},\Lambda} = -0.54 \pm 0.35$, shows that models with $w(z=0) \lesssim -1.1$ might provide a good description for the current state of the Universe.

6.2.2 FNT parameterisation

We have observed that two-parameter functions are not, in general, sufficient to recover the evolution of the dark energy $w(z)$, obtained previously in the reconstruction process. As an alternative to the CPL and JBP functional form, we

Table 6.1: Robustness of the CPL and JBP models over small variations of the prior range. The associated Bayes factor in each model is compared with respect to the ΛCDM model.

Prior w_0, w_a	$\mathcal{B}_{\mathrm{CPL},\Lambda}$	Prior w_0, w_a	$\mathcal{B}_{\mathrm{JBP},\Lambda}$
[-1.5,-0.7], [-3,2]	-1.84 ± 0.35	[-1.8,-0.6], [-6,6]	-2.35 ± 0.35
[2,0], [-0.5,1]	-2.11 ± 0.35	[-2,0], [-1,4]	-1.82 ± 0.35
[-1.5,-0.7], [-0.5,1]	-1.39 ± 0.35	[-1.8,-0.6], [-1,4]	-1.51 ± 0.35
[-1.3,-1], [0,1]	-0.26 ± 0.35	[-1.4,-1.1], [0,3]	-0.54 ± 0.35

consider a more general parameterisation introduced by Felice-Nesseris-Tsujikawa (FNT, [56]), which allows fast transitions for the dark energy equation of state:

$$w(a) = w_a + (w_0 - w_a)\frac{a^{1/\tau}[1-(a/a_t)^{1/\tau}]}{1-a_t^{-1/\tau}}, \tag{6.5}$$

where $a = 1/(1+z)$, $a_t > 0$ and $\tau > 0$. The parameter w_0 determines the $w(a)$ properties at present time $w_0 = w(a=1)$, whereas w_a the asymptotic past $w_a = w(a \ll 1)$. In this model, the equation of state $w(a)$ has an extremum at $a_* = a_t/2^\tau$ with value

$$w(a_*) = w_p + \frac{1}{4}\frac{(w_0 - w_a)a_t^{1/\tau}}{1-a_t^{-1/\tau}}. \tag{6.6}$$

Based on the assumptions given by [56], we explore the cosmological parameter-space using the following flat priors: $w_0 = [-2, 0]$, $w_a = [-2, 0]$, $a_t = [0, 1]$ and $\tau = [0, 1]$, using a full Monte-Carlo exploration. We leave the analysis of the robustness of this model under small variations on the priors, for a future work.

In Figure 6.4 we plot 2D joint constraints, with 1σ and 2σ confidence contours, for the parameters used to describe the FNT model, and its corresponding reconstruction of $w(z)$. We observe that the FNT model is in good agreement

$$\text{(FNT)}\ \mathcal{B}_{\text{FNT},\Lambda} = -1.68 \pm 0.35$$

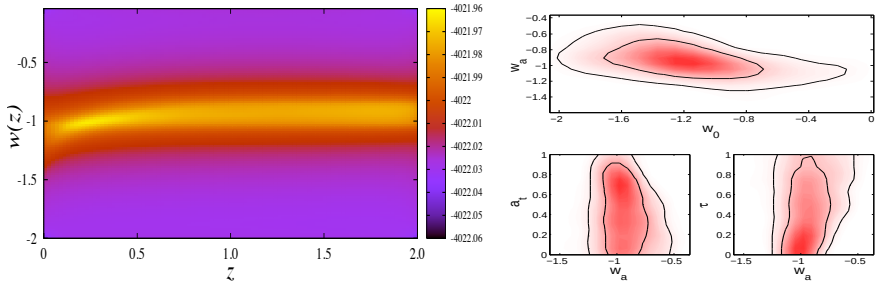

Figure 6.4: Reconstruction of the dark energy equation of state $w(z)$ assuming the Felice-Nesseris-Tsujikawa paramterisation (left panel), along with their corresponding 1D, and 2D constraints with 1σ and 2σ confidence contours (right panel). The colour-code indicates the ln(Likelihood), where lighter regions represents an improved fit; the top label in the panel denotes the associated Bayes factor with respect to the ΛCDM model.

with a simple cosmological constant $w(z) = -1$, with current constraints:

$$\text{(FNT)} \qquad w_0 = -1.19 \pm 0.32, \quad w_a = -0.94 \pm 0.15.$$

Given that the best-fit values of w_0 and w_a are very similar, the second term on the left hand side of (6.6) is almost negligible. This results in essentially unconstrained values for a_t and τ, and so w_a becomes the dominant term in the dynamics of $w(z)$. We have found that the FNT model shares a similar feature common throughout all the models: $w(z=0) \lesssim w(z \gg 1)$, in agreement with our previous results. The best-fit form of $w(z)$ presents a maximum value given by $w(a_*) = -0.95$ located at $z_* = 1/a_* - 1 = 1.59$. On the other hand, the top label of Figure 6.4 shows the Bayes factor compared to the ΛCDM model: $\mathcal{B}_{\text{FNT},\Lambda} = -1.68 \pm 0.35$. That is, the FNT model improves on the Evidence computed from the CPL and JBP models, however the inclusion of twice the number of parameters makes it significantly disfavored when compared to the cosmological constant $w(z) = -1$, and indistinguisable compared to our node-base reconstruction, i.e. $\mathcal{B}_{\text{FNT},z_2} = -0.82 \pm 0.35$.

6.3 Discussion and Conclusions

The major task for present and future dark energy surveys is to determine whether dark energy is evolving in time. Using the latest cosmological datasets, we have performed a Bayesian analysis to extract the general form of the dark energy equation-of-state parameter, employing an optimal nodal reconstruction where $w(z)$ is interpolated linearly between a set of nodes with varying w_{z_i}-values and redshifts. We find our results to be generally consistent with the cosmological constant scenario, however the dark energy does seem to exhibit a temporal evolution, although very weak. Besides the cosmological constant, the preferred $w(z)$ has $w \lesssim -1$ at the present time and a small bump located at $z \sim 1.3$, whereas at redshifts $z \gtrsim 1.5$ the accuracy of current data is not enough to place effective constraints on different parameterisations. It is also interesting to note the presence of a narrow waist in many models, situated at $z \sim 0.3$, which is where the constraints on $w(z)$ are tightest. A dominant feature throughout the reconstruction is the presence of the crossing of the PDL $w = -1$, obtained within the range $0 < z < 0.5$. Within the GR context, this phantom crossing cannot be produced by single (quintessence or phantom) scalar fields. Hence, if future surveys confirm its evidence, multiple fields or additional interactions should be taken into account to reproduce this important behaviour.

All the models considered share the set of primary cosmological parameters: $\Omega_{\rm b}h^2$, $\Omega_{\rm DM}h^2$, θ, τ, $n_{\rm s}$, $A_{\rm s}$, in addition to secondary parameters: A_{SZ}, A_p, A_c. The marginalised posterior distributions for these parameters are consistent with those obtained using only the concordance ΛCDM model (see Section 3.4). In Figure 6.5, we plot 1D posterior distributions of the cosmological parameters for some selected models. We observe that their values remain well constrained despite the freedom in $w(z)$. The only noticeable change is in the dark matter parameter, where the ΛCDM model displays the tightest constraints. In the same figure we include the corresponding Bayes factors, all of which are quoted relative to the cosmological constant model. The preferred Bayesian description of the $w(z)$ is provided by the ΛCDM model, followed by the two-internal-node model z_2, introduced in this work. It is important to note that the CPL and JBP models,

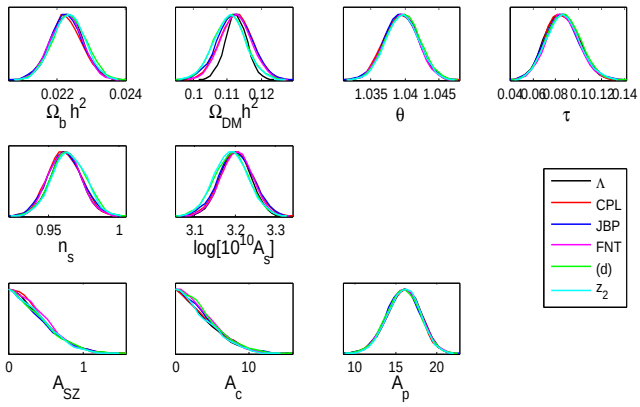

Model	N_{par}	$\mathcal{B}_{i,\Lambda}$
Λ	-	0.0 ± 0.3
CPL	$+2$	-2.8 ± 0.3
JBP	$+2$	-2.8 ± 0.3
FNT	$+4$	-1.7 ± 0.3
(d)	$+4$	-1.6 ± 0.3
z_2	$+6$	-0.8 ± 0.3

Figure 6.5: Left: 1D marginalised posterior distributions of the standard cosmological parameters, of each corresponding model listed in the right table. Right: comparison of the Bayes factor $\mathcal{B}_{i,\Lambda}$ for some selected models with an extra-number of parameters N_{par}. Each description is compared respect to the ΛCDM model.

each with two parameters, are not able to provide an adequate description for the behaviour of $w(z)$, and are hence strongly disfavoured using the priors chosen. The FNT model with four parameters, from which two of them remained unconstrained, is significantly disfavoured. We stress that for the smallest prior range, the Bayes factor for the JBP model (which does not include the case $w_0 = -1$) is indistinguishable from that of the ΛCDM model, therefore pointing to a possible departure from the cosmological constant.

Chapter 7

Missing Matter and double Dark Energy

Even though the standard ΛCDM model provides a good fit to existing observations, there have been a large number of other exotic forms of matter proposed to provide alternative explanations for the current accelerating universal expansion [50, 66], including, for example, topological defects [240].

In this chapter, we remain focussed on the ΛCDM model, but with the inclusion of a second dark energy component, which is introduced (in the first instance) to allow the Friedmann equation written in terms of conformal time η to be form invariant under the reciprocity transformation $a(\eta) \rightarrow 1/a(\eta)$ of the universal scale factor [106]. Such an invariance is of general interest, but may be particularly relevant for Penrose's recent 'Cycles of Time' cosmological model [179], which posits a cyclic universe in which the ultimate infinitely expanded state of one phase (or 'aeon') is identified with the initial singularity of the next. In the ΛCDM model, the total density parameter is usually taken to comprise of contributions from radiation ($w_{\rm r} = \frac{1}{3}$), matter (typically modelled as dust with $w_{\rm m} = 0$), curvature ($w_k = -\frac{1}{3}$), and the cosmological constant ($w_\Lambda = -1$). These are listed in Table 2.1, in which one can see an obvious 'gap' that we term 'missing matter' with $w_X = -\frac{2}{3}$. Interestingly, forms of matter have been proposed for which $w_X = -\frac{2}{3}$, such as domain walls [20, 49, 164], or particular scalar field

models [34].

The above observation is merely suggestive of a hitherto neglected additional component. As we will show below, however, the case for introducing such a component is strengthened considerably by rewriting the Friedmann equation (2.37) in terms of conformal time η. As discussed in [106], the motivation for working in terms of η is that, for currently accepted values of the density parameters $\Omega_{i,0}$, the conformal time intervals since the Big Bang ($a = 0$) and until the conformal singularity ($a = +\infty$) are both finite. By contrast, although the cosmic time since the Big Bang is finite, the future singularity occurs at $t = \infty$. This asymmetry means that it is more natural to work in terms of conformal time, if one is to realise scenarios such as Penrose's Cycles of Time model. Moreover, it is worth noting that, like cosmic time, which corresponds to the proper time of comoving observers, conformal time also has a clear operational definition as the time kept by a clock whose 'tick' is the bounce of a light pulse confined to a pair of parallel mirrors moving, and therefore separating, with the Hubble flow.

Making the change of variable $d\eta = dt/a$ in the Friedmann equation (2.37), including an additional missing matter component X, one obtains

$$\frac{1}{H_0^2}\left(\frac{da}{d\eta}\right)^2 = \Omega_{\mathrm{r},0} + \Omega_{\mathrm{m},0}a + \Omega_{k,0}a^2 + \Omega_{X,0}a^3 + \Omega_{\Lambda,0}a^4, \tag{7.1}$$

where we note that the right-hand side is simply a fourth-degree polynomial in a. Most importantly, when written in this form, the Friedmann equation has the interesting property of being form invariant under the reciprocity transformation $a(\eta) \to 1/a(\eta)$, which swaps the nature of the Big Bang and conformal singularity [106]. This is easily seen by making the change of variable $\tilde{a}(\eta) = 1/a(\eta)$, which immediately yields

$$\frac{1}{H_0^2}\left(\frac{d\tilde{a}}{d\eta}\right)^2 = \Omega_{\Lambda,0} + \Omega_{X,0}\tilde{a} + \Omega_{k,0}\tilde{a}^2 + \Omega_{\mathrm{m},0}\tilde{a}^3 + \Omega_{\mathrm{r},0}\tilde{a}^4. \tag{7.2}$$

Given the observed values of the various present-day density parameters $\Omega_{i,0}$, this equation is clearly not identical to (7.1). Nonetheless, we do find that, provided $\Omega_{X,0} \neq 0$, the Friedmann equation is *form* invariant, with a swapping of roles

between radiation and the cosmological constant, and between matter and our additional 'missing matter' component (hence our name for it). We note that the curvature density preserves its dynamical role under the reciprocity transformation and also that the remaining Einstein equations are satisfied for the new 'w' values implied by (7.2), showing that the reciprocity transformation is a symmetry of the entire set of cosmological equations. [1]

It should be noted that the true equation-of-state parameter w_i for each component will, in general, differ from the canonical values listed in Table 2.1 (although these values are assumed in most cosmological analyses). For example, non-relativistic matter does not have exactly zero pressure ($w_{\rm m} = 0$), but a pressure proportional to $(v/c)^2$. Similarly, relativistic particles such as massive neutrinos have an equation-of-state parameter slightly less than $w_{\rm r} = \frac{1}{3}$, which changes with cosmic epoch. As a consequence, the right-hand side of (7.1) will not, in general, be a fourth-degree polynomial, in which case it is no longer form-invariant under the reciprocity transformation $\tilde{a}(\eta) = 1/a(\eta)$. Nonetheless, the basic notion of swapping the Big Bang and conformal singularity remains valid, and a cosmological observer may still potentially be unable to determine whether $a(\eta)$ or $\tilde{a}(\eta)$ corresponds to the scale factor describing the expansion of his/her universe. For example, suppose the equation-of-state parameter for each component differed slightly from the canonical values listed in Table 2.1, so that $w_i \rightarrow w_i + \frac{1}{3}\epsilon_i$. Each

[1] It is further shown in [106] that, provided $\Omega_{X,0} \neq 0$, the Friedmann equation (7.1) is, in fact, form invariant under the more general Möbius transformation $\tilde{a}(\eta) = [\alpha - \gamma\, a(\eta)]/[\beta - \delta\, a(\eta)]$, where α, β, γ and δ are constants, of which the reciprocity transformation $\tilde{a}(\eta) = 1/a(\eta)$ is a special case (note that there are only three effective constant degrees of freedom in the Möbius transformation; a convenient choice is to set $\delta\alpha - \beta\gamma = 1$). Under the general Möbius transformation, however, one finds that the Friedmann equation (7.1) becomes

$$\frac{1}{H_0^2}\left(\frac{d\tilde{a}}{d\eta}\right)^2 = \sum_{i=0}^{4} \tilde{\Omega}_{i,0}\tilde{a}^i,$$

where $\tilde{\Omega}_{i,0} = \tilde{\Omega}_{i,0}(\alpha, \beta, \gamma, \delta, \Omega_{{\rm r},0}, \Omega_{{\rm m},0}, \Omega_{k,0}, \Omega_{X,0}, \Omega_{\Lambda,0})$ are a new set of 'density parameters', each of which, in general, depends on *all* the original density parameters, as well as the parameters in the Möbius transformation. Thus one loses the simple swapping of roles between different original energy densities that occurs for the reciprocity transformation.

term on the right-hand side of (7.1) would be separately multiplied by the appropriate factor $a^{-\epsilon_i}$, whereas each term on the right-hand side of (7.2) would simply inherit the additional factor $\tilde{a}^{\epsilon_i}$. In particular, strict form-invariance under the reciprocity transformation is recovered if $\epsilon_\Lambda = -\epsilon_\mathrm{r}$ and $\epsilon_X = -\epsilon_\mathrm{m}$, together with the automatic condition $\epsilon_k = 0$. In what follows, however, we will neglect this subtlety and adopt the standard practice in cosmological analysis of assuming the canonical values for the equation-of-state parameters listed in Table 2.1, in which case (7.1) and (7.2) are valid and form-invariance under the reciprocity transformation holds automatically.

Having made this point, however, once one admits the possibility of adding an extra component to the energy content of the universe, it is natural to extend one's investigation by allowing its equation-of-state parameter to vary, rather than fixing it to $w_X = -\frac{2}{3}$. This more generic 'double dark energy' model comes at the cost of breaking the reciprocity invariance of the Friedmann equation, even if the equation-of-state parameters of the other components are assumed to have their canonical values. Nonetheless, this model is also of interest in its own right since the observed acceleration of the universal expansion may be driven by more than just a single dark-energy component. We note that a generic two-component model of dark energy has previously been considered in [78].

The structure of this chapter is as follows. In Section 7.1, we give a brief summary of the phenomenology of an additional missing matter component with $w_X = -\frac{2}{3}$ by investigating its effect on the expansion history of the universe, in particular the distance-redshift relation, and on the evolution of perturbations, through the cosmic microwave background and matter power spectra. The results of these analyses are given in Section 7.2 and our conclusions are presented in Section 7.3.

7.1 Phenomenology

It is of interest to investigate the phenomenology of a cosmological model containing a second component X with negative pressure (in the event the energy

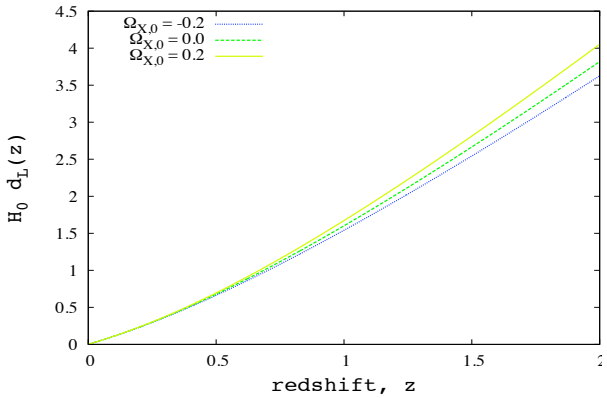

Figure 7.1: Dimensionless luminosity distance $H_0 d_L(z)$ as a function of redshift z for a concordance ΛCDM cosmology with an additional component X with equation-of-state parameter $w_X = -\frac{2}{3}$, for different values of $\Omega_{X,0}$.

density is positive), in addition to a cosmological constant. Since our missing matter model (for which $w_X = -\frac{2}{3}$) is just a special case (albeit an important one) of our double dark energy model, we will focus here on the former as being a representative example of the latter. The effect of the additional component X on the global expansion history of the universe depends only on the equation-of-state parameter w_X, whereas its effect on the evolution of perturbations will also depend on the nature of the component X, in particular its assumed dynamical properties. We therefore consider these two issues separately.

7.1.1 Background evolution

The inclusion of the $\Omega_{X,0}$ into (2.14) thus directly affects the expansion history embodied in $H(z)$, and hence can serve either to increase or decrease the luminosity distance $d_L(z)$ to an object at redshift z. Figure 7.1 illustrates this effect for a few representative values of $\Omega_{X,0}$. If $\Omega_{X,0} > 0$, the apparent luminosity is reduced and hence the luminosity distance is increased compared to the standard ΛCDM model. The opposite effect occurs for $\Omega_{X,0} < 0$. The power of the luminosity distance as a cosmological probe resides in the fact that it can be simply

related to distance modulus μ apparent brightness $m(z)$ obtained directly from a set of standard candles (see Section 3.2.1).

It should be pointed out that, for the background evolution, the combination of a cosmological constant with $w_\Lambda = -1$ and an additional component X with constant w_X is equivalent, under certain conditions outlined below, to a single dark energy component with a time-varying equation-of-state parameter $w_{\rm eff}(a)$ given by the ratio of the combined pressure of the two components to their combined density [78], namely

$$w_{\rm eff}(a) = \frac{-\Omega_{\Lambda,0} + w_X \Omega_{X,0} a^{-1}}{\Omega_{\Lambda,0} + \Omega_{X,0}\, a^{-1}}. \tag{7.3}$$

Examples of such models have been studied extensively [41, 111, 195, 208], albeit not with the particular form of $w_{\rm eff}(a)$ given above. Plotting $w_{\rm eff}(a)$, assuming 'plausible' values $\Omega_{\Lambda,0} \sim 0.7$ and $\Omega_{X,0} \sim 0.2$, shows that the variation with either a or redshift z is non-linear, so $w_{\rm eff}(a)$ is not contained within either of the common $w(z) = w_0 + w_1 z$ or $w(a) = w_0 + w_a(1-a)$ parameterisations. More importantly, however, it should be noted that if $\Omega_{\Lambda,0}$ and $\Omega_{X,0}$ have different signs, as we allow in our analysis, then $w_{\rm eff}(a)$ becomes singular at $a = |\Omega_{X,0}/\Omega_{\Lambda,0}|$. Thus, if $\Omega_{\Lambda,0}$ or $\Omega_{X,0}$ (or both) are allowed to take positive and negative values, then our missing matter (or double dark-energy) model is *not*, in general, described by a single time-varying dark-energy component.

7.1.2 Evolution of perturbations

An additional component X will affect the growth of perturbations through its contribution to $H(z)$ and the evolution of the matter density. Moreover, we assume here that X has the same dynamical behaviour as that usually assumed for a generic dark energy component. In particular, we use the CAMB [134] dark-energy module developed by [71], in which dark energy is assumed itself to exhibit Gaussian adiabatic perturbations. It is worth noting that, as the equation-of-state parameter approaches -1, the effects of the dark energy perturbations disappear,

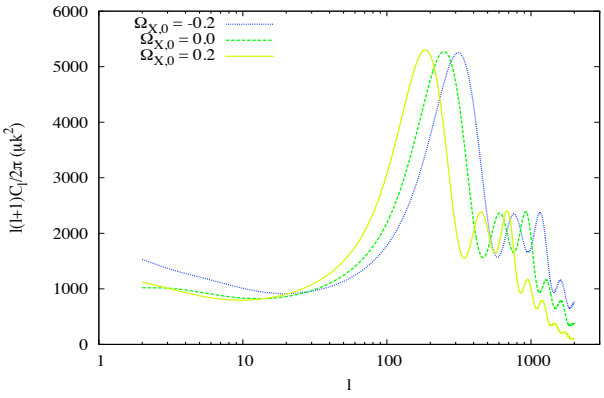

Figure 7.2: CMB power spectra for a concordance ΛCDM model with an additional component X, with equation-of-state parameter $w_X = -\frac{2}{3}$, for several values of $\Omega_{X,0}$.

as one would expect for a pure cosmological constant. [1]

We plot the CMB power spectra in Figure. 7.2, from which we see that, as one might expect, the main effect of a non-zero $\Omega_{\mathrm{X},0}$ is to shift the positions of the acoustic peaks, which are sensitive to the spatial geometry of the universe, and hence depend on the total energy density of all the components. Thus, one would expect constraints on $\Omega_{\mathrm{X},0}$ from CMB observations to be tightly correlated with the constraints on Ω_Λ and Ω_k. For positive values of $\Omega_{\mathrm{X},0}$, we also see a considerable enhancement of power on the largest scales from the late-time ISW effect.

In Figure 7.3, we plot the predicted matter power spectra for different values of $\Omega_{X,0}$; again the other parameters are set to their concordance values. We see that the dominant effect of the additional component is on the normalisation

[1] It should be borne in mind, however, that a possible physical instantiation of an additional component X with $w_X = -\frac{2}{3}$ could be in the form of domain-wall topological defects, for example, in which case the effect on the generation and evolution of pertubations may be very different to that assumed here.

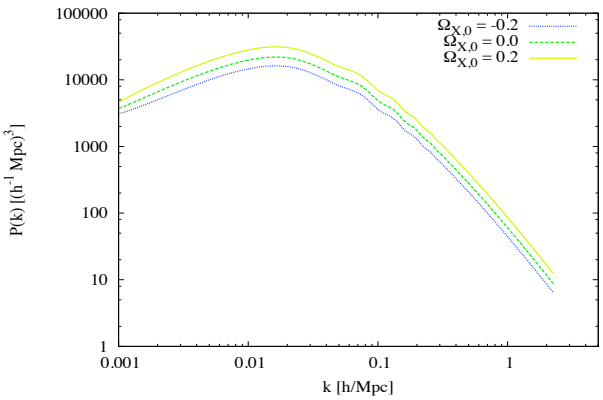

Figure 7.3: Matter power spectra for a concordance ΛCDM model with an additional component X, with equation-of-state parameter $w_X = -\frac{2}{3}$, for several values of $\Omega_{X,0}$.

of the matter power spectrum. The amplitude of fluctuations is enhanced for $\Omega_{X,0} > 0$ and suppressed for $\Omega_{X,0} < 0$. By contrast, the positions of the acoustic oscillations, which depend largely on the matter density, are unaffected by the introduction of the additional component.

It is worth noting that, although the background evolution of the universe is identical for our missing matter (or double dark-energy) model and for a model with a single time-varying dark energy component defined by (7.3) (provided $\Omega_{\Lambda,0}$ and $\Omega_{X,0}$ have the same sign), the evolution of perturbations is, in general, *different* for the two cases. This is true even in the simplest case where one assumes the same dynamical behaviour for the generic dark energy components in the two models, namely that they exhibit Gaussian adiabatic perturbations. This is illustrated in Figure. 7.4, in which we plot the CMB and matter power spectra for a specific example of each model. Consequently, we reiterate our earlier comment that the many previous studies of models containing a single time-varying dark-energy component are *not* equivalent to the study presented here.

We now perform a Bayesian parameter estimation and model comparison

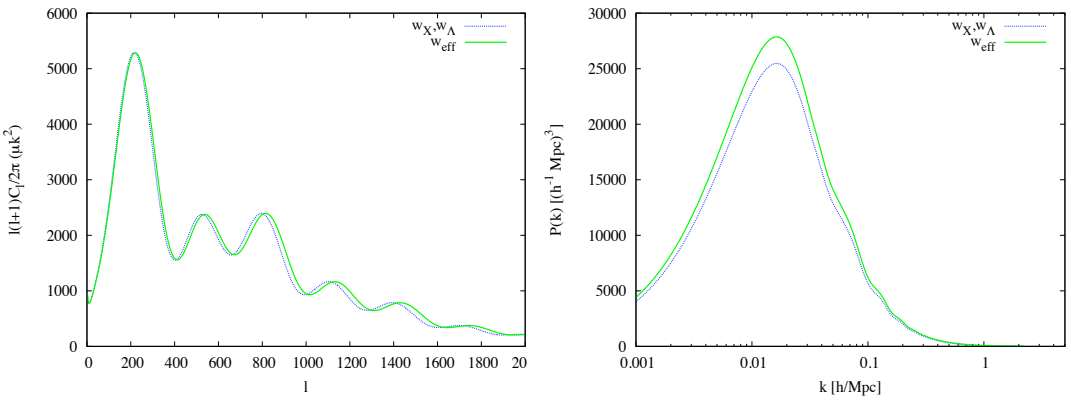

Figure 7.4: CMB power spectra (top) and matter power spectra (bottom) for: a concordance ΛCDM model with an additional component X, with equation-of-state parameter $w_X = -\frac{2}{3}$ and density $\Omega_{X,0} = 0.2$ (blue line); and a CDM model with a single time-varying dark energy component with effective equation-of-state parameter $w_{\rm eff}(a)$ defined in (7.3) (green line).

analysis of our 'missing matter' and 'double dark energy' models, using recent cosmological observations, presented as our dataset I in Section 3.4. Throughout the analysis we consider the base and secondary parameters, along with the ranges of the uniform priors, shown in Table 3.3 and curvature flat prior $\Omega_{k,0} = [-0.05, 0.05]$. Our hypothetical additional component is characterised by its density parameters $\Omega_{X,0}$ and equation-of-state parameter w_X. We assume a uniform prior on $\Omega_{\Lambda,0}$ in the range $[-1, 2]$ throughout. For the missing energy model, we have $w_X = -\frac{2}{3}$, and for the double dark energy model we assume the uniform prior $w_X = [-2, -1]$. To carry out the exploration of the parameter space, we incorporate the extra component into the standard cosmological equations, by performing the minor modifications to the CAMB code.

7.2 Results

For comparison purposes, we first assume no additional component X, in order to determine the constraints imposed by the current combined data sets on the

standard ΛCDM model. We find the constraints on the standard parameters $\{\Omega_{\mathrm{b},0}h^2,\ \Omega_{\mathrm{dm},0}h^2,\ \theta,\ \tau,\ A_{\mathrm{s}},\ n_{\mathrm{s}}\}$ remain essentially unaffected by the introduction below of our additional component X, and so we do not consider them further.

7.2.1 Missing matter model

The inclusion of a missing matter component X with $w_X = -\frac{2}{3}$ considerably broadens the parameter constraints. In particular, we find: $\Omega_{\Lambda,0} = 0.837 \pm 0.149$, which constitutes an order-of-magnitude increase in the error bars as compared with the standard ΛCDM model, $\Omega_{\mathrm{m},0} = 0.276 \pm 0.015$, $\Omega_{k,0} = -0.0047 \pm 0.0068$ and $H_0 = 69.90 \pm 1.76$. Figure 7.5 shows 1D and 2D marginalised posterior distributions for the density parameters (note that $\Omega_{\mathrm{m},0} = 1 - \Omega_{\Lambda,0} - \Omega_{k,0} - \Omega_{X,0}$). As expected, we observe a clear degeneracy between $\Omega_{X,0}$ and both $\Omega_{\Lambda,0}$ and $\Omega_{k,0}$. The 1D constraint on the density parameter of missing matter is $\Omega_{X,0} = -0.11 \pm 0.14$. The current data thus prefer a slightly negative value, which is difficult to interpret physically, although the 1D marginal shows moderate relative probability even for $\Omega_{X,0} \sim 0.2$, and so the presence of an appreciable missing matter component cannot be ruled out. Our results are, however, still consistent with a standard ΛCDM model. This view is supported by our Bayesian model comparison. We find that the log-evidence difference (or Bayes factor) between the missing matter model and the standard ΛCDM model is $\mathcal{B}_{\Lambda+X,\Lambda} = -1.45 \pm 0.30$. According to Jeffreys guideline [112, 234], the inclusion of the missing matter component is therefore significantly disfavoured by current cosmological data.

7.2.2 Double dark energy model

We now allow for the equation-of-state parameter w_X for our additional component to be a free parameter (albeit still independent of redshift), for which we assume a uniform prior in the range $w_X = [-\frac{3}{2}, -\frac{1}{2}]$. We thus allow for the possibility that this second dark-energy component could be a form of phantom energy with $w_X < -1$ [233]. Figure 7.6 shows the resulting 1D and 2D marginalised posterior distributions for w_X and the density parameters in the model (once again, note that $\Omega_{m,0} = 1 - \Omega_{\Lambda,0} - \Omega_{k,0} - \Omega_{X,0}$). At the top-right of the figure we also give a representation of the 3D posterior in the $(w_X, \Omega_{X,0}, \Omega_{\Lambda,0})$ subspace, where

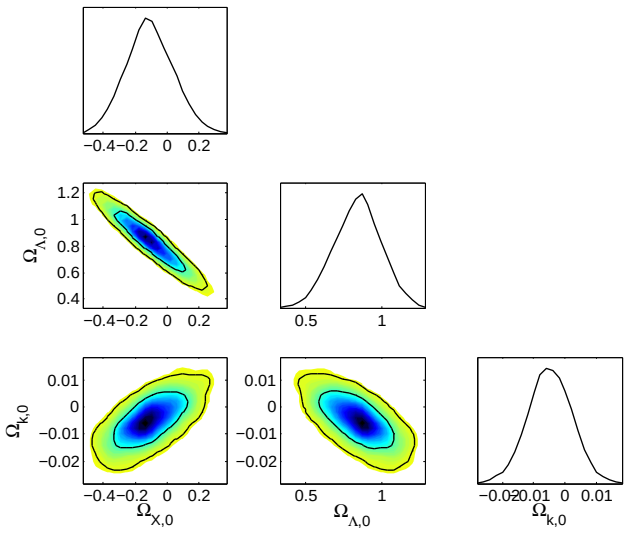

Figure 7.5: 1D and 2D marginalised posterior distributions for density parameters in the missing matter model (note that $\Omega_{\mathrm{m},0} = 1 - \Omega_{\Lambda,0} - \Omega_{k,0} - \Omega_{X,0}$). The 2D constraints are plotted with 1σ and 2σ confidence contours.

the colour indicates the value of $\Omega_{\Lambda,0}$.

The 1D constraints on the standard parameters are as follows: $\Omega_{\Lambda,0} = 0.647 \pm 0.573$, $\Omega_{\mathrm{m},0} = 0.275 \pm 0.015$, $\Omega_{k,0} = -0.0031 \pm 0.0058$, $H_0 = 69.95 \pm 1.80$. The constraints on the parameters describing the additional, second dark-energy component may be given as $w_X = -1.02 \pm 0.20$ and $\Omega_{X,0} = 0.080 \pm 0.574$, although these numbers obscure the bi-modal nature of the marginal $(w_X, \Omega_{X,0})$-space and $(w_X, \Omega_{\Lambda,0})$-space distributions (see below). These results are clearly consistent with a standard ΛCDM model, although the inclusion of the additional dark-energy component has again resulted in the uncertainties in the constraints on the standard parameters being much larger than those obtained assuming a ΛCDM model. Indeed, the 1D marginal for $\Omega_{X,0}$ shows moderate relative probability even for $\Omega_{X,0} \sim 1$.

Moreover, the 2D and 3D marginal distributions in Figure. 7.6 have some cu-

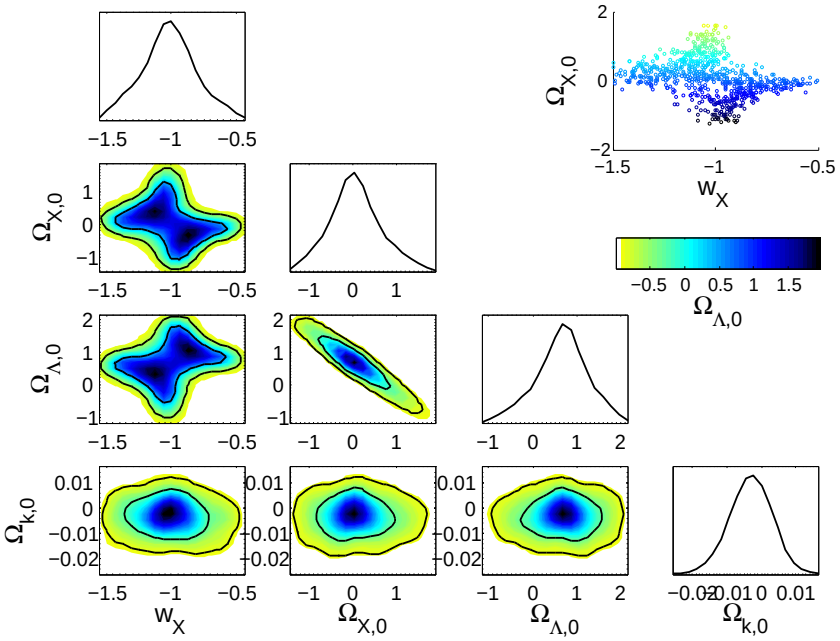

Figure 7.6: 1D and 2D marginalised posterior distributions for density parameters in the double dark energy model (note that $\Omega_{m,0} = 1 - \Omega_{\Lambda,0} - \Omega_{k,0} - \Omega_{X,0}$). The 2D constraints are plotted with 1σ and 2σ confidence contours. The top-right panel shows the 3D posterior distribution in the $(w_X, \Omega_{X,0}, \Omega_{\Lambda,0})$ subspace, where the colour code indicates the value of $\Omega_{\Lambda,0}$.

rious and interesting features that are worth noting. First, as might be expected, we again see a pronounced degeneracy between $\Omega_{\Lambda,0}$ and $\Omega_{X,0}$. Of more interest, however, is the bi-modal nature of the 2D marginals in the $(w_X, \Omega_{\Lambda,0})$ and $(w_X, \Omega_{X,0})$ planes, both of which have a distinctive 'butterfly' shape, albeit exhibiting opposite correlations. Focussing on the latter, we see that the two peaks are offset from the standard ΛCDM model $(-1, 0)$, although that model remains admissible. Indeed, with the help of the 3D marginal in the $(w_X, \Omega_{X,0}, \Omega_{\Lambda,0})$ subspace plotted in the top-right of Figure 7.6, we see that the two modes of the distribution correspond to models with $\Omega_{\Lambda,0} \approx 0.4$, $\Omega_{X,0} \approx 0.3$, $w_X \approx -1.2$ and $\Omega_{\Lambda,0} \approx 1.0$, $\Omega_{X,0} \approx -0.3$, $w_X \approx -0.8$, respectively. The former model has the advantage that the density parameters for both dark energy components are pos-

itive, but requires the second component X to be a form of phantom energy. In the latter model, the second dark energy component has a more physically reasonable value of w_X, but is required to have a negative density parameter, which is difficult to interpret physically (at least more so than a negative pressure). Indeed, we see that this latter case is broadly consistent with our findings for the missing matter model discussed in the previous subsection.

The marginal distribution in $(\Omega_{X,0}, \Omega_{\Lambda,0})$ subspace shows a strong correlation between these energy densities that would imply the potential for a trade-off between them. One might be concerned, however, that the marginal distribution plotted is strongly dominated by the contribution (after marginalising over w_X) from near $w_X = -1$. If so, one could then not infer the potential of a trade-off between these two energy densities at (any) other values of w_X. To investigate this possibility, we also calculated the conditional distributions in $(\Omega_{X,0}, \Omega_{\Lambda,0})$ subspace for a small set of fixed w_X-values in the range $[-0.7, -1.3]$. The resulting distributions were, however, very similar to that plotted in Figure 7.6, and so indicating that the two energy densities can indeed be traded-off against one another.

Also of interest is our Bayesian model comparison, which finds that the log-evidence difference (Bayes factor) between the double dark energy model and standard ΛCDM is $\mathcal{B}_{\Lambda+X,\Lambda} = -0.16 \pm 0.30$. This shows that neither model is preferred over the other; indeed they are indistinguishable to within the statistical uncertainty on the computed evidence values. Thus, the two additional parameters $\Omega_{X,0}$ and w_X in the double dark energy model allow it the freedom to fit the data sufficiently better than ΛCDM to compensate for the corresponding increase in the prior volume, and hence the model is not penalised by the evidence.

7.3 Discussion and Conclusions

We have investigated the possibility that there exist two dark-energy components in the universe: a cosmological constant, with $w_\Lambda = -1$; and an additional component X with equation-of-state parameter w_X. In the first instance, we fix the equation-of-state parameter of X to the value $w_X = -\frac{2}{3}$. This 'missing matter'

model corresponds to the special case in which the additional component is *required* for the Friedmann equation written in terms of conformal time η to be form invariant under the reciprocity transformation $a(\eta) \rightarrow 1/a(\eta)$. Foregoing this requirement, we then consider the more general 'double dark energy' model, in which w_X is a free parameter assumed to have uniform prior in the range $w_X = [-\frac{3}{2}, -\frac{1}{2}]$. For both models, we perform a Bayesian parameter estimation and model selection analysis, relative to standard ΛCDM, using recent cosmological observations

For the missing matter model, the introduction of the additional component X significantly broadens the constraints on the standard parameters in the ΛCDM model, but leaves their best-fit values largely unchanged. The 1D marginalised constraint on the missing matter density parameter is $\Omega_{X,0} = -0.11 \pm 0.14$. Thus, current cosmological observations prefer a slightly negative value, which is difficult to interpret physically, but the posterior on this parameter is sufficiently broad that significant relative probability exits even for $\Omega_{X,0} \sim 0.2$, and so the presence of a missing matter component cannot be ruled out. Nonetheless, our results are consistent with ΛCDM and our Bayesian model selection analysis disfavours the missing matter model, as compared to ΛCDM, by about 1.5 log-units of evidence.

For the double dark energy model, the constraints on standard ΛCDM parameters are again considerably broadened. The 1D marginalised constraints on the second dark energy component are $\Omega_{X,0} = 0.080 \pm 0.574$ and $w_X = -1.02 \pm 0.20$, respectively, which are again consistent with ΛCDM. Once more, however, the 1D marginalised posterior on $\Omega_{X,0}$ is sufficiently broad that even $\Omega_{X,0} \sim 1.0$ is not ruled out. More interestingly, the 2D marginal distributions in the $(w_X, \Omega_{\Lambda,0})$ and $(w_X, \Omega_{X,0})$ planes are both bi-modal, exhibiting a 'butterfly' shape. In particular, the peaks in the $(w_X, \Omega_{X,0})$-plane are offset from the ΛCDM value $(-1, 0)$, although the latter is still acceptable. The two modes of the distribution correspond to models with $\Omega_{\Lambda,0} \approx 0.4$, $\Omega_{X,0} \approx 0.3$, $w_X \approx -1.2$ and $\Omega_{\Lambda,0} \approx 1.0$, $\Omega_{X,0} \approx -0.3$, $w_X \approx -0.8$, respectively. We also find that the double dark energy model has a similar Bayesian evidence to ΛCDM to within the numerical uncertainty, and

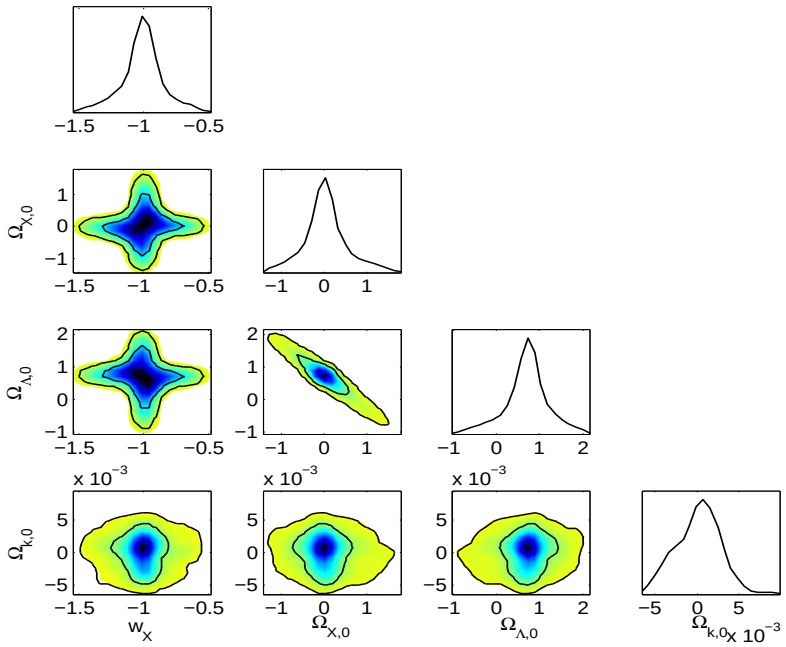

Figure 7.7: 1D and 2D marginalised posterior distributions for density parameters in the double dark energy model (note that $\Omega_{m,0} = 1 - \Omega_{\Lambda,0} - \Omega_{k,0} - \Omega_{X,0}$) as derived from simulated observations of the CMB power spectrum and Type-Ia supernovae generated assuming a concordance ΛCDM cosmology. The 2D constraints are plotted with 1σ and 2σ confidence contours.

hence neither model is preferred over the other.

One potential cause for the observed bimodality in the 2D marginalised posteriors would be some mutual inconsistency between two or more of the datasets used in our analysis, such that they preferred significantly different values for cosmological parameters. We therefore performed a Bayesian consistency analysis [94, 156] by partitioning the full combined dataset D into its four constituent parts D_i $(i = 1, \ldots, 4)$, namely WMAP, ACT, Union 2 and BAO, and analysing each independently (together, in each case, with the constraints from BBN and HST). In particular, we calculated the evidence ratio (3.23) and find that $R = 2.15$ indicating that the bimodality in the posterior is not caused by any inconsistencies

between the individual datasets. To investigate the significance of the observed bimodality of the posterior, we performed simulated observations of the CMB power spectrum and Type-Ia supernovae apparent brightness versus redshift, assuming a standard concordance ΛCDM model and observational data quality commensurate with the real CMB and supernovae data used in our analysis. These were combined with the same constraints on the baryon density from BBN [33] and Gaussian prior on H_0 from the HST key project [192] that were used in the analysis of the real data. The resulting posterior distribution of the density parameters is illustrated in Figure 7.7. As one might expect, the 2D marginal distributions in the $(w_X, \Omega_{\Lambda,0})$ and $(w_X, \Omega_{X,0})$ planes do exhibit a characteristic 'plus' shape, which is indicative of the parameter degeneracies along the coordinate axes. In contrast to the bimodal posterior obtained from the real data, however, we see that the analysis of simulated observations yields a unimodal posterior centred correctly on the input concordance parameters values. This suggests that the bimodal nature of the posterior in Figure 7.6 may be driven by features present in the real data, but absent from the ΛCDM simulation.

To explore this possibililty further, we analysed 10 more sets of simulated observations. The resulting 2D marginalised posteriors in the $(w_X, \Omega_{X,0})$-plane are shown in Figure 7.8. In the majority of cases, the posterior is unimodal, but for some realisations a weak bimodality is observed. In each such case, however, the bimodality is typically less pronounced than that observed for the real data in Figure 7.6 and lies in the orthogonal direction. It is probably safest to conclude simply that current observations are insufficient to decide whether the bimodality found for the real data is statistically significant.

Since the double dark energy model remains viable with current cosmological observations, it is of interest to generalise it further. The bimodality we observe in Figure 7.6 might be evidence of contributions from two species X and Y, with $w_X \approx -1.2$ and $w_Y \approx -0.8$. It might therefore be of interest to remove the requirement of having one fluid with $w = -1$ and investigate if the value of either w_X or w_Y settles near -1. Also of interest would be to allow the equation-of-state parameter $w_X(z)$ of the second dark energy component (and possibly also of Y)

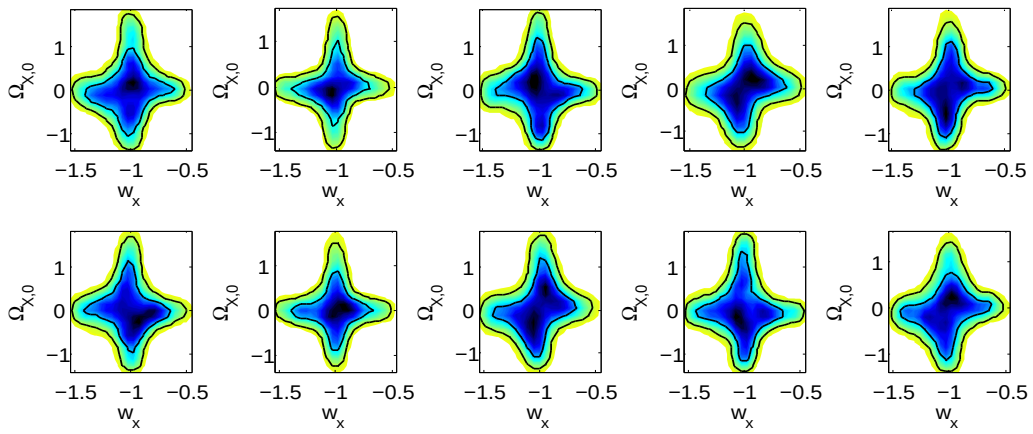

Figure 7.8: 2D marginalised posterior distributions in the $(w_X, \Omega_{X,0})$-plane in the double dark energy model, derived from 10 realisations of simulated observations of the CMB power spectrum and Type-Ia supernovae generated assuming a concordance ΛCDM cosmology. The 2D constraints are plotted with 1σ and 2σ confidence contours.

to depend on redshift [233]. We plan to investigate these possibilities in a future work.

Chapter 8

Modified Gravity

Although ΛCDM provides a good fit to current data, it still faces some theoretical challenges, such as the coincidence and fine-tuning problems [36, 174, 176]. Also, recent experiments with the use of model-independent techniques for reconstructing the properties of dark energy, support a mild time-dependent evolution of $w(z)$ [7, 79, 129, 233, 252]. Hence alternative proposals to the conventional cosmological constant term have emerged. Several options involve the introduction of new exotic fluids to the energy-momentum tensor, such as quintessence and K-essence, amongst many other scenarios [14, 43, 189, 234, 255]. Besides the dark sector, there exists a variety of models where the present expansion is realised due to modifications of the laws of gravity (MG) on cosmological scales. Some of them introduce non-linear terms to the standard Einstein-Hilbert action, like $f(R)$ theories [13, 99, 166, 197, 220], or higher dimensional braneworld models [67, 152]. Other alternatives and combinations are also considered as good candidates [for a review see: 50, 66, 72, and references therein].

As a consequence of the introduction of different models, a fundamental question arises regarding how to distinguish amongst these possibilities. The cosmic acceleration, produced by any of these proposals, might affect both the expansion history and the growth rate of large-scale structure in the Universe. Hence, a natural search for departures from the ΛCDM model is to exploit present and future cosmological observations.

The cosmic evolution driven by a modified gravity model may be described in terms of an effective equation-of-state $w_{\rm eff}(z)$, which is fitted with luminosity distance constraints. However, the extra degrees of freedom in extended GR models result in more freedom to reproduce any desired background evolution. That is, given the Hubble rate $H = H(a)$, one can identify a complete family of models such that the Friedmann equation is satisfied, and hence at the background level, suitable MG theories might be indistinguishable from ΛCDM or dark energy theories [171, 218]. Then, our analysis is mainly focussed on the cosmological perturbations. In this context, two scalar field potentials, $\Psi(t, \boldsymbol{x})$ and $\Phi(t, \boldsymbol{x})$, specify the evolution of linear perturbations around a flat FRW background:

$$ds^2 = -(1+2\Psi)dt^2 + a^2(t)(1-2\Phi)\gamma_{ij}dx^i dx^j. \tag{8.1}$$

Note the change of convention in the sign $\Phi \to -\Phi$ respect to Section 2.3; some other conventions may be found in [149]. Standard ΛCDM and models with minimally coupled scalar fields are based on the assumption that the Newtonian potentials Φ and Ψ, satisfy the relation $\Phi = \Psi$. Nevertheless, modified gravity models usually predict the existence of an effective anisotropic stress, so the two metric potentials are no longer necessarily the same. Thus, we may differentiate a dark energy model from a particular modified gravity theory via the relationship between the two metric potentials Φ, Ψ and the density perturbation δ_m [110].

For the purpose of detecting possible departures from general relativity, we incorporate time and scale-dependent functions, $\mu(a,k)$ and $\gamma(a,k)$, into the Poisson and anisotropy equations in standard GR. This approach has been employed before in the search for departures from ΛCDM, see for instance [12, 77, 158, 219, 254]. Then, for a generic MG theory, the linearised Einstein-like equations, within the quasi-static approximation (2.104), have the following form

$$\frac{k^2}{a^2}\Psi = -\frac{\kappa^2}{2}\mu(a,k)\,\delta\rho_m, \tag{8.2}$$

$$\Phi = \gamma(a,k)\,\Psi, \tag{8.3}$$

$$\ddot{\delta}_m + 2H\dot{\delta}_m + \frac{k^2}{a^2}\Psi = 0. \tag{8.4}$$

The *screened mass function* μ is interpreted as the ratio of an effective gravitational constant relative to the Newtonian constant, $\mu \equiv G_{\rm eff}(a,k)/G_{\rm N}$. The other relevant function, the gravitational *slip parameter* γ, defined as the ratio of the spatial perturbation to the time-time perturbation of the metric $\gamma \equiv \Phi/\Psi$, is seen as an effective anisotropic stress. We observe that modifications of GR, for which $\mu(a,k) = \gamma(a,k) = 1$, affect, through the Newtonian potentials, the growth of matter density perturbations δ_m, as shown in equation (8.4). Thus, current or future surveys, may allow us to distinguish modified gravity models from general relativity with a dark energy component.

We consider modified gravity models for which the action may be written as

$$S = \int d^4x\sqrt{-g}\left[\frac{1}{2\kappa^2}f(R,\phi) - \frac{1}{2}w(\phi)g^{\mu\nu}\partial_\mu\phi\partial_\nu\phi - V(\phi)\right] + S_{\rm M}(g_{\mu\nu},\psi_{\rm M}), \quad (8.5)$$

where $\kappa^2 \equiv 8\pi G$, g is the determinant of the metric $g_{\mu\nu}$. $f(R,\phi)$ is some arbitrary function of the Ricci scalar R and the scalar field ϕ; $w(\phi)$ and $V(\phi)$ are functions of ϕ, and the matter action $S_{\rm M}$ depends on $g_{\mu\nu}$ and matter fields $\psi_{\rm M}$. Notice that the action (8.5) contains theories such as Brans-Dicke theory, scalar-tensor theories, and dilaton gravity. In particular the model $f(R) = R - 2\Lambda$ corresponds to the standard Einstein-Hilbert action. We consider the standard metric formalism by performing the variation of the action with respect to the metric tensor $g_{\mu\nu}$, bearing in mind that in the Palatini formalism different field equations may arise for a Lagrangian density non-linear in R [75, 241]. Varying the action with respect to $g_{\mu\nu}$ and ϕ, the following field equations are obtained [72]

$$\begin{aligned} FG_{\mu\nu} &- \frac{1}{2}(f - RF)g_{\mu\nu} - F_{,\mu;\nu} + \Box F g_{\mu\nu} \\ &= \kappa^2\left[w\left(\phi_{,\mu}\phi_{,\nu} - \frac{1}{2}g_{\mu\nu}\partial^\lambda\phi\partial_\lambda\phi\right) - V g_{\mu\nu} + T^{(\rm M)}_{\mu\nu}\right], \quad (8.6) \\ \Box\phi &+ \frac{1}{2w}\left(w_{,\phi}\partial^\lambda\phi\partial_\lambda\phi - 2V_{,\phi} + \frac{f_{,\phi}}{\kappa^2}\right) = 0. \quad (8.7) \end{aligned}$$

where subscript '$_{,X}$' stands for the partial derivative with respect to the variable X, e.g, $F(R) \equiv \partial f/\partial R = f_{,R}$ and likewise $F_{,R} = f_{,RR} = \partial^2 f/\partial R^2$. Also $\dot{} \equiv d/dt$

and $' \equiv d/d\ln a$ below; $G_{\mu\nu}$ is the Einstein tensor.

In this chapter we focus on a version of the Starobinsky $f(R)$ model and with the use of current data we constrain the parameter-space. Finally, because the addition of parameters to the standard model may lead to an arbitrarily accurate fit, we consider the Bayesian evidence as a quantitative implementation of Occam's razor. In this way, we obtain the model preferred by current observations.

The outline of the chapter is as follows. In Section 8.1, we discuss the background evolution and scalar perturbations for a modified gravity theory, in particular $f(R)$ models. We then specify observable quantities used to constrain the parameter-space through current data sets. The constraints on the parameters used to describe the modified gravity models, along with Bayesian evidence values, are discussed in Section 8.3. We present our conclusions in Section 8.4.

8.1 $f(R)$ Gravity

The simplest family of MG models that give rise to acceleration of the universal expansion are obtained by replacing the Ricci scalar R in the usual Einstein-Hilbert Lagrangian by a non-linear function of R. Hence we consider the action (8.5) in the form of $f = f(R)$, without the inclusion of a scalar field, to describe this class of gravity models. Since modifications of gravity are more apparent at low redshift, we henceforth ignore the radiation component due to its relative unimportance for structure formation at late time. We thus base our analysis on non-relativistic matter with background energy density ρ_m and negligible pressure $p_m = 0$.

8.1.1 Background evolution

For the background evolution, the FRW metric leads to the Ricci scalar given by

$$R = 6(2H^2 + \dot{H}). \tag{8.8}$$

The modified Friedmann equation then becomes:

$$3FH^2 = (FR - f)/2 - 3H\dot{F} + \kappa^2\rho_m. \tag{8.9}$$

To find solutions for H and R, we follow [99, 157] and introduce new variables, which vanish in the high-redshift limit where $f(R)$ modifications are negligible:

$$y_H \equiv \frac{H^2}{R_c} - a^{-3}, \qquad y_R \equiv \frac{R}{R_c} - 3a^{-3}, \tag{8.10}$$

with R_c given in terms of the average matter-density today $\rho_{m,0}$, by $R_c = \kappa^2\rho_{m,0}/3$. Thus, equations (8.8) and (8.9) are expressed as a set of ordinary differential equations

$$\begin{aligned} y'_H &= \frac{1}{3}y_R - 4y_H, & (8.11)\\ y'_R &= 9a^{-3} & (8.12)\\ &- \frac{1}{y_H + a^{-3}}\frac{1}{R_c f_{,RR}}\left[y_H - (f_{,R} - 1)\left(\frac{1}{6}y_R - y_H - \frac{1}{2}a^{-3} + \frac{1}{6}\frac{f - R}{R_c}\right)\right]. \end{aligned}$$

It may be shown that the expansion history generated by a $f(R)$ model is identical to that of a standard dark-energy model with an effective equation-of-state:

$$1 + w_{\text{eff}} = -\frac{1}{3}\frac{y'_H}{y_H}. \tag{8.13}$$

8.1.2 Scalar perturbations

The evolution of the scalaron field F, is determined from the trace of Equation (8.6)

$$3\,\Box F(R) + F(R)R - 2f(R) = -\kappa^2\rho_m. \tag{8.14}$$

This field equation can be written as a Poisson equation $\Box F(R) = \partial V_{eff}/\partial f_R$, with an effective potential

$$\frac{\partial V_{eff}}{\partial f_R} = \frac{1}{3}\left[2f(R) - F(R)R - \kappa^2\rho_m\right], \tag{8.15}$$

which presents an extremum value located at $2f(R) - F(R)R = \kappa^2\rho_m$.

In the high-density region, where $|F-1| \ll 1$ and $|f-R| \ll 1$, the extremum of the potential defines the time-dependent scalaron mass M_F

$$M_F^2 \equiv \frac{\partial^2 V_{eff}}{\partial f_R^2} = \frac{R}{3}\left(\frac{1}{m}-1\right), \tag{8.16}$$

where $m = Rf_{,RR}/f_{,R}$ characterises the deviation of the background dynamics from the ΛCDM model ($m = 0$ at all times) [10]. Thus, viable $f(R)$ models are constructed such that the scalaron mass M_F is heavy enough in the regime of high matter density and becomes lighter at the present time to produce the accelerated expansion of the Universe. This process may be achieved via a chameleon mechanism [26, 116] ensuring that local gravity constraints are locally satisfied [99, 247]. On the other hand, the evolution of perturbations at linear order lead to expressions for the Newtonian potentials of the form [229]:

$$\frac{k^2}{a^2}\Phi = -\frac{\kappa^2\delta\rho_m}{2F}\frac{2k^2/a^2+3M_F^2}{3k^2/a^2+3M_F^2}, \qquad \frac{k^2}{a^2}\Psi = -\frac{\kappa^2\delta\rho_m}{2F}\frac{4k^2/a^2+3M_F^2}{3k^2/a^2+3M_F^2}. \tag{8.17}$$

It is useful to introduce a function $A(a,k)$ [186] given by the squared ratio of the Compton wavelength to the physical wavelength of a mode:

$$A(a,k) = \left(\frac{k}{aM_F}\right)^2. \tag{8.18}$$

Making a comparison of the equations for Φ and Ψ in (8.17) with those written in (8.2) - (8.3) for μ and γ, one has:

$$\mu(a,k)F = 1+\frac{A(a,k)}{3+3A(a,k)}, \qquad \gamma(a,k) = 1-\frac{2A(a,k)}{3+4A(a,k)}. \tag{8.19}$$

We observe that $f(R)$ models, through $\mu(a,k)$ and $\gamma(a,k)$, predict a characteristic scale-dependent growth of LSS which might be observationally detectable. The impact of the above relations on the evolution of the gravitational potentials and the growth of density perturbations is as follows: for a mode located in the *general relativistic regime* ($A \ll 1$) the scalaron behaves as a massive field making deviations from GR negligible, and the standard relation $\Phi \simeq \Psi$ is thus recovered. On the other hand, when a mode is situated within the *scalar-tensor*

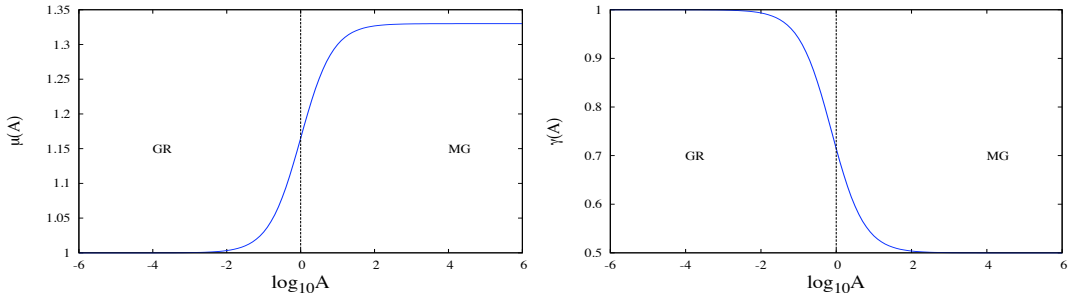

Figure 8.1: Functional behaviour of μ and γ. The vertical line $A(a,k)=1$ represents the transition regime between GR and ST. Left to this line GR is recovered, whereas right to the line the growth of structures is enhanced by modifications of gravity.

regime ($A \gg 1$), the scalaron behaves as a light particle, giving rise to an effective Newtonian constant $G_{\rm eff} = 4/(3F)$, and the relation between the metric potentials becomes $\Phi \simeq \Psi/2$. Therefore, the enhancement of the gravitational potential Ψ increases the growth rate of linear density perturbations on scales below the Compton wavelength [220]. If the transition between these two regimes ($A = 1$) occurred during matter domination, modifications of the observed matter power spectrum might signal deviations from the ΛCDM model [186]. The two regimes are described as follow:

$$\mu \simeq \frac{1}{F}, \quad \gamma \simeq 1, \qquad A \ll 1 \qquad \text{GR}, \tag{8.20}$$

$$\mu \simeq \frac{4}{3F}, \quad \gamma \simeq \frac{1}{2}, \qquad A \gg 1 \qquad \text{ST}. \tag{8.21}$$

Note that the factor F^{-1} corresponds to a rescaling of the Newtonian constant $G_{\rm N}$, for which the value is very close to unity for models that satisfy local and Galactic constraints. Figure 8.1 shows $\mu(A)$ and $\gamma(A)$ functions. The vertical axis represents the amplitude of μ and γ as a function of the squared ratio of the Compton wavelength to the physical wavelength, and the vertical line, $A(a,k)=1$, the transition between the GR and the ST regime. Left of this line the behaviour is well described by (8.20), whereas on the right hand side, the observed enhancement of the growth of structures is described by (8.21).

8.1.3 A particular $f(R)$ model

We have, so far obtained expressions to describe the background evolution (8.13) and the cosmological perturbations (8.19) for a generic $f(R)$ model. Here we consider a particular $f(R)$ model and look at its observables. By construction, we assume $f(R)$ is a well-behaved function, continuous in all its derivatives. It also has to satisfy some further conditions in order to yield to a viable theory [11, 186, 220, 230]: $f_{,R} > 0$ to avoid the appearance of ghosts; $f_{,RR} > 0$ to avoid tachyonic instability; $f(R) \to R - 2\Lambda$ to include phenomenology of ΛCDM as a limiting case, and recover BBN and CMB constraints at early times; $|F_0 - 1| \ll 1$ to satisfy Solar and Galactic constraints. Thus, we focus the study on a version of the Starobinsky model [220]:

$$f(R) = R - \lambda\, R_c \left[1 - \left(1 + \alpha \frac{R}{R_c}\right)^{-n}\right], \tag{8.22}$$

with positive constants λ, α and n, and R given by the solutions of equations (8.8) and (8.9). In the region of high density ($R \gg R_c$), model (8.22) and the Hu & Sawicki model [99] have a similar behaviour. Also model (8.22), with $n = 1$, closely mimics mCDTT [37] plus a cosmological constant, and the inverse squared-curvature model for $n = 2$ [162]. Some other $f(R)$ models with an exponential form [13] may also be considered as viable alternatives.

Given the $f(R)$ model (8.22), we are now able to compute its corresponding effective equation-of-state $w_{\rm eff}(z)$ (8.13), which dominates the dynamics of the late-time expansion rate, and μ, γ (8.19) to describe the perturbations. Another function to bear in mind is the rescaling factor F of the Newtonian constant, given by

$$F(R) - 1 = -\lambda\alpha\, n \left(1 + \alpha \frac{R}{R_c}\right)^{-n-1}. \tag{8.23}$$

An important point to emphasise is the behaviour presented by $|F-1|$: as $R \gg R_c$, $|F - 1|$ becomes negligible, thus approaching the General Relativistic limit. Previous studies have chosen $F_0 = F(t_0)$ as a sampling parameter, although in our case, we consider it more natural to sample over α, with F_0 being a derived parameter. Also notice that at the extremum of the effective potential (8.15), the expansion history can approximate ΛCDM by setting $\lambda \simeq 6\Omega_{\rm eff}/\Omega_m$, with Ω_m an

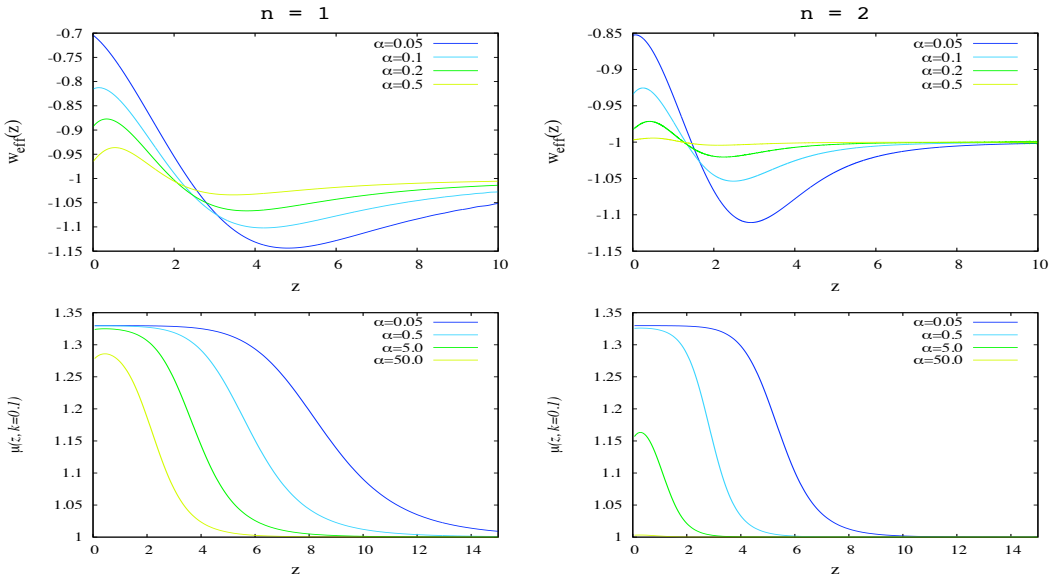

Figure 8.2: Functions used in the description of a modified gravity model, using diffent values of α and n. Effective equation-of-state $w_{\rm eff}$ (top) and the screen mass (bottom) as a function of redshift z, at scale $k = 0.1$.

effective matter density and $\Omega_{\rm eff} = 1 - \Omega_m$.

Hence, for the model (8.22) the effective equation-of-state $w_{\rm eff}$ (8.13) and the squared ratio of the Compton wavelength to the physical wavelength of a mode $A(a, k)$ (8.18) are now parameterised in terms of α, n and the cosmological parameters $\Omega_{m,0}$ and H_0. These parameters together determine the epoch and scale on which modifications to GR may be relevant. In general, having a dependence on space and time makes the analysis more challenging. To understand the relationship of the new parameters with current observations let us consider some particular cases. In Figure 8.2 we show some of the relevant functions which parameterise the MG models using different α values, for $n = 1$ (left panel) and $n = 2$ (right panel); in both cases we have maintained fixed values of $\Omega_{m,0} = 0.25$ and $H_0 = 70$. The top panels show the behaviour of the effective equation-of-state for different values of α. We observe that at the background level, modified gravity models with $\alpha \gtrsim 0.5$ $(n = 1)$ or $\alpha \gtrsim 0.2$ $(n = 2)$ are essentially indistinguishable

from the cosmological constant through current observations [234]. However, at the perturbations level (bottom panel), larger values of α are differentiated by the epoch they cross the regime line $A = 1$, and therefore μ is described by (8.21). A similar interpretation is used for the n parameter: a transition taking place at later times corresponds to higher values of n. One notices the existence of a pronounced degeneracy: for an increment in n, small values of α mimic the same behaviour, for instance, models with $\{n = 1, \alpha = 5\}$ and $\{n = 2, \alpha = 0.5\}$ behave very similar. We also observe that in the limits of $\alpha \gg 1$ and/or high n the phenomenology of ΛCDM is thus recovered. This will be helpful in the choice of an appropriate prior of α, for instance, values of $\alpha > 50$ ($n = 1$) can essentially be considered as the ΛCDM model, similarly for $n = 2$ with $\alpha > 5$. Finally, we emphasise that the screened mass function μ and the gravitational slip parameter γ must equal one, at high redshifts to recover GR. That is, in order to maintain the properties of Big Bang Nucleosynthesis (BBN) at early times, we should impose the condition

$$\mu(z, k) = \gamma(z, k) = 1, \qquad z \gg z_0. \tag{8.24}$$

This condition is translated into $A \ll 1$ at $z \gg z_0$ for the whole range of physically relevant wavenumbers.

8.2 Analysis

We seek to impose constraints on the aforementioned parameterisations from cosmological observables as well as determine which model best describes current data. Since the evolution of matter perturbations and gravitational potentials may differ from standard GR, observations of CMB anisotropy, cosmic evolution and growth of structure are important probes for discriminating amongst modified gravity models. In order to compare the modified gravity influence on observable quantities, such as the CMB, matter power spectrum and luminosity distances, we incorporate μ and γ functions to the standard Boltzmann CAMB code [134] up to $z \sim 30$, when deviations introduced by modified gravity become negligible. Different versions of the Modified CAMB code have also released by

[95, 101, 254]. Also, with the use of a post-Friedmann prescription (PPF) implemented by [71], we have included the effective equation-of-state $w_{\rm eff}$ predicted by a modified gravity model. To constrain the parameter-space, we consider the set observations II introduced in Section 3.4.

The parameterisations of MG models contain the ΛCDM model as a subset in their parameter space, thus the flat priors on the parameters in common are kept identical for each considered case (see Table 3.3). In the MG models we have also included the running parameter $n_{\rm run}$ defined at pivot point $k_0 = 0.015$ Mpc^{-1}. With regards to the additional parameters, we assume three illustrative cases: $n = 1, 2$ with flat priors $\alpha = [0, 5]$ and $\alpha = [0, 50]$ respectively; and varying n within the range $n = [0, 2]$ and $\alpha = [0, 50]$.

8.3 Results

In this section we present the resulting posterior distributions and model evidences computed from the gravity models using our data sets. Despite the additional parameters, the mean values of the standard cosmological parameters remained basically unaffected. That is, their likelihoods peak around standard ΛCDM values, and so we do not consider them further.

We have restricted our analysis to the model presented in (8.22). As we pointed out, this particular parameterisation can be studied in terms of α, n and the cosmological parameters $\Omega_{m,0}$, H_0; although, constraints on H_0 and $\Omega_{m,0}$ present no significant deviations from the ΛCDM model. Figure 8.3 shows 2-D marginalised posterior distributions of the modified gravity parameter α along with the rescaling factor and the effective equation of state at the present time, $|F_0 - 1|$ and $w_{\rm eff,0}$, respectively. The top panel corresponds to $n = 1$, whereas $n = 2$ to bottom panel. We observe that the effective equation-of-state at the present time $w_{\rm eff,0} \equiv w_{\rm eff}(z = 0)$ exhibits only slight deviations from the cosmological constant with $w_{\rm eff,0} < -0.996$ $(n = 1)$ and $w_{\rm eff,0} < -0.997$ $(n = 2)$. At the perturbations level, preferred values of the field amplitude at the present time are $|F_0 - 1| < 0.003$

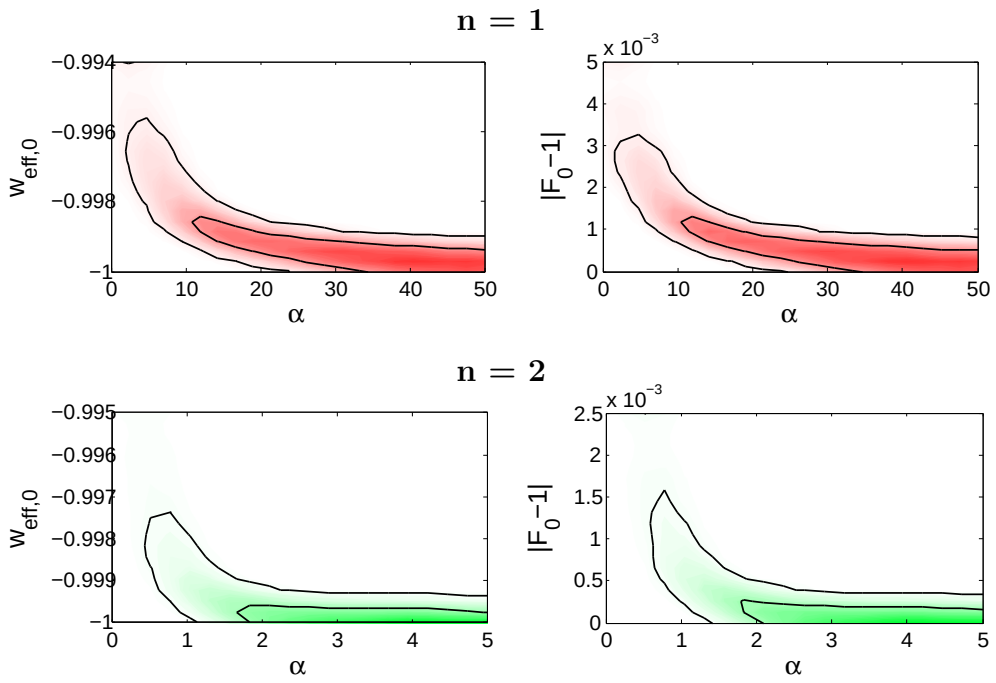

Figure 8.3: 2D Marginalised posterior distributions of sampling parameter α along with derived parameters: the effective equation-of-state $w_{\text{eff},0}$ and the field amplitude $|F_0 - 1|$ at present time; using $n = 1$ (top panels) and $n = 2$ (bottom panels).

($n = 1$), and $|F_0 - 1| < 0.002$ ($n = 2$). Higher values of α may be seen as approaching the ΛCDM model where $|F_0 - 1| \to 0$ and $|w_{\text{eff},0} + 1| \to 0$, as illustrated previously in Figure 8.2. Modified gravity models lead to broader constraints on density fluctuations, σ_8, where higher values are preferred, as shown in Table 8.1. With regards to the case where n is treated as a free parameter, $0 < n < 2$, we observe that constraints on α, $w_{\text{eff},0}$ and $|F_0 - 1|$ are slightly broader: $w_{\text{eff},0} < -0.99$ and $|F_0 - 1| < 0.007$ (see Figure 8.4). Here it is noticeable that higher values of n lead to ΛCDM standard values, for instance, on the behaviour of σ_8 shown in the right panel of Figure 8.4. The summary of the parameter constraints is given in Table 8.1. One-tailed constraints are quoted at 95% C.L. whilst for two tails 68% is shown. We note that similar constraints on λ and $|F_0 - 1|$ have been found by using a subset of the parameter-space and particular values of the wavenumber k [204, 251].

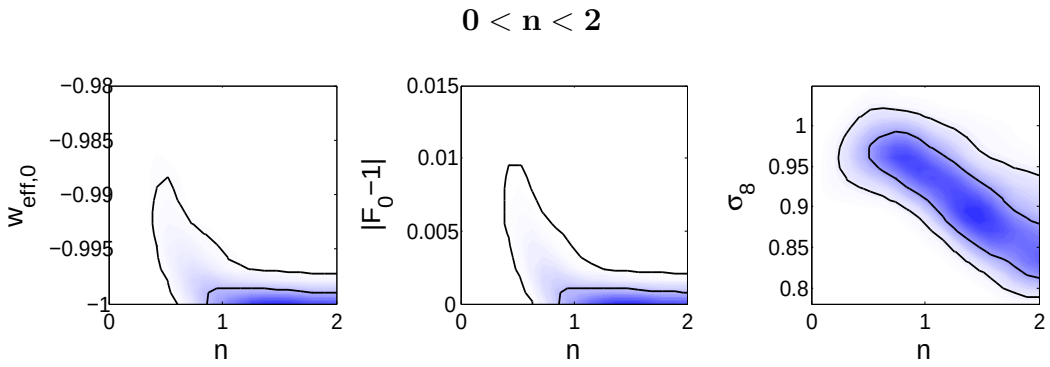

Figure 8.4: 2D Marginalised posterior distributions of sampling parameter α along with the effective equation-of-state $w_{\rm eff,0}$, the field amplitude at the present epoch $|F_0 - 1|$, and the density fluctuations σ_8 in spheres of radius $R = 8h^{-1}$ Mpc.

We have computed the Bayesian evidence for each model to perform a model comparison, according to the Jeffreys guideline. When the set of models are ranked with respect to its Bayesian value, the variously parameterised $f(R)$ models are preferred, despite having extra parameters, when compared to the ΛCDM model. Important attention is paid to the evidence of the $f(R)$ with $n = 2$, which is significantly preferred, $\mathcal{B}_{i,\Lambda} = +1.0 \pm 0.3$, and also presents the largest the difference in the minimum chi-squared, as shown in the last rows of Table 8.1.

8.4 Conclusions

We have undertaken an analysis of modified gravity models by studying its background history as well as linear perturbations. At the background level, the dynamics of $f(R)$ models is encoded in the effective equation-of-state $w_{\rm eff}$, whereas at the perturbations level, it depends on the ratio of the metric potentials μ and the effective gravitational constant γ. Initially, we provided a description for these three functions with a general $f(R)$ model. Then, we use a variant of the Starobinsky model and constrain the parameter-space using current cosmological observations. We have found that constraints on the standard cosmological

Table 8.1: Constraints on modified-gravity parameters. For one-tailed distributions, the upper limit 95% CL is given. For two-tailed the 68 % is shown.

	ΛCDM	$n = 1$	$n = 2$	$0 < n < 2$
α	–	> 0.7	> 0.4	unconstrained
n	–	–	–	> 0.53
λ	–	15.8 ± 1.3	15.6 ± 1.3	15.4 ± 1.4
H_0	68.5 ± 1.4	69.7 ± 1.4	69.6 ± 1.4	69.4 ± 1.4
$\Omega_{m,0}$	0.293 ± 0.017	0.276 ± 0.017	0.278 ± 0.016	0.281 ± 0.018
σ_8	0.819 ± 0.019	0.945 ± 0.027	0.914 ± 0.032	0.915 ± 0.049
$w_{\mathrm{eff},0}$	–	< -0.996	< -0.998	< -0.99
$\lvert F_0 - 1 \rvert$	–	< 0.003	< 0.002	< 0.007
$-2 \ln \mathcal{L}_{\max}$	8238.94	8238.72	8237.73	8238.45
$\mathcal{B}_{i,\Lambda}$	0.0 ± 0.3	$+0.5 \pm 0.3$	$+1.0 \pm 0.3$	$+0.8 \pm 0.3$

parameters are largely unaffected by the introduction of these three effective functions. That is, best-fit values for the standard parameters shift by less than 1σ. The only notable exception is σ_8, whose marginalised uncertainties increase by up to a factor of two upon the introduction of extra parameters. This is consistent with the observation that μ and γ principally modify the growth history of cosmological perturbations. Figure 8.5 shows the reconstructed w_{eff} and μ at $k = 0.1$, from the posterior samples in the region (2σ) using the best-fit values. We observe that measurements on the screen mass function present slightly deviations from unity at the latest times ($z < 2$), but is still consistent with $\mu = \gamma = 1$. Deviation from $\mu = 1$ increases at smaller scales (larger k), however at the smallest scales non-linear physics plays an important role and linear perturbation theory is no longer valid. We used a Bayesian criterion to carry out cosmological model selection and found, in the sense of Jeffreys guideline, that the variant of the Starobinsky $f(R)$ model with $n = 2$ is significantly preferred through its Bayes factor, and also presents the best-fit of all the models, although the differences in log-likelihoods are small.

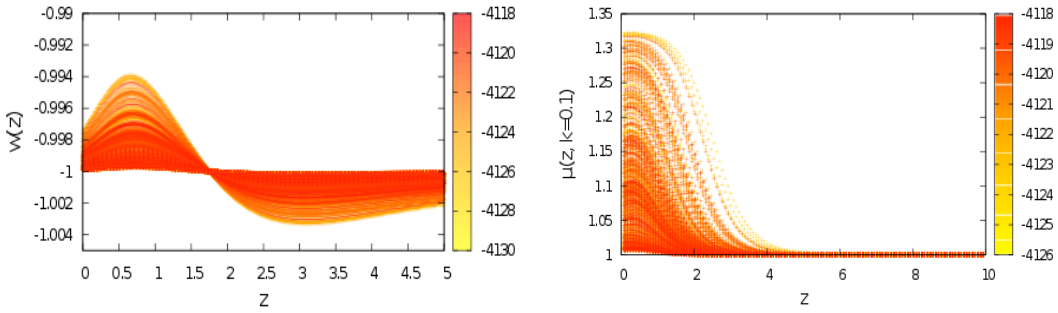

Figure 8.5: Reconstruction of the effective equation-of-state $w_{\rm eff}$ and screen mass function μ, using best-fit values obtained in the analysis, for a $f(R)$ with $n = 2$. The colour-code indicates the ln(Likelihood), where darker regions represent an improved fit.

Chapter 9

Conclusions

The best model in agreement with present data is given by, so far, the concordance ΛCDM model. However this model might not be the final one and several extensions have already been implemented. In this work, given current cosmological observations and using the Bayesian evidence as an implementation of Occam's razor, we have developed a model-independent reconstruction to determine the optimal shape of the primordial power spectrum and the dark energy equation-of-state. We have found the preferred primordial spectrum exhibits a fall-off at large scales and a reduced power at small scales; the turn-over in the initial scalar spectrum is enhanced when a tensor component is included in the analysis. With regards to the dark energy equation-of-state, we have obtained results generally consistent with the cosmological constant scenario, however the dark energy does seem to exhibit a temporal evolution, although very weak. In the search of a better description of cosmological observations, we have also incorporated features beyond the standard ΛCDM model: a second dark energy component, and modifications to the laws of gravity at cosmological scales. These models have a similar Bayesian evidence to ΛCDM to within the numerical uncertainty, and hence describe current data equally well.

Determining the main properties of both the primordial spectra and the dark energy equation-of-state is one of the biggest challenges of observational cosmology today, as it requires precise measurements of the expansion history and the growth-rate of structure in the universe. An impressive set of high accuracy sur-

veys are underway, or have been planned, to constrain the dynamical properties of the universe and hence the search of possible signatures for new cosmology. For instance, the Planck satellite will significantly improve measurements on the E and B polarisation modes; the Euclid satellite will explore the expansion history of the universe and the evolution of cosmic structures over a very large fraction of the sky; the Dark Energy Survey will probe the origin of the accelerating universe and help uncover the nature of dark energy. The improved data, along with advanced statistical techniques, will therefore provide a more accurate description of the universe and narrow down the list of candidates in best agreement with experimental observations.

Appendix A

Cubic spline interpolated spectrum

In this appendix we illustrate how the type of interpolation in our node-based approach can influence the reconstruction of the primordial spectrum. We use the same example shown in Figure 4.9 but now we use a cubic spline to interpolate through the k-nodes. From Figure A.1 we note that the spectrum used as an input lies well outside the error bar on the reconstruction at low k-values. Therefore, the spline fails to recover the input spectrum correctly, contrary to the linear interpolation where the recovered spectrum, shown in Figure 4.9, is more representative, with the true spectrum lying comfortably within the error-bars on the reconstruction at all k-values. This is mainly because a function with rapidly changing higher derivatives, such as the input primordial spectrum used here, is less accurately approximated by higher order polynomials. In particular, the requirement of continuous first and second derivatives, combined with the tight constraints at small and intermediate length scales, leads to a significant overestimation of the power at the less well constrained region at the largest scales. Hence, in this case, the linear interpolation describes the shape of the primordial spectrum better than the spline.

For comparison with the results presented earlier, we also use the cubic spline to perform similar node-based reconstructions of the spectrum to those shown in

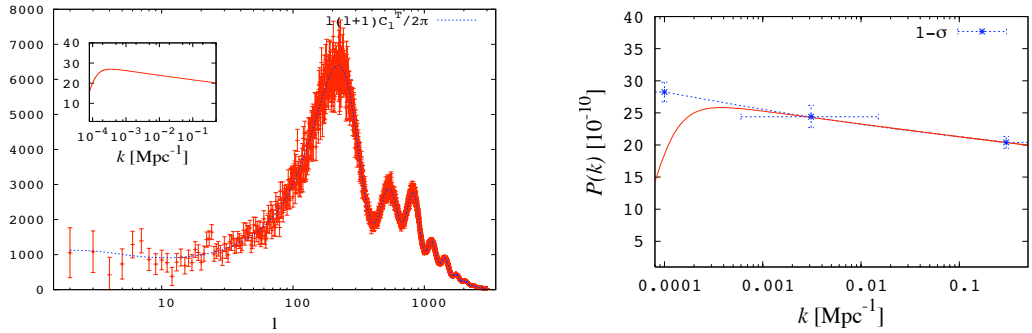

Figure A.1: Reconstruction of the Lasenby & Doran primordial scalar spectrum based on the binning format with cubic spline described in Section 4.1.2. We have assumed an idealised CMB spectrum with limitation only due cosmic variance (left). Right panel shows the reconstructed spectrum in the binning format together with the LD input spectrum.

Figures 4.1 and 4.2. The low number of bins used to describe the global structure of the spectrum yield to similar shapes by using both interpolation methods. The reconstructed spectra for three and four bins, along with one and two internal k-nodes, are plotted in Figure A.2 using the spline interpolation.

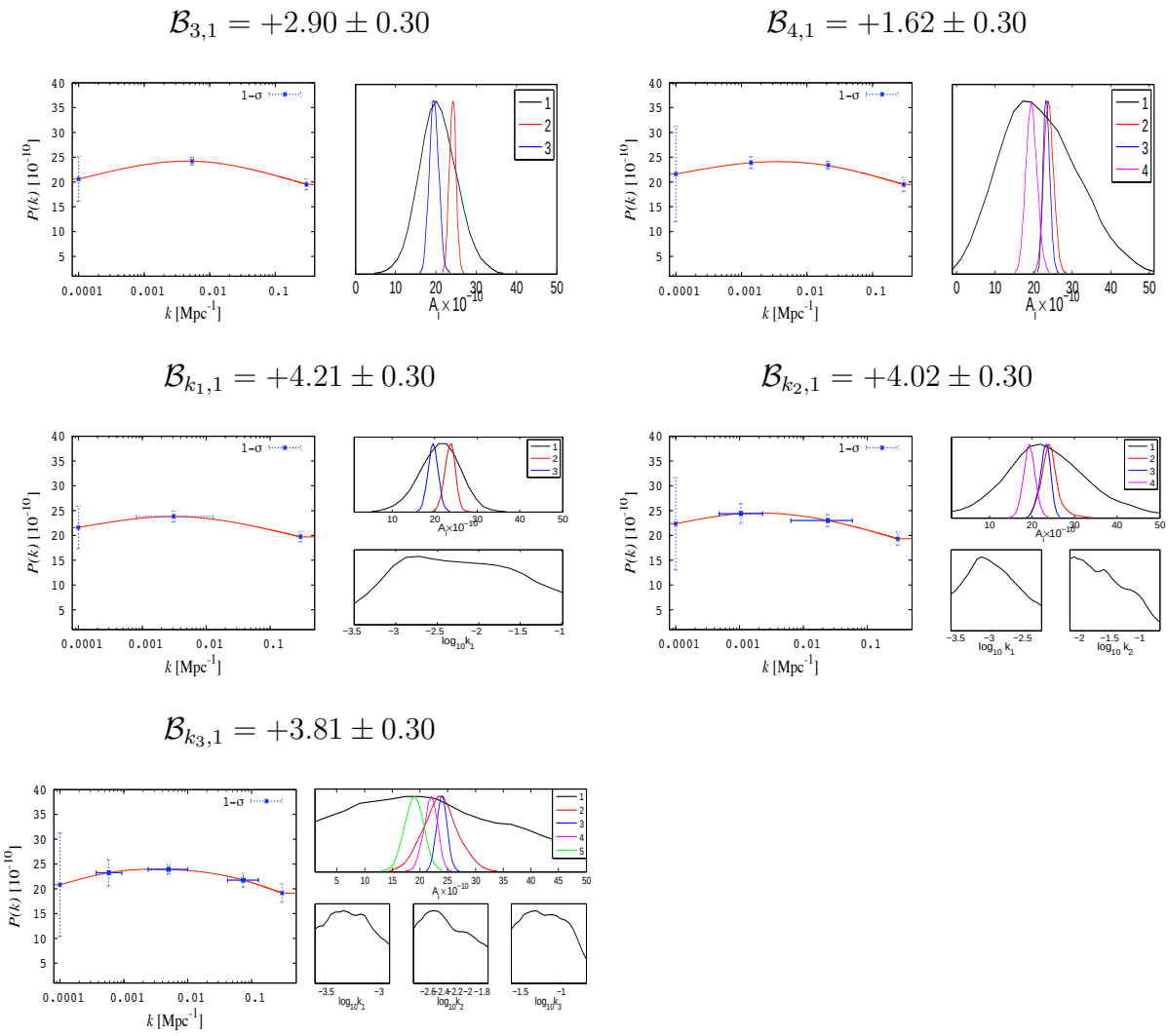

Figure A.2: Reconstruction of the primordial scalar spectrum using the cubic spline. Top panel resembles plots (b) and (c) shown in Figure 4.1, whereas bottom panel the reconstruction for the models shown in Figure 4.2. To the right of each reconstruction we plot the 1D marginalised posterior distribution of the amplitudes A_i and k-node position k_i. The top label in each panel denotes the associated Bayes factor with respect to the base model (HZ) shown in Figure 4.1 (a).

A. CUBIC SPLINE INTERPOLATED SPECTRUM

Appendix B

Gauge invariant quantities

The gauge invariant energy-momentum perturbations, following Doran [63], Durrer [65], are defined by

$$
\begin{aligned}
V &\equiv v - \frac{1}{k}\dot{H}_T = v^{(\mathrm{longit})}, && \text{(B.1)}\\
D_g &\equiv \delta + 3(1+w)\left(H_L + \frac{1}{3}H_T\right), && \text{(B.2)}\\
&= \delta^{(\mathrm{longit})} + 3(1+w)\Phi, && \text{(B.3)}\\
D &\equiv \delta^{(\mathrm{longit})} + 3(1+w)\frac{a'}{a}\frac{V}{k}, && \text{(B.4)}\\
\Gamma &\equiv \pi_L - \frac{c_\mathrm{s}^2}{w}\delta. && \text{(B.5)}
\end{aligned}
$$

where (longit) labels perturbations in the longitudinal gauge.

Einstein's equations in gauge invariant variables become:

$$
\begin{aligned}
4\pi G\, a^2 \bar{\rho} D &= k^2\Phi, && \text{(B.6)}\\
4\pi G\, a^2(\bar{\rho}+\bar{p})V &= k\left(\frac{a'}{a}\Psi - \Phi'\right), && \text{(B.7)}\\
8\pi G\, a^2 \bar{p}\Pi &= -k^2(\Phi+\Psi), && \text{(B.8)}
\end{aligned}
$$

and the energy-momentum conservation:

$$D_g' + 3(c_s^2 - w)\frac{a'}{a}D_g + kV(1+w) + 3\frac{a'}{a}w\Gamma = 0, \tag{B.9}$$

$$V' = \frac{a'}{a}(3c_s^2 - 1)V + k[\Psi - 3c_s^2\Phi] + \frac{c_s^2 k}{1+w}D_g + \frac{wk}{1+w}\left[\Gamma - \frac{2}{3}\Pi\right]. \tag{B.10}$$

The gauge invariant expression for the *comoving curvature perturbation* is given by

$$\mathcal{R} = H_L + \frac{1}{3}H_T + \frac{a'}{ak}(V - B). \tag{B.11}$$

This is the perturbation to the intrinsic curvature scalar of comoving hypersurfaces: hypersurfaces orthogonal to the worldlines that comove with the total matter ($v_i = 0$) [39]. For a universe dominated by a scalar field, $\mathcal{R}$ in gauge invariant form can be written as

$$\mathcal{R} = H_L + \frac{1}{3}H_T - \frac{a'}{a}\frac{\delta\phi}{\bar{\phi}'}. \tag{B.12}$$

Bibliography

[1] N. Aghanim, S. Majumdar, and J. Silk. Secondary anisotropies of the CMB. Reports on Progress in Physics, 71(6):066902, 2008. 45

[2] C. P. Ahn et al. The Ninth Data Release of the Sloan Digital Sky Survey: First Spectroscopic Data from the SDSS-III Baryon Oscillation Spectroscopic Survey. Astrophys.J.Suppl., 203:21, 2012. 60

[3] Ö. Akarsu and C. Klnç. Bianchi type III models with anisotropic dark energy. General Relativity and Gravitation, 42:763–775, 2010. 10.1007/s10714-009-0878-7. 113

[4] J. Akeret, S. Seehars, A. Amara, A. Refregier, and A. Csillaghy. CosmoHammer: Cosmological parameter estimation with the MCMC Hammer. 2012. [arXiv:1212.1721]. 64

[5] U. Alam, V. Sahni, T. Deep Saini, and A. A. Starobinsky. Exploring the expanding Universe and dark energy using the statefinder diagnostic. Monthly Notices of the Royal Astronomical Society, 344(4):1057–1074, 2003. 114

[6] U. Alam, V. Sahni, T. Deep Saini, and A. A. Starobinsky. Is there supernova evidence for dark energy metamorphosis? Monthly Notices of the Royal Astronomical Society, 354(1):275–291, 2004. 114

[7] U. Alam, V. Sahni, and A. A. Starobinsky. Exploring the properties of dark energy using type-Ia supernovae and other datasets. Journal of Cosmology and Astroparticle Physics, 2007(02):011, 2007. 114, 147

[8] R. Amanullah and *et. al.* Spectra and Hubble Space Telescope Light Curves of Six Type Ia Supernovae at $0.511 < z < 1.12$ and the Union2 Compilation. The Astrophysical Journal, 716(1):712, 2010. 60

[9] Ambrosio and *et. al.* Final results of magnetic monopole searches with the macro experiment. The European Physical Journal C - Particles and Fields, 25(4):511–522, 2002. 23

[10] L. Amendola, G. C. Campos, and R. Rosenfeld. Consequences of dark matter-dark energy interaction on cosmological parameters derived from type Ia supernova data. Phys. Rev. D, 75:083506, Apr 2007. 113, 152

[11] L. Amendola, R. Gannouji, D. Polarski, and S. Tsujikawa. Conditions for the cosmological viability of $f(R)$ dark energy models. Phys. Rev. D, 75: 083504, Apr 2007. 154

[12] L. Amendola, M. Kunz, and D. Sapone. Measuring the dark side (with weak lensing). Journal of Cosmology and Astroparticle Physics, 2008(04): 013, 2008. 148

[13] S. A. Appleby and R. A. Battye. Do consistent models mimic general relativity plus Λ? Physics Letters B, 654(1–2):7 – 12, 2007. 113, 117, 147, 154

[14] C. Armendariz-Picon, V. Mukhanov, and P. J. Steinhardt. Dynamical Solution to the Problem of a Small Cosmological Constant and Late-Time Cosmic Acceleration. Phys. Rev. Lett., 85:4438–4441, Nov 2000. 113, 147

[15] T. Auld, M. Bridges, and M. P. Hobson. Cosmonet: fast cosmological parameter estimation in non-flat models using neural networks. Monthly Notices of the Royal Astronomical Society, 387(4):1575–1582, 2008. 68

[16] B-Pol Collaboration.*http://www.b-pol.org/documents.php*, 2010. 61, 63

[17] J. M. Bardeen. Gauge-invariant cosmological perturbations. Phys. Rev. D, 22:1882–1905, Oct 1980. 30, 33

[18] J. Barriga, E. Gaztañaga, M. Santos, and S. Sarkar. On the APM power spectrum and the CMB anisotropy: evidence for a phase transition during inflation? Monthly Notices of the Royal Astronomical Society, 324(4):977–987, 2001. 75, 81, 83

[19] B. A. Bassett, P. S. Corasaniti, and M. Kunz. The Essence of Quintessence and the Cost of Compression. The Astrophysical Journal Letters, 617(1): L1, 2004. 113

[20] R. A. Battye, M. Bucher, and D. Spergel. Domain Wall Dominated Universes. [arXiv:9908047]. 13, 129

[21] D. Baumann. Cosmological Inflation: Theory and Observations. Advanced Science Letters, 2(2):105–120, 2009. 20, 28

[22] G. Bertone, D. Hooper, and J. Silk. Particle dark matter: evidence, candidates and constraints. Physics Reports, 405(5–6):279 – 390, 2005. 12

[23] B. Boisseau, G. Esposito-Farèse, D. Polarski, and A. A. Starobinsky. Reconstruction of a Scalar-Tensor Theory of Gravity in an Accelerating Universe. Phys. Rev. Lett., 85:2236–2239, Sep 2000. 117

[24] M. Bowden and et. al. Scientific optimization of a ground-based CMB polarization experiment. Monthly Notices of the Royal Astronomical Society, 349(1):321–335, 2004. 62

[25] D. Branch and G. A. Tammann. Type Ia Supernovae as Standard Candles. Annual Review of Astronomy and Astrophysics, 30(1):359–389, 1992. 59

[26] P. Brax, C. van de Bruck, A.-C. Davis, and D. J. Shaw. $f(R)$ gravity and chameleon theories. Phys. Rev. D, 78:104021, Nov 2008. 152

[27] M. Bridges, A. N. Lasenby, and M. P. Hobson. A Bayesian analysis of the primordial power spectrum. Monthly Notices of the Royal Astronomical Society, 369(3):1123–1130, 2006. 67, 75

[28] M. Bridges, A. N. Lasenby, and M. P. Hobson. WMAP 3-yr primordial power spectrum. Monthly Notices of the Royal Astronomical Society, 381 (1):68–74, 2007. 75

[29] M. Bridges, F. Feroz, M. P. Hobson, and A. N. Lasenby. Bayesian optimal reconstruction of the primordial power spectrum. [arXiv:0812.3541], 2008. 75

[30] S. L. Bridle, A. M. Lewis, J. Weller, and G. Efstathiou. Reconstructing the primordial power spectrum. Monthly Notices of the Royal Astronomical Society, 342(4):L72–L78, 2003. 75, 83

[31] M. L. Brown and et. al. Improved Measurements of the Temperature and Polarization of the Cosmic Microwave Background from QUaD. The Astrophysical Journal, 705(1):978, 2009. 57, 70

[32] C. Burigana, C. Destri, H. J. de Vega, and et al. Forecast for the planck precision on the tensor-to-scalar ratio and other cosmological parameters. The Astrophysical Journal, 724(1):588, 2010. 101

[33] S. Burles, K. M. Nollett, and M. S. Turner. Big Bang Nucleosynthesis Predictions for Precision Cosmology. The Astrophysical Journal Letters, 552(1):L1, 2001. 70, 144

[34] R. R. Caldwell, R. Dave, and P. J. Steinhardt. Cosmological Imprint of an Energy Component with General Equation of State. Phys. Rev. Lett., 80: 1582–1585, Feb 1998. 113, 130

[35] S. Capozziello. Curvature quintessence. Int.J.Mod.Phys., D11:483–492, 2002. 113

[36] S. M. Carroll. The Cosmological Constant. Living Reviews in Relativity, 4 (1), 2001. 8, 12, 147

[37] S. M. Carroll, V. Duvvuri, M. Trodden, and M. S. Turner. Is cosmic speed-up due to new gravitational physics? Phys. Rev. D, 70:043528, Aug 2004. 154

[38] J. L. Cervantes-Cota, R. de Putter, and E. V. Linder. Induced gravity and the attractor dynamics of dark energy/dark matter. Journal of Cosmology and Astroparticle Physics, 2010(12):019, 2010. 113

[39] A. Challinor. Part III- Large Scale Strucutre Formation. *http://nefertiti.hpc.phys.ucl.ac.uk/cosmology/cosmology.html*, 2008. 5, 30, 41, 44, 170

[40] A. Challinor and H. Peiris. Lecture notes on the physics of cosmic microwave background anisotropies. AIP Conference Proceedings, 1132(1): 86–140, 2009. 44, 45

[41] M. Chevallier and D. Polarski. Accelerating Universes with Scaling Dark Matter. International Journal of Modern Physics D, 10(2):213–223, 2001. 113, 121, 134

[42] H. C. Chiang and et. al. Measurement of Cosmic Microwave Background Polarization Power Spectra from Two Years of BICEP Data. The Astrophysical Journal, 711(2):1123, 2010. 56, 70

[43] T. Chiba and T. Nakamura. Feasibility of reconstructing the quintessential potential using type Ia supernova data. Phys. Rev. D, 62:121301, Nov 2000. 114, 147

[44] L. P. Chimento, R. Lazkoz, R. Maartens, and I. Quiros. Crossing the phantom divide without phantom matter. Journal of Cosmology and Astroparticle Physics, 2006(09):004, 2006. 117

[45] T. Clemson, K. Koyama, G.-B. Zhao, R. Maartens, and J. Väliviita. Interacting dark energy: Constraints and degeneracies. Phys. Rev. D, 85:043007, Feb 2012. 113

[46] S. Cole and *et. al.* The 2dF Galaxy Redshift Survey: power-spectrum analysis of the final data set and cosmological implications. Monthly Notices of the Royal Astronomical Society, 362(2):505–534, 2005. 6

[47] P. Coles and F. Lucchin. Cosmology. WILEY, 1995. 23

[48] C. R. Contaldi, M. Peloso, L. Kofman, and A. Linde. Suppressing the lower multipoles in the CMB anisotropies. Journal of Cosmology and Astroparticle Physics, 2003(07):002, 2003. 81

[49] L. Conversi, A. Melchiorri, L. Mersini, and J. Silk. Are domain walls ruled out? Astroparticle Physics, 21(4):443 – 449, 2004. 129

[50] E. Copeland, M. Sami, and S. Tsujikawa. Dynamics of Dark Energy. International Journal of Modern Physics D, 15(11):1753–1935, 2006. 129, 147

[51] M. Cortês, A. R. Liddle, and P. Mukherjee. On what scale should inflationary observables be constrained? Phys. Rev. D, 75:083520, Apr 2007. 85

[52] M. Cortês, A. R. Liddle, and P. Mukherjee. On what scale should inflationary observables be constrained? Phys. Rev. D, 75:083520, Apr 2007. 100, 103

[53] M. Cortês, A. R. Liddle, and D. Parkinson. On the prior dependence of constraints on the tensor-to-scalar ratio. Journal of Cosmology and Astroparticle Physics, 2011(09):027, 2011. 53, 101

[54] B. P. Crill and *et. al.* SPIDER: a balloon-borne large-scale CMB polarimeter. Proc. SPIE 7010, Space Telescopes and Instrumentation 2008, pages 70102P–70102P–12, 2008. 61

[55] R. A. Daly and S. G. Djorgovski. A Model-Independent Determination of the Expansion and Acceleration Rates of the Universe as a Function of Redshift and Constraints on Dark Energy. The Astrophysical Journal, 597 (1):9, 2003. 114

[56] A. de Felice, S. Nesseris, and S. Tsujikawa. Observational constraints on dark energy with a observational constraints on dark energy with a fast varying equation of state. [arXiv:1203.6760], 2012. 113, 124

[57] A. de la Macorra. Scalar Field Dark Energy Parametrization. [arXiv:1108.0876], 2011. 113

[58] R. de Putter and E. V. Linder. To bin or not to bin: Decorrelating the cosmic equation of state. Astroparticle Physics, 29(6):424 – 441, 2008. 114

[59] C. Deffayet, O. Pujolàs, I. Sawicki, and A. Vikman. Imperfect dark energy from kinetic gravity braiding. Journal of Cosmology and Astroparticle Physics, 2010(10):026, 2010. 117

[60] S. Dodelson. Modern Cosmology. Academic Press, 2003. 5, 18, 30, 47

[61] A. Dolgov. Neutrinos in cosmology. Physics Reports, 370:333 – 535, 2002. 11

[62] M. Doran. CMBEASY: an object oriented code for the cosmic microwave background. Journal of Cosmology and Astroparticle Physics, 2005(10): 011, 2005. 38, 64

[63] M. Doran. The Theory of the Cosmic Microwave Background. *http://www.thphys.uni-heidelberg.de/ cosmo/view/main/cmbdoran*, 2010. 30, 32, 34, 36, 38, 44, 169

[64] J. Dunkley and *et. al.* The Atacama Cosmology Telescope: Cosmological Parameters from the 2008 Power Spectra. [arXiv:1009.0866], 2010. 57, 70, 75, 79, 85, 101

[65] R. Durrer. The theory of CMB anisotropies. [arXiv:0109522], 2001. 30, 32, 169

[66] R. Durrer and R. Maartens. Dark energy and dark gravity: theory overview. General Relativity and Gravitation, 40:301–328, 2008. 10.1007/s10714-007-0549-5. 129, 147

[67] G. Dvali, G. Gabadadze, and M. Porrati. 4D gravity on a brane in 5D Minkowski space. Physics Letters B, 485(1–3):208 – 214, 2000. 147

[68] G. Efstathiou. Is the low cosmic microwave background quadrupole a signature of spatial curvature? Monthly Notices of the Royal Astronomical Society, 343(4):L95–L98, 2003. 75

[69] Ø. Elgarøy and O. Lahav. Neutrino masses from cosmological probes. New Journal of Physics, 7(1):61, 2005. 11

[70] Euclid Missin Consortium.*http://www.euclid-ec.org/*, 2012. 61

[71] W. Fang, W. Hu, and A. Lewis. Crossing the phantom divide with parametrized post-Friedmann dark energy. Phys. Rev. D, 78:087303, Oct 2008. 114, 134, 157

[72] A. D. Felice and S. Tsujikawa. f(R) Theories. Living Reviews in Relativity, 13(3), 2010. 147, 149

[73] F. Feroz and M. P. Hobson. Multimodal nested sampling: an efficient and robust alternative to Markov Chain Monte Carlo methods for astronomical data analyses. Monthly Notices of the Royal Astronomical Society, 384(2): 449–463, 2008. 68, 71

[74] F. Feroz, M. P. Hobson, and M. Bridges. MultiNest: an efficient and robust Bayesian inference tool for cosmology and particle physics. Monthly Notices of the Royal Astronomical Society, 398(4):1601–1614, 2009. 68

[75] E. E. Flanagan. Palatini Form of $1/R$ Gravity. Phys. Rev. Lett., 92:071101, Feb 2004. 149

[76] J. A. Frieman and *et. al.* The Sloan Digital Sky Survey-II Supernova Survey: Technical Summary. The Astronomical Journal, 135(1):338, 2008. 59

[77] T. Giannantonio, M. Martinelli, A. Silvestri, and A. Melchiorri. New constraints on parametrised modified gravity from correlations of the CMB with large scale structure. Journal of Cosmology and Astroparticle Physics, 2010(04):030, 2010. 148

[78] Y. Gong and X. Chen. Two-component model of dark energy. Phys. Rev. D, 76(12):123007, Dec. 2007. 132, 134

[79] Y. Gong, R.-G. Cai, Y. Chen, and Z.-H. Zhu. Observational constraint on dynamical evolution of dark energy. Journal of Cosmology and Astroparticle Physics, 2010(01):019, 2010. 114, 119, 147

[80] P. Graff, F. Feroz, M. P. Hobson, and A. Lasenby. BAMBI: blind accelerated multimodal Bayesian inference. Monthly Notices of the Royal Astronomical Society, 421(1):169–180, 2012. 68

[81] Z.-K. Guo and Y.-Z. Zhang. Uncorrelated estimates of the primordial power spectrum. Journal of Cosmology and Astroparticle Physics, 2011(11):032, 2011. 75, 81, 110

[82] Z.-K. Guo, D. J. Schwarz, and Y.-Z. Zhang. Reconstruction of the primordial power spectrum from CMB data. Journal of Cosmology and Astroparticle Physics, 2011(08):031, 2011. 75, 80, 110

[83] G. Gupta, E. N. Saridakis, and A. A. Sen. Nonminimal quintessence and phantom with nearly flat potentials. Phys. Rev. D, 79:123013, Jun 2009. 113

[84] A. Guth. The Inflationary Universe. Ed. Vintage, 1997. 22

[85] A. H. Guth. Inflationary universe: A possible solution to the horizon and flatness problems. Phys. Rev. D, 23:347–356, Jan 1981. 20

[86] J. Hamann, A. Shafieloo, and T. Souradeep. Features in the primordial power spectrum? A frequentist analysis. Journal of Cosmology and Astroparticle Physics, 2010(04):010, 2010. 75

[87] S. Hannestad. Primordial Neutrinos. Annual Review of Nuclear and Particle Science, 56(1):137–161, 2006. 11

[88] S. Hannestad and E. Mörtsell. Cosmological constraints on the dark energy equation of state and its evolution. Journal of Cosmology and Astroparticle Physics, 2004(09):001, 2004. 113

[89] A. Heavens. Statistical techniques in cosmology. [arXiv:0906.0664], 2010. 63

[90] G. Hinshaw and *et. al.* Nine-Year Wilkinson Microwave Anisotropy Probe (WMAP) Observations: Cosmological Parameter Results. [arXiv:1212.5226], 2013. 56

[91] R. Hlozek and *et. al.* The Atacama Cosmology Telescope: a measurement of the primordial power spectrum. [arXiv:1105.4887], 2011. 60, 61, 75

[92] M. Hobson, G. P. Efstathiou, and A. N. Lasenby. General Relativity: An Introduction for Physicists. Cambridge University Press, 2006. 5, 18

[93] M. P. Hobson and C. McLachlan. A Bayesian approach to discrete object detection in astronomical data sets. Monthly Notices of the Royal Astronomical Society, 338(3):765–784, 2003. 66

[94] M. P. Hobson, S. L. Bridle, and O. Lahav. Combining cosmological data sets: hyperparameters and bayesian evidence. Monthly Notices of the Royal Astronomical Society, 335(2):377–388, 2002. 68, 143

[95] A. Hojjati, L. Pogosian, and G.-B. Zhao. Testing gravity with CAMB and CosmoMC. Journal of Cosmology and Astroparticle Physics, 2011(08):005, 2011. 157

[96] T. Holsclaw, U. Alam, B. Sansó, H. Lee, K. Heitmann, S. Habib, and D. Higdon. Nonparametric Dark Energy Reconstruction from Supernova Data. Phys. Rev. Lett., 105:241302, Dec 2010. 114

[97] T. Holsclaw, U. Alam, B. Sansó, H. Lee, K. Heitmann, S. Habib, and D. Higdon. Nonparametric reconstruction of the dark energy equation of state. Phys. Rev. D, 82:103502, Nov 2010. 114

[98] W. Hu and S. Dodelson. COSMIC MICROWAVE BACKGROUND ANISOTROPIES. Annual Review of Astronomy and Astrophysics, 40(1): 171–216, 2002. 30

[99] W. Hu and I. Sawicki. Models of $f(R)$ cosmic acceleration that evade solar system tests. Phys. Rev. D, 76:064004, Sep 2007. 113, 117, 147, 151, 152, 154

[100] W. Hu, U. c. v. Seljak, M. White, and M. Zaldarriaga. Complete treatment of CMB anisotropies in a FRW universe. Phys. Rev. D, 57:3290–3301, Mar 1998. 37

[101] J. hua He. Testing $f(R)$ dark energy model with the large scale structure. [arXiv:1207.4898], 2012. 157

[102] E. Hubble. A relation between distance and radial velocity among extra-galactic nebulae. Proceedings of the National Academy of Sciences, 15(3): 168–173, 1929. 6, 19

[103] D. Huterer and A. Cooray. Uncorrelated estimates of dark energy evolution. Phys. Rev. D, 71:023506, Jan 2005. 114

[104] D. Huterer and G. Starkman. Parametrization of Dark-Energy Properties: A Principal-Component Approach. Phys. Rev. Lett., 90:031301, Jan 2003. 114

[105] D. Huterer and M. S. Turner. Probing dark energy: Methods and strategies. Phys. Rev. D, 64:123527, Nov 2001. 114

[106] M. Ibison. An Exploration of Symmetries in the Friedmann Equation. [arXiv:1106.3783], 06 2011. 129, 130, 131

[107] K. Ichiki, R. Nagata, and J. Yokoyama. Cosmic discordance: Detection of a modulation in the primordial fluctuation spectrum. Phys. Rev. D, 81: 083010, Apr 2010. 75

[108] Ishida, E. E. O. and de Souza, R. S. Hubble parameter reconstruction from a principal component analysis: minimizing the bias. A&A, 527:A49, 2011. 114

[109] A. Jaffe. H0 and odds on cosmology. The Astrophysical Journal, 471(1): 24, 1996. 66

[110] B. Jain and P. Zhang. Observational tests of modified gravity. Phys. Rev. D, 78:063503, Sep 2008. 148

[111] H. K. Jassal, J. S. Bagla, and T. Padmanabhan. WMAP constraints on low redshift evolution of dark energy. Monthly Notices of the Royal Astronomical Society: Letters, 356(1):L11–L16, 2005. 113, 121, 134

[112] H. Jeffreys. Theory of Probability. Oxford University Press, 1998. 67, 138

[113] M. V. John and J. V. Narlikar. Comparison of cosmological models using Bayesian theory. Phys. Rev. D, 65:043506, Jan 2002. 66

[114] W. C. Jones and *et. al.* A Measurement of the Angular Power Spectrum of the CMB Temperature Anisotropy from the 2003 Flight of BOOMERANG. The Astrophysical Journal, 647(2):823, 2006. 57

[115] R. Keisler and *et. al.* A Measurement of the Damping Tail of the Cosmic Microwave Background Power Spectrum with the South Pole Telescope. [arXiv:1105.3182], 2011. 57, 75, 85, 101

[116] J. Khoury and A. Weltman. Chameleon Fields: Awaiting Surprises for Tests of Gravity in Space. Phys. Rev. Lett., 93:171104, Oct 2004. 152

[117] M. Kilbinger, K. Benabed, O. Cappe, J.-F. Cardoso, G. Fort, et al. CosmoPMC: Cosmology Population Monte Carlo. arXiv:1101.0950, 2011. 68

[118] C. Knobel. An introduction into the theory of cosmological structure formation. 2012. [arXiv:1208.5931]. 30

[119] H. Kodama and M. Sasaki. Cosmological Perturbation Theory. Progress of Theoretical Physics Supplement, 78:1–166, 1984. 30

[120] E. Komatsu and *et. al.* Seven-year Wilkinson Microwave Anisotropy Probe (WMAP) Observations: Cosmological Interpretation. The Astrophysical Journal Supplement Series, 192(2):18, 2011. 6, 21, 56, 70, 75, 85, 92, 101

[121] A. Kosowsky, M. Milosavljevic, and R. Jimenez. Efficient cosmological parameter estimation from microwave background anisotropies. Phys. Rev. D, 66:063007, Sep 2002. 52

[122] M. Kowalski and *et. al.* Improved Cosmological Constraints from New, Old, and Combined Supernova Data Sets. The Astrophysical Journal, 686(2): 749, 2008. 60, 70

[123] H. Kurki-Suonio. Cosmological Perturbation Theory. *http://www.helsinki.fi/∼hkurkisu/*, 2008. 30

[124] O. Lahav and A. R. Liddle. The Cosmological Parameters 2010. 2010. [arXiv:1207.4898]. 50

[125] D. Larson and *et. al.* Seven-year Wilkinson Microwave Anisotropy Probe (WMAP) Observations: Power Spectra and WMAP-derived Parameters. The Astrophysical Journal Supplement Series, 192(2):16, 2011. 21, 22, 56

[126] A. Lasenby and C. Doran. Closed universes, de Sitter space, and inflation. Phys. Rev. D, 71:063502, Mar 2005. 75, 88, 89, 90, 107

[127] A. N. Lasenby. Conformal geometry and the universe. http://www.mrao.cam.ac.uk/ clifford/publications/abstracts/anlima2002.html. 89, 92

[128] A. N. Lasenby and C. Doran. Conformal Models of de Sitter Space, Initial Conditions for Inflation and the CMB. AIP Conference Proceedings, 736 (1):53–70, 2004. 89, 92

[129] R. Lazkoz, V. Salzano, and I. Sendra. Revisiting a model-independent dark energy reconstruction method. [arXiv:1202.4689], 02 2012. 114, 147

[130] B. Leibundgut. Supernovae and cosmology. General Relativity and Gravitation, 40:221–248, 2008. 59

[131] J. Lesgourgues. The Cosmic Linear Anisotropy Solving System (CLASS) I: Overview. arXiv:1104.2932, 2011. 38

[132] J. Lesgourgues and S. Pastor. Massive neutrinos and cosmology. Physics Reports, 429(6):307 – 379, 2006. 11

[133] A. Lewis and S. Bridle. Cosmological parameters from CMB and other data: A Monte Carlo approach. Physical Review D, 66(10), 2002. 64, 68, 71

[134] A. Lewis, A. Challinor, and A. Lasenby. Efficient Computation of Cosmic Microwave Background Anisotropies in Closed Friedmann-Robertson-Walker Models. The Astrophysical Journal, 538(2):473, 2000. 38, 70, 114, 134, 156

[135] A. R. Liddle. An Introduction to cosmological inflation. pages 260–295, 1999. astro-ph/9901124. 20

[136] A. R. Liddle. How many cosmological parameters? Monthly Notices of the Royal Astronomical Society, 351(3):L49–L53, 2004. 50, 66

[137] A. R. Liddle. Statistical Methods for Cosmological Parameter Selection and Estimation. Annual Review of Nuclear and Particle Science, 59(1):95–114, 2009. 63, 64

[138] A. R. Liddle and D. H. Lyth. COBE, gravitational waves, inflation and extended inflation. Physics Letters B, 291(4):391 – 398, 1992. 28, 52

[139] A. R. Liddle and D. H. Lyth. Cosmological Inflation and Large-Scale Structure. Cambridge University Press, 2000. 5, 15, 20, 23, 29, 30, 35

[140] A. R. Liddle, P. Parsons, and J. D. Barrow. Formalizing the slow-roll approximation in inflation. Phys. Rev. D, 50:7222–7232, Dec 1994. 28

[141] A. R. Liddle, P. Mukherjee, and D. Parkinson. Cosmological model selection. [arXiv:0608184], 2006. 63, 65, 66

[142] A. Linde. A new inflationary universe scenario: A possible solution of the horizon, flatness, homogeneity, isotropy and primordial monopole problems. Physics Letters B, 108(6):389 – 393, 1982. 20

[143] A. Linde. Particle Physics and Inflationary Cosmology. CRC Press, 1990. 20

[144] A. D. Linde. Inflationary Cosmology. Lect.Notes Phys., 738:1–54, 2008. 26

[145] E. V. Linder. Exploring the Expansion History of the Universe. Phys. Rev. Lett., 90:091301, Mar 2003. 113, 121

[146] E. V. Linder and D. Huterer. How many dark energy parameters? Phys. Rev. D, 72:043509, Aug 2005. 114

[147] J. Lu, Y. Wu, Y. Jin, and Y. Wang. Investigate the interaction between dark matter and dark energy. [arXiv:1203.4905], 03 2012. 113

[148] D. H. Lyth and A. Riotto. Particle physics models of inflation and the cosmological density perturbation. Physics Reports, 314(1–2):1 – 146, 1999. 20, 26, 29

[149] C.-P. Ma and E. Bertschinger. Cosmological Perturbation Theory in the Synchronous and Conformal Newtonian Gauges. [arXiv:9506072], 1995. 30, 148

[150] J.-Z. Ma and X. Zhang. Probing the dynamics of dark energy with novel parametrizations. Physics Letters B, 699(4):233 – 238, 2011. 113

[151] Y.-Z. Ma, W. Zhao, and M. L. Brown. Constraints on standard and non-standard early universe models from CMB B -mode polarization. Journal of Cosmology and Astroparticle Physics, 2010(10):007, 2010. 63

[152] R. Maartens. Brane-World Gravity. Living Reviews in Relativity, 7(7), 2004. 113, 147

[153] G. Mangano, G. Miele, S. Pastor, T. Pinto, O. Pisanti, and P. D. Serpico. Relic neutrino decoupling including flavour oscillations. Nuclear Physics B, 729:221 – 234, 2005. 11

[154] M. C. March, N. V. Karpenka, F. Feroz, and M. P. Hobson. Comparison of cosmological parameter inference methods applied to supernovae lightcurves fitted with SALT2. [arXiv: 1207.3705], 2012. 54

[155] V. Marra, M. Paakkonen, and W. Valkenburg. Bias on w from large-scale structure. [arXiv:1203.2180], 2012. 113

[156] P. Marshall, N. Rajguru, and A. c. v. Slosar. Bayesian evidence as a tool for comparing datasets. Phys. Rev. D, 73:067302, Mar 2006. 68, 143

[157] M. Martinelli, A. Melchiorri, and L. Amendola. Cosmological constraints on the Hu-Sawicki modified gravity scenario. Phys. Rev. D, 79:123516, Jun 2009. 151

[158] M. Martinelli, E. Calabrese, F. De Bernardis, A. Melchiorri, L. Pagano, and R. Scaramella. Constraining modified gravitational theories by weak lensing with Euclid. Phys. Rev. D, 83:023012, Jan 2011. 148

[159] S. Matarrese, C. Baccigalupi, and F. Perrotta. Approaching Λ without fine-tuning. Phys. Rev. D, 70:061301, Sep 2004. 113

[160] J. C. Mather and *et. al.* Calibrator design for the cobe far infrared absolute spectrophotometer (firas). The Astrophysical Journal, 512(2):511, 1999. 56

[161] P. McDonald, U. Seljak, S. Burles, and et al. The ly forest power spectrum from the sloan digital sky survey. The Astrophysical Journal Supplement Series, 163(1):80, 2006. 60

[162] O. Mena, J. Santiago, and J. Weller. Constraining Inverse-Curvature Gravity with Supernovae. Phys. Rev. Lett., 96:041103, Feb 2006. 154

[163] G. Miknaitis and *et. al.* The ESSENCE Supernova Survey: Survey Optimization, Observations, and Supernova Photometry. The Astrophysical Journal, 666(2):674, 2007. 59

[164] A. Mithani and A. Vilenkin. Did the universe have a beginning? [arXiv:1204.4658]. 129

[165] D. F. Mota, J. R. Kristiansen, T. Koivisto, and N. E. Groeneboom. Constraining dark energy anisotropic stress. Monthly Notices of the Royal Astronomical Society, 382(2):793–800, 2007. 113

[166] H. Motohashi, A. A. Starobinsky, and J. Yokoyama. f(R) Gravity and its Cosmological Implications. Int.J.Mod.Phys., D20:1347–1355, 2011. 117, 147

[167] V. Mukhanov. Physical Foundations of Cosmology. Cambridge University Press, 2005. 5, 20, 30, 34, 39

[168] V. Mukhanov, H. Feldman, and R. Brandenberger. Theory of cosmological perturbations. Physics Reports, 215:203 – 333, 1992. 30, 33

[169] P. Mukherjee and Y. Wang. Primordial power spectrum reconstruction. Journal of Cosmology and Astroparticle Physics, 2005(12):007, 2005. 75

[170] P. Mukherjee, D. Parkinson, and A. R. Liddle. A Nested Sampling Algorithm for Cosmological Model Selection. The Astrophysical Journal Letters, 638(2):L51, 2006. 68

[171] S. Nojiri and S. D. Odintsov. Modified $f(R)$ gravity consistent with realistic cosmology: From a matter dominated epoch to a dark energy universe. Phys. Rev. D, 74:086005, Oct 2006. 113, 148

[172] K. A. Olive. Inflation. Physics Reports, 190(6):307 – 403, 1990. 20, 26

[173] P. Oxley, P. A. Ade, and et al. The EBEX experiment. Proc. SPIE 5543, Infrared Spaceborne Remote Sensing XII, pages 320–331, 2004. 61

[174] T. Padmanabhan. Cosmological constant—the weight of the vacuum. Physics Reports, 380(5–6):235 – 320, 2003. 8, 12, 147

[175] D. Parkinson and A. R. Liddle. Application of bayesian model averaging to measurements of the primordial power spectrum. Phys. Rev. D, 82:103533, Nov 2010. 103

[176] P. J. E. Peebles and B. Ratra. The cosmological constant and dark energy. Rev. Mod. Phys., 75:559–606, Apr 2003. 12, 147

[177] H. Peiris. Cosmology Part I: The Unperturbed Universe. *http://nefertiti.hpc.phys.ucl.ac.uk/cosmology/cosmology.html*, 2008. 5

[178] H. V. Peiris and L. Verde. The shape of the primordial power spectrum: A last stand before Planck data. Phys. Rev. D, 81:021302, Jan 2010. 76

[179] R. Penrose. Cycles of Time. Bodley Head (UK), 2010. 129

[180] S. Perlmutter, G. Aldering, G. Goldhaber, and et al. Measurements of Ω and Λ from 42 High-Redshift Supernovae. The Astrophysical Journal, 517 (2):565, 1999. 6, 59, 113

[181] L. Perotto, J. Lesgourgues, S. Hannestad, H. Tu, and Y. Y. Y. Wong. Probing cosmological parameters with the CMB: forecasts from Monte Carlo simulations. Journal of Cosmology and Astroparticle Physics, 2006(10): 013, 2006. 63

[182] M. Pettini. Physical Cosmology. *http://www.ast.cam.ac.uk/∼pettini/physical%20cosmology*, 2008. 5

[183] V. Pettorino, C. Baccigalupi, and F. Perrotta. Scaling solutions in scalar–tensor cosmologies. Journal of Cosmology and Astroparticle Physics, 2005 (12):003, 2005. 113

[184] C. Pitrou. The package CMBquick. 2011. *http://www2.iap.fr/users/pitrou/*. 38

[185] Planck Collaboration. The Science Programme of Planck. [astro-ph/0604069], 2012. 61, 63

[186] L. Pogosian and A. Silvestri. Pattern of growth in viable $f(R)$ cosmologies. Phys. Rev. D, 77:023503, Jan 2008. 152, 153, 154

[187] B. A. Powell. Tensor tilt from primordial b-modes. [arXiv:1106.5059], 2011. 62

[188] B. A. Powell. Scalar runnings and a test of slow roll from CMB distortions. [arXiv:1209.2024], 2012. 103

[189] B. Ratra and P. J. E. Peebles. Cosmological consequences of a rolling homogeneous scalar field. Phys. Rev. D, 37:3406–3427, Jun 1988. 113, 147

[190] B. A. Reid and *et. al.* Cosmological constraints from the clustering of the Sloan Digital Sky Survey DR7 luminous red galaxies. Monthly Notices of the Royal Astronomical Society, 404(1):60–85, 2010. 60, 70

[191] A. G. Riess and *et. al.* New Hubble Space Telescope Discoveries of Type Ia Supernovae at $z \geq 1$ Narrowing Constraints on the Early Behavior of Dark Energy. The Astrophysical Journal, 659(1):98, 2007. 60

[192] A. G. Riess and *et. al.* A Redetermination of the Hubble Constant with the Hubble Space Telescope from a Differential Distance Ladder. The Astrophysical Journal, 699(1):539, 2009. 70, 144

[193] A. G. Riess, A. V. Filippenko, P. Challis, and et al. Observational evidence from supernovae for an accelerating universe and a cosmological constant. The Astronomical Journal, 116(3):1009, 1998. 6, 59, 113

[194] A. Riotto. Inflation and the theory of cosmological perturbations. pages 317–413, 2002. arXiv:0210162. 20, 35

[195] D. Rubin and *et. al.* Looking Beyond Lambda with the Union Supernova Compilation. The Astrophysical Journal, 695(1):391, 2009. 114, 134

[196] J. Rubino-Martin, R. Rebolo, M. Tucci, R. Genova-Santos, S. Hildebrandt, et al. The Quijote CMB Experiment. 2008. arXiv:0810.3141. 61

[197] A. T. S. Capozziello, S. Carloni. Quintessence without scalar fields. Recent Res. Dev. Astron. Astrop., 1(625), 2003. 147

[198] R. Sachs and A. Wolfe. Perturbations of a cosmological model and angular variations of the microwave background. Astrophys.J., 147:73–90, 1967. 43

[199] V. Sahni and S. Habib. Does Inflationary Particle Production Suggest $\Omega_m > 1$. Phys. Rev. Lett., 81:1766–1769, Aug 1998. 113

[200] V. Sahni and Y. Shtanov. Braneworld models of dark energy. Journal of Cosmology and Astroparticle Physics, 2003(11):014, 2003. 117

[201] V. Sahni and A. Starobinsky. Reconstructing Dark Energy. International Journal of Modern Physics D, 15(12):2105–2132, 2006. 114

[202] V. Sahni, A. Shafieloo, and A. A. Starobinsky. Two new diagnostics of dark energy. Phys. Rev. D, 78:103502, Nov 2008. 114

[203] T. D. Saini, S. Raychaudhury, V. Sahni, and A. A. Starobinsky. Reconstructing the Cosmic Equation of State from Supernova Distances. Phys. Rev. Lett., 85:1162–1165, Aug 2000. 114

[204] F. Schmidt, A. Vikhlinin, and W. Hu. Cluster constraints on $f(R)$ gravity. Phys. Rev. D, 80:083505, Oct 2009. 158

[205] M. Seikel, C. Clarkson, and M. Smith. Reconstruction of dark energy and expansion dynamics using Gaussian processes. [arXiv:1204.2832], 2012. 114

[206] U. Seljak and M. Zaldarriaga. A Line of sight integration approach to cosmic microwave background anisotropies. Astrophys.J., 469:437–444, 1996. 38, 42

[207] J. Sellwood and A. Kosowsky. Does dark matter exist? 2000. astro-ph/0009074. 12

[208] I. Sendra and R. Lazkoz. SN and BAO constraints on (new) polynomial dark energy parametrizations: current results and forecasts. [arXiv:1105.4943], 05 2011. 113, 134

[209] P. Serra, A. Cooray, D. E. Holz, A. Melchiorri, S. Pandolfi, and D. Sarkar. No evidence for dark energy dynamics from a global analysis of cosmological data. Phys. Rev. D, 80:121302, Dec 2009. 114, 119

[210] A. Shafieloo. Crossing Statistic: Reconstructing the Expansion History of the Universe. [arXiv:1204.1109], 2012. 114

[211] A. Shafieloo, U. Alam, V. Sahni, and A. A. Starobinsky. Smoothing supernova data to reconstruct the expansion history of the Universe and its age. Monthly Notices of the Royal Astronomical Society, 366(3):1081–1095, 2006. 114

[212] A. Shafieloo, V. Sahni, and A. A. Starobinsky. Is cosmic acceleration slowing down? Phys. Rev. D, 80:101301, Nov 2009. 113

[213] A. Shafieloo, A. G. Kim, and E. V. Linder. Gaussian Process Cosmography. [arXiv:1204.2272], 2012. 114

[214] Sievers and *et. al.* The Atacama Cosmology Telescope: Cosmological parameters from three seasons of data. [arXiv: 1301.0824], 2013. 54, 57

[215] J. L. Sievers and *et. al.* Cosmological Parameters from Cosmic Background Imager Observations and comparisons with boomerang, dasi, and maxima. The Astrophysical Journal, 591(2):599, 2003. 57

[216] D. Sivia and J. Skilling. Data Analysis: A Bayesian Tutorial. OUP Oxford, 2006. 63

[217] J. Skilling. Nested sampling for general Bayesian computation. Bayesian Analysis, 1(4):833–860, 2006. 68

[218] Y.-S. Song, W. Hu, and I. Sawicki. Large scale structure of $f(R)$ gravity. Phys. Rev. D, 75:044004, Feb 2007. 148

[219] Y.-S. Song, H. Peiris, and W. Hu. Cosmological constraints on $f(R)$ acceleration models. Phys. Rev. D, 76:063517, Sep 2007. 148

[220] A. Starobinsky. Disappearing cosmological constant in $f(R)$ gravity. JETP Letters, 86:157–163, 2007. 10.1134/S0021364007150027. 113, 117, 147, 153, 154

[221] G. Steigman. Primordial Nucleosynthesis in the Precision Cosmology Era. Annual Review of Nuclear and Particle Science, 57(1):463–491, 2007. 11

[222] J. Stewart. Advanced General Relativity. Cambridge Monographs on Mathematical Physics, 1994. 31

[223] K. T. Story and *et. al.* A Measurement of the Cosmic Microwave Background Damping Tail from the 2500-square-degree SPT-SZ survey. [arXiv:1210.7231], 2012. 57

[224] M. Sullivan and *et. al.* SNLS3: Constraints on Dark Energy Combining the Supernova Legacy Survey Three-year Data with Other Probes. The Astrophysical Journal, 737(2):102, 2011. 59

[225] N. Suzuki and *et. al.* The Hubble Space Telescope Cluster Supernova Survey. V. Improving the Dark-energy Constraints above $z > 1$ and Building an Early-type-hosted Supernova Sample. The Astrophysical Journal, 746 (1):85, 2012. 60

[226] The Dark Energy Survey.*http://www.darkenergysurvey.org/index.shtml*, 2012. 61

[227] D. Tocchini-Valentini, Y. Hoffman, and J. Silk. Non-parametric reconstruction of the primordial power spectrum at horizon scales from WMAP data. Monthly Notices of the Royal Astronomical Society, 367(3):1095–1102, 2006. 75

[228] R. Trotta. Bayes in the sky: Bayesian inference and model selection in cosmology. Contemporary Physics, 49(2):71–104, 2008. 53, 54, 63, 65, 66

[229] S. Tsujikawa. Matter density perturbations and effective gravitational constant in modified gravity models of dark energy. Phys. Rev. D, 76:023514, Jul 2007. 152

[230] S. Tsujikawa. Observational signatures of $f(R)$ dark energy models that satisfy cosmological and local gravity constraints. Phys. Rev. D, 77:023507, Jan 2008. 154

[231] L. A. Ureña López and T. Matos. New cosmological tracker solution for quintessence. Phys. Rev. D, 62:081302, Sep 2000. 113

[232] W. Valkenburg. Perceiving the equation of state of Dark Energy while living in a Cold Spot. Journal of Cosmology and Astroparticle Physics, 2012(01): 047, 2012. 113

[233] J. A. Vazquez, M. Bridges, M. Hobson, and A. Lasenby. Reconstruction of the Dark Energy equation of state. [arXiv:1205.0847]. 138, 145, 147

[234] J. A. Vazquez, M. Bridges, M. Hobson, and A. Lasenby. Model selection applied to reconstruction of the Primordial Power Spectrum. Journal of Cosmology and Astroparticle Physics, 2012(06):06, 2012. [arXiv:1203.1252]. 108, 110, 114, 138, 147, 156

[235] J. A. Vazquez, M. Hobson, A. Lasenby, M. Ibison, and M. Bridges. Reciprocity invariance of the Friedmann equation, Missing Matter and double Dark Energy. [arXiv:1208.2542], 2012. 13

[236] J. A. Vázquez, A. N. Lasenby, M. Bridges, and M. P. Hobson. A Bayesian study of the primordial power spectrum from a novel closed universe model. Monthly Notices of the Royal Astronomical Society, 422(3):1948–1956, 2012. 92, 93, 108

[237] L. Verde. A practical guide to Basic Statistical Techniques for Data Analysis in Cosmology. [arXiv:0712.3028], 2008. 63

[238] L. Verde. Statistical methods in cosmology. [arXiv:0911.3105], 2009. 63

[239] A. Vikman. Can dark energy evolve to the phantom? Phys. Rev. D, 71: 023515, Jan 2005. 113

[240] A. Vilenkin. Cosmic strings and domain walls. Physics Reports, 121(5):263 – 315, 1985. 13, 129

[241] D. N. Vollick. On the viability of the Palatini form of 1/ R gravity. Classical and Quantum Gravity, 21(15):3813, 2004. 149

[242] U. von Toussaint. Bayesian inference in physics. Rev. Mod. Phys., 83: 943–999, Sep 2011. 63

[243] Y. Wang and M. Tegmark. New Dark Energy Constraints from Supernovae, Microwave Background, and Galaxy Clustering. Phys. Rev. Lett., 92:241302, Jun 2004. 114

[244] Y. Wang and M. Tegmark. Uncorrelated measurements of the cosmic expansion history and dark energy from supernovae. Phys. Rev. D, 71:103513, May 2005. 114

[245] J. Weller and A. Albrecht. Future supernovae observations as a probe of dark energy. Phys. Rev. D, 65:103512, May 2002. 114

[246] C. Wetterich. Phenomenological parameterization of quintessence. Physics Letters B, 594(1–2):17 – 22, 2004. 113

[247] C. M. Will. The Confrontation between General Relativity and Experiment. Living Reviews in Relativity, 4(4), 2001. 152

[248] M. Zaldarriaga and U. c. v. Seljak. All-sky analysis of polarization in the microwave background. Phys. Rev. D, 55:1830–1840, Feb 1997. 38

[249] H. Zhang. Crossing the phantom divide. [arXiv:0909.3013], 2009. 117

[250] Q.-J. Zhang and Y.-L. Wu. Modelling Time-varying Dark Energy with Constraints from Latest Observations. [arXiv:1103.1953], 2011. 113

[251] W.-S. Zhang and et. al. Testing modified gravity models with recent cosmological observations. [arXiv:1202.0892], 2012. 158

[252] G.-B. Zhao and X. Zhang. Probing dark energy dynamics from current and future cosmological observations. Phys. Rev. D, 81:043518, Feb 2010. 114, 147

[253] G.-B. Zhao, D. Huterer, and X. Zhang. High-resolution temporal constraints on the dynamics of dark energy. Phys. Rev. D, 77:121302, Jun 2008. 114

[254] G.-B. Zhao, L. Pogosian, A. Silvestri, and J. Zylberberg. Searching for modified growth patterns with tomographic surveys. Phys. Rev. D, 79: 083513, Apr 2009. 148, 157

[255] I. Zlatev, L. Wang, and P. J. Steinhardt. Quintessence, Cosmic Coincidence, and the Cosmological Constant. Phys. Rev. Lett., 82:896–899, Feb 1999. 113, 147

[256] C. Zunckel and R. Trotta. Reconstructing the history of dark energy using maximum entropy. Monthly Notices of the Royal Astronomical Society, 380(3):865–876, 2007. 114